

**Carbonated water flooding**  
**Process overview in the frame of co2 flooding**

Peksa, Anna

**DOI**

[10.4233/uuid:ed994629-1130-4c92-a6ec-1d03f5f5f211](https://doi.org/10.4233/uuid:ed994629-1130-4c92-a6ec-1d03f5f5f211)

**Publication date**

2017

**Document Version**

Final published version

**Citation (APA)**

Peksa, A. (2017). *Carbonated water flooding: Process overview in the frame of co2 flooding*. [Dissertation (TU Delft), Delft University of Technology]. <https://doi.org/10.4233/uuid:ed994629-1130-4c92-a6ec-1d03f5f5f211>

**Important note**

To cite this publication, please use the final published version (if applicable).  
Please check the document version above.

**Copyright**

Other than for strictly personal use, it is not permitted to download, forward or distribute the text or part of it, without the consent of the author(s) and/or copyright holder(s), unless the work is under an open content license such as Creative Commons.

**Takedown policy**

Please contact us and provide details if you believe this document breaches copyrights.  
We will remove access to the work immediately and investigate your claim.

# **CARBONATED WATER FLOODING**

PROCESS OVERVIEW IN THE FRAME OF CO<sub>2</sub> FLOODING





# **CARBONATED WATER FLOODING**

PROCESS OVERVIEW IN THE FRAME OF CO<sub>2</sub> FLOODING

## **Proefschrift**

ter verkrijging van de graad van doctor  
aan de Technische Universiteit Delft,  
op gezag van de Rector Magnificus prof. ir. K.C.A.M. Luyben,  
voorzitter van het College voor Promoties,  
in het openbaar te verdedigen op maandag 3 juli 2017 om 10:00 uur

door

**Anna Ewelina PEKSA**

Master of Science in Applied Earth Sciences  
geboren te Zakopane, Polen.

Dit proefschrift is goedgekeurd door de

promotor: Prof. dr. P.L.J. Zitha

copromotor: Dr. K.H.A.A. Wolf

Samenstelling promotiecommissie:

Rector Magnificus,	voorzitter
Prof. dr. P.L.J. Zitha	Technische Universiteit Delft
Dr. K.H.A.A. Wolf	Technische Universiteit Delft

*Onafhankelijke leden:*

Prof. dr. ir. H.E.J.G. Schlangen	Technische Universiteit Delft
Prof. dr. J. Bruining	Technische Universiteit Delft
Prof. dr. ir. E.C. Slob	Technische Universiteit Delft
Dr. H. Hajibeygi	Technische Universiteit Delft
Dr. K. Elewaut	Nederlandse Organisatie voor Wetenschappelijk Onderzoek

*Overige leden:*

Prof. dr. W.R. Rossen	Technische Universiteit Delft, reservelid
-----------------------	---



*Funded by:* Dutch CCS research programme CO2 Afvang, Transport en Opslag (CATO2)

*Keywords:* Enhanced oil recovery, carbonated water flooding, carbon capture and storage, Bentheimer sandstone, mineralogy, molecular diffusion, dielectric behavior, zeta potential, stagnant zone

Copyright © 2017 by Anna Pekska

ISBN 978-94-028-0687-8

An electronic version of this dissertation is available at  
<http://repository.tudelft.nl/>.

# CONTENTS

<b>1</b>	<b>Introduction</b>	<b>1</b>
1.1	Process outline . . . . .	1
1.2	Carbonated water flooding – history . . . . .	4
1.3	Carbonated water flooding - theory. . . . .	5
1.4	Outline of the thesis. . . . .	6
	References . . . . .	9
<b>2</b>	<b>General rock characterization</b>	<b>11</b>
2.1	Introduction . . . . .	14
2.2	Literature overview . . . . .	15
2.3	Geological setting. . . . .	16
2.4	Materials . . . . .	19
	2.4.1 Sample materials . . . . .	19
	2.4.2 Sample textures, structures and mineralogy . . . . .	21
2.5	Methods . . . . .	21
	2.5.1 Image analysis procedures . . . . .	21
	2.5.2 Laboratory procedures. . . . .	23
2.6	Results and discussion . . . . .	26
	2.6.1 Petrography and mineralogy. . . . .	26
	2.6.2 Petrophysical data . . . . .	31
2.7	Conclusions. . . . .	44
	References . . . . .	48
<b>3</b>	<b>Rock characterization for electrokinetic studies</b>	<b>59</b>
3.1	Introduction . . . . .	62
3.2	Materials and methods . . . . .	63
	3.2.1 Firing . . . . .	63
	3.2.2 Characterization of unfired and fired samples and thermal analysis . . . . .	63
	3.2.3 Dielectric spectroscopy . . . . .	65
3.3	Results and discussion . . . . .	70
	3.3.1 XRD/XRF analysis and SEM interpretation: general results . . . . .	70
	3.3.2 Thermal analysis and phase transformations . . . . .	73
	3.3.3 Porosity and permeability . . . . .	74
	3.3.4 Surface charge . . . . .	76
	3.3.5 Dielectric spectroscopy . . . . .	76
3.4	Conclusions. . . . .	82
	References . . . . .	83

<b>4</b>	<b>Electrokinetic effects in rock–fluid interaction</b>	<b>89</b>
4.1	Introduction . . . . .	92
4.2	Electrokinetic phenomena . . . . .	93
4.3	Experimental approach . . . . .	95
4.3.1	Materials. . . . .	95
4.3.2	Experimental setup . . . . .	96
4.3.3	Experimental procedure . . . . .	98
4.4	Results and discussion . . . . .	99
4.4.1	Calibration tests . . . . .	100
4.4.2	Baseline experiment . . . . .	100
4.4.3	Effect of CO <sub>2</sub> concentration on wetting behavior and CO <sub>2</sub> storage . . . . .	104
4.4.4	Effect of porous material. . . . .	106
4.5	Conclusions. . . . .	108
	References . . . . .	109
<b>5</b>	<b>Fluid–fluid interactions in stagnant pore geometries</b>	<b>117</b>
5.1	Introduction . . . . .	119
5.2	Experimental approach . . . . .	120
5.2.1	Materials. . . . .	120
5.2.2	Experimental setup . . . . .	121
5.2.3	Experimental procedure . . . . .	121
5.2.4	Physical and chemical properties . . . . .	122
5.3	Results and discussion . . . . .	122
5.3.1	Mechanisms in the stagnant zone during different CO <sub>2</sub> injection schemes . . . . .	124
5.3.2	Flow rate - factor influencing molecular diffusion in DEP . . . . .	125
5.3.3	Effect of water barrier and oil volume entrapped in DEP. . . . .	128
5.3.4	Discussion on efficiency of different scenarios used for EOR. . . . .	132
5.4	Conclusions. . . . .	133
	References . . . . .	134
<b>6</b>	<b>Influence of fluid–fluid interactions on diffusion</b>	<b>139</b>
6.1	Introduction . . . . .	141
6.2	Oil recovery by CWF. . . . .	142
6.2.1	Binary system CO <sub>2</sub> -H <sub>2</sub> O . . . . .	143
6.2.2	Binary system CO <sub>2</sub> - oil . . . . .	143
6.2.3	Three component system . . . . .	144
6.2.4	Model of the single dead-end pore . . . . .	144
6.3	Experimental approach . . . . .	148
6.3.1	Materials. . . . .	148
6.3.2	Experimental setup . . . . .	148
6.3.3	Experimental procedure . . . . .	149
6.4	Results and discussions . . . . .	150
6.4.1	Simulations . . . . .	150
6.4.2	Experiment: base case . . . . .	151

---

6.5 Overall results and discussion. . . . .	155
6.6 Conclusions. . . . .	157
References . . . . .	159
<b>7 Combined EOR and CO<sub>2</sub> storage</b>	<b>163</b>
7.1 Introduction . . . . .	165
7.2 Theoretical CO <sub>2</sub> storage capacity . . . . .	166
7.3 Experimental approach . . . . .	166
7.3.1 Materials. . . . .	166
7.3.2 Experimental setup . . . . .	168
7.3.3 Experimental procedure . . . . .	168
7.3.4 CT scanning . . . . .	169
7.4 Results and discussion . . . . .	170
7.4.1 Baseline experiment . . . . .	170
7.4.2 Effect of injection scenarios on oil recovery . . . . .	176
7.4.3 Effect of experimental conditions on CO <sub>2</sub> storage . . . . .	177
7.5 Conclusions. . . . .	178
References . . . . .	179
<b>8 Conclusion</b>	<b>183</b>
<b>Samenvatting</b>	<b>189</b>
<b>About the Author</b>	<b>195</b>
<b>List of Publications</b>	<b>197</b>



# 1

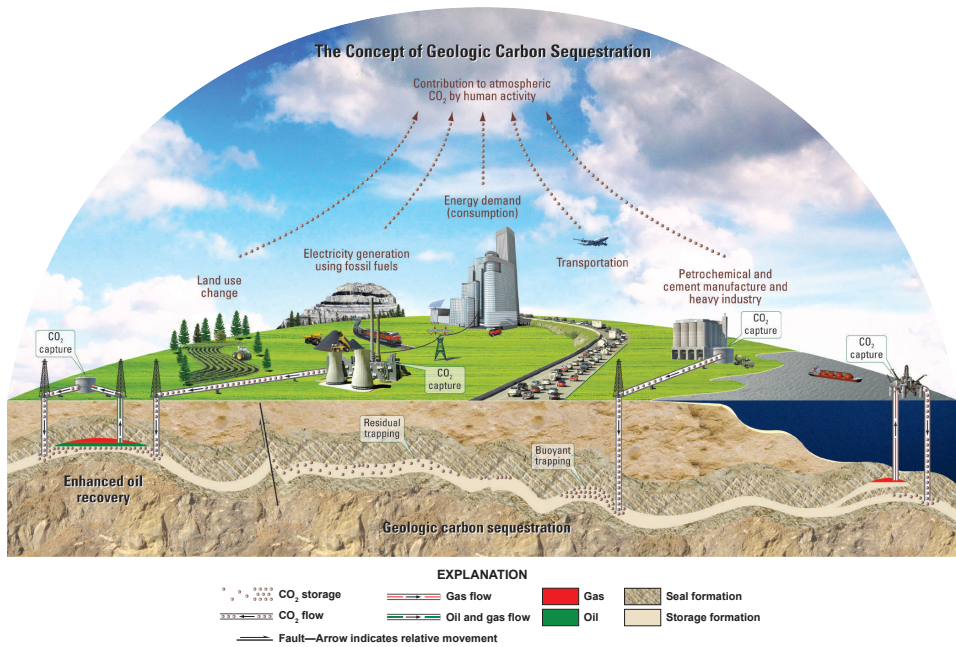
## INTRODUCTION

### 1.1. PROCESS OUTLINE

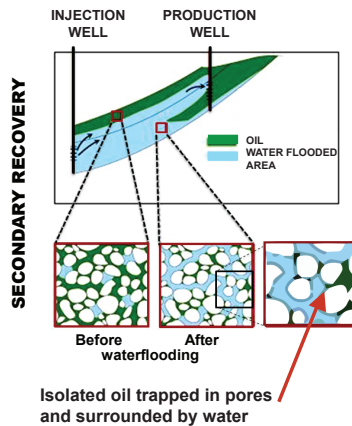
Carbon dioxide is a by-product of many industrial operations around the world, including the burning of fossil fuels (oil, gas, coal) in power plants, steel works and the manufacturing of cement. The release of CO<sub>2</sub> into the atmosphere has an adverse impact on the environment. One approach to keep carbon emissions under control is to develop safe and continuous methods for CO<sub>2</sub> Capture and Storage (CCS). The possible mitigation techniques are the immobilization and safe disposal of CO<sub>2</sub> underground in porous strata: saline porous reservoir rocks (deep underground rock formations saturated with saline fluids), coal formations and principally depleted oil and gas reservoirs can be used for efficient storage of CO<sub>2</sub>. The immobilization and safe disposal of CO<sub>2</sub> may occur by the following mechanisms (Fig. 1.1): (1) trapping below an impermeable layer; (2) dissolution in the in-situ formation fluids; (3) capillary trapping as an immobile phase confined in the pores of the reservoir matrix; (4) adsorption onto organic matter in coal and shale; (5) and mineral carbonation.

In the Netherlands, in 2001, substantial interest in environmental protection, especially the mitigation of the greenhouse gases, resulted in the establishment of a national R&D program for CO<sub>2</sub> capture, transport, and storage called CO<sub>2</sub> Afdwang, Transport en Opslag (CATO 1 and 2). The first phase of the CATO program focused on technical, economical, societal and ecological issues related to CCS as a contributor to a more sustainable energy system. "CATO has developed into a successful research network in the Netherlands and has become the Dutch national CCS program. It should be noted that this was not the original intention, but through the nature of the activity, CATO has initiated numerous CCS projects in the Netherlands that are now highly relevant to the new national Dutch policy on climate change, where CCS is recognized as an important element. CATO is therefore a 'gift to government' and has established a much-needed basis of a national capability in CCS. CATO is well linked to CCS research activities internationally and, especially, in Europe. It is one of the few national European CCS programs covering the entire CCS chain. The active participation of industry, research institutes





(a)



(b)

Figure 1.1: (a) Graphical representation of terrestrial and geological sequestration of CO<sub>2</sub> emissions [1]; (b) Oil trapped in the pore spaces after secondary recovery.

universities and NGO's makes CATO a powerful consortium which is similar in nature to the highly influential Zero Emission European Union Technology Platform" (Internat-

tional review committee, 2007). The second phase of CATO focuses on research and an integrated development in five subprogram lines: CO<sub>2</sub> capture; transport and CCS chain integration; subsurface storage of CO<sub>2</sub> and monitoring storage; regulation and safety; and finally, public perception.

The thesis research is a part of the CATO2 storage activities and particularly concerned with storage of CO<sub>2</sub> in depleted oil reservoirs, i.e. oil reservoirs which were subject to primary production and secondary extensive water flooding. In the early life of an oilfield, oil is produced either by pumping or due to natural pressures present in the formation (primary recovery). When pressure is too low to force oil to the surface, water injection is applied for maintaining pore pressure (secondary recovery). The recovery factors of combined primary and secondary recovery typically vary between 40 and 60% [2]. Water flooding performance can be affected by the reservoir factors, such as heterogeneity, connectivity in the porous matrix, and by interactions between injected and in place fluids, like the mobility ratio [3]. Therefore, techniques that modify the fluid properties, or influence the rock-fluids interactions, have to be applied to increase oil production. Such techniques belong to the Enhanced Oil Recovery (EOR) category. CO<sub>2</sub> flooding is one of such EOR techniques, involving a transfer of CO<sub>2</sub> into the oil phase, and, as a result, induces volume increase, viscosity, and interfacial tension reduction. It offers an advantage, i.e. high miscibility with light oil at relatively low minimum miscibility pressures. However, the main disadvantage is that the differential buoyancy of CO<sub>2</sub> and oil impose gravity separation and, in the worst case, CO<sub>2</sub> leakage from the storage reservoir upwards into groundwater and finally to the surface. Therefore, dissolving CO<sub>2</sub> in water and creating sparkling water (carbonated water) as a recovery enhancing agent, has the potential to minimize issues arising during CO<sub>2</sub> flooding.

The main objective of all CCS EOR projects is an optimal oil recovery together with effective storage of CO<sub>2</sub> in the final stage of the injection process. Whereas the CO<sub>2</sub> flooding process requires a continuous source of large volumes of CO<sub>2</sub>, the above-mentioned technique, called carbonated water flooding (CWF), requires small volumes of this gas. Moreover, CWF has two additional advantages over pure CO<sub>2</sub> flooding: (1) Related to oil recovery: At specific pressure–temperature ( $P$ - $T$ ) reservoir conditions, CO<sub>2</sub> primarily dissolved in water and further transferred to an oil phase. So, the CO<sub>2</sub> front advances more gradually than the water front [4]. Further, the dissolution of CO<sub>2</sub> in the oil phase increases oil mobility. The oil volume expansion and viscosity reduction have an influence on the oil relative permeability increase and enhancement of oil mobility. As a result, firstly CWF has better sweep efficiency than gas due to the comparable viscosities of CW and oil and secondly, there is a much better flooding (Fig. 1.2) due to the lower mobility and density contrasts [5]; (2) Related to geological storage: CO<sub>2</sub> cannot escape from the formation as it is dissolved in water under in-situ  $P$ - $T$  and thus cannot rise to the surface.

From a technical point, at the field scale, the injectivity rate of CO<sub>2</sub> (for CW) improves over water, but it is expected to be lower than for pure CO<sub>2</sub> flooding, resulting in a slower response of oil in the reservoir (i.e., swelling and viscosity reduction). In contrast to water flooding, for both CO<sub>2</sub> and CW flooding the corrosion of carbon steel facilities, due to the formation of carbonic acid, might be an issue additionally leading to asphaltene and paraffins. Subsequently, reservoir and pipeline blockage can be expected.

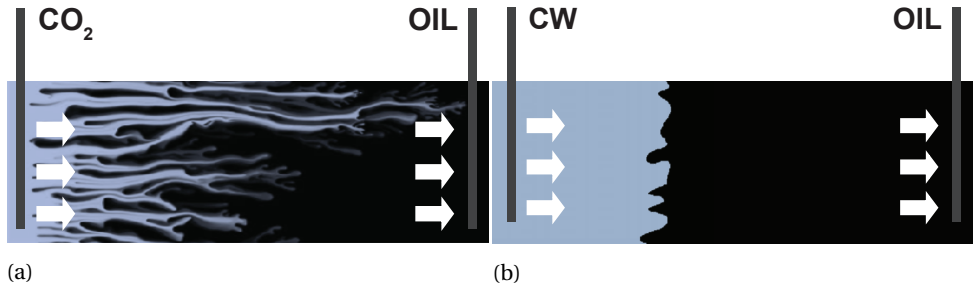


Figure 1.2: Schematic illustration of the oil sweep efficiency in a 2-D cross-section of a typical reservoir: (a) CO<sub>2</sub> flooding (b) CWF [15].

From an economical point of view, the trends of cost and profits of the coupled EOR-CCS projects fluctuate. An example of the costs and profits of CO<sub>2</sub>/CW-EOR investment is shown in (Fig. 1.3). To balance the high up-front, operating and production costs and to improve the financial feasibility, tax incentives were introduced [7]. As a result, cash flow improvement can be obtained.

## 1.2. CARBONATED WATER FLOODING – HISTORY

The CWF process is known under the names 'soda pop drive' and 'fizzy water-flooding'. It was introduced in the 1940s and since then the initial theoretical and experimental studies were conducted at core scale: (1) in sand-packs and (2) in intact rock samples at various operating  $P$ - $T$  conditions (e.g. [3, 4, 8–16]). An elaborate literature review was given by Mosavat (2014) [15]. In 1951 Martin studied the impact of natural gases, organic components and wetting agents on CWF oil recovery and reported that CWF reduced the initial oil saturation by about 12% [8]. Successive coreflood experiments by Johnson et al. (1952) that studied the effect of CWF on oil recovery observed an increase in the recovery factor by 15% to 25% and Holm (1959) reported 19% and 21% of recovery improvement [10]. Panteleev and Tumasyan (1972) showed that CW imbibition led to an 11% increase of oil recovery compared to water imbibition.

In the intervening time, the CWF process and the imbibition mechanisms by CW were studied theoretically [4, 17–19]. More recent, Sohrabi et al. (2000) simulated core-scale CW floods and further validated the results with experimental data. They reported a lack of consistency between experimental and simulated by a commercial numerical software (Eclipse) recoveries [20]. In 2008 Sohrabi et al. confirmed increased oil recovery by CWF both as a secondary and tertiary recovery method [21]. They proved that the mechanisms controlling oil recovery in CWF include sweep efficiency due to a volume increase of the isolated oil ganglia with the resulting fluid redistribution. Riazi and co-workers (2011) proposed a theoretical approach to simulate the pore-scale behavior of a model oil exposed to direct and indirect contact with a CO<sub>2</sub> source [22]. Moreover, the process of the mass transfer was studied by conducting a series of sensitivity analysis on relevant variables. Mosavat and Torabi (2014) increased the number of free parameters and conducted CWF laboratory experiments in unconsolidated, artificial sand-packs at

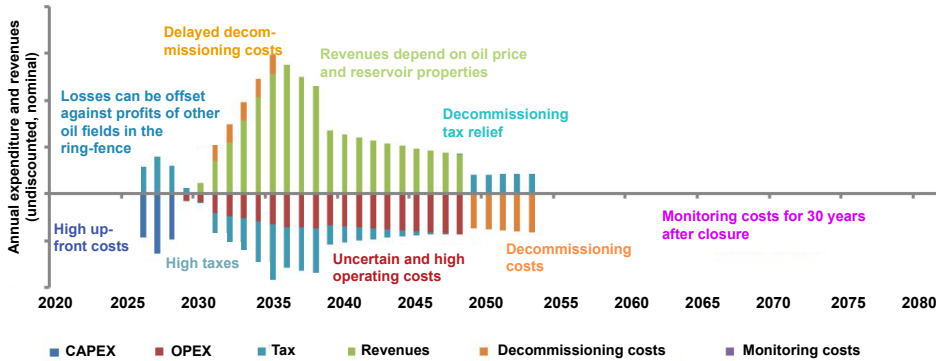


Figure 1.3: Example of CO<sub>2</sub>/CW-EOR expenditure and revenues (after [6]).

different operating conditions using light-oil samples [23]. They found out that the efficiency of CWF is mainly dependent on the temperature of the system and the injection pressure. Moreover, in good agreement with Sohrabi et al. [20], they reported an incremental secondary and tertiary recovery. Ahmadi et al. (2016) showed, by core flood experiments and field scale numerical analysis, the optimal performance of oil recovery at the concentration of 3.2 mol% and injection rate of  $\sim 0.101 \text{ m}^3/\text{s}$  [16]. Additional references on parameters in the previous paragraphs are discussed in the following chapters.

### 1.3. CARBONATED WATER FLOODING - THEORY

CWF models were developed based on the Buckley and Leverett theory [24]. De Nevers made the following extended assumptions [4]: (1) there is no dissolution of oil in water or vice versa; (2) the formation pressure is high enough that all CO<sub>2</sub> will be dissolved; (3) the oil and water are in equilibrium at any location where CO<sub>2</sub> is present; (4) lack of mass diffusion of CO<sub>2</sub> in the direction of the flow. The movement of CO<sub>2</sub> occurs due to the flow of oil and water phases and is not a result of diffusion within the two phases.

The solution obtained by De Nevers with the method of characteristics is presented in Figure 1.4. The CWF process is compared to plain water injection by presenting data for a cumulative oil and CO<sub>2</sub> production, the water saturation, and the CO<sub>2</sub> concentrations in the reservoir. In Fig. 1.4a the primary propagation of the water with a constant CO<sub>2</sub> concentration (G–E) can be observed. At this stage, the water saturation is much higher for the CWF (Fig. 1.4b) producing a larger volume of oil. It can be confirmed by a formation of an oil bank without CO<sub>2</sub> (C–B). The carbonated stage is indicated by the E–C section. In Figure 1.4c, the cumulative production of CO<sub>2</sub> is discussed, where the total volume of CO<sub>2</sub> injected is represented by projecting point D on the y-axis. At the same time, point D denotes the end point of the CO<sub>2</sub> production. The cumulative oil production from both scenarios is presented in Figure 1.4d. It is visible that the total oil recovery is higher for CWF. The oil recovery exhibits a similar trend till reaching point B, where an increase in oil production starts for CWF. De Nevers, in his study, explained the above difference in terms of two processes: (1) oil volume increase due to mass transfer

and dissolution of CO<sub>2</sub>; (2) oil shrinkage due to a plain water flood following the CWF. After CWF the injected pure water removes CO<sub>2</sub> from oil causing oil shrinkage.

#### 1.4. OUTLINE OF THE THESIS

The background of the thesis is related to the fact that the efficient implementation of CWF in the field requires an examination and understanding of the physical and dynamical processes, and of the associated phenomena that occur during CWF into porous systems containing brine and oil. Moreover, this thesis focuses on the importance of conducting CWF studies in the scope of CO<sub>2</sub> injection in order to determine similarities and differences, and related advantages and disadvantages of CO<sub>2</sub> over CW.

The thesis consists of four separate studies that cover research on (1) fluid–rock interactions, i.e. electrokinetic phenomena, which is investigated via zeta potential and potentiometric titration measurements; (2) fluid–fluid interactions or fundamental mechanisms that control mobilization and recovery of residual oil, i.e. molecular diffusion of CO<sub>2</sub> from CO<sub>2</sub> rich source (carbonated water/CO<sub>2</sub>) into oil, (3) fluid–fluid–rock interactions: thermodynamics, coupled flow and mass transfer via core flooding experiments, and; (4) a detailed study on Bentheimer sandstone as being the reference reservoir rock. It is conducted by qualitative and quantitative laboratory and theoretical analysis (rock characterization). A graphical overview of the research is presented in Figure 1.5.

The research program starts with the definition of a reference porous system of Bentheimer sandstone through spatial characterisation of the matrix, mineral distribution and pores (Chapter 2). The sandstone was used for all experiments as the model reservoir rock, because of its lateral continuity and homogeneous nature at block scale (meters) and core scale (centimeters). In addition, it was chosen as a most promising candidate, because over the years researchers have been using it to investigate reservoir related matters ranging from passive and active properties of oil/gas/water/rock interaction and processes to flow and transport. The chapter evaluates the sandstone properties and their characteristics to advance understanding on the presence of mineral accessory and the grain surface physical and electrical transport properties.

Chapter 3 is dedicated to understanding and assessing the effect of the accessory constituents besides quartz (clays, feldspars, carbon and oxides) on the physical and electrical transport properties. Fluids, especially formation water, CW and CO<sub>2</sub>, cause geochemical reactions such as dissolution and recrystallization that lead to changes in mineralogy and by that matrix structure. They modify fluid flow path characteristics and electrical response.

Successively, conducting detail interpretation of Bentheimer matrix and determining the role of particular constituents, the focus in Chapter 4 is on rock–fluid interaction. The relation between the efficiency of CWF (both oil recovery and CO<sub>2</sub> trapping) and the sensitivity of the reservoir minerals to variations in properties of the reservoir fluids is studied. This phenomenon depends on changes in the rock surface charge and wettability, which is a function of the film stability between rock surface and oil. Therefore, Bentheimer sandstone surface charge behavior in an aqueous solution (water and brine), with and without CO<sub>2</sub> are presented.

In the next two chapters interaction occurring between fluids (oil/water/CO<sub>2</sub>) in the zones of relatively low flow are discussed. As a reference, the performance of fluids dur-

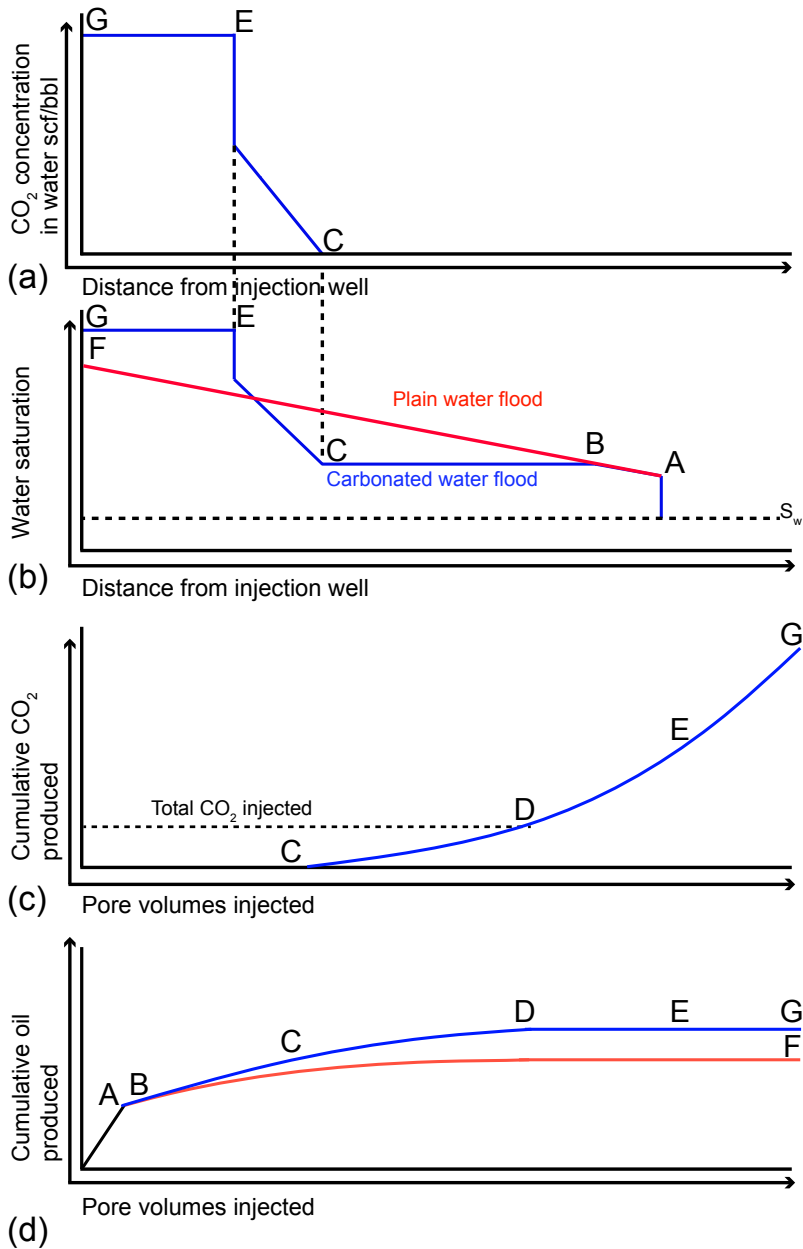


Figure 1.4: Comparison of carbonated water and plain water flooding according to Buckley–Leverett theory: (a) CO<sub>2</sub> concentration in water as a function of distance from injector well; (b) Water saturation as a function of distance from injector well; (c) Produced cumulative CO<sub>2</sub> as a function of pore volumes injected; (d) Cumulative oil produced as a function of pore volumes injected (after [4, 25]).

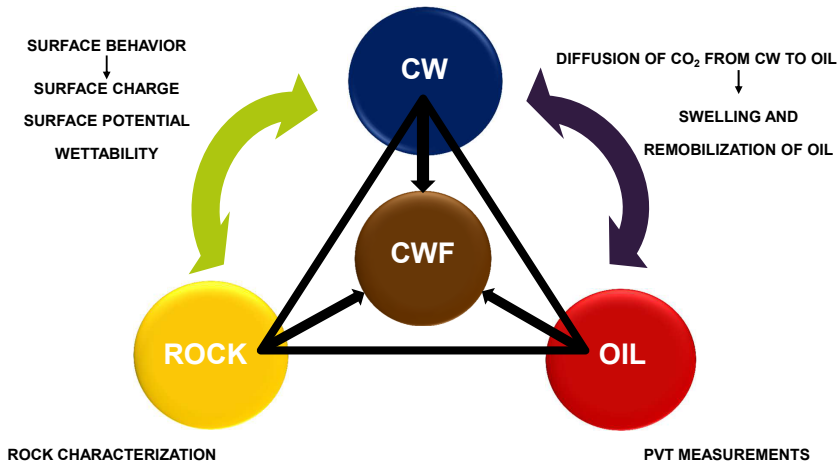


Figure 1.5: Scope of the research presented in this thesis.

ing CO<sub>2</sub> floods in stagnant geometries is necessary for further analyzing studies on CW. In Chapter 5, I evaluate and compare three different CO<sub>2</sub> injection scenarios introduced after water flooding. To mimic the stagnant zone, a glass micromodel with a single dead-end pore placed down was designed. After defining its geometry, the efficiency of the processes in relation to oil recovery and CO<sub>2</sub> storage was studied. Additionally, the influence of the nature of the flow and the oil volume in the system geometry was investigated.

In Chapter 6, having the knowledge of fluid behavior at different densities ratios and at various flow rates from Chapter 5, I investigated the phase behavior of the CW-oil system in indirect pore-scale diffusion experiments. In essence, swelling of oil due to CO<sub>2</sub> diffusion under  $P$ - $T$  conditions was recorded and visualized over time. In addition, a mathematical model was developed with Comsol Multiphysics<sup>TM</sup> that explains the processes observed in the experiments. The results predicted by the model were linked to the results obtained during the experiments to determine the diffusion coefficient.

Chapter 7 involves the mechanisms controlling the oil displacement and CO<sub>2</sub> sequestration, the interaction between pore and the matrix system, and between the flow and phase equilibrium. For this purpose, a series of CO<sub>2</sub> and CW flooding experiments were conducted and I injected CO<sub>2</sub>/CW as a 2<sup>nd</sup> stage EOR action after water flooding while monitor and measure CO<sub>2</sub> in the system. This chapter explains three phase trapping mechanisms and shows results on the CO<sub>2</sub> phase behavior with various injection flow rates. Finally, I present the overall conclusions of this thesis in Chapter 8.

Note from the author: This text includes published papers in reviewed journals and scientific conferences. Consequently, the reader may find similar texts and sentences in some parts of the thesis.



**REFERENCES**

- [1] D. Duncan and E. Morrissey, *The concept of geologic carbon sequestration*, U.S. Geological Survey Fact Sheet 2010-3122 , 2 (2011), available at <https://pubs.usgs.gov/fs/2010/3122/>.
- [2] M. Bidner and G. Savioli, *On the mechanisms of mobilization of residual oil left after waterflooding*, in *SPE Latin American and Caribbean Petroleum Engineering Conference* (Society of Petroleum Engineers, 2003).
- [3] Y. Dong, B. Dindoruk, C. Ishizawa, and E. J. Lewis, *An experimental investigation of carbonated water flooding*, in *SPE Annual Technical Conference and Exhibition* (Society of Petroleum Engineers, 2011).
- [4] N. De Nevers, *A calculation method for carbonated water flooding*, Society of Petroleum Engineers Journal **4**, 9 (1964).
- [5] G. P. Willhite, D. W. Green, and G. Paul, *Enhanced Oil Recovery*, SPE Textbook series **6**, 302 (1998).
- [6] E. Durusut, H. Pershad, A. Crerar, and A. Kemp, *CO<sub>2</sub>-EOR in the UK: Analysis of fiscal incentives*, Tech. Rep. (SCCS, 2014).
- [7] M. Al-Juaied, *Analysis of financial incentives for early CCS deployment* (Harvard Kennedy School, Belfer Center for Science and International Affairs, 2010).
- [8] J. W. Martin, *Additional oil production through flooding with carbonated water*, Producers Monthly **15**, 18 (1951).
- [9] W. Johnson, R. Macfarlane, and J. Breston, *Changes in physical properties of Bradford crude oil when contacted with CO<sub>2</sub> and carbonated water*, Producers Monthly **16**, 16 (1952).
- [10] L. W. Holm, *Carbon dioxide solvent flooding for increased oil recovery*, (1959).
- [11] L. Holm, *CO<sub>2</sub> Slug and carbonated water oil recovery processes*, Producers Monthly **27**, 6 (1963).
- [12] L. Holm, *CO<sub>2</sub> Requirements in CO<sub>2</sub> Slug and Carbonated Water Recovery Processes*, Producer Monthly. September (1963).
- [13] N. I. Kechut, M. Riazi, M. Sohrabi, M. Jamiolahmady, *et al.*, *Tertiary oil recovery and CO<sub>2</sub> sequestration by carbonated water injection (CWI)*, in *SPE International Conference on CO<sub>2</sub> Capture, Storage, and Utilization* (Society of Petroleum Engineers, 2010).
- [14] M. Sohrabi, N. I. Kechut, M. Riazi, M. Jamiolahmady, S. Ireland, and G. Robertson, *Coreflooding studies to investigate the potential of carbonated water injection as an injection strategy for improved oil recovery and CO<sub>2</sub> storage*, Transport in porous media **91**, 101 (2012).



- [15] N. Mosavat, *Utilization of Carbonated Water Injection (CWI) as a Means of Improved Oil Recovery in Light Oil Systems: Pore-Scale Mechanisms and Recovery Evaluation*, Thesis (2014).
- [16] M. A. Ahmadi, M. zeinali Hasanvand, S. S. Behbahani, A. Nourmohammad, A. Vahidi, M. Amiri, and G. Ahmadi, *Effect of operational parameters on the performance of carbonated water injection: Experimental and numerical modeling study*, *The Journal of Supercritical Fluids* **107**, 542 (2016).
- [17] E. L. Claridge and P. L. Bondor, *A Graphical Method for Calculating Linear Displacement With Mass Transfer and Continuously Changing Mobilities*, (1974), 10.2118/4673-pa.
- [18] A. B. Ramesh and T. N. Dixon, *Numerical Simulation of Carbonated Waterflooding In A Heterogeneous Reservoir*, (Society of Petroleum Engineers, 1973).
- [19] S. H. Shenawi and C. H. Wu, *Compositional Simulation of Carbonated Waterfloods in Naturally Fractured Reservoirs*, Society of Petroleum Engineers (1994), 10.2118/27741-MS.
- [20] M. Sohrabi, G. D. Henderson, D. H. Tehrani, and A. Danesh, *Visualisation of oil recovery by water alternating gas (WAG) injection using high pressure micromodels - Water-wet system*, SPE Reservoir Engineering (Society of Petroleum Engineers) , 319 (2000).
- [21] M. Sohrabi, M. Riazi, M. Jamiolahmady, S. Ireland, and C. Brown, *Carbonated water injection for oil recovery and CO<sub>2</sub> storage*, in *Sustainable energy UK conference: meeting the science and engineering challenge*, Oxford, UK (2008).
- [22] M. Riazi, M. Jamiolahmady, and M. Sohrabi, *Theoretical investigation of pore-scale mechanisms of carbonated water injection*, *Journal of Petroleum Science and Engineering* **75**, 312 (2011).
- [23] N. Mosavat and F. Torabi, *Experimental evaluation of the performance of carbonated water injection (CWI) under various operating conditions in light oil systems*, *Fuel* **123**, 274 (2014).
- [24] S. E. Buckley and M. Leverett, *Mechanism of fluid displacement in sands*, *Transactions of the AIME* **146**, 107 (1942).
- [25] A. Steffens, *Modeling and laboratory study of carbonated water flooding*, Thesis (2010).

# 2

## GENERAL ROCK CHARACTERIZATION

### BENTHEIMER SANDSTONE

*Bentheimer sandstone outcrop samples are ideal for laboratory studies due to their lateral continuity and block scale homogeneous nature. Over the years they have been used to investigate reservoir topics ranging from passive and active properties of oil/gas/water/rock interaction and processes to flow and transport. This chapter shows an evaluation of Bentheimer sandstone properties and their characteristics to advance the understanding of the mineral accessory and the physical and electrical transport properties. On the basis of the nature of depositional environments and diagenesis, we measure and characterize spatial attributes of the matrix, mainly by qualitative analysis, laboratory and stereological measurements and statistical 2D/3D reconstructions. The main contribution of this chapter is the impact of mineral composition on the petrophysical quality and block scale homogeneity of the reservoir. With 3D techniques, reconstructions of the new rock grain framework pore structures were created. Based on measurements, a review of literature data and interpretation of variation between the outcrops and flow relevant parameters, we conclude that Bentheimer sandstone is a rock that shows a constant mineralogy and is largely free of paramagnetic impurities. In accordance with the results of 3D reconstructions techniques and in line with the depositional settings, they show a well-sorted grain framework and a pore network that can be used to calculate the permeability and resistivity without conducting any direct laboratory measurements of either parameter. Based on our work and the literature, it is found that a high permeability, together with similar distribution of pore throats and bodies, makes the sandstone an attractive and easy obtainable candidate for comparative experimental studies. Moreover, we state by comparing various techniques, that the efficiency and resolution accuracy of the applied method must be taken into consideration when planning the measurements.*

This chapter has been published as: Anna E. Peksa, Karl-Heinz A.A. Wolf, Pacelli L.J. Zitha, Bentheimer sandstone revisited for experimental purposes, Marine and Petroleum Geology, Volume 67, November 2015, Pages 701-719, ISSN 0264-8172, <http://dx.doi.org/10.1016/j.marpetgeo.2015.06.001>.

## NOMENCLATURE

$A$	Area, $m^2$
$C$	Constant associated with the tortuosity, [-]
$D$	Diameter, mm
$\Delta n$	Dissolution rate, mmol
$E$	Young's modulus, GPa
$F$	Faraday constant, C/mol
$\gamma$	Surface tension of the liquid surface, $J/m^2$
$K$	Permeability, D
$K_0$	Kozeny constant, [-]
$L$	Height, mm
$L_e/L$	Tortuosity, where $L_e$ is the effective length and $L$ the curved length, [-]
$M$	Mass, g
$\nu$	Poisson's ratio, [-]
$P$	Pressure, Pa
$p$	Perimeter, mm
$\varphi$	Effective porosity, [-]
$r$	Radii of curvature, m
$R$	Ideal gas constant, $J/K \text{ mol}$
$\rho$	Bulk density, $kg/m^3$
$S$	Saturation [-]
$S_s$	Specific surface, $m/m^2$
$\zeta$	Charge, $C/m^2$
$\sigma$	Stress, MPa
$T$	Temperature, K
$V$	Volume, $m^3$

## SUBSCRIPTS

$a$	Area
$Ave$	Average
$b$	Pore body
$g$	Grain
$max$	Maximum
$m$	Molar
$p$	Pore
$rw$	Residual water
$s$	Surface
$sol$	Dissolution
$st$	Standard
$t$	Tangent
$v$	Vapor
$w$	Water

## ABBREVIATIONS

ASTM	American Society for Testing and Materials Standard Documents (+reference code)
BET	Brunauer-Emmett-Teller
BS	Bentheimer sandstone
CO <sub>2</sub>	Carbon dioxide
CT	Computed tomography
FS	Fresh core samples
FSQ	Fresh core samples collected at different locations of the Romberg Quarry
GM	Gravimetric method
H <sup>+</sup>	Hydrogen ion
H <sub>2</sub> O	Water
HCl	Hydrogen chloride
IS	Intermediate core samples
Max	Maximum
μCT	Micro-CT scanner
N <sub>2</sub>	Nitrogen
NaCl	Sodium chloride
NaOH	Sodium hydroxide
OS	Old core samples
PZC	Point of zero charge
SEM	Scanning Electron Microscope
STD	Standard deviation
STP	Standard Test Procedure
TS	Thin section
UP	Ultra Pycnometer
XRD	X-ray Diffraction
XRF	X-ray Fluorescence

## 2.1. INTRODUCTION

Bentheimer Sandstone (BS) is a shallow marine formation deposited during the Lower Cretaceous located on the border between the Netherlands and Germany and outcropping in Bentheim. BS forms shallow oil reservoirs between Enschede and Schoonebeek [1–6]. The sandstone is considered an ideal sedimentary rock for reservoir studies due to its lateral continuity and homogeneous block-scale nature. Both in its natural appearance and thermally treated, it has a limited number of minerals, a constant grain size distribution, porosity, permeability and dielectric values, which makes it suitable for standard laboratory experiments and the associated comparison with existing theory [7, 8]. Therefore, Bentheimer sandstone is used to investigate a variety of reservoir topics, ranging from passive and active properties of oil recovery processes to flow and transport in the groundwater zone and environmental remediation. Researchers have often used Bentheimer sandstone in energy production studies and related processes such as geothermal energy [9–12] and geological storage of carbon dioxide [13–19]. The homogeneity and isotropy of rocks have a strong relation to the propagation of underground fluids. The major characteristics that are responsible for sandstone's homogeneity and isotropy at the small scale relate to grain size distribution, the orientation of the mineral grains/pores along a preferential direction [20], porosity and permeability - and even for samples obtained from different locations, the lack of mineral dissolution and precipitation processes, that may increase the anisotropy and effectively decrease the connectivity. At field scale, the homogeneity of the reservoir can be related to layering [21], the existence of clay minerals in the zones of shear [22], and the preferred alignment of fractures and faults.

In this study, we examine the degree of block-scale homogeneity of the sample for conventional experiments and for the more recent types of experiments (i.e. wettability and electrokinetic studies). The objective is to conduct and analyze the Bentheimer sandstone parameters and further to compare them to the literature data. Knowing depositional environments and diagenesis, we measure and characterize spatial attributes of the matrix, mainly by qualitative analysis, laboratory and stereological measurements and statistical 2D/3D reconstructions. In addition, we focus on the grain size distribution by using a micro-CT scanner and on the surface charge profile of Bentheimer sandstone with emphasis on the role of hematite and goethite.

This study was conducted at three different scales: (1) site scale (outcrop investigation); (2) laboratory scale (standard core testing); (3) microscopic scale (optical microscope, electron scanning environmental microscope), and computed micro-scale (micro-CT and medical-CT scanner). In addition, the dielectric behavior of the sandstone is considered as a measure for the definition of impurities in the quartz-rich sandstone, as this information, for instance, is important in wettability studies for enhanced oil recovery and CO<sub>2</sub> storage. The research starts with the introduction of geological settings, variations on the environmental interpretations between the outcrops and, where possible, flow relevant parameters. Here, primarily core measurements are considered, as they provide input data to classical reservoir evaluations and possible spread in data. Uncertainties in macroscopic reservoir characterization may originate from uncertainties in core data and consequently, a more detailed microstructure characterization of Bentheimer sandstone was performed. The microstructure has a significant effect on

bulk physical properties such as permeability, mechanical behavior (elastic moduli, relaxation times), electrical conductivity and heat capacity. For that reason, we conducted XRD and XRF analysis and gathered the data from previous studies (to make a comparison of mineral composition) [4, 5, 23–26]. A mineral distribution, based on mole-, weight-, and volume-percentage, was calculated as a synthetic composition [27].

Furthermore, new, polished thin sections were used to verify the XRD/XRF-results by petrography. Considering that grain and pore size are significant variables contributing to permeability, the grain and pore size distribution and mineral distribution were analyzed for a more detailed description of the rock. For that purpose, the 2D grain size distribution obtained from polished thin sections was reconstructed into a 3D distribution. Additionally, a series of micro-CT scans and regular CT scans were performed to reconstruct 3D grain diameter and pore throat/bodies distributions, where the results on mineral spread, porosity and permeability were compared with results obtained with different techniques.

Moreover, the rock's physical and chemical properties are affected by the surface charge. This is a property of Bentheimer sandstone in contact with the electrolyte solution, since it controls adsorption/adhesion from the electrolyte [28]. The surface reactions and the concentration of the "potential determining ions" are essential to determine the interfacial behavior. In addition, the effects of clay minerals and iron oxides/hydroxides may cause "contradictory" results but can be quantified. The specific surface area, a parameter necessary for the correct interpretation of the electrical behavior of Bentheimer sandstone, was measured using the nitrogen adsorption method.

The main contribution of this chapter is to combine all the determined petrophysical properties with the mineral composition of Bentheimer sandstone. The 3D reconstruction of the rock's grain and pore structure gives an irregular network that represents the flow path and that can be used to predict permeability and resistivity (conductivity of rock) without conducting any direct laboratory measurements of either parameter.

## 2.2. LITERATURE OVERVIEW

Over the past 50 years, the Bentheimer sandstone has been characterized by several German authors [2–5, 29]. They have investigated, interpreted and summarized basic geology, structural setting, lithology and depositional environments of the Bentheimer sandstone. Correlations of sedimentary facies, diagenetic features and reservoir modeling were executed by Swedish scientists [30, 31]. Moreover, Wonham et al. (1997) assessed the reservoir characteristics of the Bentheim sandstone at the outcrop in the Bad Bentheim area and in the subsurface in the Röhlermoor field [32]; Mutterlose et al. (2000) described the distribution and regional settings of the formation [33] and recently Dubelaar et al. (2015) characterized the geology and petrophysics of it as a building stone [1]. However, in prior works, the main focus was either on geological and paleontological settings or on a certain parameter like, porosity and permeability [34–39], mineral composition [4, 5, 23–26], as well as pore throat/bodies size distribution, that is described extensively and in much detail.

Over the past decades, many permeability measurements have been performed with the same Ruska permeameter [24, 26, 27]. Bentheimer sandstone, as a whole, was considered in experimental and modeling work focusing on its bulk behavior. Only the

grain and pore aggregates, and not the grains and pores themselves, were taken into account [40–46]. Now, CT scanning, MRI and confocal microscopy are increasingly applied when studying the rock/fluid/gas-oil behavior of permeability, capillarity and wettability in greater detail. Image analysis methods are able to distinguish spatial matrix and pore properties at micrometer scale [47–52]. Grain/pore size and pore throat distribution, pore coordination numbers and specific pore space and surfaces can be more accurately calculated at micro- and nano-level. Minerals can be assigned to volumes and coordinates in a sample, so that petrophysical parameters, such as dielectric constants, can be calculated.

Other data, such as grain size distribution, mineralogical content and/or mechanical behavior, can be found in the literature, but mainly as additional information provided by the author as a background to conducted research. Researchers were determining particular properties of Bentheimer sandstone, while conducting investigation on oil recovery [17, 35, 38, 43, 46, 50, 53–79], formation of gas hydrates [18, 42, 45, 80], distributions of fluid velocities [81].

### 2.3. GEOLOGICAL SETTING

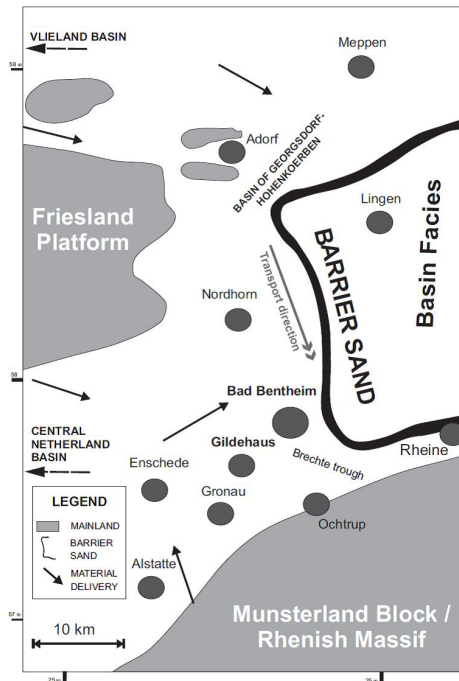
The description of the physical properties of Bentheimer sandstone requires a good understanding of the depositional and diagenetic history. The physical properties are a function of provenance, transport depositional environment, and any diagenesis that took place.

Bentheimer sandstone occurs in the southwestern part of the Lower Saxony Basin (Fig. 2.1) and outcrops along the east of the Dutch-German border, within the area outlined by Meppen, Adorf, Nordhorn, Bentheim and Ochtrup [3–5, 29–33, 82, 83]. It belongs to the late Early Valanginian of the Lower Cretaceous [5] and was deposited in one of the Lower Cretaceous basins to the north of the London-Brabant Massif and the Rhenish Massif. According to Dubelaar et al. (2015), for the duration of Valanginian times, a slow eustatic sea-level rise caused flooding of the Lower Saxony Basin [1]. As a result, marine conditions were established, which is proven by the presence of ammonites *Platylenticeras* [33]. The Valanginian age deposits are distributed preferentially along salt anticlines [84]. The overall consensus is that the initial Valanginian transgressions (in the early and the earliest late Valanginian) progressed from the southern North Sea through the East Netherlands High to the eastern parts of the Altmark-Fláming Basin. As a result, the main marine offshore sedimentation took place in the area of the Emsland Basin. Based on palaeoecological and palaeobathymetric studies, during regressive-transgressive Valanginian cycles, the progression of two sandstones (the Bentheim and the Dichotomites) occurred into the basin as the intercalated fragments of a thick deposition of marine claystones.

These sandstones are hundreds of kilometers long and few kilometers wide barrier sand and form a rim around the Lower Saxony Basin (Fig. 2.1). The hinterland sources consist mainly of Bunter sandstone from the Munsterland Block, the Rhenish Massif and the Friesland High [83]. In accordance with micropalaeontological data, the Bentheim Sandstone was deposited from the upper part of the Lower Valanginian to the lowermost Upper Valanginian. The formation is a sequence of massive shallow marine sandstones deposited in a deltaic to inner/middle-neritic setting. The abundant coarse clasts

Emsland area						
System			Lithostratigraphy	Type locality (Romberg)	Sequence stratigraphy	
Lower Cretaceous	Valanginian	Upper	Grenz Sandstone			
			Unnamed unit			
			Dichotomites Sandstone			
			Erectum Clay			
		Lower	Upper Benthem Sandstone		3	
			Romberg Clay		Benthem Sandstone	2
			Haupt Sandstone			
			Heterolithic Facies			
			Basisbank		1	
			Lower bioturbated zone			
Platylenticeras Clay						

(a)



(b)

Figure 2.1: (table) The lithostratigraphic and sequence stratigraphic division of the Valanginian in Emsland area [33]; (map) Sedimentary interpretation of the Lower Cretaceous and Benthem sandstone environment, revised after [33], [83] and [85].



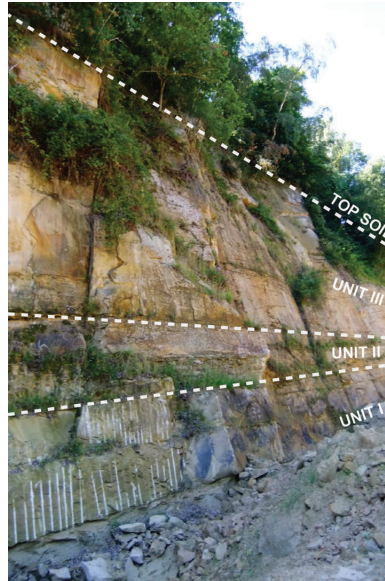


Figure 2.2: The lithographic units in the Gildehaus-Romberg quarry. It represents three visibly different units of the Bentheim formation. Unit I represents the Lower Bentheim sandstone; Unit II represents the intermediate Romberg - fine sandy shaly layer (~4 m). Unit III is Upper Bentheim sandstone.

and lignite fragments are indications of a high-energy, near-shore depositional environment [33]. The Bentheim sandstone overlies the Bentheim Claystone Member. Locally, in the absence of the Bentheim Claystone Member, the lower boundary of the formation has unconformable conditions due to contact with the Coevorden Claystone Formation (Niedersachsen Group). At the top, Bentheimer sandstone is conformably overlain by the Ruinen Member of Vlieland Claystone Formations, which consists of a thin sequence of fossiliferous claystones topped by thin silt or sandstones. In the absence of the Ruinen Member, due to palaeogeographically elevated settings, it is covered by the Westerbork Member, which belongs to Vlieland Claystone Formations and is represented by glauconitic claystones to marls with marine fauna. The transition of Bentheimer sandstone towards the east into the Vlieland Claystone Formations (marine shales) created stratigraphic oil traps (the Bramberge Field) (Fig. 2.1).

Since the 11<sup>th</sup> and 12<sup>th</sup> centuries, Bentheimer sandstone has been mined in Bentheim county in 22 quarries. All outcrops located in the Emslands area are associated to east-west striking salt anticlines [32]. Today, it is excavated mainly at two locations: (1) in the Romberg Quarry in Gildehaus, where the beige-colored sandstone with the brand name "Gildehaus" can be found; (2) next to Bentheim, south of the Romberg Quarry, where outcrops are rich in the characteristic reddish sandstone that exists under the name "Bentheim".

In our work and in previous studies [4, 5, 23, 24, 26, 30, 31, 40, 43, 44, 48, 86–89], type locality was sampled in the Romberg Quarry. Essentially, more descriptive information about the lithological units in which the samples originated is included.

A first attempt at a unit - lithographic interpretation of the Bentheimer Formation was reported in [4] and [32] completed the division of this formation. Bentheimer sandstone was divided there into three different lithographic units (I-III) that can be distinguished by rock mass classification and, in our case, by variation in color and by the strength of the grain framework (friability) (Fig. 2.1 and Fig. 2.2). Unit I - Lower Bentheim Sandstone, deposited under high energy conditions, consists of large cross-bedded units. It was subdivided by [32] into four subzones: (1) at the bottom, the Lower bioturbated zone with thick sands at the bottom; (2) the Basisbank with a bioturbated zone (12 m); (3) a Heterolithic facies with several thin layers (~1 m) intercalated by thinner shale layers, and (4) at the top, the "Haupt sandstein" or main sandstone (~20 m), a barrier sand with low angle stratifications, deposited by currents parallel to the coast. Unit II represents Romberg Shale, a fine sandy shaly layer (~4 m) [5], showing the results of intense bioturbation (i.e., Arenicolites, Skolithos, Ophiomorpha) [90]. Unit II is overlain by the Upper Bentheim sandstone that was deposited under lower energy conditions.

The samples, normally used in laboratory work, originate from Unit III. Note, that the framework mineralogy of Bentheimer sandstone at the field scale can to some extent vary with increasing burial depth, temperature and circulation of acidic fluids, originating from the maturation of hydrocarbons. Moreover, in the near geological history, groundwater and glacial effects may have changed the sandstones, resulting in leaching of K-feldspars and limestone and further creation of secondary porosity. Therefore, the samples from the Romberg Quarry are less representative of the same reservoir under in-situ conditions.

## 2.4. MATERIALS

In the past 50 years, Bentheimer sandstone characteristics were studied around the world and in the TU Delft laboratory. Porosity, permeability, grain size distribution, pores bodies and throat distribution, etc., were obtained from laboratory measurements on plugs, from statistical reconstruction of 2D thin section images and high resolution X-ray microtomography (micro-CT scans) [4, 5, 24, 42, 47–49, 51, 52, 87, 91–95]. The mentioned methods partly cover each of the spatial and petrophysical parameters, i.e., pore and grain size distribution and porosity.

### 2.4.1. SAMPLE MATERIALS

For this study four series of samples with different dates of origin were used:

- Old core samples (OS) - collected at the Romberg Quarry in 2007;
- Intermediate core samples (IS) - collected at the Romberg Quarry in 2012;
- Fresh core samples (FS) - collected at the Romberg Quarry in 2013;
- Four fresh samples were collected at 4 different locations of the Romberg Quarry: FSQI-IV (Fig. 2.3a).

The samples of Bentheimer sandstone (type Gildehaus) were collected from the Romberg Quarry in Gildehaus (the Bentheim 3 member). They were gathered at various times and used during experimental work over the past ten years. The sets of laboratory cores and

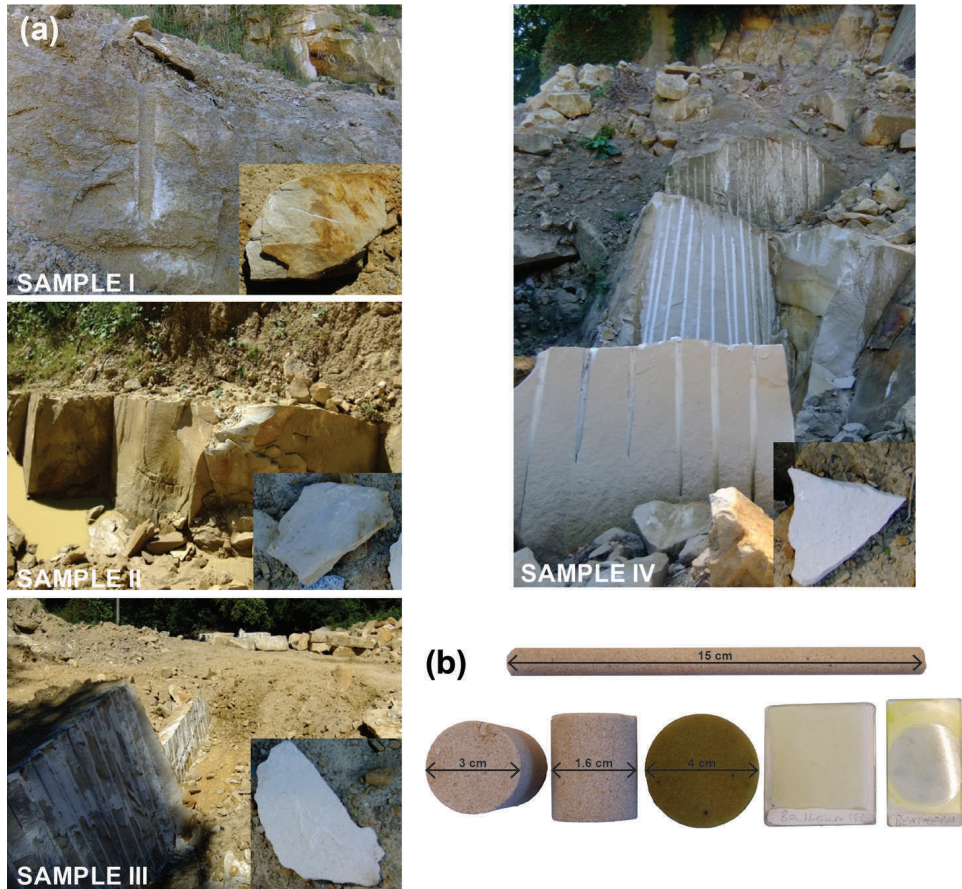


Figure 2.3: (a) Sample locations in the Gildehaus-Romberg quarry FQI-IV. (b) Representation of the rock sampling of Bentheimer cores and thin sections. The yellow colors are the fluorescing dye in the pores.

blocks were drilled in the quarry samples, but according to the specifications required for the various measurement programs (Fig. 2.2 and Fig. 2.3). The variation in data collection over the years and the use of different wet/dry porosity/permeability measurements made use of the statistical "iterative sampling" approach for an unbiased conclusion.

### 2.4.2. SAMPLE TEXTURES, STRUCTURES AND MINERALOGY

Thin sections (Fig. 2.3b): For texture characterization of the grain framework and pores, samples were impregnated with a blue dye or fluorescent resin. Thereafter, they were used for the preparation of glass covered and polished thin sections. The advantage of polished, uncovered thin sections is the highly reflective surface and absence of the interfering effects of glass plates, i.e., a sharper boundary between pores and grains can be distinguished. The thin sections are used to qualify and quantify mineral content (grain framework), grain/pore size distribution, and grain contacts by using a polarized light microscope and fluorescing option combined with an incident light microscope.

## 2.5. METHODS

### 2.5.1. IMAGE ANALYSIS PROCEDURES

#### 2D AND 3D DISCRETE CT-IMAGE ANALYSIS METHODS

Image analysis of polished thin sections and stacked CT-images were used to determine the size distribution and other spatial parameters of the grains (e.g. volume, area, perimeter, length, width and orientation).

#### 2D-MICROSCOPY

2D thin sections image analysis: By using a polarization microscope with parallel and crossed nicols, thin sections were transformed into binary images and analyzed on their spatial characteristics by using a Leica Qwin<sup>TM</sup>. The 2D grain size distribution results were recalculated to an empirical 3D sphere size distribution by stereological methods with a numerical method for fixed thickness steps [96], thickness intersection planes based on Wicksell transform [97], and the Russ conversion method [98]. Twenty cuttings with a random orientation show a data variation providing values for the isotropy and heterogeneity of the grain size, orientation and texture. The image processing steps and generation of the size distribution are shown in Fig. 2.4a.

#### 3D DISCRETE IMAGE ANALYSIS METHODS

A Phoenix Nanotom<sup>TM</sup> Micro-CT scanner ( $\mu$ CT) of 180 kV/15 W, with a nanofocus computed tomography system, was used to create 2D images of Bentheimer sandstone. The Micro-CT scanner is equipped with a 5-megapixel detector and a maximum voxel resolution of  $<0.5 \mu\text{m}$ , which was used for the samples. The pencil type sample, 120 mm in length and with a diameter of 10 mm (or ca. 50 grains width), provides a representative number of grains and associated pore framework. The stacked 3D volumes were reconstructed with AVIZO<sup>TM</sup> software. The image processing steps and generation of the size distribution are based on dilation/erosion algorithms for body separations (see flow chart, Fig. 2.4b). Pore bodies and throats volumes were identified and connected to the original image voxels. A spherical shape of the pore bodies is assumed based on

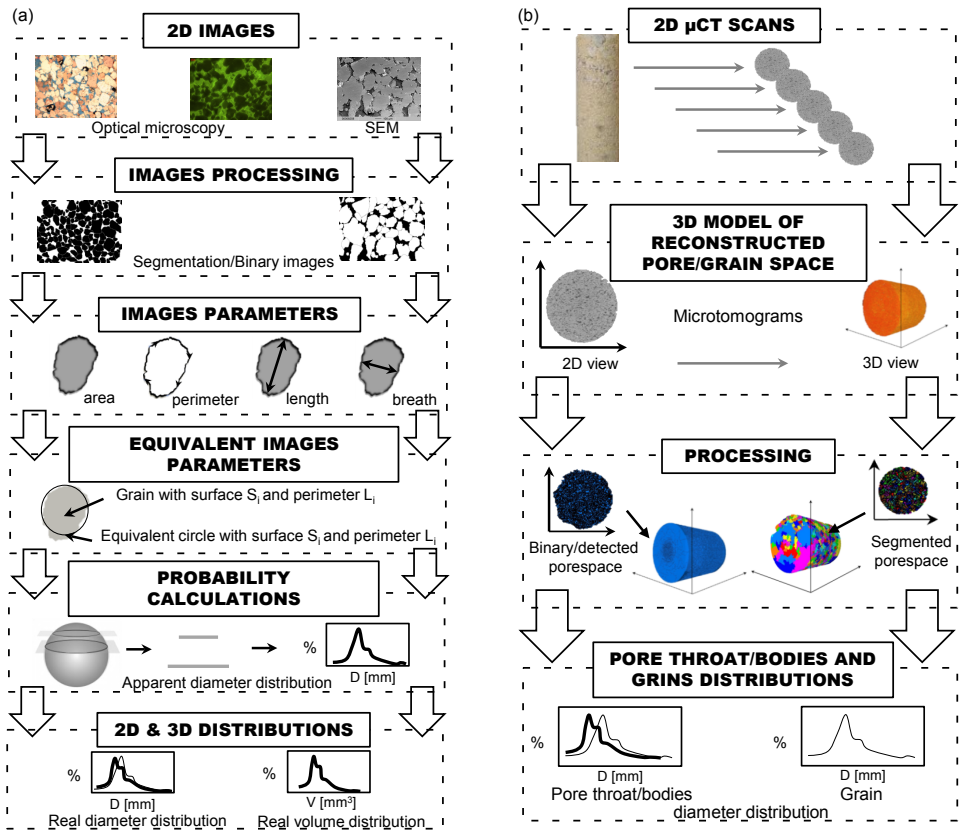


Figure 2.4: (a - left) Flow chart spatial results on 2D thin sections image analysis; (b - right) 3D micro-CT scan discrete image analysis.

area and perimeter, and overlapping is taken into account. Subsequently, the effective pore body diameter is computed. An effective throat radius is calculated, with the modification of the throat volume being assigned to a corresponding cylindrical volume. The height of the cylindrical structure is equivalent to the maximum distance computed between any two spheres representing a pore body.

The spatial categorizations (pore/grain-matrix) are used to define in 3D and 2D the specific grain surfaces, pore volumes, etc., as needed for the permeability model. In 3D, permeability computations are based on the modified Kozeny-Carman equation (Eq. 2.1). A 3D pore network with complex cross-sections in shape can be simplified into a 2D geometrical model of average constant areas, presuming that the heterogeneity of the matrix in all directions is the same [99]. It relates permeability ( $K$ ) to porosity ( $\varphi$ ), specific surface area ( $S_{sa}$ ) and tortuosity ( $L_e/L$ ) of the pore system by the following equation:

$$K = \frac{\varphi^3}{K_0 \left(\frac{L_e}{L}\right)^2 (1-\varphi)^2 S_{sa}^2} \quad (2.1)$$

where  $K_0$  represents the Kozeny constant, an empirical constant that depends on the cross-sectional shape of the flow paths. For the thin section calculations, Ruzyla's conversion is used:

$$K = \frac{\varphi^3}{c(1-\varphi)^2 \left(\frac{4p_p}{\pi A_p}\right)^2}, \quad (2.2)$$

where  $p_p$  is the pore perimeter,  $A_p$  is the pore area and  $c$  is a constant associated with the tortuosity ( $L_e/L$ ).

The spatial results on grain bodies, e.g. area, perimeter, contact number and contact area as a part of the total grain surface, are used for grain density specification. The spatial results on pore volume and pore body measurements are translated to pore area distributions, perimeter, coordination numbers, pore throat diameter, etc. These distributions can be used for the construction of pore/grain frameworks in Monte Carlo simulations on permeability and capillarity. This subject will not be discussed further in this chapter.

In addition, the orientations of the long axes of grains were measured on thin sections and SEM images, and further plotted in the circular histogram to identify preferred directions.

## 2.5.2. LABORATORY PROCEDURES

### XRD/XRF MINERAL COMPOSITION

Samples for X-ray diffraction and X-ray fluorescence were pulverized to a 2  $\mu\text{m}$  powder and used for the determination of mineral composition and element oxide distribution. The XRD was recorded in Bragg-Brentano geometry with a Bruker D5005<sup>TM</sup> diffractometer, equipped with a Huber incident-beam monochromator and a Braun PSD detector. To prove the identification of authigenic minerals, some samples were examined using an electron microprobe JEOL 8800 M JXA Superprobe (1993). The XRF measurements were done with a Panalytical Axios Max WD-XRF spectrometer, measuring the element oxides and elements with an estimated accuracy of 2% that are presented with >0.5 wt%.



### POROSITY AND ABSOLUTE PERMEABILITY

Porosity and permeability for Bentheimer sandstone were determined on cylindrical samples 30 mm in diameter and 36 mm in length (Fig. 2.3b). Dry porosity tests were conducted with a gas expansion Ultra Pycnometer 1000 (Quantachrome Instruments<sup>TM</sup>) using Boyle's gas expansion law. The resulting matrix volume values ( $1 - \phi$ ) provide the bulk density ( $\rho$ ) and effective porosity ( $\phi$ ). The permeability of dry cores was measured with  $N_2$  using a Ruska gas permeameter; next, the samples were saturated with de-ionized water in a desiccator and weighed before and after saturation to calculate the wet porosity, following Archimedes' law. The cores were kept submerged to avoid air intrusion during measurements. Thereafter, absolute wet permeability was calculated from liquid permeameter experiments by using the flow velocities and differential pressure, following Darcie's law (Ruska Instruments<sup>TM</sup>).

### MECHANICAL PROPERTIES

The uniaxial mechanical properties of wet and dry Bentheimer sandstone samples (stress-strain behavior) were examined using the ASTM D2938-95 and D 3148-96 Standard Test Procedure (STP) for the determination of unconfined compressive strength, Young's modulus and Poisson's ratio. The samples were loaded until failure while the axial load and vertical and horizontal deformation were monitored. The load was applied with a constant stress rate in between 0.5 and 1Mpa/sec (1% accuracy).

For four fresh cylindrical samples (FS1-4), with shape tolerances according to ASTM 4543, but with different height to diameter ratios ( $L/D$ -ratios in between 2 and 1), the tangent modulus  $E_t$  was measured at a stress level of 50% of the assumed yield stress, and the strain modulus  $E_{ave}$  was determined from the average slope of the straight-line part of the stress-strain curve.

### DIELECTRIC BEHAVIOR

To determine the surface behavior, potentiometric titration experiments were conducted. The procedure is as follows: (1) Before starting the dielectric measurements, a given amount of solid, dissolved in the electrolyte, was stirred with a Teflon-coated magnetic stirrer for 24 h, followed by potentiometric titration to measure the acid/base properties of mixtures. Then, potentiometric titrations were performed in a nitrogen atmosphere (continuously stirred), adding HCl or NaOH to the solution cell in 10-15 steps of 2.0 ml each. The pH data were recorded at 5 min time lapses (5 min) with the stirrer switched off. Titrations were performed for 3 different masses of solids (0.5 g, 5.0 g and 10 g) in 75 and 100 ml of  $H_2O$  (demineralized and degassed), and in 75 and 100 ml of 2.2 mol/dm<sup>3</sup> NaCl solution; (2) Additionally, titrations of blank electrolytes were performed for calculation purposes. The initial pH was established by addition of 8 ml 0.1 mol/dm<sup>3</sup> NaOH; 0.1 mol/dm<sup>3</sup> HCl was used as a titrant.

The pH-dependent surface charge ( $\zeta_0$ ) was calculated with Equation 2.3 [100]:

$$\zeta_0(pH) = - \frac{F \cdot (\Delta n_{sol,H^+}(pH) - \Delta n_0)}{Ma_s} = \frac{f_{surf}(pH)}{S_s}, \quad (2.3)$$

where  $F$  is the Faraday constant ( $F = 96500 \text{ C/mol}$ ),  $M$  is sample mass;  $S_s$  surface area and  $\Delta n_0$  the pH-dependent amount of acid/base consumed. The dissolution effect ( $\Delta n_{sol,H^+}$ )

was obtained by comparison of the balance of protons and hydroxyl ions in the potentiometric titration of Bentheimer samples with blank potentiometric titration results:

$$\Delta n_{sol,H^+}(pH) = \Delta n_{acid\ base(BS)}(pH) - \Delta n_{acid\ base(blank)}(pH) \quad (2.4)$$

where  $\Delta n_{sol,H^+}(pH)$  represents the balance of protons and hydroxyl ions in titration of solid with electrolyte titration.

#### SPECIFIC SURFACE AREA

The specific surface area, a parameter necessary for the determination of the homogeneity of the sample and the correct interpretation of the electrical behavior of Bentheimer sandstone, was measured. The specific surface areas of rock samples were obtained in two ways: (1) at pore level, discussed previously, from thin section analysis on a consolidated Bentheimer sandstone sample, and (2) at electron level, by adsorption of nitrogen, at low temperatures (77 K).

Before each measurement, the Bentheimer samples were degassed at 150 °C for at least 24 h. The nitrogen adsorption of samples was measured with a Gemini<sup>TM</sup> Micro-metrics system. The adsorption behavior in porous material is related to both fluid-wall interactions and the attractive interactions occurring among fluid molecules. It results in multilayer adsorption and the existence of capillary condensation in the pore space. Capillary condensation occurs mainly in small capillaries and pores at vapor pressures below the saturated vapor pressure  $P_0$ . The vapor pressure can be predicted by the Kelvin Equation 2.5:

$$RT \ln \frac{P_v}{P_0} = \gamma V_m \left( \frac{1}{r_1} + \frac{1}{r_2} \right) \quad (2.5)$$

where  $P_v$  stands for the vapor pressure above the curved surface,  $P_0$  is the pressure above the flat surface,  $V_m$  represents the molar volume of the liquid,  $r_1$  and  $r_2$  the low principal radii of curvature, and  $\gamma$  the surface tension of the liquid surface [96]. In the experiment, we kept the temperature constant and, by varying the external gas pressure and simultaneously monitoring and quantifying adsorption at certain pressures, we obtained the adsorption isotherm.

The specific surface data was estimated using the BET sorption theory [101]. The obtained specific surface area represents the "external" surface area since the penetration of the interlayer of smaller clay particles surfaces by weakly adsorbed nitrogen is not entirely possible.

In addition, to support this investigation, a data set was obtained from literature dealing with the petrophysical and petrographical properties of Bentheimer sandstone. We collected data on the mineralogical composition of sandstone samples obtained from Romberg Quarry. We standardized and compared in graphical form the available data on pore and grain size distribution obtained by different methods, starting from microscopic and macroscopic image inspection, image analysis and mercury intrusion (see section 2.6.2. Furthermore, we gathered information obtained by other researchers about porosity and permeability values.



## 2.6. RESULTS AND DISCUSSION

### 2.6.1. PETROGRAPHY AND MINERALOGY

#### TEXTURE AND STRUCTURE

Polarization microscopy, SEM and XRD show that Bentheimer sandstone consists predominantly of monocrystalline quartz with authigenic overgrowth, detrital polycrystalline feldspars, authigenic clay as a weathering product of original feldspars, and dispersed organic matter with some iron (hydr)oxides (Table 2.1). Weathering and dissolution of feldspars occasionally created some intragranular porosity - depositional pores and oversized pores, i.e., a moldic type of porosity. The secondary minerals (mainly kaolinite and smectite) clogged pores and necks (pore lining and filling type); however, quartz overgrowths are the main reducers of the primary intergranular porosity. The iron (hydr)oxides concretions are secondary products filling former fossils and pyrite spaces.

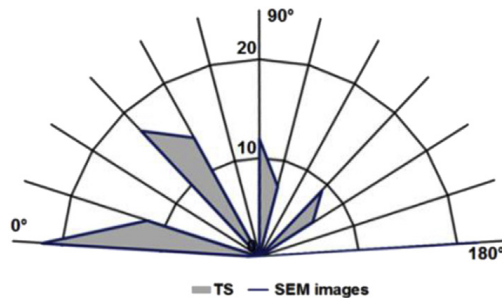


Figure 2.5: Grain orientation distribution of length.

#### ORIENTATION

The SEM and thin section images and the statistical analysis indicate random orientation of the elongated grains (Fig. 2.5). As the permeability is normally higher in the direction of the orientation of the grains, here, random orientation of the grains indicates the lack of a preferred direction of permeability. Thus, homogeneous grain aggregates may be expected.

#### MINERALS

The minerals are described in order of abundance:

**Quartz (91.70 wt%)** In the grains framework, quartz cement is the main reducer of pore space due to diagenetic syntaxial overgrowths around the original detrital quartz grains (Figs. 2.6a and 2.6b). The boundaries between the overgrown grains are well marked, because of clean rims of epitaxial cement with clay- and fluid-inclusions. In addition, traces of cementation by pressure solution were observed (Fig. 2.6 and Fig. 2.8b). Furthermore, grains boundaries migrations are visible in the form of coarsening of quartz grains sizes into chert and largely unstrained quartz composed of small recrystallized grains (Fig. 2.6c).

Table 2.1: XRD-mineralogy of Bentheimer sandstone of the Romberg Quarry in Gildehaus.

Mineral	Al-Muntasheri et al., 2010		This study		Maloney et al., 1990		Van Baaren et al., 1990		Mayr and Burkhardt, 2006 after Holl		Kemper 1976	
	wt %	Vol %	wt %	Vol %	wt %	Vol %	wt %	Vol %	wt %	Vol %	wt %	Vol %
Silicate minerals	88	91.70	91.62	97.50	95	90-96 (+2 chert)	>90					
Quartz	2				3		Acc.					
Illite	2	2.50	2.55	0.50								
Kaolinite	2	0.18	0.18			2-4						
Montmorillonite	1											
Chlorite	2			2	2		Acc.					
Feldspar	2	4.86	5.03									
Albite (na)												
K-feldspar	3											
Microcline												
Alkali												
Siderite				T								
Dolomite	2	0.26	0.24	T								
Calcite		0.15	0.14	T								
Hematite/		0.16	0.08									Acc.
Gibbsite												Acc.
Rutile		0.03	0.04									
Pyrite		0.01	0.01									
Fe sulfide mineral												
Ca-phosphate		0.07	0.06									
Halite (nacl)		0.03	0.04									
Sum	100.00	100	100	100	100	100	100	100	100	100	100	100

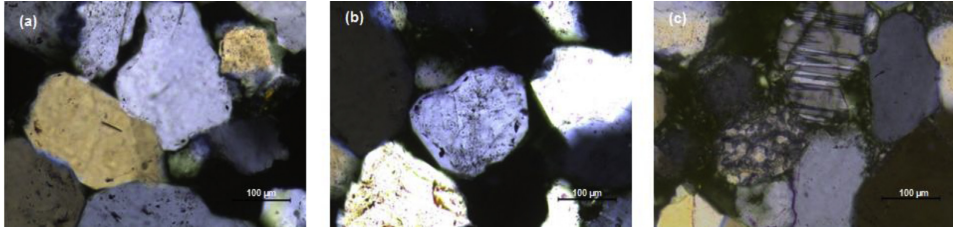


Figure 2.6: Thin-section optical micrographs that represent: (a) overgrowth cement on rounded detrital quartz grains and pressure solution contacts; (b) detrital quartz grains with overgrowths in crystallographic continuity and different generation of fluid inclusions: at the boundary between the detrital quartz grain and the overgrowths and along the quartz micro fractures; (c) unstrained quartz, alkali feldspar, and illitic fractions incorporated by bioturbation and mechanical infiltration.

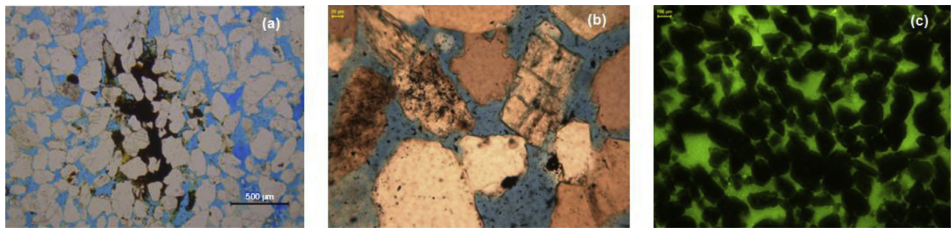


Figure 2.7: Thin-section optical micrographs that represent: (a) loosely packed quartz and weathered feldspar and pore filling with hematite; (b) weathering of a feldspar; (c) fluorescing view providing a binary view of the pore framework (green) and grain framework (dark).

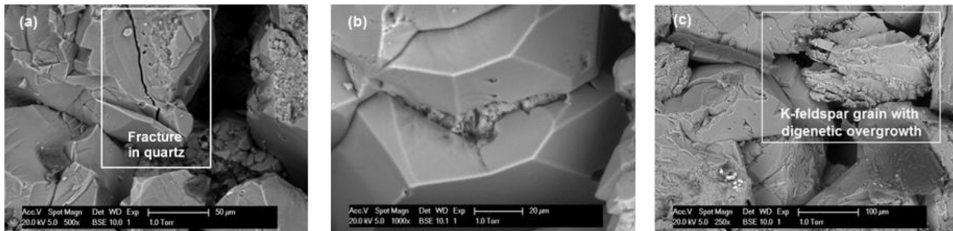


Figure 2.8: SEM microphotographs that represent: (a) fracture in quartz grain; (b) quartz overgrowth; (c) K-feldspar grain with diagenetic overgrowth.

**Feldspars (4.86 wt%)** The brownish K-feldspars exhibit a distinct cleavage (Fig. 2.8 and Fig. 2.9a-c), which is even more distinguished by weathering to small patches of carbonates and clays (among others, kaolinite and illite/sericite). Weathering occurs mainly along the cleavage planes (Fig. 2.6 and Fig. 2.9) and at the grain rims. The elongated and angular shape of the feldspars grains is a result of the damage along cleavage planes during sedimentary transport.

**Clay minerals (2.68 wt%)** These mainly consist of kaolinite, montmorillonite and illite/sericite. Kaolinite and illite/sericite are weathering products. Some inclusions in

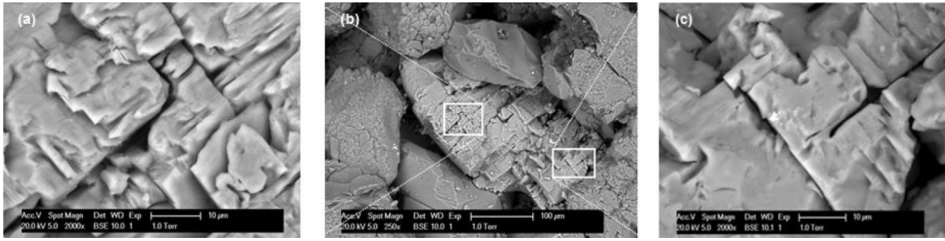


Figure 2.9: SEM microphotographs of the K-feldspar grain.

the rims of quartz overgrowths prove that primary clay is present. The SEM images show predominantly book-type pore lining and pore filling kaolinite. Illitic fractions occur as a pore lining and as a grain replacement (Fig. 2.10a, 2.10b).

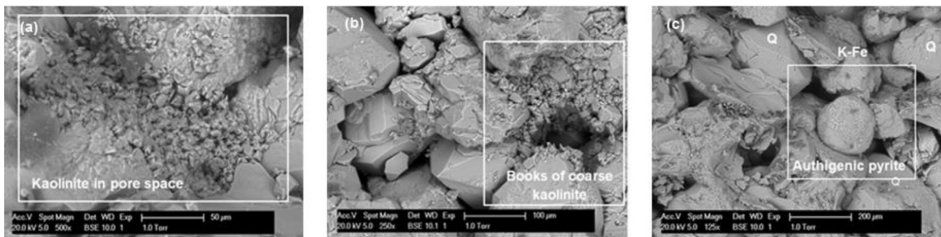


Figure 2.10: SEM microphotographs that represent: (a) kaolinite; (b) books of coarse kaolinite partly occluding pores; (c) pyrite framboids.

**Pyrite and iron (hydr)oxides (0.17 wt%)** Occasionally these can be recognized as framboidal shapes between the grains as a secondary phase (Fig. 2.10c). As pyrite is unstable in oxidizing environments, in the outcrop samples, they are often changed to an amorphous hematite or goethite mineral type. Hematite pore filling was identified in small spots, which can be recognized in the thin sections as random brownish spots in the sandstone cores (Fig. 2.7a). Besides, occasionally larger (mm to cm scale) iron (hydr)oxide inclusions are present, hidden as lumps in whole cores. Pyrite, occurring as the characteristic early diagenetic mineral, confirms the marine sedimentary environment.

Based on the sections and SEM, it can be concluded that authigenic quartz overgrowths reduce the average pore throat size. Moreover, the alteration of unstable minerals, such as feldspars, may lead to the creation of the permeability reducing secondary porosity. However, the small amounts of K-feldspar (4.86 wt%) did not generate enough of clays precipitation to significantly affect the bulk reservoir porosity and permeability, except a migration of clays results in clogging zone production, which incidentally happens.

The XRD and XRF analysis showed some minor differences in the results. In most studies [4, 24, 25] quartz content ranged from 90 to 98 wt%, and only one study [23]

reported 88 wt% of quartz in Bentheimer samples. In most of the samples, the feldspar component was recognized (2-5 wt%), with the difference that in this work and other studies [4, 24] orthoclase was found, whereas [23] showed the existence of albite and microcline. This is a result of the XRD interpretation. We suggest to sum all the feldspar minerals to a total of 4.86 wt%. For all the studies presented in the table, kaolinite was reported as a main clay representative (0.5-2.5 wt%), apart from [26], who found only illite.

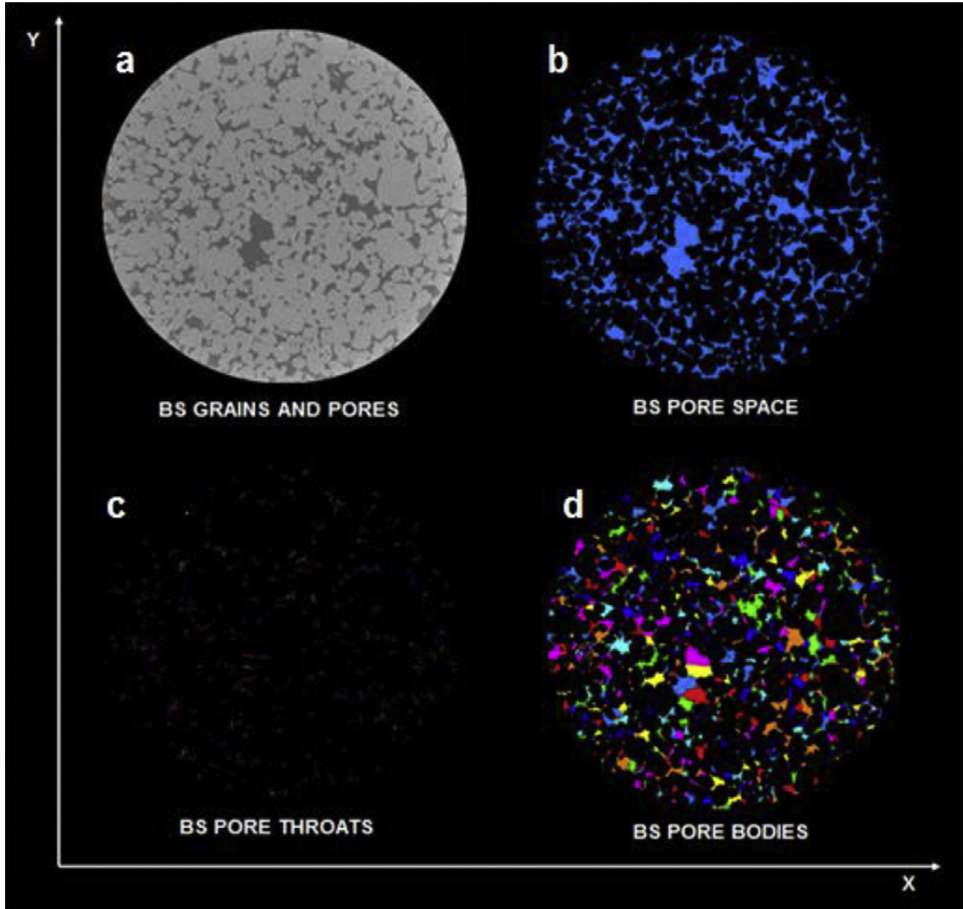


Figure 2.11: Micro-CT images of porous media. They represent cross-sectional images of (a) Bentheimer sandstone grains. Pores are in dark gray, and light gray represents mostly quartz grains. The small white spots represent feldspars; (b) Bentheimer sandstone pore space that poses 0.24 of volume; (c) Bentheimer sandstone pore throats; (d) Bentheimer sandstone pore bodies with voxel size  $0.0025 \times 0.0025 \times 0.0025$  [mm<sup>3</sup>].



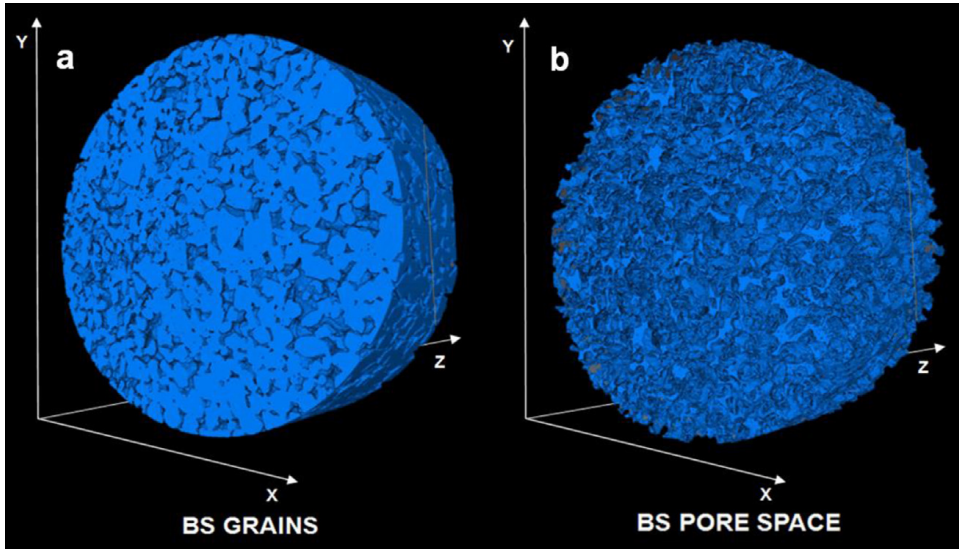


Figure 2.12: 3D view of the reconstructed (a) grains and (b) pore space.

## 2.6.2. PETROPHYSICAL DATA

### PORE AND GRAIN SIZE DISTRIBUTION

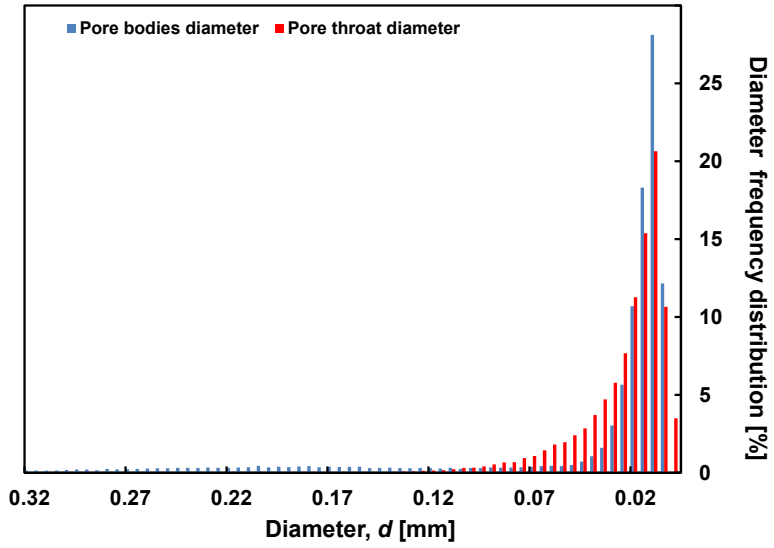
CT scans and thin sections were used to reconstruct 3D grain size and pore size distributions. The methods used were discussed previously.

### PORE BODIES AND PORE THROAT DISTRIBUTION BY CT SCANNING

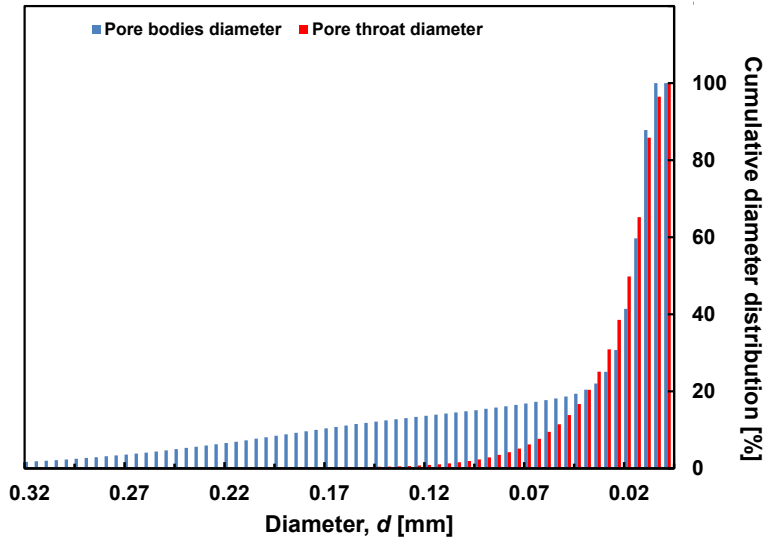
The pencil size Bentheimer samples (Fig. 2.3b) were scanned to get high-resolution images ( $5 \mu\text{m}$ ) for stacking. The pore space was obtained in two ways: first as a gray level threshold binary grain and pore network, followed by a series of separation algorithms to reconstruct the discrete pore/grain bodies and associated spherical pore throats. The results of the binary file were stacked into three-dimensional data sets to measure size distributions. Figs. 2.11 a-d show an example of the reconstruction of a single micro-CT scan that represent grains and pore space, pore throats and pore bodies, respectively. The final result of reconstruction - the 3D view of the rendered pore space and grain framework - is shown in Fig. 2.12. Additional statistical measurements provided pore bodies and throat diameter distributions (Fig. 2.13a and 2.13b, respectively). Note, that averaging techniques were applied for results obtained by different segmentation settings used for both (1) the type of connectivity considered for processing adjacent voxels in the matrix, and (2) a contrast factor that was applied to reduce the number of seeds for watershed processing.

The pore body and pore throat diameter maxima are in the range 0.015-0.025 mm. The average pore body diameter is 0.014 mm and average pore throat diameter is 0.012 mm.

The porosity results from image analysis methods were compared to porosity methods obtained by microscopic examination, mercury intrusion and capillary flow porom-



(a)



(b)

Figure 2.13: (a) Pore bodies and throats diameter frequency distribution; (b) Pore bodies and throats cumulative diameter distribution.

etry. To compare the various results, it was necessary to normalize the distribution curves of the other methods from the literature. Figs. 2.14a and 2.14b show a variation in the pore throat and pore body diameter of the different measuring techniques. The pore throat diameter distribution obtained in this study is in line with the mercury intrusion results reported in the literature [24, 92, 102]. The capillary flow porometry results published by [92] show larger values. The pore body diameter distribution results are comparable to the pore throat results. Fig. 2.14b shows that the mercury intrusion technique and its interpretation underestimate the large pore bodies and overestimate the small pore bodies. As the pore bodies can be surrounded by pore throat and smaller pore bodies, the intrusion pressure will be larger/smaller than the real pressure equivalent for certain pores. As a result, this will increase the number of intermediate diameter pores.

Moreover, it is found that small diameter pore bodies tend to be more accurately calculated by micro-CT analysis, larger pore bodies by 2D image analysis, and the largest diameter pore bodies by thin section analysis. This variation in pore body size is due to the definition of circle-type cross-sectional results in 2D and voxel-size spherical volume distributions in 3D measurements. Both optical inspection and image analysis tend to estimate pore bodies that are too large [24]. Since pore radii smaller than 0.01 mm can mainly be determined by mercury porosimetry, and pores with a radius larger than 0.05 mm (the macropore class) are better measured with a combination of thin sections, image analysis and micro-CT techniques, it can be concluded that a combination of different methods is required to determine a realistic image of the pore system.

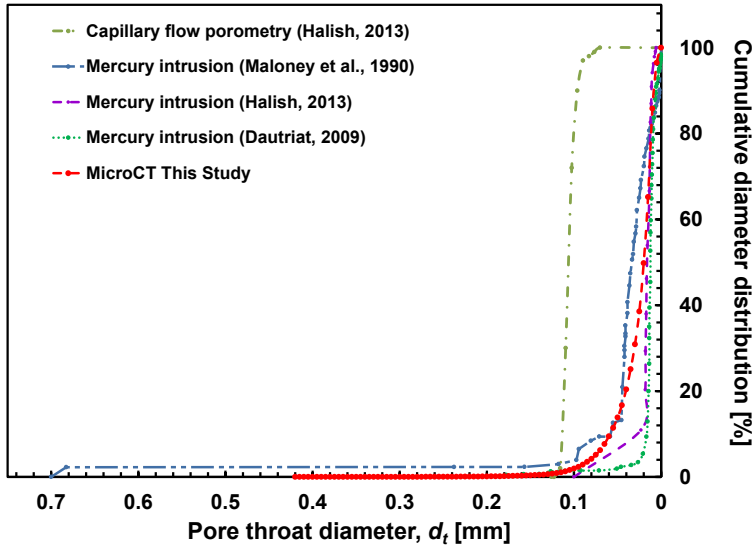
It should be noted, that the micro-CT scan approach provides a direct description of the pore space, but is limited by the machine resolution ( $5\ \mu\text{m}$ ). The mercury injection method, although able to determine micro- and mesopores, is a time-consuming technique that contaminates samples with mercury and hydraulically fractures the friable grain framework [103].

## POROSITY

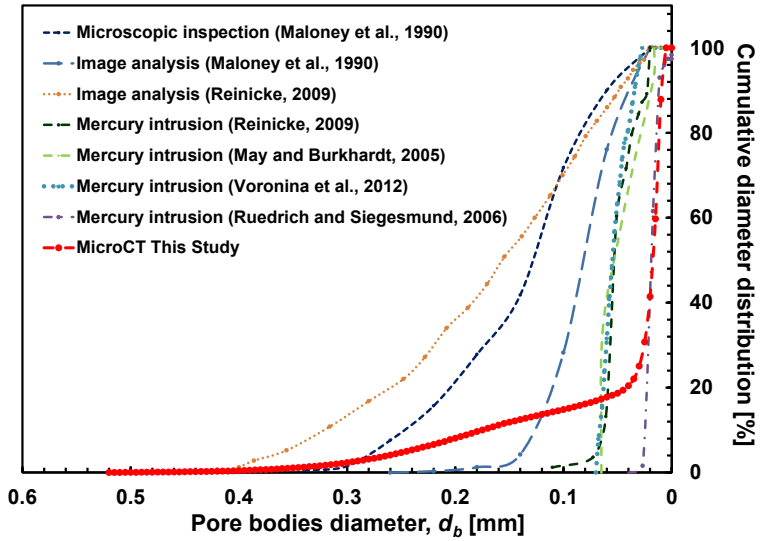
In this section, the porosity results obtained by Ultra Pycnometer, gravimetric and CT scan measurements are compared.

First, we conducted laboratory measurements to investigate the influence on the porosity of wet/dry conditions and the origins of the sample collection points at the quarry. The obtained data sets (Fig. 2.15) show porosity with values around 0.248 ( $\pm 0.019$ ). The plotted data shows the extreme values. The results obtained from the old core samples (OS) are lower than those from fresh (FS) and intermediate cores (IS); differences of ca. 7-8% in porosity for dry conditions (Ultra Pycnometer) and for wet conditions (gravimetric method) were observed. The reduction in the porosity of Bentheimer sandstone can be incorporated in pore clogging with time, as was exhibited in both methods. This restriction and blocking of pore throats can be a result of clay expansion within the sandstone matrix. Based on SEM analyses (Fig. 2.10a-b), the reduction in porosity can be attributed to kaolinite crystals. In addition, the degree of compaction and cementation by hematite and quartz overgrowth on the original beach sand reduced the intergranular pores and decreased permeability by about two orders of magnitude [104]. Laboratory data were compared with image analysis and X-ray techniques. All measurement results





(a)



(b)

Figure 2.14: (a) Comparison of the cumulative pore-throat diameter distributions; (b) Comparison of the cumulative pore-bodies diameter distributions.

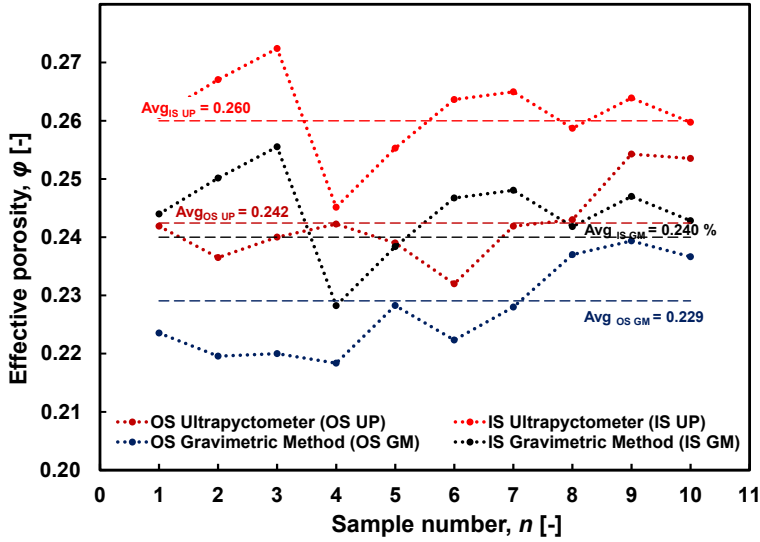


Figure 2.15: Laboratory measurements of porosity of intermediate core samples (IS) and old core samples (OS).

are presented in Table 2.2. Porosities measured with the Ultra Pycnometer and gravimetric method give the effective porosity, as only connected pores are included. The laboratory methods gave an average porosity of  $0.248 (\pm 0.019)$ . In order to arrive at a more relevant comparison of all the conducted measurements, the small pores obtained from image analysis (diameter smaller than  $2.5 \mu\text{m}$ ) were excluded from the pore distribution due to the resolution of the equipment. The slightly higher ( $\sim 2\%$ ) porosity values, obtained by both image analysis and X-ray techniques in comparison to laboratory measurements, confirmed that total porosity was determined.

In summary, Bentheimer sandstone presents a high porosity within a range of 0.23–0.27 (average = 0.251). In the case of the samples taken from the same block, the bandwidth decreases significantly, for example, 0.25–0.27 for old, 0.23–0.24 for intermediate samples and 0.25–0.26 for all Ultra Pycnometer results. In general, the measured values were in good agreement (Table 2.2), with an average deviation for the group of intermediate samples of 4% for the Ultra Pycnometer results, 1% for the gravimetric results, and 9% and 4% for the old and 3% and 1% for fresh samples, respectively. From the results, it appears that image analysis of random thin sections and CT scans give comparable outcomes. It should be noted that porosity at reservoir conditions is less than that determined under ambient conditions in the laboratory by analytical methods (98%–80% of porosity in ambient conditions, as confirmed by [105]).

The porosities measured in this study are in good agreement with those reported in the literature [4, 24, 26, 87, 94, 103] showing a good correlation (Table 2.3). All results are in the range 0.20–0.25. It should be noted that none of the porosity determined by image analysis took the presence of clay matrices into account.

Table 2.2: All porosity results obtained by applying different laboratory measurement methods.

Method	Samples type	Average porosity	
Laboratory	Ultra Pycnometer	0.242 ± 0.005	
	Gravimetric methods	0.229 ± 0.005	
	Ultra Pycnometer	0.261 ± 0.005	
	Gravimetric methods	0.249 ± 0.005	
	Ultra Pycnometer	0.259 ± 0.005	
	Gravimetric methods	0.245 ± 0.005	
	Gravimetric methods	0.239 ± 0.005	
	FSQ 1	0.257 ± 0.005	
	FSQ 2	0.238 ± 0.005	
	FSQ 3	0.265 ± 0.005	
	FSQ 4	<b>0.248</b> ± (0.019)	
	Average from laboratory methods	Image analysis	0.247
		Micro-CT scanner	0.260
		Medical-CT scanner	0.255
Stereology	Thin sections average		
	Pencil core sample		
X-ray technique	FS		
X-ray technique			
Average from imaging methods		<b>0.254</b>	

Table 2.3: Bentheimer sandstone porosity data gathered from literature.

Method	Porosity
Mercury porosimeter (Dautriat et al., 2009)	0.240
Mercury porosimeter (Klov, 2000)	0.213–0.226
Mercury porosimeter (Halisch, 2013a)	0.200–0.230
Thresholded Gaussian Fields (Thovert and Adler, 2011)	0.230
Optical porosity (Klov, 2000)	0.202–0.227
Visual observation (Andrew et al., 2013b)	0.220
Visual observation (Blunt et al., 2013)	0.200
Gravimetric method (Louis et al., 2003)	0.245
Boyl's law expansion technique (Fired sample) (Maloney et al., 1990)	0.247

### GRAIN SIZE DISTRIBUTION AND SORTING

Grain size distributions of Bentheimer sandstone are plotted for data obtained from stereological measurements of thin sections and from Avizo evaluation of the measurements obtained from micro-CT scans. The calculations were done on 2D data sets obtained from the thin sections images after processing (Fig. 2.16). The grain size distributions obtained for 20 thin sections and 10 SEM images and micro-CT scans were plotted as grain diameter size frequency histograms % and grain volume frequency histograms % (Fig. 2.17a). The volume % conversion was created with spherical particles. Cumulative frequency distribution curves are constructed for the grain diameter and the grain volume (Fig. 2.17b). Based on Fig. 2.17b, the median grain size obtained from thin sections is  $D_{TS50} = 0.235$  mm, 90% of the distribution lies above  $D_{TS90} = 0.180$ , and 10% of the population lies above the  $D_{TS10} = 0.320$  mm. Similarly, for grain diameter distribution obtained from micro-CT scans  $D_{CT50} = 0.320$  mm,  $D_{CT10} = 0.475$  mm,  $D_{CT90} = 0.250$  mm. In addition, a Trask sorting factor of 1.33 was calculated by estimating the 1<sup>st</sup> and 3<sup>rd</sup> quartiles of the cumulative grain-size distribution [105]. The grain size distribution and degree of sorting are strongly related to the sediments transport and the energy of the depositional environment [106]. Consequently, we can conclude that determined well sorted Bentheimer grains are a result of the rather constant energy of the waves during transgressive-regressive cycles. The wave velocity was too low to carry the coarser grained sediments.

Comparison of the image/CT scans measurements with data from the literature [24, 87, 95] shows that all the data display similar results (Fig. 2.18). The median grain size is in the range 0.20–0.33 mm. With respect to the image analysis method used, there were some discrepancies between the results obtained. Both 2D and 3D image analysis have lower detection boundaries that are set by the size of pixels. In the case of the presented data, the resolutions were 0.58 [24], 10 [87], 68–89 [95], and 2.5  $\mu\text{m}$  for micro-CT scan studies. However, the variation of the sample types (different scales) and origin should be as well attributed to the spread in the results. Nevertheless, the magnitudes of the predicted grain size were comparable.

### PERMEABILITY

Absolute gas and liquid permeability, and permeability measured in flow experiments were investigated for old, intermediate and fresh samples (Table 2.4). An example of the

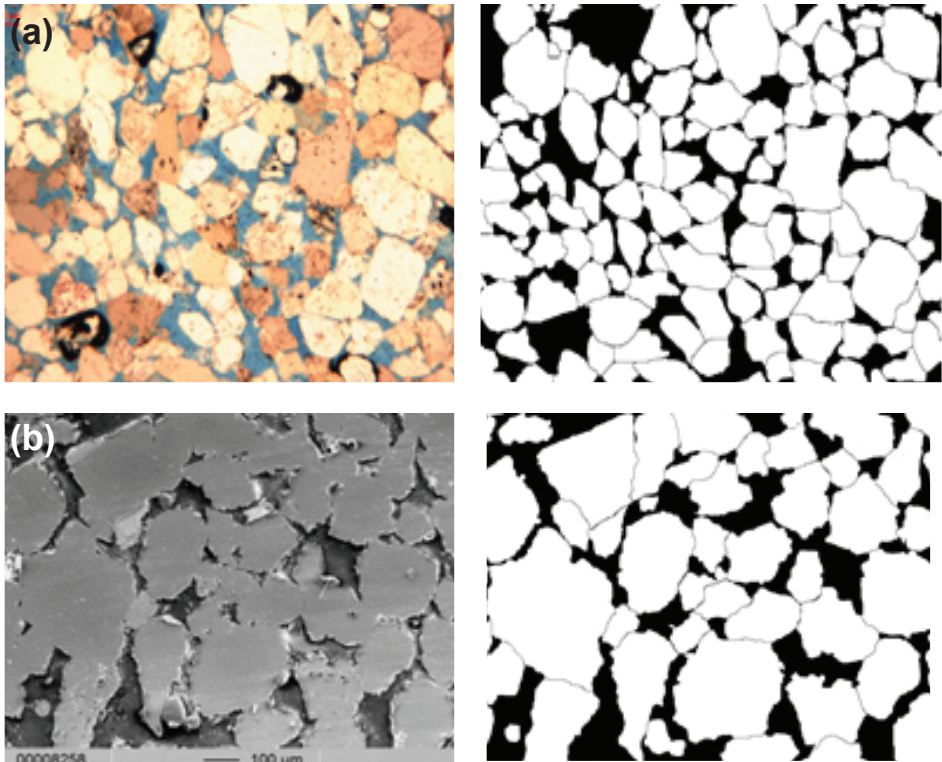
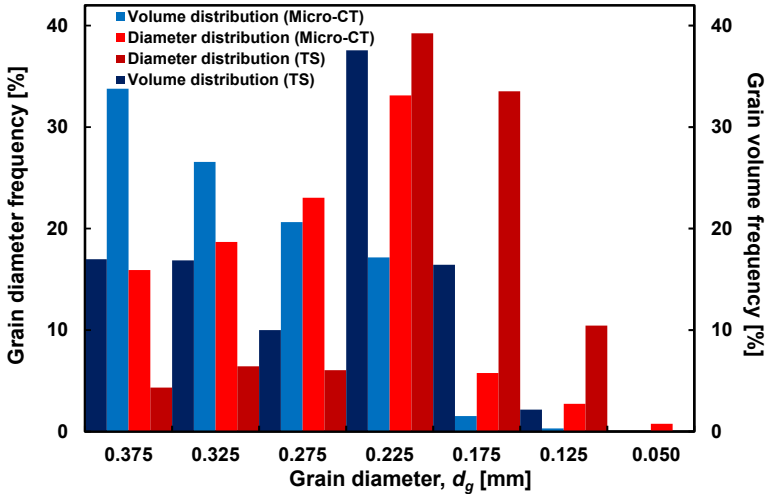
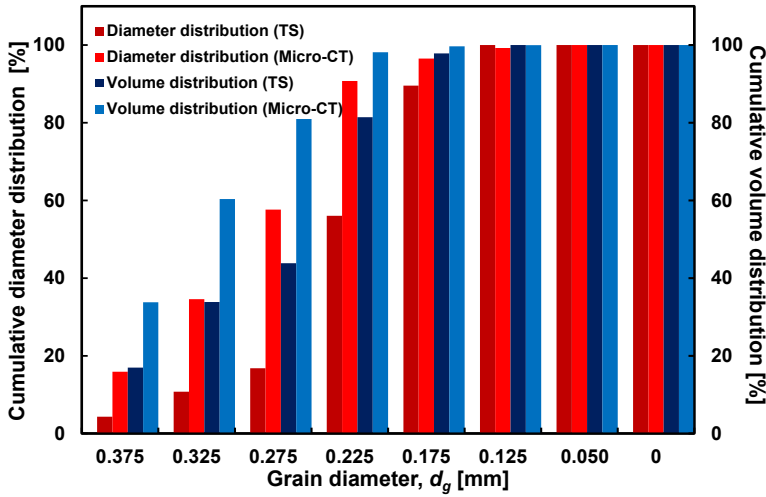


Figure 2.16: 2D images of a Bentheimer sandstone sample obtained by: (a) optical microscopy on polished sections; and (b) SEM. On the left side are the original images and on the right binary segmented images, where the quartz matrix is represented by white patterns and the pore space and grain contacts by black patterns. The porosity measurements were done on images with absence of grain contact determination. The feldspars grains were neglected in the matrix but subtracted in the pore space estimation.



(a)



(b)

Figure 2.17: (a) Grain size frequency histograms and grain volume frequency histograms obtained from statistical reconstruction of 2D thin sections of Bentheimer sandstone; (b) Cumulative percent frequency distribution of diameter curve and cumulative percent frequency distribution of volume curve.

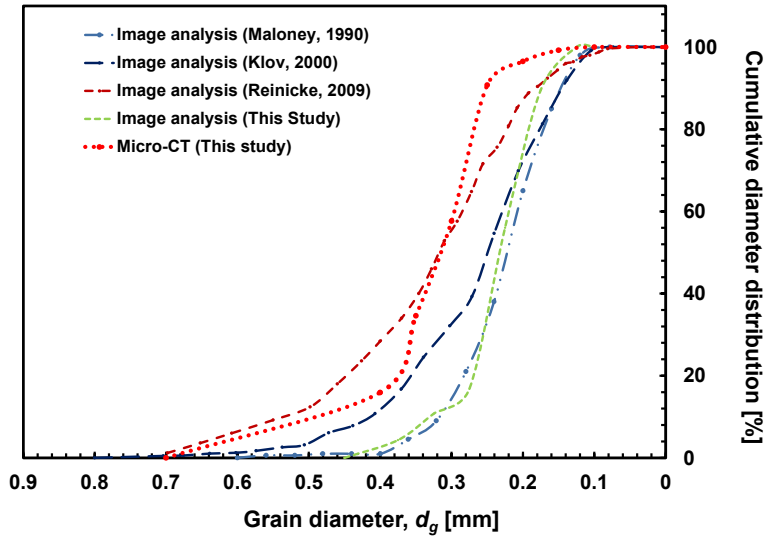


Figure 2.18: Comparison of cumulative grain size distribution obtained in various studies with values determined in this study.

obtained results for absolute gas permeability is presented in Fig. 2.19a. For comparison with image analysis methods, the absolute permeability was calculated from the grain size distribution (Table 2.4) using Carman-Kozeny. In addition, to examine the impact of the geographic location of the sample collection, the flow permeability was measured for all sample types (OS, IS, FS, FQ1-4). The different methods and all sample results show a close agreement in the range 1.35-3.09 Darcy, with an average of 1.80 Darcy. It can be seen that the mean values for each type of the measured samples shows a good representation of the values for each original block from which the samples were drilled ( $OS_{Ave} = 1.53 \pm 0.14$  Darcy,  $IS_{Ave} = 2.89 \pm 0.14$  Darcy,  $FS_{Ave} = 2.78 \pm 0.19$  Darcy). The four measurement methods used for all sample types show consistency in the trend of obtained values, i.e., from the highest to the lowest values, respectively, the Ruska gas permeability, the Ruska liquid permeability, liquid permeability measured flow experiments and the permeability obtained from stereological measurements. The permeability values obtained for intermediate and fresh samples show close agreement, however, the results on the old samples are lower. The old samples were measured again following the original measurement method. As a result, the original measurements show higher values (35%). This reduction in permeability with the old samples can be attributed to pore clogging and possibly volume increase by hydroxylation of fines.

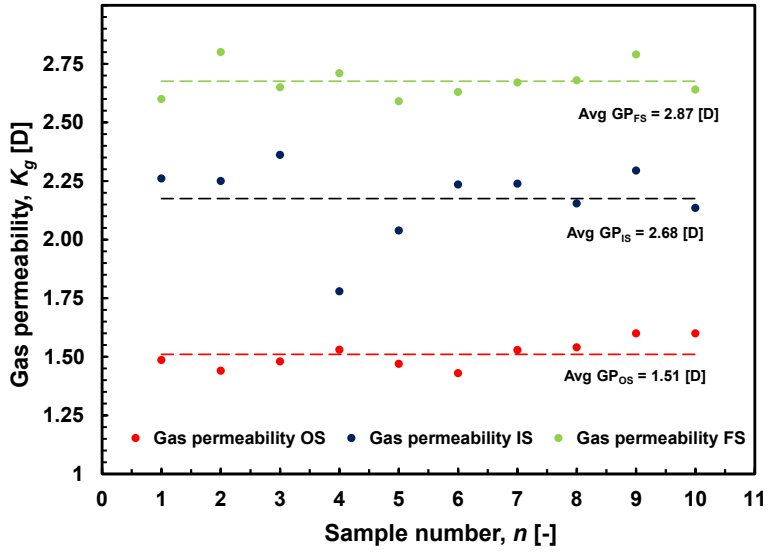
The spread of the values obtained from four different blocks with their locations is visualized in Table 2.4 ( $FQ_{Ave} = 1.54 \pm 0.52$ ). It can be concluded that the values depend on both the time when the samples were obtained and the location of the blocks in the quarry. As in the case of porosity, the block homogeneity is clearly visible.

Fig. 2.19b shows the relationship between the Ultra Pycnometer porosity and gas permeability of the old, intermediate and fresh samples; the permeability increases log-

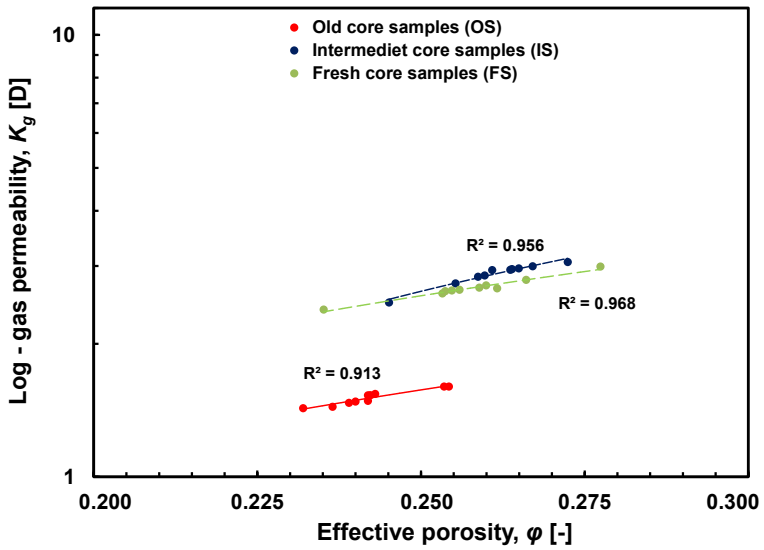
Table 2.4: Bentheimer sandstone permeability data obtained by various methods, per sample and per block. Number of measurements per block and per method is  $n = 10$ .

Method for each block	Samples type	Average permeability [D]	Average permeability for all methods [D]
Ruska gas permeameter	Old core samples	$1.74 \pm 0.07$	$1.53 \pm 0.14$
Liquid permeameter		$1.51 \pm 0.10$	
Flow experiment		$1.67 \pm 0.05$	
Grain size distribution from thin sections (Carmen–Kozeny)	Intermediate core samples	$1.45 \pm 0.12$	$2.89 \pm 0.14$
Ruska gas permeameter		$3.02 \pm 0.17$	
Liquid permeameter		$2.87 \pm 0.18$	
Flow experiment		$2.98 \pm 0.04$	
Grain size distribution from thin sections (Carmen –Kozeny)	Fresh samples	$2.70 \pm 0.15$	$2.78 \pm 0.19$
Ruska gas permeameter		$2.98 \pm 0.17$	
Liquid permeameter		$2.68 \pm 0.12$	
Flow experiment	Quarry samples 1 Quarry samples 2 Quarry samples 3 Quarry samples 4	$2.90 \pm 0.07$	–
Grain size distribution from thin sections (Carmen–Kozeny)		$2.56 \pm 0.10$	
Flow experiment		$1.48 \pm 0.04$	
Flow experiment		$1.04 \pm 0.03$	
Flow experiment		$2.27 \pm 0.09$	
		$1.35 \pm 0.04$	





(a)



(b)

Figure 2.19: (a) Laboratory measurements of gas permeability of old (OS) and intermediate (IS) core samples; (b) Por/Perm cross-plot for Bentheimer old and fresh cores analysis. Porosity was measured with the Ultra Pycnometer and permeability with a Ruska gas permeameter.

Table 2.5: Bentheimer sandstone permeability data gathered from literature.

Method	Absolute permeability [Darcy]
Perimeter (Ersland et al., 2010)	1.10
Perimeter (Dautriat et al., 2009)	1.60
Gas perimeter (Klinkenberg permeabilities) (Halisch, 2013a)	0.52–0.69
Gas perimeter (fired samples) (Maloney et al., 1990)	2.39
Water flow experiments	2.37
Water flow experiments	1.41

Table 2.6: Stress/strain measurements.

Samples	Max stress $\sigma_{\max}$ [MPa]	Loading type	
		Monotonic load	
		E-module tangent 50% $E_t$ [GPa]	Poisson ratio $\nu$
5 BS dry cores	38.93	14.69	0.25
5 BS water -saturated cores	33.99	13.52	0.28

linearly with the porosity. As the quarry samples are investigated, a linear relation between porosity and permeability is observed, which is mainly the characteristic feature of the shallow buried parts. With increasing buried depth, diagenetic alterations reduce the permeability relatively more than the porosity, which would result in a power function relation.

Comparison of our results with the literature data shows a close agreement of the absolute permeability (Table 2.5).

### MECHANICAL BEHAVIOR

The dry and water-saturated Bentheimer sandstone samples were subjected to monotonic loading and alternating loading (the unloading and reloading). The elastic constants of Bentheimer sandstone exhibit different characteristics for different scenarios. The axial compressive strength and elastic constants of dry and water saturated sandstones under monotonic loading and alternating loading are listed in Table 2.6. Tests result in the smaller tangent modulus for monotonic loading than for alternating loading. The elastic modulus of water-saturated Bentheimer sandstone is smaller than that of dry sandstone at the same strain rate, although the difference between Poisson ratios of dry and water-saturated sandstones is insignificant. The Poisson ratio of dry samples is slightly smaller than that of water-saturated samples. The wetting softening behavior of Bentheimer sandstone can be expressed by the softening coefficient - ratio of the axial compressive strength of water saturated sandstone and the axial compressive strength of dry sandstone. Based on the experiments the softening coefficient of Bentheimer sandstone is 87.3%. The determined slight strength reduction is related to the existence of pore fluid and the fluctuations in the physical state, and is a result of a decrease in the bonding strength of the rock matrix while wetting [107]. The measured values represent mechanical stability of the Bentheimer sandstone and are a result of quartz rich com-

position and the good sorting. Quartz does not exhibit twinning and cleavages, and are considered to be stiff [31].

#### SPECIFIC SURFACE CHARGE AREA

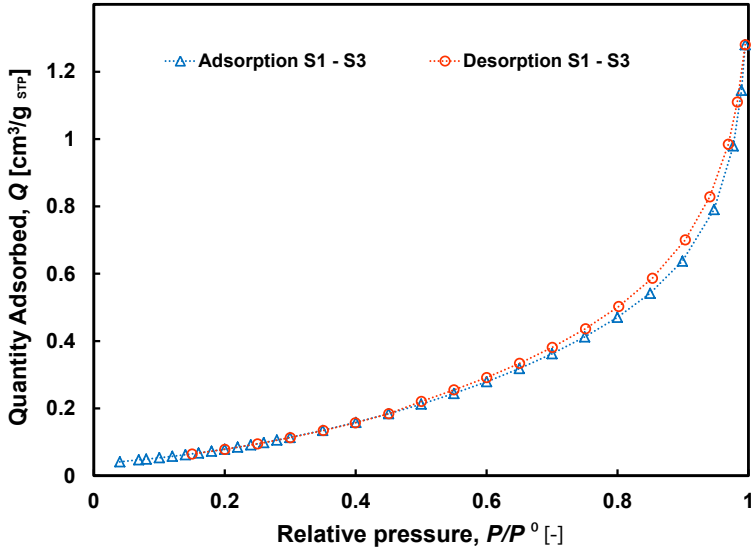
The adsorption and desorption isotherms were obtained by measuring the amount of nitrogen adsorbed and desorbed across a range of pressure steps at a constant temperature of 77 K (Fig. 2.20a). The three samples (S1-S3) show adsorption/desorption hysteresis that fits with a Type III isotherm of the Brunauer classification [101, 108]. The presence of very narrow hysteresis - adsorption and desorption branches - which almost coincide, indicates the lack of structural heterogeneity of Bentheimer sandstone and percolation. The capillary condensation region is recognized to be above a relative pressure of 0.4. The phenomenon of capillary condensation is an effect of the difference in the filling and emptying mechanisms of the mesopores (2-50 nm in accordance with the IUPAC Pore Size Classification Scheme [109]), giving rise to a hysteresis loop between adsorption and desorption. Specifically, at low relative pressures, coverage occurs first on a monolayer, followed by the adsorbed film, which acts as a nucleus. Applying the BET equation to the part of the adsorption isotherms corresponding to relative pressures in the range of 0.16 and 0.24 (where capillary condensation does not occur), we obtain a surface area equal to  $0.45 \text{ m}^2/\text{g}$  (Fig. 2.20b). The above value is in accordance with the value reported by [103].

#### DIELECTRIC BEHAVIOR

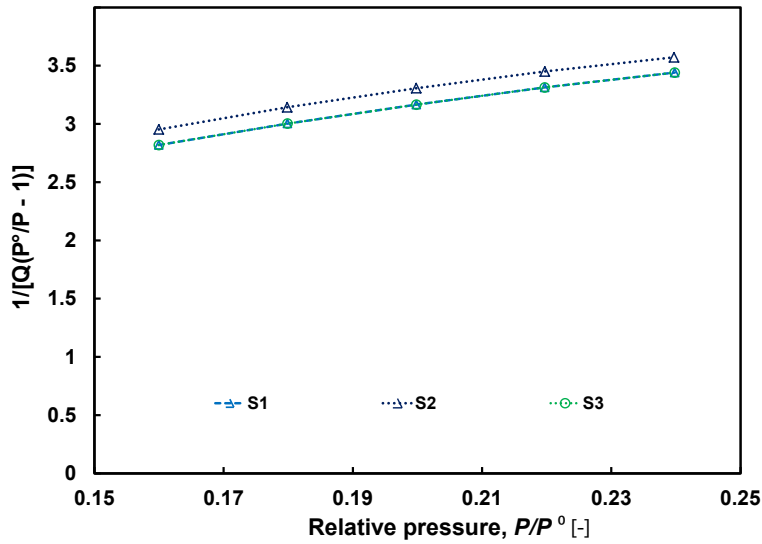
The dielectric behavior of Bentheimer sandstone is evaluated based on the change in surface charge due to the change in pH of the solution. Fig. 2.21 shows the surface charge,  $\zeta_0$ , and the proton balance related to the solid dissolution effects. The differences in the acid/base consumption balance are used to calculate the surface charge (from the slope of the graph) and the acid/base consumption for sample dissolution (assumption - the solution is saturated with dissolved sample matter (e.g. sample impurities or sample matter itself) for the smallest sample mass used in this plot). The Point of Zero Charge (PZC) value for the Bentheimer sandstone surface indicates that, at pH values higher than 8, the surface becomes negatively charged and the electrostatic repulsion of clays occurs. A similar phenomenon was observed in the clay dispersion and release studies of [110] and [111]. Clay particles were probably distributed in the sample and became mobile in contact with pH > 8 fluid. The higher the pH, the more visible the effect is. These effects may reduce the permeability of the rock. In addition, the effect of the presence of goethite and hematite in the samples on the point of zero charge was noted. Iron oxides represent the point of zero charge in the range of 8.5-11 [112]. The value of PZC measured in this study differs from value observed by [113] by the zeta potential determination of Bentheimer in water and in different electrolytic solutions. Further work on this topic is not within the scope of this study. It is suggested that the sandstone be fired to glass before performing dielectric experiments [114].

## 2.7. CONCLUSIONS

In this chapter, we determined the properties of Bentheimer sandstone for petrophysical and petrological behavior and dielectric impurities, especially for multiphase flow stud-



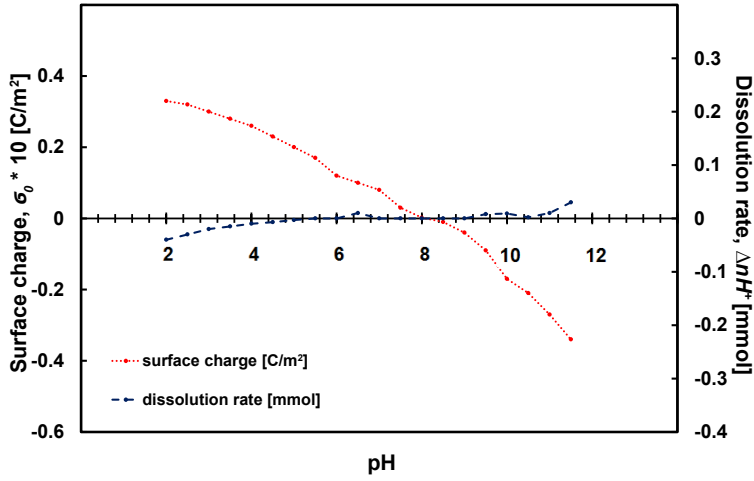
(a)



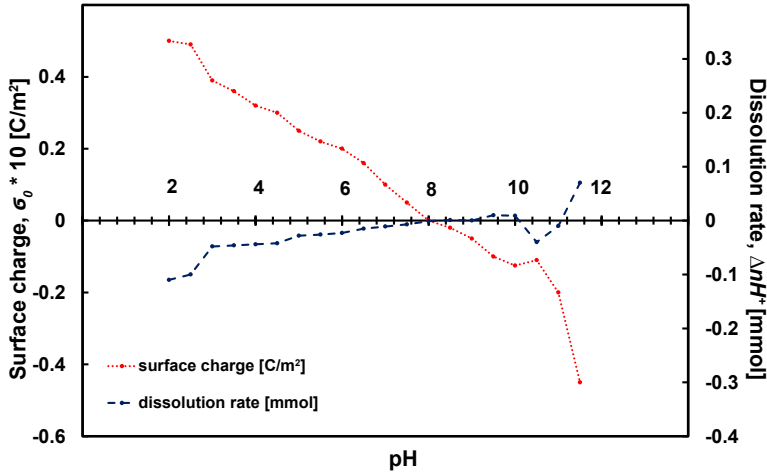
(b)

Figure 2.20: (a) An isotherm linear plot, representing the relation between the quantity adsorbed and the equilibrium pressure of the nitrogen (at constant temperature -77 K); (b) Example of a BET plot.

ies. Additionally, we estimated a variation in the accuracy of predictions of the sandstone properties based on estimations of the grain and pore size distribution. The results were compared to our own laboratory and literature data. After the results were gathered and



(a)



(b)

Figure 2.21: Surface charge density  $\sigma_0$  and sample dissolution effect  $\Delta n_{H^+}$  for Bentheimer sandstone in (a) de-ionized water; (b) 2.2M NaCl solution. Temperature is 294 K.

analyzed, they show a spread in values that can be summarized as follows:

- Bentheimer sandstone is an easily obtainable, well sorted porous material for comparative non-conductive physical experiments and preparing 3D pore frameworks for theoretical studies. The presence of accessory clay and (hydr)oxides makes it less favorable for conductive behavior;
- Bentheimer sandstone shows a constant mineralogy over the investigated samples, predominantly consisting of monocrystalline detrital quartz with authigenic

quartz overgrowths. The high quartz content results in a high mechanical stability what was proven by the uniaxial compressive test. However, the variety of accessory minerals in the Bentheimer sandstone (feldspars, clays, iron oxides and carbonate minerals) might lower to a smaller extent its chemical and mechanical stability. For example, as a result of the interaction of the sandstone with electrolytes, random dissolution of heterogeneous K-feldspars and precipitation of clays occurred and occurs (softening coefficient of Bentheimer is 87.3%). However, the small amounts of K-feldspar did not produce enough of the secondary clays to significantly affect the bulk reservoir porosity and permeability, unless a migration of clays created a proportionally large clogging zone, which incidentally happens;

- The sandstone presents high porosity in the range of 0.23-0.27. The porosity values, obtained by high-resolution microtomography or thin sections, were slightly lower than those found in laboratory measurements. This can be due to pixel resolution, because some of the smaller pores (pixel level) are merged with the matrix and not visible. However, the pore space information, obtained using microtomography or thin sections, is shown to be sufficient for spatial sample characterization. Combining all approaches to porosity determination gives a better estimation of the pore space (body and throat distribution, specific pore space, specific surface, etc.), and ultimately provides a more detailed description, covering a wider range of pore sizes from microns to mm (sizes varying by more than three orders of magnitude);
- Bentheimer sandstone is composed of well-sorted, mostly rounded to subrounded, grains resulting from the depositional environment of the sandstone. It shows a regular and narrow distribution of pore sizes (~10-50  $\mu\text{m}$  diameter of pore throats), which results in a high permeability. In addition, a narrow band in its grain size distribution and a specific surface area make Bentheimer sandstone a candidate for reference rock for laboratory studies;
- The repeatability of the experimental results is high, both in our work and compared to literature studies, i.e., porosity ( $\varphi$ ) is 0.20-0.26, the median grain diameter lies in the range 0.20-0.33 mm, the median pore throat and body diameters are 0.01-0.12 mm and 0.02-0.18 mm, respectively;
- Surface charge problems due to the occurrence of dispersed accessory, i.e., iron (hydr)oxides and clay mineral, were observed. It is suggested that the sandstone be fired before performing dielectric experiments.

By comparing different techniques to measure certain parameters, we conclude that the efficiency and accuracy of the various techniques must be taken into consideration when planning the measurements, even though the difference between the obtained values remains relatively low. It should be noted that it was not possible to eliminate natural variation of the samples for all measurements, mainly because of different types of samples needed for certain tests. The variations can be concluded as follows:

- Porosity measurements - Ultra Pycnometer measurements with gas give higher values than gravimetric methods (4-5% difference). Using  $\text{N}_2$  or He gas instead of water has the advantage of being non-reactive (important when samples contain more clays). Image analysis gives results close to the average values obtained by

laboratory methods;

- Permeability measurements: gas measurements show higher results than water permeability due to slip flow of gas at the pore walls and can increase with increasing pore pressure. The water permeability values can be estimated based on gas permeability measurements;
- Pore bodies and throat distribution: the most appropriate method to measure the small diameter pore bodies are micro-CT analysis (discrete result) and mercury porosimetry (bulk result) for pore radii smaller than 0.01 mm. The larger pore bodies and pores with a radius larger than 0.05 mm are more accurately measured with a combination of thin sections, image analysis and micro-CT. The assumption that isotropy and block - scale homogeneity are present in the entire matrix means that the results are assumed to be realistic. Hence, a combination of different methods provides a representative image of the pore system through different scales;
- Grain size distribution: both 2D and 3D image analysis have smaller values due to the pixel size measurements. The orders of magnitude of the grain size distribution results for the 2D and 3D methods were comparable.

## REFERENCES

- [1] C. Wim Dubelaar and T. G. Nijland, *The Bentheim Sandstone: Geology, Petrophysics, Varieties and Its Use as Dimension Stone*, in *Engineering Geology for Society and Territory - Volume 8: Preservation of Cultural Heritage*, edited by G. Lollino, D. Giordan, C. Marunteanu, B. Charstaras, I. Yoshinori, and C. Margottini (Springer International Publishing, Cham, 2015) pp. 557–563.
- [2] H. Füchtbauer, *Paleogeography and reservoir properties of the Lower Cretaceous "Bentheim Sandstone"*, Excursion Guide Book I, 6th World Petroleum Congress **M**, 42 (1963).
- [3] H. Füchtbauer, *Zur Petrographie des Bentheimer Sandsteins im Emsland*, Erdöl und Kohle **8**, 616 (1955).
- [4] E. Kemper, *Geologischer Führer durch die Grafschaft Bentheim und die angrenzenden Gebiete* (1968).
- [5] E. Kemper, *Geologischer Führer durch die Grafschaft Bentheim und die angrenzenden Gebiete mit einem Abriß der Emsländischen Unterkreide* (1976).
- [6] W. Knaap and M. Coenen, *Exploration for oil and natural gas, Seventy-five Years of Geology and Mining in the Netherlands (1912-1987)*, 207 (1987).
- [7] E. Klein and T. Reuschlé, *A model for the mechanical behaviour of Bentheim Sandstone in the brittle regime*, Thermo-hydro-mechanical Coupling in Fractured Rock. Pageoph Topical Volumes. Birkhäuser Basel, Basel, 833 (2003).
- [8] J. Ruedrich and S. Siegesmund, *Salt and ice crystallisation in porous sandstones*, Environmental Geology **52**, 343 (2007).

- [9] A. Jacquy, M. Cacace, G. Blöcher, E. Huenges, and M. Scheck-Wenderoth, *Hydro-mechanical evolution of transport properties in porous media: constrains for numerical modeling of geothermal systems*, Paper presented at the 3rd European Geothermal Workshop, Karlsruhe, Germany, October, 15-16, 2014 (2014).
- [10] A. Jacquy, M. Cacace, and G. Blöcher, *Scheck-Wenderoth M modelling of fractured reservoirs: fluid-rock interactions within fault domains*, GeoMod Potsdam, 31.08-05.09. 2014 , 407 (2014).
- [11] D. Reyer and S. Philipp, *Empirical relations of rock properties of outcrop and core samples from the Northwest German Basin for geothermal drilling*, Geotherm. Energy Sci. **2**, 21 (2014).
- [12] T. Smith and R. McKibbin, *An investigation of boiling processes in hydrothermal eruptions*, Paper presented at the World Geothermal Congress, Kyushu-Tohoku, Japan, May 28-June 10, 2000 (2000).
- [13] A. Al-Menhali, C. Reynolds, P. Lai, B. Niu, N. Nicholls, J. Crawshaw, and S. Krevor, *Advanced reservoir characterization for CO<sub>2</sub> storage*, Paper Presented at the IPTC 2014: International Petroleum Technology Conference, December, 10-12, 2014 (2014).
- [14] L. Andersson, A. Herring, D. Newell, and B. Carey, *Wildenschild D high-resolution X-ray tomography imaging of supercritical CO<sub>2</sub>: investigating capillary trapping under reservoir conditions and addressing wettability alteration*, AGU Fall Meeting Abstracts (2013).
- [15] M. Andrew, B. Bijeljic, and M. Blunt, *Pore-scale imaging of geological carbon dioxide storage under in situ conditions*, Geophysical Research Letters **40**, 3915 (2013).
- [16] A. Herring, *Saturation, Morphology, and Topology of Nonwetting Phase Fluid in Bentheimer Sandstone Application to Geologic Sequestration of Supercritical CO<sub>2</sub>*, Ph.D. thesis, Oregon State University (2012).
- [17] T. Holt, J.-I. Jensen, and E. Lindeberg, *Underground storage of CO<sub>2</sub> in aquifers and oil reservoirs*, Energy Conversion and Management **36**, 535 (1995).
- [18] B. Kvamme, A. Graue, T. Kuznetsova, T. Buanes, and G. Ersland, *Exploitation of natural gas hydrate reservoirs combined with long term storage of CO<sub>2</sub>*, WSEAS TRANSACTIONS on Environment and Development **2**, 699 (2006).
- [19] N. Shojaikaveh, C. Berentsen, S. Rudolph-Floter, K. Wolf, and W. Rossen, *Wettability determination by equilibrium contact angle measurements: reservoir rock - connate water system with injection of CO<sub>2</sub>*, Paper presented at the SPE Europec/EAGE Annual Conference, Copenhagen, Denmark, January, 1, 2012 (2012).
- [20] H. Wright, J. Roberts, and K. Cashman, *Permeability of anisotropic tube pumice: Model calculations and measurements*, Geophysical Research Letters **33** (2006), 10.1029/2006GL027224.



- [21] M. A. Chandler, G. Kocurek, D. J. Goggin, and L. W. Lake, *Effects of stratigraphic heterogeneity on permeability in eolian sandstone sequence, Page Sandstone, Northern Arizona*, American Association of Petroleum Geologists Bulletin **73**, 658 (1989).
- [22] J.-B. Clavaud, A. Maineult, M. Zamora, P. Rasolofosaon, and C. Schlitter, *Permeability anisotropy and its relations with porous medium structure*, Journal of Geophysical Research: Solid Earth **113** (2008), 10.1029/2007JB005004.
- [23] G. Al-Muntasheri, P. Zitha, and H. Nasr-Ei-Din, *A new organic gel system for water control: A computed tomography study*, SPE Journal **15**, 197 (2010).
- [24] D. Maloney, M. Honarpour, and A. Brinkmeyer, *The Effects of Rock Characteristics on Relative Permeability* (1990).
- [25] S. Mayr and H. Burkhardt, *Ultrasonic properties of sedimentary rocks: Effect of pressure, saturation, frequency and microcracks*, Geophysical Journal International **164**, 246 (2006).
- [26] J. Van Baaren, M. Vos, and H. Heller, *Selection of Outcrop Samples 1* (1990), tU Delft, Delft, The Netherlands.
- [27] K.-H. Wolf and M. Hettema, *Petrophysical and Mineralogical Properties of Overburden Rock and Coal, Part 2 (R)* **22** (1995), 10.2118/129659-PA.
- [28] J. Calvo, A. Hernández, P. Prádanos, and F. Tejerina, *Charge adsorption and zeta potential in cyclopore membranes*, Journal of Colloid and Interface Science **181**, 399 (1996).
- [29] A. Stadler, *Der Bentheimer Sandstein (Valangin, NW-Deutschland): eine palökologische und sequenzstratigraphische analyse* (1998).
- [30] P. Malmberg, *Correlation between Diagenesis and Sedimentary Facies of the Bentheim Sandstone, the Schonebeek Field, The Netherlands: Petrographic and Sedimentological Re-evaluation of a Petroleum Reservoir* (2002), dissertation.
- [31] H. Mansurbeg, *Modelling of Reservoir Quality in Quartz-rich Sandstones of the Lower Cretaceous Bentheim Sandstones, Lower Saxony Basin, NW Germany*, Ph.D. thesis, Lunds Universitet, Lund, Sweden (2001).
- [32] J. Wonham, H. Johnson, J. Mutterlose, A. Stadler, and A. Ruffell, *Characterization of a shallow marine sandstone reservoir in a syn-rift setting: the Bentheim Sandstone Formation (Valanginian) of the Rühlermoor Field, Lower Saxony Basin, NW Germany*, Paper presented at the GCSSEPM Foundation 18th Annual Research Conference Shallow Marine and Nonmarine Reservoirs, December 7-10, 1997 (1997).
- [33] J. Mutterlose and A. Bornemann, *Distribution and facies patterns of lower Cretaceous sediments in northern Germany: A review*, Cretaceous Research **21**, 733 (2000).

- [34] T. Al Ghamdi and C. Arns, Predicting Relative Permeability from NMR Relaxation-diffusion Responses Utilizing High Resolution Micro X Ray-CT Images (2012).
- [35] D. Doughty and L. Tomutsa, *Multinuclear NMR microscopy of two-phase fluid systems in porous rock*, Magnetic Resonance Imaging **14**, 869 (1996).
- [36] M. Johns, A. Sederman, L. Gladden, A. Wilson, and S. Davies, *Using MR techniques to probe permeability reduction in rock cores*, AIChE Journal **49**, 1076 (2003).
- [37] P. Mansfield and B. Issa, *Studies of fluid transport in porous rocks by echo-planar MRI*, Magnetic Resonance Imaging **12**, 275 (1994).
- [38] J. Mitchell, A. Sederman, E. Fordham, M. Johns, and L. Gladden, *A rapid measurement of flow propagators in porous rocks*, Journal of Magnetic Resonance **191**, 267 (2008).
- [39] I. Swaid, K. Wilke, and D. Kessel, *Relative permeabilities and rheology of polymers in sandstone cores*, Revue de l'Institute Francais du Petrole **52**, 263 (1997).
- [40] G. Blöcher, T. Reinsch, A. Hassanzadegan, H. Milsch, and G. Zimmermann, *Direct and indirect laboratory measurements of poroelastic properties of two consolidated sandstones*, International Journal of Rock Mechanics and Mining Sciences **67**, 191 (2014).
- [41] W. De Boever, T. Bultreys, M. Traska, A. Mock, L. Brabant, and V. Cnudde, *3D characterisation of the Bentheimer Sandstone and Euville Limestone, in relation to fluid flow through their pore networks*, Paper presented at the 14th Euroseminar on Microscopy Applied to Building Materials (EMABM 2013), June, 10-14, 2013 (2013).
- [42] G. Ersland, J. Husebø, A. Graue, B. Baldwin, J. Howard, and J. Stevens, *Measuring gas hydrate formation and exchange with CO<sub>2</sub> in Bentheim sandstone using MRI tomography*, Chemical Engineering Journal **158**, 25 (2010).
- [43] M. Fernø, . Haugen, S. Wickramathilaka, J. Howard, A. Graue, G. Mason, and N. Morrow, *Magnetic resonance imaging of the development of fronts during spontaneous imbibition*, Journal of Petroleum Science and Engineering **101**, 1 (2013).
- [44] E. Klein, P. Baud, T. Reuschlé, and T.-F. Wong, *Mechanical behaviour and failure mode of Bentheim sandstone under triaxial compression*, Physics and Chemistry of the Earth, Part A: Solid Earth and Geodesy **26**, 21 (2001).
- [45] B. Kvamme, A. Graue, T. Buanes, T. Kuznetsova, and G. Ersland, *Storage of CO<sub>2</sub> in natural gas hydrate reservoirs and the effect of hydrate as an extra sealing in cold aquifers*, International Journal of Greenhouse Gas Control **1**, 236 (2007).
- [46] M. Smeets and M. Golombok, *Application of shear induced structure materials for brine flooding in sandstone oil reservoirs*, Journal of Petroleum Science and Engineering **72**, 270 (2010).

- [47] S. Bakke and P. Øren, *3-D pore-scale modelling of sandstones and flow simulations in the pore networks*, SPE J. **2**, 136 (2013).
- [48] T. Bultreys, W. De Boever, L. Brabant, and V. Cnudde, *Comparison of pore network models for the investigation of fluid flow properties in building stones*, Paper presented at the 5th International Conference on Porous Media & Annual Meeting of the International Society for Porous Media (InterPore 2013), May, 22-24, 2013 (2013).
- [49] L. Louis, C. David, V. Metz, P. Robion, B. Menéndez, and C. Kissel, *Microstructural control on the anisotropy of elastic and transport properties in undeformed sandstones*, International Journal of Rock Mechanics and Mining Sciences **42**, 911 (2005).
- [50] Q. Nguyen, W. Rossen, P. Zitha, and P. Currie, *Determination of gas trapping with foam using X-ray computed tomography and effluent analysis*, SPE Journal **14**, 222 (2009).
- [51] T. Ramstad, P.-E. Øren, and S. Bakke, *Simulation of two-phase flow in Reservoir rocks using a lattice Boltzmann method*, SPE Journal **15**, 923 (2010).
- [52] J.-F. Thovert and P. Adler, *Grain reconstruction of porous media: Application to a Bentheim sandstone*, Physical Review E - Statistical, Nonlinear, and Soft Matter Physics **83** (2011), 10.1103/PhysRevE.83.056116.
- [53] A. Al-Futaisi and T. Patzek, *Impact of microscopic NAPL-water interface configurations on subsequent gas injection into water-wet permeable rocks*, Developments in Water Science **55**, 139 (2004).
- [54] M. Amro and D. Kessel, *Feasibility of microbially improved oil recovery (MIOR) in Northern German oil reservoirs [Bakterien zur Erhöhung des Entölungsgrades in norddeutschen Erdöllagerstätten]*, Erdoel Erdgas Kohle/EKEP **112**, 193 (1996).
- [55] C. Berg, *Re-examining Archie's law: Conductance description by tortuosity and constriction*, Physical Review E - Statistical, Nonlinear, and Soft Matter Physics **86** (2012), 10.1103/PhysRevE.86.046314.
- [56] R. Borschinsky and H. Kulke, *Facies model of an oil reservoir using three-dimensional modeling: example Bentheimer sandstone, field Georgsdorf (north-eastern Part), Germany*, Erdoel Erdgas Kohle **108**, 442 (1992).
- [57] M. Feali, W. Pinczewski, Y. Cinar, C. H. Arns, J.-Y. Arns, N. Francois, M. L. Turner, T. Senden, M. A. Knackstedt, *et al.*, *Qualitative and quantitative analyses of the three-phase distribution of oil, water, and gas in bentheimer sandstone by use of micro-CT imaging*, SPE Reservoir Evaluation & Engineering **15**, 706 (2012).
- [58] H. Fodisch, J. Wegner, R. Hincapie-Reina, and L. Ganzer, *Characterization of glass filter micromodels used for polymer EOR flooding experiments*, DGMK Tagungsbericht , 325 (2013).

- [59] O. Frette and J. Helland, *A semi-analytical model for computation of capillary entry pressures and fluid configurations in uniformly-wet pore spaces from 2D rock images*, *Advances in Water Resources* **33**, 846 (2010).
- [60] E. Hansen, M. Stöcker, K. Olafsen, and P. Kvernberg, *Gelation kinetics of polymers confined in water/oil-saturated porous materials probed by NMR*, *Journal of Dispersion Science and Technology* **20**, 723 (1999).
- [61] F. Hesselink and M. Faber, *Polymer-surfactant interaction and its effect on the mobilization of capillary-trapped oil*, (1981) pp. 861–869.
- [62] T. Maldal and H. Hølland, *Phase behaviour and chemical flooding properties of water-oil-nonionic amphiphile mixtures*, *In Situ* **21**, 271 (1997).
- [63] T. Maldal, A. Gulbrandsen, and E. Gilje, *Correlation of capillary number curves and remaining oil saturations for reservoir and model sandstones*, *In Situ* **21**, 239 (1997).
- [64] P. Mansfield, R. Bowtell, S. Blackband, and D. Guilfoyle, *Magnetic resonance imaging: Applications of novel methods in studies of porous media*, *Magnetic Resonance Imaging* **10**, 741 (1992).
- [65] W. McLendon, P. Koronaios, R. Enick, G. Biesmans, L. Salazar, A. Miller, Y. Soong, T. McLendon, V. Romanov, and D. Crandall, *Assessment of CO<sub>2</sub>-soluble non-ionic surfactants for mobility reduction using mobility measurements and CT imaging*, *Journal of Petroleum Science and Engineering* **119**, 196 (2014).
- [66] W. McLendon, *Assessment of CO<sub>2</sub>-soluble surfactants for mobility reduction using mobility measurements and CT imaging*, Paper presented at the 18th SPE Improved Oil Recovery Symposium, Tulsa, OK, United States, April 14-18, 2012 (2012).
- [67] O. Olafuyi, Y. Cinar, M. Knackstedt, and W. Pinczewski, *Downscaled capillary pressure and relative permeability of small cores for network model validation*, *International Journal of Engineering Research in Africa* **4**, 15 (2011).
- [68] R. Reichenbach-Klinke, A. Stavland, B. Langlotz, B. Wenzke, and G. Brodt, *New insights into the mechanism of mobility reduction by associative type copolymers*, Paper presented at the SPE Enhanced Oil Recovery Conference, Kuala Lumpur, Malaysia, July 2-4, 2013 (2013).
- [69] K. Romanenko and B. Balcom, *An assessment of non-wetting phase relative permeability in water-wet sandstones based on quantitative MRI of capillary end effects*, *Journal of Petroleum Science and Engineering* **110**, 225 (2013).
- [70] S. Sheppard, M. Mantle, A. Sederman, M. Johns, and L. Gladden, *Magnetic resonance imaging study of complex fluid flow in porous media: Flow patterns and quantitative saturation profiling of amphiphilic fracturing fluid displacement in sandstone cores*, *Magnetic Resonance Imaging* **21**, 365 (2003).

- [71] N. Shojai Kaveh, E. Rudolph, P. Van Hemert, W. Rossen, and K.-H. Wolf, *Wettability evaluation of a CO<sub>2</sub>/water/bentheimer sandstone system: Contact angle, dissolution, and bubble size*, Energy and Fuels **28**, 4002 (2014).
- [72] L. Siggel, *A new class of viscoelastic surfactants for enhanced oil recovery*, Paper presented at the PE Improved Oil Recovery Symposium, Tulsa, OK, USA, January, 1, 2012 (2012).
- [73] M. Simjoo, Y. Dong, A. Andrianov, M. Talanana, and P. Zitha, *CT scan study of immiscible foam flow in porous media for enhancing oil recovery*, Industrial and Engineering Chemistry Research **52**, 6221 (2013).
- [74] A. Skauge, P. Ormehaug, T. Gurholt, B. Vik, I. Bondino, and G. Hamon, *2-D visualisation of unstable waterflood and polymer flood for displacement of heavy oil*, Paper presented at the 18th SPE Improved Oil Recovery Symposium, Tulsa, OK, United States, April, 14-18, 2012 (2012).
- [75] K. Taugbøl, T. Ly, and T. Austad, *Chemical flooding of oil reservoirs 3. Dissociative surfactant-polymer interaction with a positive effect on oil recovery*, Colloids and Surfaces A: Physicochemical and Engineering Aspects **103**, 83 (1995).
- [76] D. Wever, F. Picchioni, and A. Broekhuis, *Comblike polyacrylamides as flooding agent in enhanced oil recovery*, Industrial and Engineering Chemistry Research **52**, 16352 (2013).
- [77] D. Xiao and B. Balcom, *K-t Acceleration in pure phase encode MRI to monitor dynamic flooding processes in rock core plugs*, Journal of Magnetic Resonance **243**, 114 (2014).
- [78] Y. Zhou, J. Helland, and D. Hatzignatiou, *A dimensionless capillary pressure function for imbibition derived from pore-scale modelling in mixed-wet rock images*, Paper presented at the 18th SPE Improved Oil Recovery Symposium, Tulsa, OK, United States, April, 14-18, 2012 (2012).
- [79] Y. Zhou, J. Helland, and D. Hatzignatiou, *Pore-scale modelling of water flooding in mixed-wet rock images: effects of initial saturation and wettability*, Paper presented at the 18th SPE Improved Oil Recovery Symposium, Tulsa, OK, United States, April, 14-18, 2012 (2012).
- [80] B. Kvamme, A. Graue, T. Buanes, T. Kuznetsova, and G. Ersland, *Effects of solid surfaces on hydrate kinetics and stability*, Geological Society Special Publication **319**, 131 (2009).
- [81] P. Mansfield and B. Issa, *A microscopic model of fluid transport in porous rocks*, Magnetic Resonance Imaging **14**, 711 (1996).
- [82] D. Betz, F. Führer, G. Greiner, and E. Plein, *Evolution of the Lower Saxony Basin*, Tectonophysics **137**, 127 (1987).
- [83] E. Kemper, *Die Tiefe Unterkreide Im Vechte-Dinkel-Gebiet* (1992).

- [84] C. Hinze, *Geologische Karte von Niedersachsen 1: 25.000 Erläuterungen zu Blatt* (1988).
- [85] J. De Jager and M. Geluk, *Petroleum geology, Geology of the Netherlands*, 241 (2007).
- [86] G. Dresen, S. Stanchits, and E. Rybacki, *Borehole breakout evolution through acoustic emission location analysis*, *International Journal of Rock Mechanics and Mining Sciences* **47**, 426 (2010).
- [87] T. Klov, *High Velocity Flow in Fractures*, Ph.D. thesis, Norwegian University of Science and Technology, Trondheim, Norway (2000).
- [88] H. Milsch and G. Blöcher, *Direct and simultaneous measurements of sandstone porosity, permeability, and electrical conductivity at elevated pressures*, (2013) pp. 1415–1424.
- [89] S. Stanchits, J. Fortin, Y. Gueguen, and G. Dresen, *Initiation and propagation of compaction bands in dry and wet Bentheim Sandstone*, *Rock Physics and Natural Hazards*. Pageoph Topical Volumes. Birkhäuser Basel, Germany, 846 (2009).
- [90] J. Jeremiah, S. Duxbury, and P. Rawson, *Lower Cretaceous of the southern North Sea Basins: Reservoir distribution within a sequence stratigraphic framework*, *Geologie en Mijnbouw/Netherlands Journal of Geosciences* **89**, 203 (2010).
- [91] J. Dautriat, N. Gland, J. Guelard, A. Dimanov, and J. Raphanel, *Axial and radial permeability evolutions of compressed sandstones. end effects and shear-band induced permeability anisotropy*, *Rock physics and natural hazards (Pageoph topical volumes)*, 1037 (2009).
- [92] M. Halisch, *Assessment of porous rocks by Capillary flow porometry*, Paper presented at the International Symposium of the Society of Core Analysts, Napa Valley, California, USA, 2013 (2013).
- [93] S. Hassan, *Electric properties and its effect on microporosity rocks*, Paper presented at the SPE International Production and Operations Conference & Exhibition, Doha, Qatar, 14-16 May 2012 (2012).
- [94] L. Louis, C. David, and P. Robion, *Comparison of the anisotropic behaviour of undeformed sandstones under dry and saturated conditions*, *Tectonophysics* **370**, 193 (2003).
- [95] A. Reinicke, *Mechanical and Hydraulic Aspects of Rock-Proppant Systems-Laboratory Experiments and Modelling Approaches*, Ph.D. thesis, Deutsches Geoforschungszentrum, Potsdam, Germany (2009).
- [96] K. Gubbins, *Hysteresis Phenomena in Mesoporous Materials*, Ph.D. thesis, Universität Leipzig, Leipzig, Germany. (2009).

- [97] S. Wicksell, *The corpuscle problem. A mathematical study of a biometric problem*, *Biometrika* **17**, 84 (1925).
- [98] J. Russ and R. Dehoff, *Practical Stereology* (Plenum Press, New York and London, 1991).
- [99] K. Ruzyla, *Characterization of Pore Space By Quantitative Image Analysis*, Society of Petroleum Engineers , 389 (1986).
- [100] W. Janusz, *Electrical double layer at the metal oxide-electrolyte interface*, in *Interfacial Forces and Fields: Theory and Applications*, Vol. 85, edited by J. Hsu (CRC Press, Taipei, Taiwan, 1999).
- [101] S. Brunauer, P. Emmett, and E. Teller, *Adsorption of gases in multimolecular layers*, *Journal of the American Chemical Society* **60**, 309 (1938).
- [102] W. Kahl, V. Feeser, R. Hinkes, A. Holzheid, and J. Raphanel, *Anisotropy of Elastic Waves in Sandstone: Correlation with Microstructural Observations* (2013).
- [103] M. Halisch, *Application and Assessment of the Lattice Boltzmann Method for Fluid Flow Modeling in Porous Rocks*, Ph.D. thesis, Technische Universität Berlin, Berlin, Germany. (2013).
- [104] R. Sneider, *Practical Petrophysics for Exploration and Development: AAPG Education Dept. Short Course Notes* (1987).
- [105] R. Selley, *Applied Sedimentology* (Academic Press, San Diego, California, United States, 2000).
- [106] S. Dutton and B. Willis, *Comparison of outcrop and subsurface sandstone permeability distribution, lower cretaceous fall river formation, south dakota and wyoming*, *Journal of Sedimentary Research* **68**, 890 (1998).
- [107] M. Lin, F. Jeng, L. Tsai, and T. Huang, *Wetting weakening of tertiary sandstones - Microscopic mechanism*, *Environmental Geology* **48**, 265 (2005).
- [108] S. Brunauer, L. S. Deming, W. E. Deming, and E. Teller, *On a theory of the van der Waals adsorption of gases*, *Journal of the American Chemical society* **62**, 1723 (1940).
- [109] K. Sing, D. Everett, R. Haul, L. Moscou, R. Pierotti, J. Rouquerol, and T. Siemieniowska, *Reporting physisorption data for gas/solid systems*, *Handbook of Heterogeneous Catalysis* , 1217 (2008).
- [110] D. Gray and R. Rex, *Formation damage in sandstones caused by clay dispersion and migration*, *Clays Clay Miner.* , 355 (1966).
- [111] D. Simon, B. McDaniel, and R. Coon, *Evaluation of fluid pH effects on low permeability sandstones*, *SPE Annual Fall Technical Conference and Exhibition* (1976).

- [112] C. Appel, L. Ma, R. Rhue, and E. Kennelley, *Point of zero charge determination in soils and minerals via traditional methods and detection of electroacoustic mobility*, *Geoderma* **113**, 77 (2003).
- [113] U. Farooq, M. Tweheyo, J. Sjöblom, and G. Oye, *Surface characterization of model, outcrop, and reservoir samples in low salinity aqueous solutions*, *Journal of Dispersion Science and Technology* **32**, 519 (2011).
- [114] J. Shaw, P. Churcher, and B. Hawkins, *The Effect of Firing on Berea Sandstone*, *Society of Petroleum Engineers* **6**, 72 (1991).





# 3

## ROCK CHARACTERIZATION FOR ELECTROKINETIC STUDIES

### UNFIRED VS FIRED BENTHEIMER SANDSTONE

*Bentheimer sandstone is a quartz-rich permeable hard sedimentary rock used for core flooding experiments. When fired (subjected to high temperatures) to stabilize clays, pyrometamorphical phase changes induce texture and pore framework alteration. As a consequence, the new dielectric response may influence wettability. The literature regarding pyrometamorphical behavior during and after thermal treatment is unambiguous, so we evaluate desirable (fixation of clay minerals) and undesirable effects (dielectric surface changes) in the matrix. Porosity, permeability, surface charge, specific surface area and dielectric response were measured before and after firing of samples, at temperatures up to ~1000°C under oxidizing and non-oxidizing conditions. The matrix properties were determined using XRD/XRF, scanning electron microscope imaging and thermomechanical- and thermogravimetric analysis with differential scanning calorimetry. Firing causes dehydration, dehydroxylation and irreversible transformation of original clays, organic matter, and carbonates to glass, oxides and feldspars. During heating quartz transfers from  $\alpha$ - to  $\beta$ -quartz and back during cooling. This thermal transformation changes the grain volumes and, consequently, reduces the matrix integrity. The sandstone has a slight porosity and permeability increase (~ 5%). Further, a shift in the point of zero charge toward a higher pH may result in wettability alteration from strongly water-wet to oil-wet. Additionally, a decrease in the permittivity value and marginal dispersion of the dielectric constant (~ 5%) between the high and the low frequencies was observed. Due to firing and related dispersion of the iron oxides within the matrix framework, Bentheimer sandstone becomes a weaker insulator.*

---

This chapter has been published as: Anna E. Pęksa, Karl-Heinz A.A. Wolf, Evert C. Slob, Łukasz Chmura, Pacelli L.J. Zitha, Original and pyrometamorphical altered Bentheimer sandstone; petrophysical properties, surface and dielectric behavior, Journal of Petroleum Science and Engineering, Available online 19 October 2016, ISSN 0920-4105, <http://dx.doi.org/10.1016/j.petrol.2016.10.024>.

## NOMENCLATURE AND SUBSCRIPTS

$\alpha$	Average coefficient of expansion, [-]
$A$	Effective area of the electrode, mm <sup>2</sup>
$\Delta\epsilon'_r$	Dielectric dispersion magnitude
$\Delta n$	Dissolution rate, mmol
$C_0$	Capacitance of space in a parallel-plate capacitor, pF
$C_s$	Capacitance of dielectric in a parallel-plate capacitor, pF
DAR	Dielectric Absorption Ratio, [-]
$\epsilon^*$	Complex electric permittivity in the frequency domain, F/m
$\epsilon_0$	Permittivity of space, $\epsilon_0 = 8.854 \cdot 10^{-12}$ F/m
$\epsilon'$	Real part of the electric permittivity, F/m
$\epsilon''$	Imaginary part of the electric permittivity, F/m
$\epsilon'_r$	Real value of the relative permittivity, [-]
$\epsilon''_r$	Imaginary value of the relative permittivity, [-]
$\mathbf{E}$	Electric field vector, V · m <sup>-1</sup>
$f$	Frequency, Hz
$F$	Faraday constant, C/mol
$G$	Conduction, S
$G_{AC}$	AC conduction, S
$G_{DC}$	DC conduction, S
$g(t)$	Dielectric response function of Bentheimer sandstone sample
$\mathbf{I}$	Total current density vector, A/m <sup>2</sup>
$I$	Electric current, A
$\mathbf{I}_C$	Capacitive part of the current density vector, A/m <sup>2</sup>
$I_C$	Capacitive part of the electric current, A
$\mathbf{I}_L$	Leakage part of the current density vector, A/m <sup>2</sup>
$I_L$	Leakage part of the electric current, A
$I_p$	Polarization current through the sample, A
$I_r$	Insulation resistance, $\Omega$
$L$	Sample length, mm
$L_0$	Initial sample length, mm
$(\delta L/\delta T)$	Slope of the expansion curve at the temperature, mm/°C
$M$	Mass, g
$P$	Polarization, C/m <sup>2</sup>
PI	Polarization index, [-]
$\varphi$	Effective porosity, [-]
$\rho$	Bulk density, kg/m <sup>3</sup>
$R$	Lossy part of the dielectric, $\Omega$
$\tau_r$	Relaxation time, s
$S_s$	Specific surface, m/m <sup>2</sup>
$\sigma_0$	Charge, C/m <sup>2</sup>
$\sigma$	Electrical conductivity, S/m
$T$	Temperature, °C
$t_p$	Polarization duration, min
$\tan \delta$	Dissipation factor, [-]
$\tan \delta_{pol}$	Polarization losses on the dielectric, [-]
$\tan \delta_{cond}$	Conduction losses on the dielectric, [-]
$U$	Voltage, V
$V_m$	Matrix volume, m <sup>3</sup>
$\omega$	Angular frequency, Hz

## ABBREVIATIONS

AC	Alternating current
Ant-Rt	Rutile formed as a result of the polymorphic transformation of anatase
BET	Brunauer-Emmett-Teller
BS	Bentheimer sandstone
CTE	Coefficient of thermal expansion
CT	Computed tomography
D	Dimension
DC	Direct current
DSC	Differential Scanning Calorimetry
F	Fired samples
Fsp	Feldspar
G	Glass
$H^+$	Hydrogen ion
Kln	Kaolinite
M	Molar concentration
Mul	Mulite
PZC	Point of zero charge
Qtz	Quartz
Rt	Rutile
SEM	Scanning Electron Microscope
SOL	Dissolution
TGA	Thermogravimetric analysis
UF	Unfired samples
WL	Wave length
wt%	Weight percent
XRD	X-ray diffraction
XRF	X-ray fluorescence

### 3.1. INTRODUCTION

Bentheimer Sandstone (BS) is widely used as a model rock for studying fluid flow in porous media and preparing 3D pore-network model studies [1–3]. It is an easy to obtain, inexpensive sample material that has a matrix composed of well-sorted, mostly rounded to sub-rounded grains with a regular distribution of pore bodies and pore throats diameter [4]. The presence of accessory clay, organic matter and oxides or hydroxides is often ignored. Nevertheless, they influence petrophysical behavior such as permeability and electrical conductivity behavior.

## 3

**Motivations for firing.** Sandstone samples are heated to temperatures exceeding 500 °C as a common step in core preparations to limit the risk of permeability reduction during displacement experiments [5, 6]. The objective is to remove the chemically bounded water and to transform and stabilize clays. A strong influence of clays in contact with water on sandstone porosity/permeability, pore size geometry and electrical behavior was reported in the literature [7–15]. The high cation exchange capacity of clays, the large surface area and the strong interaction with interstitial fluids result in swelling and/or migration. In addition, permeability reduction can be expected because of pore clogging downstream, which causes serious injectivity problems [10, 16–19]. Clay migration was even found to clog high permeable sandstones (>0.5 Darcy). Note, that besides clay fines, other components, such as organic matter, very fine quartz and feldspars particles, are considered as mobile fines [10].

**Firing controls on wettability.** The firing of the sandstone caused disintegration of clay minerals, a partial transformation of feldspar and quartz into glass and iron oxides. Moreover, according to Barclay and Worden (2009), if the specific surface of the iron oxides increases, a positive correlation of oil-wetting iron mineral content in the sandstones is observed [20]. González and Moreira (1991) reported iron oxides to be strongly oil-wet due to substantial adsorption of asphaltenes. They observed a significantly higher maximum of asphaltenes adsorption for hematite than for clay minerals (up to 1.5 times) [21]. According to Wang and Guidry [22], the mechanisms of the strong oil-wetness of iron oxides can be explained by (1) ferric ions, allocated on the mineral surface. They represent possible adsorption sites for carboxylic acid anions, which can change the wettability of the mineral surface; (2) ferric ions, mainly on the surfaces. They can cause oxidation of the petroleum components, using catalysts, and produce polar wettability-altering compounds; (3) ferric ions in the solution. They may behave as bridges between petroleum and a silica surface. In addition, it must be noted, that the wettability state of the reservoirs containing ferric ions ( $\text{Fe}^{3+}$ ) is indirectly controlled by the chemistry i.e. redox state, of the reservoir fluids [20].

**Firing characterization.** High temperatures cause changes in the mineralogical composition of sandstones and in the physical and electrical properties [23–25]. The information on pyrometamorphical and electrical properties for Bentheimer sandstone avail-

able in the literature is rather limited [26–28]. In particular, we are not aware of publications on the role of high-temperature minerals that are resistive to chemical weathering after firing and the effect on wettability. To fill the gap in the understanding of these systems, we decided to perform a series of thermal treatment experiments at temperatures  $\geq 600$  °C and petrophysical, petrological and dielectric experiments. Bentheimer samples were therefore fired to temperatures where silica and carbonate minerals other than quartz are dehydrated, dehydroxylized, decarbonized and disintegrated.

**Electrical behavior.** Clay minerals are an important source of ions in sandstones [17, 23, 29, 30]. In a previous study [4], we concluded that iron oxides also influence the surface charge response of the sandstone. Therefore, we decided to perform a series of potentiometric titration experiments to determine the influence of firing on the surface charge. We performed a thermo-physical analysis of fired and unfired samples, by measuring the dielectric properties in the frequency and time domain. Knowing these properties is important in evaluating the influence of the firing process, as they are related to the constituent materials and the geometrical microstructure of the rock.

The results of this study may help experimentalists in planning combined flow and electrokinetic experiments with Bentheimer sandstone. This chapter first discusses experimental methods, followed by results and discussions and conclusions.

## 3.2. MATERIALS AND METHODS

### 3.2.1. FIRING

The sample material, Bentheimer sandstone, placed in a temperature-programmable furnace, was heated at atmospheric pressure at a rate of 5 °C/min, up to 573 °C. This temperature was maintained for 2 hours for the mineral transformation of  $\alpha$ - to  $\beta$ -quartz. Then, the samples were heated further at the same thermal rate up to 970 °C, where the temperature again was maintained for 2 hours. Thereafter, the samples were cooled down by setting the temperature to 573 °C, and again kept for 2 hours stabilization at 573 °C, followed by another cool down to room temperature (Fig. 3.1). The aim of this procedure was to limit thermal shock effects that may cause differential expansion and contraction, that would lead to micro-fracturing in grains and cracking of grain contacts.

### 3.2.2. CHARACTERIZATION OF UNFIRED AND FIRED SAMPLES AND THERMAL ANALYSIS

**X-ray diffraction (XRD)/X-ray fluorescence (XRF) and texture composition.** Samples characterized for XRD and XRF analysis were pulverized to a powder with a particle size of less than 2  $\mu\text{m}$  and analyzed for their mineral composition and element-oxide distribution. The XRF measurements were conducted with a Panalytical Axios Max WD-XRF<sup>TM</sup> spectrometer measuring the element oxides and elements (>0.5 wt%) with an accuracy of 2%. The XRD was recorded in a Bragg-Brentano geometry, with a Bruker D5005<sup>TM</sup> diffractometer, equipped with a Huber incident beam monochromator and a Braun PSD<sup>TM</sup> detector. Details on XRD and XRF and corresponding setups are provided in literature [31, 32].

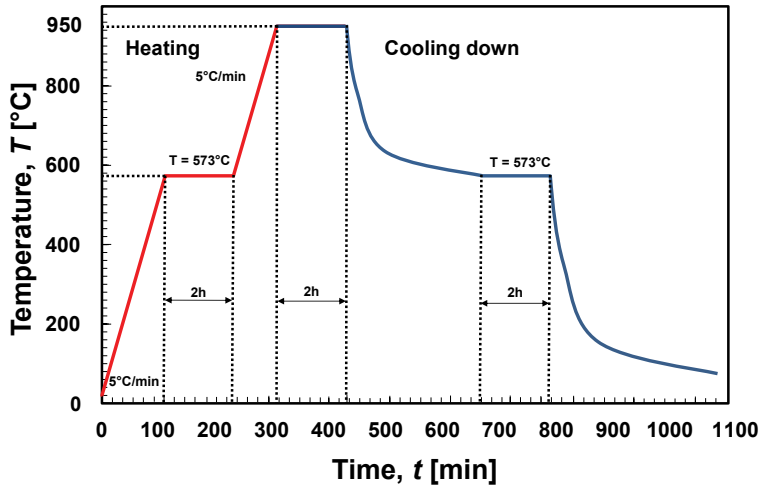


Figure 3.1: Temperature path for the firing process of Bentheimer sandstone.

**Scanning Electron Microscope (SEM).** To identify changes in the matrix structure, selected samples were examined using a scanning electron microscope (JEOL 8800 M JXA Super probe<sup>TM</sup>). The methodology of SEM and further image analysis can be found elsewhere [33].

**Porosity and permeability measurements.** Porosity and permeability were determined on cylindrical samples having a diameter of 30 mm and length of 36 mm. Dry porosity tests were conducted with a Gas Expansion UltraPycnometer 1000 (Quantachrome Instruments<sup>TM</sup>) using Boyle's gas expansion law [34]. The results are the matrix volume ( $V_m$ ), the bulk density ( $\rho$ ) and the porosity ( $\varphi$ ). The permeability of dry cores was measured with  $N_2$  gas by using a Ruska gas permeameter (Ruska Instruments<sup>TM</sup>) [35].

**Thermogravimetry (TGA) and Differential Scanning Calorimetry (DSC) analysis.** For thermal analysis, the samples were crushed to powders with particles smaller than 50  $\mu\text{m}$ . The thermos-analyzer Netzsch STA F3 Jupiter<sup>TM</sup> with the QMS403C Aëolos<sup>TM</sup> gas analysis system was simultaneously used to conduct thermogravimetric analysis (mass change  $\pm 1 \mu\text{g}$ ) and differential scanning calorimetry (heat difference  $\pm 0.1 \mu\text{W}$ ). The instrument measures the mass changes and provides endo-/exothermic results as a function of temperature against a reference measurement in an empty crucible [36]. The measurements were performed in both argon and air conditions at atmospheric pressure. The standard firing procedure was done in the air, although to acquire more information about thermal mineral behavior in a neutral or reducing environment, argon was introduced. The gas velocities were 20 ml/min, with a dynamic temperature program at a rate of 10  $^\circ\text{C}/\text{min}$ . In order to detect possible drying of the sample, the measurement started at 30  $^\circ\text{C}$  and went up to a maximum temperature of  $\sim 1000 \text{ }^\circ\text{C}$  ( $\pm 1.5 \text{ }^\circ\text{C}$ ).

**Thermal expansion.** To measure the changes in the physical properties of sandstone such as coefficient of thermal expansion ( $\alpha$ ) and linear thermal expansion ( $\Delta L/L$ ), mechanical analysis techniques in the thermal analysis were used [37]. The cuboid sample of  $5.34 \text{ mm} \pm 0.01 \text{ mm}$  in length and with a cross-sectional area  $4 \text{ mm} \times 4 \text{ mm}$  was placed in the PerkinElmer<sup>TM</sup> thermomechanical analyzer to measure small changes in sample dimensions. The sample was evenly heated over a programmed temperature range of  $10 \text{ }^\circ\text{C}/\text{min}$  up to maximum  $600 \text{ }^\circ\text{C}$  and kept constant for 2 hours. Thereafter, it was cooled down at the same rate. The thermomechanical analyzer converts movements of the probe into an electrical signal and generates the thermal response curves from which the coefficient of thermal expansion was derived. The average coefficient of thermal expansion (CTE) is represented by  $\alpha$ , as a function of temperature:

$$\alpha(T) = \frac{1}{L_0} \left( \frac{\partial L}{\partial T} \right), \quad (3.1)$$

where  $\left( \frac{\partial L}{\partial T} \right)$  is the change in the sample length ( $L$ ) over a temperature range expressed as a slope of the expansion curve at temperature  $T$ ;  $L_0$  is the initial sample length.

**Surface charge and specific surface area.** Potentiometric titrations were performed in a nitrogen atmosphere to investigate the change in surface charge of Bentheimer sandstone due to the firing process. Before starting the experiments, a sample of Bentheimer (0.5, 5 and 10 g) was dispersed in the electrolyte (100ml  $\text{H}_2\text{O}$  with 9 ml of 0.1M NaOH) and then stirred vigorously with a Teflon-coated magnetic stirrer for 24 hours. The potentiometric titrations were performed by adding 0.1M HCl droplet by droplet, while continuously stirring the solution. The pH data were recorded every 5 minutes. The pH-dependent surface charge ( $\sigma_0$ ) was calculated as [38]:

$$\sigma_0(\text{pH}) = - \frac{F \cdot (\Delta n_{\text{sol},\text{H}^+}(\text{pH}) - \Delta n_0)}{M a_s} = \frac{f_{\text{surf}}(\text{pH})}{S_s}, \quad (3.2)$$

where  $F$  is the Faraday constant ( $F = 96500 \text{ C/mol}$ );  $M$  is the sample mass;  $S_s$  the surface area and  $\Delta n_0$  the pH-dependent amount of acid/base consumed. The dissolution effect ( $\Delta n_{\text{sol},\text{H}^+}$ ) was obtained by comparison of the balance of protons and hydroxyl ions in the potentiometric titration of Bentheimer samples with blank potentiometric titration results:

$$\Delta n_{\text{sol},\text{H}^+}(\text{pH}) = \Delta n_{\text{acid}\backslash\text{base}(\text{BS})}(\text{pH}) - \Delta n_{\text{acid}\backslash\text{base}(\text{blank})}(\text{pH}). \quad (3.3)$$

For a correct interpretation of the electrical behavior of the powdered fresh and fired Bentheimer sandstone, the specific surface area was measured by adsorption of liquid nitrogen at low temperatures ( $-196.5 \text{ }^\circ\text{C}$ ). The detailed methodology is provided elsewhere [4]. The specific surface data was calculated using the BET sorption theory [39]. The obtained specific surface area represents the "external" surface area, since the penetration through the interlayer of smaller clay particles surfaces by weakly adsorbed nitrogen is not possible.

### 3.2.3. DIELECTRIC SPECTROSCOPY

**Principle and apparatus.** The main objective of the dielectric spectroscopy studies was to examine differences between unfired and fired samples through the frequency



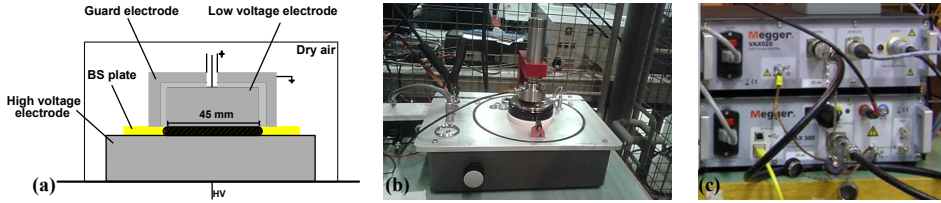


Figure 3.2: (a) Schematic of the three-terminal parallel-plate capacitor, showing the high voltage electrode at the bottom and the low voltage electrode surrounded by the guard electrode at the top; (b) the electrode terminal; (c) Megger<sup>TM</sup> device for capacity measurements at atmospheric conditions.

3

dependence of the permittivity and dissipation factor. The secondary objective was to conduct the dielectric adsorption test under DC conditions to recognize a change in the conductive behavior. For the tests, flat circular discs with a diameter  $d$  of 140 mm and thickness,  $h$  of 8 to 10 mm were placed between two electrodes to arrange a parallel-plate capacitor of plate area,  $A \sim 15.9 \cdot 10^2 \text{ mm}^2$ . The contact surface of the samples and the electrodes was sufficiently smooth for the current transfer to occur.

The apparatus used for the measurement of the dielectric properties of the samples was a three-terminal parallel-plate capacitor connected to a Megger<sup>TM</sup> capacity meter (Fig. 3.2) consisting of: (1) a bottom electrode directly connected to a high voltage unit, and (2) a top electrode connected to a low voltage terminal. The internal part of the upper electrode is used for measurements, while the external part acts as a guard and eliminates the influence of surface leakage currents from the measurement results (Fig. 3.2a). The electrode terminal is covered by a tight glass shade to prevent the entrance of moisture from the atmosphere.

**Sample preparation.** Prior to the experiments, several techniques are employed to remove the water, including heating in the oven at 105 °C for 48 hours, and further saturation of the cores placed in the three-terminal parallel-plate capacitor with dry air. The drying procedure in the capacitor was implemented three times for each sample. Samples were subsequently: saturated with 90 °C dry air, evacuated, re-saturated with dry air, and then stored in a dry air atmosphere for 24 hours. Measurements were later made with the cores in vacuum. The above procedure ensured the removal of free water from the samples. To reduce and quantify the effect of the electrode polarization (ionic charge accumulations at the electrodes) [40] the following methods were used when measuring dielectric properties: (1) varying the thickness of the samples to quantify the polarization effect; (2) using aluminum films as spacers to reduce the effect as much as possible.

**Dielectric permittivity test.** The test cell was connected to a capacity meter that measures the capacity and the dissipation factor of a sample as a function of frequency at a desired voltage of  $U = 0.5 \text{ kV}$ . A non-ideal dielectric like BS supports a varying charge, adsorbs and dissipates the electric energy in the form of heat. When a potential difference is applied to a capacitor, energy is dissipation dissipated due to two main factors: (1) a flow of free charges through the material, called conduction loss (DC term), and (2) a dis-

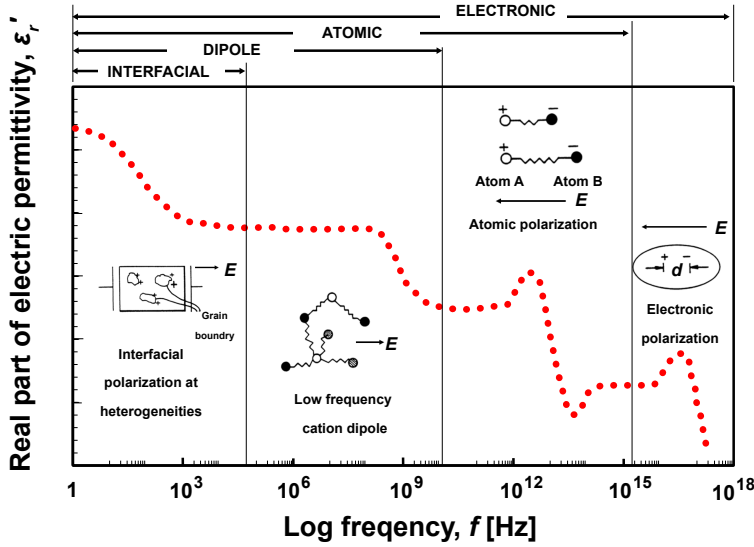


Figure 3.3: The real part of electric permittivity spectrum over a range of frequencies [43].

placement of electric charges that gives rise to the creation of dipoles in the sample (AC term). The second mechanism, called polarization  $P$ , arises as a result of an electronic and an ionic polarization, a dipole orientation and an interfacial polarization [41]. The polarization of heterogeneous materials, like Bentheimer sandstone, depends on the individual properties of minerals, their proportion and the distribution across the sample volume. This mechanism is related to the space charge accumulation along the interface in the presence of the electrical field. For this reason, it can be expected that the relative permittivity of a mixture of minerals may exceed that of a single mineral. Different types of polarization have varying time response abilities to an applied field frequency. Therefore, the real part of electric permittivity is frequency dependent (Fig. 3.3). The frequency dependence of the polarization process on the relative permittivity value is presented elsewhere in greater detail [42]. The measurements described in this chapter cover the frequency domain from 0.1 Hz to 15 kHz. Application of the electric field  $\mathbf{E}$  gives rise to the electric displacement field  $\mathbf{D}$  flowing the relation [44]:

$$\mathbf{D} = \epsilon^* \mathbf{E}. \tag{3.4}$$

The interactions of a material with an electric field  $\mathbf{E}$  are described by the complex electric permittivity  $\epsilon^*$ :

$$\epsilon^* = \epsilon' - i\epsilon'', \tag{3.5}$$

where the expressions  $\epsilon'$  and  $\epsilon''$  define the real, non-negative component of the permittivity and the energy dissipation due to polarization, respectively. The real part of the complex permittivity can be calculated at the various frequencies by using the measured capacitance values of a sample in a parallel-plate capacitor between the high and

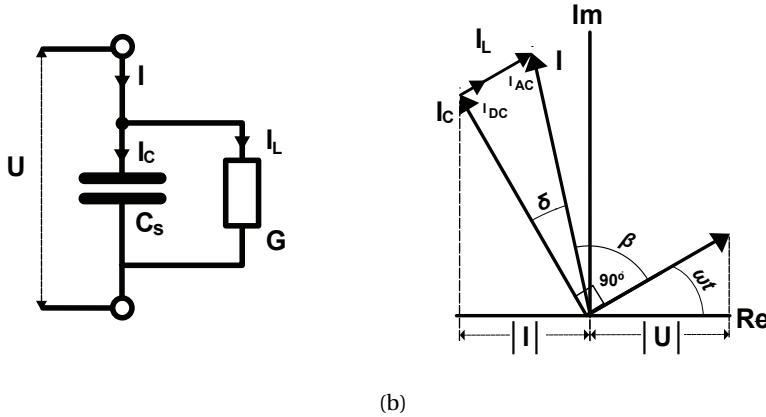


Figure 3.4: (a) Schematic of the parallel equivalent circuit. Note that it corresponds to one voltage and frequency level; (b) corresponding phasor diagram representing the electric loss angle  $\delta$ , and power factor angle  $\beta$ . As a result of the introduced voltage  $\mathbf{U}$ , the current  $\mathbf{I}_L$  follows in phase with the applied voltage, and the charging current  $\mathbf{I}_C$  is  $\pi/2$  out of phase.

low voltage electrode ( $C_s$ ) at the strong accumulation region from the relation [45]

$$C_s = \epsilon'_r C_0, \quad (3.6)$$

where  $C_0$  is the capacitance without the sample,  $\epsilon'_r$  denotes the real part of the relative permittivity, represented by the ratio  $\epsilon'/\epsilon_0$ , where  $\epsilon_0$  is the permittivity in vacuum.

To account for the loss current, the BS in the parallel-plate capacitor can be defined as a "leaky" dielectric and can be represented by the equivalent circuit (Fig. 3.4a). The losses in the sample can be represented by a conductance  $G$ . If an AC voltage source  $U$  is applied on the capacitor, the total current  $\mathbf{I}$  propagating in the sample consists of two components:

$$\mathbf{I} = \mathbf{I}_C + \mathbf{I}_L. \quad (3.7)$$

A charging current  $\mathbf{I}_C$  leads the in-phase component current by  $90^\circ$  (Fig. 3.4b) and can be expressed by

$$\mathbf{I}_C = \omega C_s \mathbf{U}, \quad (3.8)$$

where  $\omega$  denotes the angular frequency ( $\omega = 2\pi f$ ). A loss current  $\mathbf{I}_L$  that is in phase with the applied voltage includes the AC conduction from the inertial resistance  $G(\omega)_{AC}$  and the DC conduction  $G_{DC}$

$$\mathbf{I}_L = (G(\omega)_{AC} + G_{DC}) \mathbf{U} \quad (3.9)$$

$$\text{with } G(\omega)_{AC} = \omega C_0. \quad (3.10)$$

The DC conductance  $G_{DC}$  of the samples can be expressed in terms of the electrical conductivity  $\sigma$  as  $G_{DC} = \sigma A/d$ . Thus, implementing (3.8), (3.9) and (3.10) into (3.7), the total current for a BS sample can be expressed as

$$\mathbf{I} = (i\omega\epsilon'_r C_0 + \omega\epsilon''_r C_0 + G_{DC}) \mathbf{U} = ((i\omega C_0)\epsilon_r^* + G_{DC}) \mathbf{U} \quad (3.11)$$

where  $\epsilon_r''$  is the imaginary value of the relative permittivity, represented by  $\epsilon_r''/\epsilon_0$  ratio. From the above expressions and from the parallel circuit presented in Figs. 3.4a and 3.4b, the total dissipation factor value of the sample can be derived as [46, 47]

$$\tan \delta = \frac{I_L}{I_C} = \frac{G_{DC} + \omega \epsilon_r'' C_0}{\omega \epsilon_r' C_0} = \frac{G_{DC}}{\omega \epsilon_r' C_0} + \frac{\epsilon_r''}{\epsilon_r'}. \quad (3.12)$$

The total dissipation factor of a dielectric is characterized by the sum of: a) the polarization losses,  $\tan \delta_{pol}$ , and b) the losses caused by conduction,  $\tan \delta_{cond}$  when the resistance of the dielectric is sufficiently small. Hence, the dissipation factors related to the polarization and conduction are equal to:

$$\tan \delta_{pol} = \frac{\epsilon_r''}{\epsilon_r'} = \frac{\epsilon''}{\epsilon'}, \quad (3.13)$$

$$\tan \delta_{cond} = \frac{\sigma}{\omega \epsilon_0 \epsilon_r'}. \quad (3.14)$$

Assuming that the DC contribution of loss current is much smaller than the AC contributions ( $G_{DC} \ll \omega \epsilon_r'' C_0$ ), the total dissipation factor simplifies to

$$\tan \delta = \frac{\epsilon''}{\epsilon'}. \quad (3.15)$$

**Polarization current measurements and dielectric absorption test.** The main concept of this test is the increase in insulation resistance due to the polarization of the atoms in sandstone over time. The DC voltage ( $U = 0.2$  kV) is applied to samples placed in the same three-terminal parallel-plate capacitor during a polarization duration,  $t_p > 10$  minutes. Thus, due to the application of a DC voltage  $U$ , a pulse-like polarization current flows through the sample. During the polarization duration, the current decreases to a certain value corresponding to the conduction current, assuming that the sample in the parallel-plate capacitor is totally discharged prior to the measurement and that a step voltage is applied with the following characteristics [48]

$$U(t) = \begin{cases} 0 & t < 0 \\ U_0 & 0 \leq t \leq t_p \\ 0 & t > t_p \end{cases}. \quad (3.16)$$

The above relation gives zero current for times before  $t = 0$ , and polarization currents for times  $0 \leq t \leq t_p$ . The polarization current through the sample can be expressed as [48]

$$I_p = U_0 C_0 \left[ \frac{\sigma}{\epsilon_0} + \epsilon_\infty \gamma(t) + g(t) \right], \quad (3.17)$$

The formula contains three parts: (1) process independent of any polarization, being in relation to the conductivity of the sample; (2) the gamma function, arising from the suddenly applied step voltage, at  $t = 0$  and  $t = t_p$ . It cannot be recorded in practice and is ignored in the calculation, because of a large dynamic range of current amplitudes

related to the sudden polarization processes at the initial stage; (3) the activation process of the certain polarization within the sample,  $g(t)$ . Therefore, (3.17) can be rewritten as

$$I_p = U_0 C_0 \left[ \frac{\sigma}{\epsilon_0} + g(t) \right], \quad (3.18)$$

NOTE: The dimension of  $g(t)$  is l/s and its magnitude is dependent on  $C_0$ . Moreover, the simultaneous measurements of the insulation resistance ( $I_r$ ) at different time intervals allow the calculation of: a) dielectric absorption ratio (DAR) that is the ratio of the insulation resistance at 60 seconds to the insulation resistance at 30 seconds, and b) the polarization index (PI) that is the ratio of the insulation resistance value measured at 600 seconds to the insulation resistance value measured at 60 seconds. All reported polarization current measurements were performed at ambient temperature.

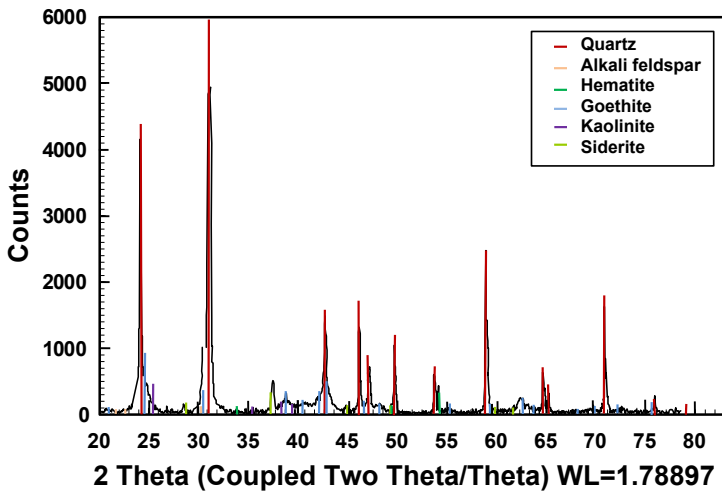
### 3.3. RESULTS AND DISCUSSION

#### 3.3.1. XRD/XRF ANALYSIS AND SEM INTERPRETATION: GENERAL RESULTS

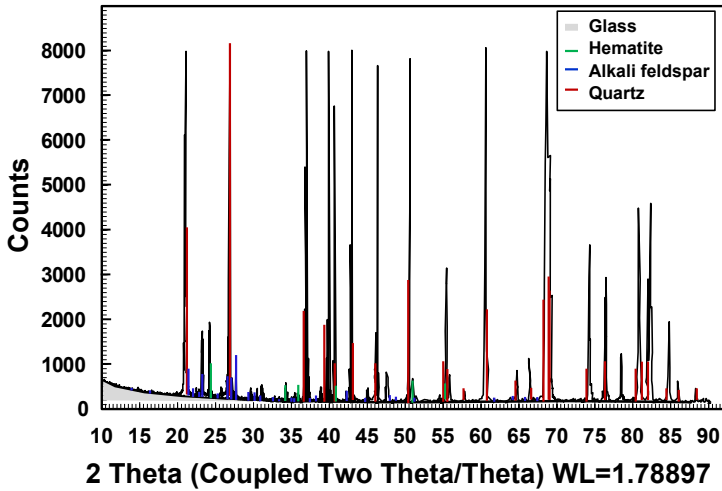
The pyrometamorphic alterations up to 970 °C were evaluated by XRD/XRF-analysis and SEM. The primary constituents of the Bentheimer sandstone are quartz (91.7 wt%), feldspars (4.9 wt%), clay minerals (2.7 wt%), carbonates (0.4 wt%), pyrite and iron hydroxides (0.2 wt%). Note, that the wt% are average values from the analysis of our previous study [4]. Additionally, SEM analyses show the presence of kaolinite, illite, and mixed-layer clays in Bentheimer sandstone.

Fig. 3.5 mainly shows the reduction of intensity corresponding to kaolinite in the XRD patterns between unfired and fired Bentheimer sandstone. In samples fired to 970 °C the structure became amorphous and may only represent traces of meta-kaolinite and mulite (Figs. 3.6c-d) [49, 50]. Quartz and feldspars were transformed to a lesser extent in comparison to other components, as most of the sandstone components have a lower melting point than quartz. Quartz and feldspars melt, first creating vitrified textures, and consequently, the quartz grains dissolve into the glassy matrix (Figs. 3.6c-d). In the case of the feldspar grains, a disappearance of clay minerals is observed. It results in irregular grain shapes and in small amounts of glass at the grain boundaries (Fig. 3.6d). Therefore, it indicates an initial integration of the feldspars into melts. Moreover, distinct interfaces between the grains were recognized in the SEM-photos (Fig. 3.6b). Before firing, the boundary between the detrital quartz grains was merged by overgrowths and/or pressure solutions.

Furthermore, hematite was identified as a minor component in the unfired sample and as well in an increased amount as a secondary phase. Decomposition of most of the iron (hydro)oxides/carbonates (goethite, siderite) and iron-rich cement resulted in conversion to mainly hematite and probably wüstite, giving the rock a distinctive reddish color. The destruction of the cementing material by firing made Bentheimer more friable. An interesting observation was the SEM identification of rutile, as an accessory component, occurring both as a precursor and as a polymorph phase after anatase (Figs. 3.6e-f).



(a)



(b)

Figure 3.5: XRD pattern of (a) the unfired Bentheimer sandstone sample; (b) the fired Bentheimer sandstone sample.

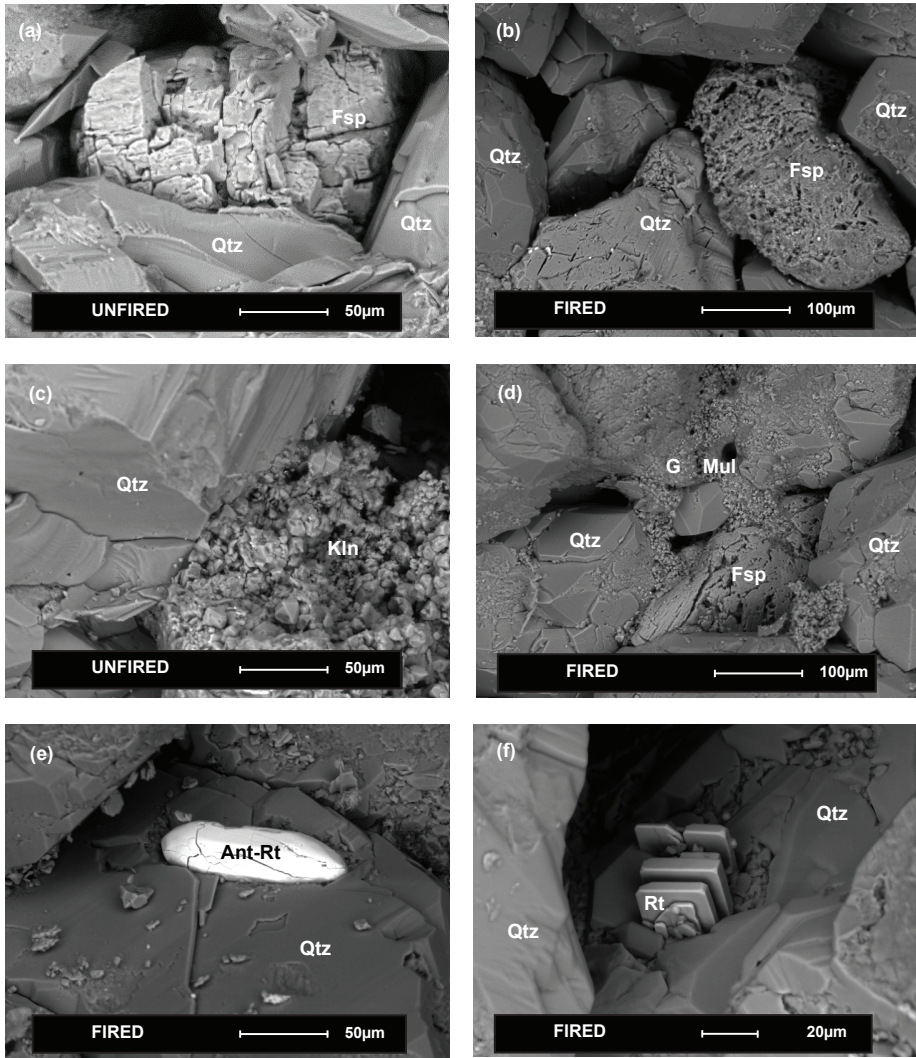


Figure 3.6: Scanning electron microscope (SEM) image of: (a) original quartz (Qtz), lower right see the quartz overgrowth and alkaline feldspar (Fsp); (b) thermally affected quartz grain (Qtz) and a deteriorated feldspar (Fsp) with discrete interfaces between the grains; (c) kaolinite (Kln) and quartz (Qtz) grain in unfired samples; (d) glass-like regions (G) formed as an occurrence of clays vitrification. The deteriorated feldspar grain (Fsp), metakaolin and initial formation of mullite (Mul) formation are observed; (e) rutile formed as a result of the polymorphic transformation of anatase (Ant-Rt); (f) rutile in a form of accessory precursor phase (Rt).



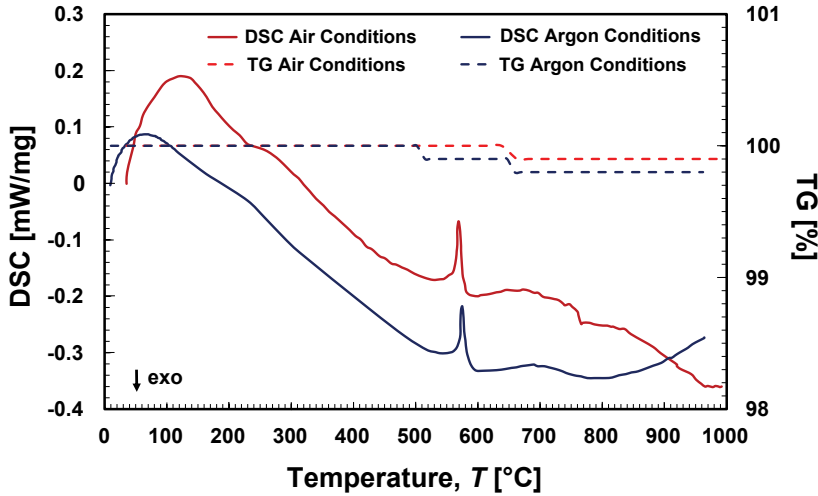


Figure 3.7: Thermogravimetry and differential scanning calorimetry analysis of Bentheimer sandstone under the air and argon atmosphere, at heating rate 10 °C/min.

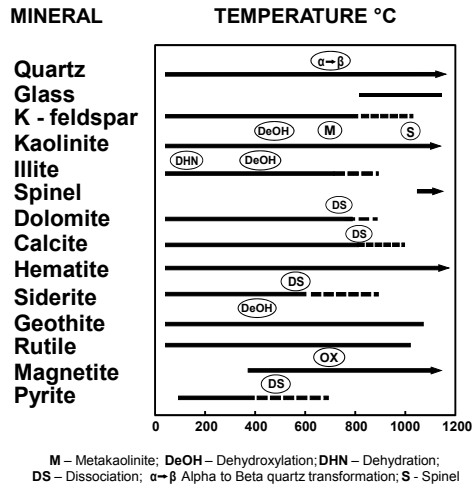
### 3.3.2. THERMAL ANALYSIS AND PHASE TRANSFORMATIONS

TGA and DSC analyses were carried out in an argon and in an air environment, and the results are illustrated in Fig. 3.7. The dehydration of sandstone components is observed in the DSC traces with an initial endothermic peak observed between 40 °C and 170 °C, and between 20 °C and 90 °C in the air and argon environment, respectively. The process is related to free water being removed from the minerals. In the range of 200 °C to 350 °C, small endothermic peaks demonstrate the dehydration of iron-oxides and -hydroxides and the crystallization of iron oxide, mainly hematite [51, 52]. The slight mass losses observed in the thermal data in the region of 470 to 650 °C in each of the TG curves indicate dehydroxylation processes and thermal decomposition leading to oxidation in air and reduction with oxygen release in an argon environment. In the range of 470 to 650 °C (in each of the DSC curves) peaks, centered at 580 °C corresponding to the dehydroxylation of kaolinite, are observed [53]. For the argon atmosphere, an additional endothermic reaction took place above about 750 °C, while endothermic disintegration and exothermic oxidation occurred in the air. In the air environment, the exothermic peak can be associated with mullite formation [49, 50, 54].

The results of thermal expansion measurements are presented in Figs. 3.8a and 3.8b. It can be observed that the slope is unlikely to be constant, varying from  $10.9 \cdot 10^{-6}/^{\circ}\text{C}$  to  $35.2 \cdot 10^{-6}/^{\circ}\text{C}$  (1-4 boxes in Fig. 3.8a). The most visible expansion occurs above 500 °C. The structure of the kaolinite breaks down in the endothermic reaction results into meta-kaolinite and a consequent distortion of structures (Fig. 3.6 and Table 3.1). Quartz undergoes a trigonal  $\alpha$ -quartz to hexagonal  $\beta$ -quartz transformation. Above 800 °C disintegrated feldspars create a vitrified textures with melting illite (Fig. 3.6d and Table 3.1). The cooling curve of Bentheimer differs significantly from the heating curve; this difference is due to the elongation of quartz grains during heating.



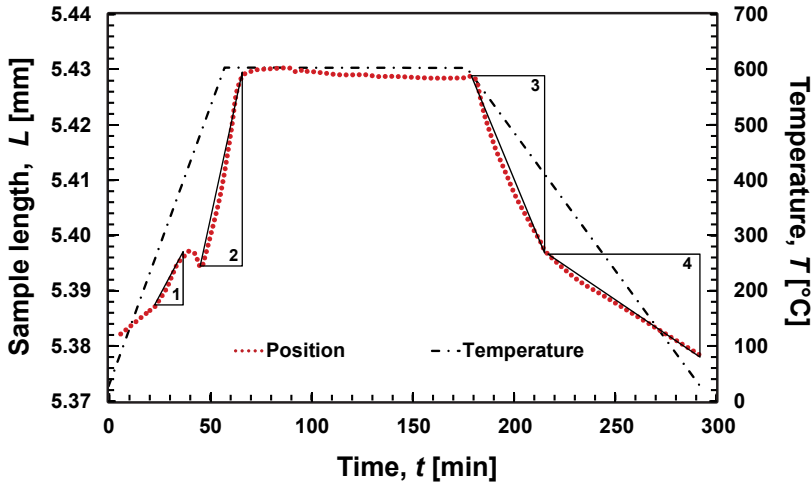
Table 3.1: Thermal behavior of the minerals present in the Bentheimer sandstone after [55, 56].



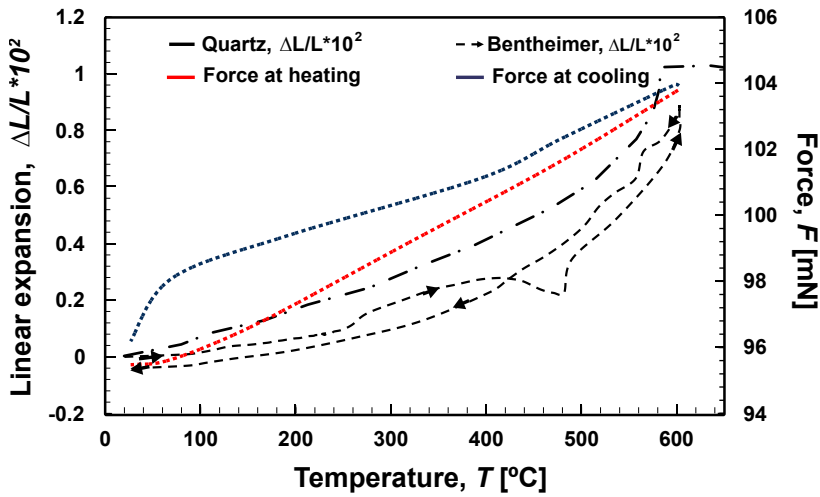
To a lesser extent, the change in sample length between the beginning and the end of the experiment can be attributed to the greater force acting on the sample at the final stage of the experiment. For comparison, the linear thermal expansion of quartz is included in Fig. 3.8b. A similarity in the heating curve trend between Bentheimer and quartz is observed. As shown above, the deformation and expansion of the sample is mainly governed by quartz; however, at temperatures above 573 °C (where the transition from  $\alpha$ - to  $\beta$ -quartz occurs) the coefficient becomes negative (Fig. 3.8b), which suggests that more constituents than quartz control the expansion process in Bentheimer sandstone. The thermal expansion curves prove again that there are no high-temperature forms of quartz.

### 3.3.3. POROSITY AND PERMEABILITY

Permeability and porosity of Bentheimer Sandstone cores can be expected to vary as a consequence of firing along with texture and mineral alteration. Firstly, a differential thermal expansion may cause cracking of the grain contacts and, consequently, an increase of the pore volume. Secondly, the disintegration and recrystallization of minerals that have a lower melting point than quartz may slightly increase the quartz grain volume. The differential expansion of minerals separates grains at the interfaces (Fig. 3.6b) as well and thus, creates an irreversible volume increase [55–58]. Fig. 3.9 shows that the absolute gas permeability against porosity hardly changed before and after thermal treatment. The porosity and permeability both increased by less than 5%, which is within the experimental error for usual core flood tests. The slight change in the porosity and permeability is most likely due to textural and compositional changes. As stated by Klimentos (1990), clays, even in small amounts, may strongly influence flow parameters of the rock [12]. Due to exposure to high temperatures (~970 °C), clays undergo decom-



(a)



(b)

Figure 3.8: (a) Thermal expansion ranges: (1)  $10.9 \cdot 10^{-6} / ^\circ\text{C}$ , (2)  $35.2 \cdot 10^{-6} / ^\circ\text{C}$ , (3)  $32.9 \cdot 10^{-6} / ^\circ\text{C}$ , (4)  $15.4 \cdot 10^{-6} / ^\circ\text{C}$ ; (b) linear thermal expansion of Bentheimer sandstone and quartz [57] vs. temperature.

position and degradation and, as a result, change the sandstone matrix structure. On the other hand, quartz undergoes a reversible reaction at 573 °C from  $\alpha$ - to  $\beta$ -quartz. This is related to the increasing vibrations and a slight displacement of the atoms in the crystal lattice, and further volume increase [59]. Moreover, the firing process leads to a weakening and releasing of the cementing material, which results in dispersion and relocation of fine particles within the sandstone pore matrix [23].

### 3.3.4. SURFACE CHARGE

The potentiometric titration for establishing surface charge behavior was started at a high pH (>12). Comparing the titrated surface charge curve obtained from fired Bentheimer sandstone samples, Fig. 3.9b, to the unfired surface charge [4] shows that protons bind to surfaces at the highest protons affinity sites. Subsequently, with an addition of HCl the sites with a lower proton affinity come to be protonated.

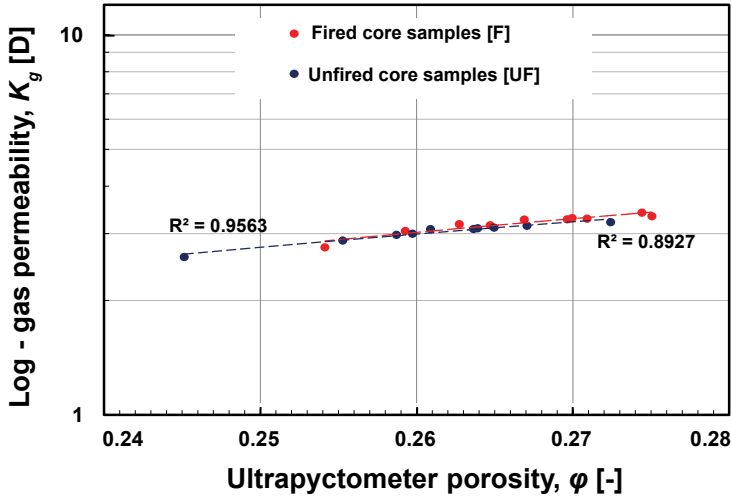
For unfired and fired samples the change in pH value, with the addition of 0.1M HCl titrant, showed a similar trend for the same mass of the samples, however with a steeper gradient for fired samples, so that the Point of Zero Charge (PZC) for unfired and fired samples is respectively at pH = 8 and pH = 10.6. The shift in the PZC can be attributed to a higher concentration of iron oxides present in the sample after firing.

In the Bentheimer sandstone, the iron oxide coatings on quartz grains can give large local specific surface areas. At low pH, the iron oxide coatings may have a contribution to the surface charge distribution, due to (1) the physical blockage of negative charges by iron oxides coatings on e.g. quartz grains, and (2) the mutual neutralization of negatively charged particles [60]. It proves the previous remark, that as a result of firing, iron becomes grain coating material, which can significantly influence the surface response of the sample. Iron oxides might be strongly oil-wet and result in a change of the wettability of Bentheimer sandstone. Nevertheless, in the terms of the volume, the iron oxides can be neglected.

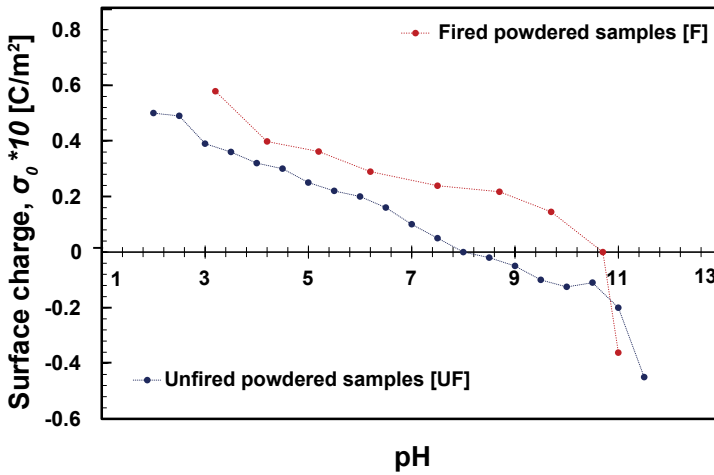
### 3.3.5. DIELECTRIC SPECTROSCOPY

The frequency dependence of the electric parameters for fired and unfired samples was examined at a pressure of 2 bar and a temperature of 30 °C. The obtained values were compared with predictions made using the model of Lichtenecker and Rother [61].

**Dielectric permittivity.** The variation of the real part of electric permittivity  $\epsilon'_r$  and the dissipation factor  $\tan \delta$  as a function of frequency are depicted in Figs. 3.10a and 3.10b. The results represent average values over three consecutive tests. It is observed that the real part of electric permittivity decreases after the samples are thermally treated. Fig. 3.10a shows that over the frequency range of 0.1 Hz - 10 Hz where the counter ion diffusion polarization occurs, the dielectric dispersion magnitude is  $\Delta\epsilon'_{rmin} = 0.5$  (for sample 13A) and  $\Delta\epsilon'_{rmax} = 3.27$  (for sample 12A). It decreases with increasing frequency, reaching  $\Delta\epsilon'_{rmin} = 0.13$  (for sample 13A) and  $\Delta\epsilon'_{rmax} = 0.39$  (for sample 12A) over the frequency range of 10 Hz - 15 kHz. This phenomenon in the low-frequency regimes is common for rocks and is attributed to the variation in polarization, being a result of the charge accumulation at the grain boundaries, and/or grain imperfections, and further, the composition heterogeneity in the rock matrix [62, 63]. This was explained by a



(a)



(b)

Figure 3.9: (a) Por/permeability cross plot for unfired and fired Bentheimer samples; (b) surface charge of fired Bentheimer sandstone.

Maxwell-Wagner model [41]. For high frequencies (>1 MHz), this effect will be negligible [64].

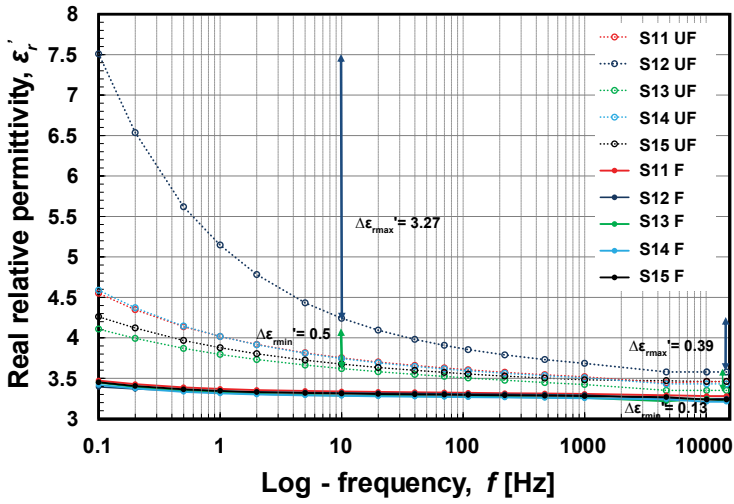
For the thermally treated samples, the dielectric constants measured at low frequencies are up to ~5% larger than those at the high frequencies, which is a much smaller variation than that observed in the unfired samples. Differences in permittivity results between fired and unfired samples are mainly due to the transformations of clay. The high specific surface area minerals (i.e. clays) usually exhibit higher dielectric dispersion magnitudes than low specific surface area minerals [65]. The low dielectric constant value for fired samples that contain iron oxides (the large specific surface and capillary retention capacity) was discussed by Van Dam et al. [66]. They demonstrated that the iron oxides do not directly alter the relative permittivity of the solid phase in the sediment. However, a correlation exists between the larger specific surface and capillary retention capacity of iron oxides, as compared with quartz grains. Thus, iron oxides can have a profound influence on the relative permittivity if they occur in larger quantities than in the Bentheimer sandstone (TGA measurements and XRD).

**Dissipation factor.** Fig. 3.10b shows the dissipation factor vs. frequency. At low frequencies, losses are much higher than at higher frequencies for both fired and unfired samples. For the fired samples, at frequencies larger than 10 Hz, the dissipation factor is almost independent of frequency. This can be explained by a Maxwell-Wagner effect for a widespread distribution of conductivity of the accessory minerals and thermomineralogical alterations within Bentheimer [62]. With increasing frequency, a slightly different approach influencing the behavior of the dissipation factor, the Garton's mechanism [67] is observed. More tests at higher frequencies should be conducted to entirely confirm this statement. Note, that the mechanism of invariance with frequency is a special case for quartz [68].

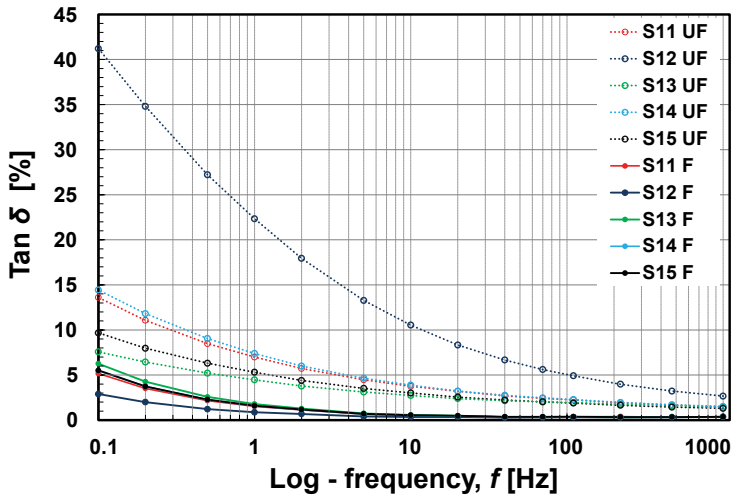
The observed general dispersion in the obtained results can be attributed to local heterogeneities due to varying clay concentrations in the Bentheimer samples. The variation in the dielectric constant is directly related to differences in the mineral composition, the crystal structure and the relation and interaction of the various constituents of the rocks to one another, besides clay.

The trend of a decrease in dielectric permittivity and the corresponding change in the dielectric properties were ascertained by the extended drying process and repeated measurements. Attention was taken to eliminate any possible moisture and instrumental sources causing variations in the measurements. While conducting the measurements, we found that there is a difference between results obtained at certain stages of the drying. Hence, the measurements, accounting as "dry rock", were obtained after the third drying when the value of the loss tangent varied <0.5% between repeated measurements. Fig. 3.11b shows the influence of water content on the dielectric constant of unfired sample no. 14 with a different moisture content in the frequency domain covering the interval from 1 Hz to 1 kHz. The trend of spectrum variation is close to the dry rock samples, although a noticeable role of moisture is observed.

**Polarization current and the dielectric absorption test.** For the dielectric absorption test, the DC voltage  $U = 0.2$  kV was used. As a result, a polarization current,  $I_p$ , flows

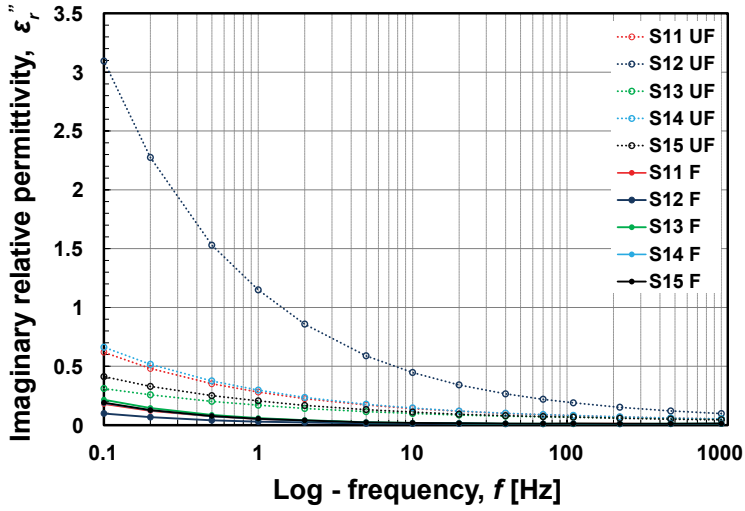


(a)

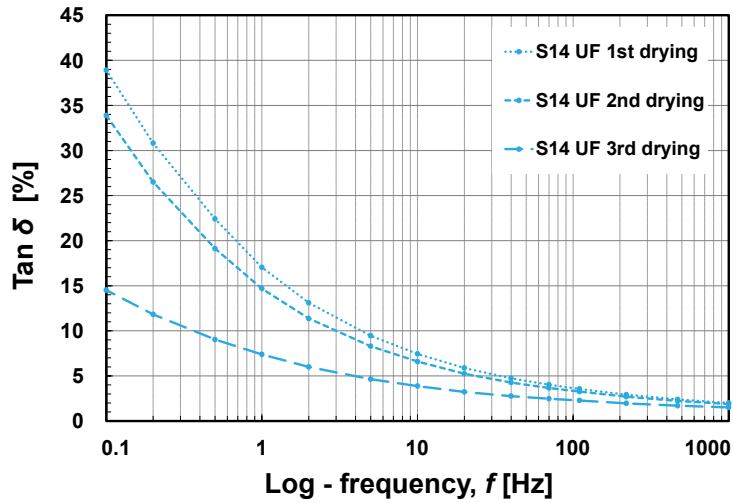


(b)

Figure 3.10: (a) The frequency domain dielectric constant spectrum for unfired and fired samples; (b) tangent loss spectrum over the frequencies; S11UF-S15UF corresponds to samples before thermal treatment, and S11F-S15F to samples after firing.



(a)



(b)

Figure 3.11: (a) The imaginary permittivity spectrum over the logarithm of the range of the frequencies for unfired and fired samples; (b) effect of moisture on the tangent loss value over the logarithm of the range of the frequencies for sample 14UE.

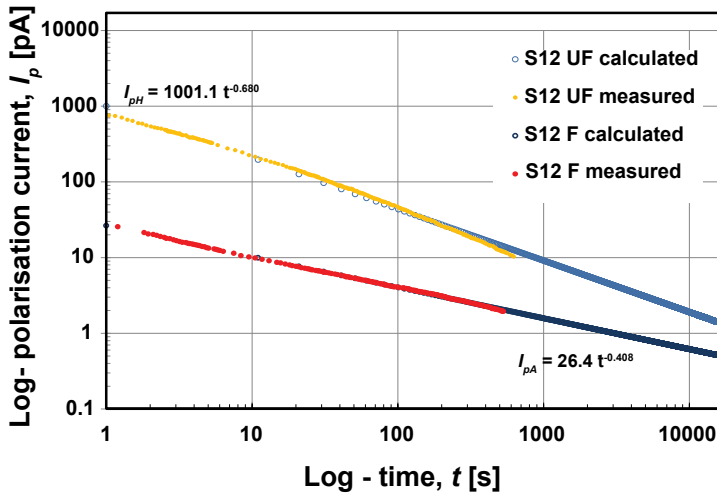


Figure 3.12:  $t - I_p$  characteristic of a dielectric after voltage application.

Table 3.2: The dielectric absorption test results.

Fired samples	Unfired	Fired
Average Insulation Resistance 60 s [TΩ]	15.57	26.35
Average Dielectric Absorption Ratio (DAR)	1.64	1.3
Average Polarization Index (PI)	4.7	2.2
Insulation Condition	Good	Questionable

through the dielectric. Subsequently with time, the transient phenomena "polarization current decay" heads to a small steady state conduction current (Fig. 3.12).

For both samples, the application of a DC electric field results in a current jump as an effect of fast electronic, ionic and orientation polarization. Subsequently, the current gradually decreases due to slow polarization processes. A good fit of the Curie-von Schweidler model [69, 70] with the measured data was obtained. The observed decay phenomena can be described by a power function, where the space charge formation creates an inner electric field of the opposite direction, which progressively decreases the current. Fig. 3.12 shows the variation of the polarization current with time and sample treatment (unfired and fired).

The application of DC voltage for fired samples showed that changes in mineral composition and their conductivity tend to affect the tail of polarization currents. Due to firing and related dispersion of the iron oxides within the matrix framework, Bentheimer sandstone becomes a weaker insulator (Table 3.2).



### 3.4. CONCLUSIONS

I have investigated the effects of firing of the Bentheimer samples, a commonly used procedure in core preparation, to impose the internal rock properties uniform and improve reproducibility of displacement experiments. The petrophysical, petrological, pyrometamorphical and electrical properties of unfired and fired samples were measured using various complementary methods. The following main conclusions can be drawn:

- In unfired samples, ion exchange between minerals (mainly clays) and injected fluids caused clay migration (kaoline and illite) and swelling (illite and smectite) leading to partial or total plugging. The local clay concentrations, differences in crystal structure and the interaction of the various constituents were validated by dispersion in the dielectric permittivity over frequencies.
- Firing of Bentheimer sandstone above 900 °C led to gradual changes in the mineral composition, color, surface roughness and physical properties of the samples, through transformation, disintegration and pyrometamorphism of the components.
- Fine loose particles were created by thermal disintegration and still may migrate during liquid flow experiments. An XRD and decrease in the permittivity value and its insignificant dispersion (~5%) between the high and the low frequencies indicated the clay transformations.
- Thermal stresses also caused variation in the pore geometry, caused changes in grain boundaries and contacts and particle cracking, i.e. as a result, the porosity and permeability increased by up to 5% and samples became more friable.
- The mechanical strength of the cementing material decreased due to dehydration-rehydration and heterogeneous thermal expansion. The boundary between the detrital quartz grains was detached by better connected, larger and wider throats.
- Firing resulted in decomposition of minerals with Fe content and caused the formation of a source of amorphous oxides that influence the wettability. The iron oxides do not directly alter the relative permittivity of the solid phase. However, the correlation exists between the larger specific surface and the capillary retention capacity of iron oxides, as compared with quartz grains.
- The firing of Bentheimer sandstone cores eliminates problems related to clays, but creates fines, originated from the destroyed cement that may affect the flow as well, so reproducibility of experiments might not be possible. Moreover, the change in the equilibria for the altered ion exchange is observed, such that local wettability varies.

## REFERENCES

- [1] W. De Boever, T. Bultreys, M. Traska, A. Mock, L. Brabant, and V. Cnudde, *3D Characterization of the Bentheimer sandstone and Euville Limestone, in relation to fluid flow through their pore networks*, (2013) paper presented at the 14<sup>th</sup> Euro Seminar on Microscopy Applied to Building Materials, Helsingør, Denmark, 10 - 14 June 2013.
- [2] E. Klein and T. Reuschlé, *A Model for the mechanical behaviour of Bentheim sandstone in the brittle regime*, in *Thermo-Hydro-Mechanical Coupling in Fractured Rock*, Pageoph Topical Volumes, edited by H.-J. Kümpel (Birkhäuser Basel, Basel, 2003) Book section 3, pp. 833–849.
- [3] J. Ruedrich and S. Siegesmund, *Salt and ice crystallisation in porous sandstones*. *Environmental Geology* **52**, 225 (2007).
- [4] A. E. Peksa, K.-H. A. A. Wolf, and P. L. J. Zitha, *Bentheimer sandstone revisited for experimental purposes*, *Marine and Petroleum Geology* **67**, 701 (2015).
- [5] D. E. Potts and D. L. Kuehne, *Strategy for alkaline/polymer flood design with Berea and reservoir-rock corefloods*, *SPE Reservoir Engineering* **3**, 1143 (1988).
- [6] R. D. Sydansk, *Discussion of the effect of temperature and confining pressure on single-phase flow in consolidated rocks*, *Journal of Petroleum Technology and Alternative Fuels* **32** (1980).
- [7] R. Al-Mjeni, F. Günzel, X. Jing, C. A. Grattoni, and R. W. Zimmerman, *The influence of clay fraction on the complex impedance of shaly sands*, *Symbolic Computational Algebra* **29** (2002).
- [8] F. Civan and R. M. Knapp, *Effect of clay swelling and fines migration on formation permeability*, (Society of Petroleum Engineers, 1987).
- [9] G. A. Gabriel and G. R. Inamdar, *An Experimental Investigation of Fines Migration in Porous Media*, (Society of Petroleum Engineers, 1983).
- [10] D. H. Gray and R. W. Rex, *Formation damage in sandstones caused by clay dispersion and migration*, *Clays and Clay Minerals* **14**, 355 (1966).
- [11] D. Huntley, *Relations between permeability and electrical resistivity in granular aquifers*, *Ground Water* **24**, 466 (1986).
- [12] T. Klimentos and C. McCann, *Relationships among compressional wave attenuation, porosity, clay content, and permeability in sandstones*, *Geophysics* **55**, 998 (1990).
- [13] J. W. Neasham, *The morphology of dispersed clay in sandstone reservoirs and its effect on sandstone shaliness, pore space and fluid flow properties*, (Society of Petroleum Engineers, 1977).

- [14] M. M. Sharma and Y. C. Yortsos, *Fines migration in porous media*, Journal of the American Chemical Society **33**, 1654 (1987).
- [15] D. Wildenschild, J. J. Roberts, and E. D. Carlberg, *Electrical properties of sand-clay mixtures: the effect of microstructure*, (1999), paper presented at the International Exposition and 69th Annual Meeting of the Society of Exploration Geophysicists, Houston, Texas, 31 October - 5 November 1999.
- [16] F. O. J. Jones, *Influence of chemical composition of water on clay blocking of permeability*, Journal of Petroleum Technology (1964), 10.2118/631-pa.
- [17] K. K. Mohan and H. S. Fogler, *Effect of pH and layer charge on formation damage in porous media containing swelling clays*, Langmuir **13**, 2863 (1997).
- [18] K. K. Mohan, R. N. Vaidya, M. G. Reed, and H. S. Fogler, *Water sensitivity of sandstones containing swelling and non-swelling clays*, Colloids and surfaces A: Physicochemical and engineering aspects **73**, 237 (1993).
- [19] K. Norrish, *The swelling of montmorillonite*, Discussions of the Faraday Society **18**, 120 (1954).
- [20] S. A. Barclay and R. H. Worden, *Effects of reservoir wettability on quartz cementation in oil fields*, in *Quartz cementation in oil field sandstones: a review of the key controversies*, edited by W. R. and S. M. (Blackwell Publishing Ltd., 2009) pp. 103–117.
- [21] G. González and M. B. C. Moreira, *The wettability of mineral surfaces containing adsorbed asphaltene*, Colloids and Surfaces **58**, 293 (1991).
- [22] F. H. L. Wang and L. J. Guidry, *Effect of oxidation-reduction condition on wettability alteration*, SPE Formation Evaluation **9**, 140 (1994).
- [23] S. Ma and N. R. Morrow, *Effect of firing on petrophysical properties of Berea Sandstone*, SPE Formation Evaluation (1994), 10.2118/21045-pa.
- [24] J. C. Shaw, P. L. Churcher, and B. F. Hawkins, *The effect of firing on Berea Sandstone*, SPE Formation Evaluation (1991), 10.2118/18463-pa.
- [25] S. Wu and A. Firoozabadi, *Effects of firing and chemical treatments on Berea permeability and wettability*, Energy & Fuels **25**, 197 (2010).
- [26] N. Loahardjo, W. Winoto, and N. R. Morrow, *Oil recovery from Bentheim sandstone by sequential waterflooding and spontaneous imbibition*, (2012), paper presented at the International Society of Core Analysts Annual Meeting, Scotland, 12-22 August 2012.
- [27] D. R. Maloney, A. D. Brinkmeyer, and M. M. Honarpour, *Relative permeabilities and other characteristics of 700-millidarcy, fired Berea sandstone*, Report (National Institute for Petroleum and Energy Research, 1990).

- [28] O. A. Olafuyi, A. P. Sheppard, C. H. Arns, R. M. Sok, Y. Cinar, M. A. Knackstedt, and W. V. Pinczewski, *Experimental verification of effect of size on drainage capillary pressure computed from digitized tomographic images*, *International Journal of Engineering Research in Africa* **1**, 1 (2010).
- [29] P. Leroy and A. Revil, *A triple-layer model of the surface electrochemical properties of clay minerals*, *Journal of Colloid and Interface Science* **270**, 371 (2004).
- [30] L. L. Schramm, K. Mannhardt, and J. J. Novosad, *Electrokinetic properties of reservoir rock particles*, *Colloids and Surfaces* **55**, 309 (1991).
- [31] J. G. Morse, *Nuclear methods in mineral exploration and production*, Vol. 7 (Elsevier, 2013).
- [32] D. M. Moore and R. C. Reynolds, *X-ray diffraction and the identification and analysis of clay minerals*, Vol. 378 (Oxford university press Oxford, 1989).
- [33] D. H. Krinsley, K. Pye, S. Boggs Jr, and N. K. Tovey, *Backscattered scanning electron microscopy and image analysis of sediments and sedimentary rocks* (Cambridge University Press, 2005).
- [34] R. C. Selley and S. A. Sonnenberg, *Elements of petroleum geology* (Academic Press, 2014).
- [35] D. Tiab and E. C. Donaldson, *Petrophysics: theory and practice of measuring reservoir rock and fluid transport properties* (Gulf professional publishing, 2015).
- [36] P. Gabbott, *Principles and applications of thermal analysis* (John Wiley & Sons, 2008).
- [37] P. J. Haines, *Principles of thermal analysis and calorimetry* (Royal society of chemistry, 2002).
- [38] W. Janusz, *Electrical double layer at the metal oxide-electrolyte interface*, in *Interfacial Forces and Fields: Theory and Applications*, Vol. 85, edited by J. Hsu (CRC Press, Taipei, Taiwan, 1999).
- [39] S. Brunauer, P. H. Emmett, and E. Teller, *Adsorption of gases in multimolecular layers*, *Journal of the American Chemical Society* **60**, 309 (1938).
- [40] P. B. Ishai, M. S. Talary, A. Caduff, E. Levy, and Y. Feldman, *Electrode polarization in dielectric measurements: a review*, *Measurement Science and Technology* **24**, 102001 (2013).
- [41] B. Howell and P. Licastro, *Dielectric behavior of rocks and minerals*, *American Mineralogist* **46**, 269 (1961).
- [42] T. W. Dakin, *Conduction and polarization mechanisms and trends in dielectric*, *Electrical Insulation Magazine*, *IEEE* **22**, 11 (2006).

- [43] E. I. Izgorodina, M. Forsyth, and D. R. MacFarlane, *On the components of the dielectric constants of ionic liquids: ionic polarization*, Physical chemistry **11**, 2452 (2009).
- [44] C. Laj and J. Channell, *Geomagnetic excursions*, Treatise on Geophysics **5**, e416 (2007).
- [45] R. Bartnikas, *Engineering dielectrics: Electrical properties of solid insulating materials: measurement techniques*, Vol. 926 (American Society for Testing and Materials, Baltimore, 1987).
- [46] R. Arora and W. Mosch, *High voltage and electrical insulation engineering*, Vol. 69 (John Wiley & Sons, 2011).
- [47] M. N. Nabighian, *Electromagnetic methods in applied geophysics: theory*, Vol. 1 (Society of Exploration Geophysicist, Tulsa, Oklahoma, 1987).
- [48] A. K. Jonscher, *Dielectric Polarisation/depolarisation in Solids* (Chelsea Dielectric Press, London, 1984).
- [49] K. H. Friolo, A. S. Ray, B. H. Stuart, and P. S. Thomas, *Thermal analysis of heritage stones*, Journal of thermal analysis and calorimetry **80**, 559 (2005).
- [50] A. K. Ismailov, *Thermodynamic analysis of the formation of mullite from kaolinite*, Glass and Ceramics **38**, 363 (1981).
- [51] S. V. S. Prasad and V. Sitakara Rao, *Thermal transformation of iron (III) oxide hydrate gel*, Journal of Materials Science **19**, 3266 (1984).
- [52] C. L. Sharma, M. Nath, and N. Bharti, *Thermal studies on praseodymium-iron (1:9 wt%) oxyhydroxide*, Journal of Materials Science Letters **13**, 1010 (1994).
- [53] R. E. Grim, *Clay mineralogy* (McGraw-Hill Book Company, New York, 1968).
- [54] D. Carroll, *Clay minerals: a guide to their X-ray identification*, Vol. 126 (Geological society of America, Boulder, Colorado, 1970).
- [55] R. A. Kühnel, *Atlas of minerals and related phases in unaltered and thermally altered materials from the Rocky Mountain 1 underground coal gasification field site: Topical report*, Report (Gas Research Institute, North Dakota, 1998).
- [56] K. H. Wolf, *The interaction between underground coal fires and their roof rocks*, Dissertation, Delft University of Technology, Delft, The Netherlands (2006).
- [57] W. H. Somerton, *Thermal properties and temperature-related behavior of rock/fluid systems*, Vol. 37 (Elsevier Science, New York, 1992).
- [58] S. K. Bhargava, A. Garg, and N. D. Subasinghe, *In situ high-temperature phase transformation studies on pyrite*, Fuel **88**, 988 (2009).

- [59] M. S. Ghiorso, I. S. E. Carmichael, and L. K. Moret, *Inverted high-temperature quartz*, Contributions to Mineralogy and Petrology **68**, 307 (1979).
- [60] M. E. Sumner, *Effect of iron oxides on positive and negative charges in clays and soils*, Clay Min. Bull **5**, 218 (1963).
- [61] K. Lichtenecker and K. Rother, *Die Herleitung des logarithmischen Mischungsgesetzes aus allgemeinen Prinzipien der stationären Strömung*, phys. Z. **32**, 255 (1931).
- [62] M. Saint-Amant and D. W. Strangway, *Dielectric properties of dry, geologic materials*, Geophysics **35**, 624 (1970).
- [63] R. J. Sengwa and A. Soni, *Low-frequency dielectric dispersion and microwave dielectric properties of dry and water-saturated limestones of Jodhpur region*, Geophysics **71**, G269 (2006).
- [64] K. V. Rao and A. Smakula, *Dielectric properties of cobalt oxide, nickel oxide, and their mixed crystals*, Journal of Applied Physics **36**, 2031 (1965).
- [65] K. Arulanandan, *Soil structure: in situ properties and behavior* (Department of Civil and Environmental Engineering, University of California, Davis, California, 2003).
- [66] R. L. Van Dam, W. Schlager, M. J. Dekkers, and J. A. Huisman, *Iron oxides as a cause of GPR reflections*, Geophysics **67**, 536 (2002).
- [67] C. G. Garton, *Dielectric loss in thin films of insulating liquids*, Journal of the Institution of Electrical Engineers - Part II: Power Engineering **88**, 103 (1941).
- [68] F. Argall and A. K. Jonscher, *Dielectric properties of thin films of aluminium oxide and silicon oxide*, Thin Solid Films **2**, 185 (1968).
- [69] J. Curie, *Recherches sur le pouvoir inducteur spécifique et sur la conductibilité des corps cristallisés*, par M. Jacques Curie (La Lumière électrique, 1888).
- [70] E. R. V. Schweidler, *Studien über die Anomalien im Verhalten der Dielektrika*, Annalen der Physik **329**, 711 (1907).



# 4

## ELECTROKINETIC EFFECTS IN ROCK–FLUID INTERACTION

### ROLE OF ELECTRICAL POTENTIAL AT MINERAL/FLUID INTER- FACE IN CWF PROCESS

*Carbonated water flooding is an alternative enhanced oil recovery and CO<sub>2</sub> storage method, where an oil reservoir is flooded with CO<sub>2</sub>-enriched water. One of the parameters that control the residual oil saturation is wettability. The literature about in-situ wettability alteration during carbonated water floods is limited. This study concerns the behavior of the Bentheimer sandstone electrical potential at the mineral/fluid interface, mainly as a function of the CO<sub>2</sub> concentration in an aqueous solution. To investigate the electrokinetic properties of the Bentheimer Sandstone surface, the effective coupling coefficient, and the conductivity of the pore fluid were measured in streaming potential experiments. The zeta potential was estimated. The results showed that the zeta potential strongly depends on CO<sub>2</sub> concentration and pH of the pore fluid, as well as the distribution of minerals within the matrix. Due to CO<sub>2</sub> dissolution, alteration in wettability was observed through a diminishing of the silica surface charge, as the repulsive interactions on the interfaces decrease. The obtained results can be used as a base case for the determination of the surface behavior of Bentheimer sandstone with the presence of oil. Furthermore, they have an application in planning CWF processes and post-production monitoring. The streaming potential exhibits values high enough to be measurable, the monitoring of CO<sub>2</sub> sequestration in reservoirs with the use of the streaming potential method is feasible.*



## NOMENCLATURE

$A$	Cross-sectional area of core, m
$C_c$	relative streaming potential coupling coefficient, mV/mbar
$\delta$	Distance, m
$\Delta P$	Pressure drop across the core of length $L$ , mbar
$\Delta V_s$	Streaming potential between two electrodes placed a distance $L_1$ apart from each other, mV
$\epsilon_0$	Vacuum permittivity, $8.854 \cdot 10^{-12}$ F/m
$\epsilon_r$	Relative permittivity
$F$	Formation factor, [-]
$f$	Frequency, Hz
$I_c$	Conduction current, A
$I_i$	Ionic current, A
$I_s$	Streaming current, A
$L$	Length of core, m
$\Lambda$	Characteristic length scale that describes the size of the pore network
$L_1$	Distance between the two electrodes, m
$m$	Cementation exponent
$\mu_e$	Electrolyte viscosity, Pa-s
$P$	Pressure, bar
$P_{bp}$	Back pressure, bar
$P_s$	Saturation pressure, bar
$\phi$	Porosity, [-]
$\psi$	Electric potential, mV
$\psi_0$	Electric potential on mineral surface, mV
$\psi_\beta$	Electric potential at Stern layer, mV
$q$	Flow rate, ml/min
$R_{el}$	Resistance of operational fluid, $\Omega\text{m}$
$\Sigma_{DL}$	Surface conductance of ionic conduction in EDL, S
$\Sigma_P$	Surface conductance linked to proton transfer, S
$\Sigma_s$	Specific surface conductance, S
$\Sigma_{St}$	Surface conductance in Stern layer, S
$\sigma_{eff}$	Effective conductivity, S/m
$\sigma_e$	Electrolyte conductivity, S/m
$\sigma_s$	Surface conductivity, S/m
$T$	Temperature, K
$t$	time, s
$\zeta$	Zeta potential, mV

## ABBREVIATIONS

BS	Bentheimer sandstone
$\text{CO}_3^{2-}$	Carbonate ion
CW	Carbonated water
CWF	Carbonated water flooding
EDL	Electrical double layer
$\text{H}^+$	Hydrogen ion
$\text{H}_2\text{CO}_3$	Carbonic acid
$\text{HCO}_3^-$	Bicarbonate anion

---

HS	Helmholtz-Smoluchowski
IEP	Isoelectric point
IHP	Inner Helmholtz plane
OHP	Outer Helmholtz plane
PZC	Point of Zero Charge
PRSPM	Pressure ramping streaming potential measurement
PV	Pore volume
SP	Streaming potential
wt%	Weight percent
$x_{CO_2}$	Mole fraction of $CO_2$

## 4.1. INTRODUCTION

The efficiency of Carbonated Water Flooding (CWF), in terms of oil recovery and CO<sub>2</sub> trapping, depends on reservoir properties and the sensitivity of the reservoir minerals to variations in properties of the reservoir fluids. Transport of carbonated water within the sandstone reservoir and fluid distribution [1–4] are associated with the reservoir rock surface charge and, consequently, with wettability [5]. Variations in surface charge due to changes in pH, resulting from the injection of CW may affect adsorption and/or chemical mobilization [6]. This affects rock-fluid properties, such as wetting behavior, relative permeability [7–9] and capillary pressure [10–13]. Wettability mainly depends on constituent mineral surfaces and pore fluid solutions [14]. In this study, the behavior of water-wet reservoir rock is considered in the context of CO<sub>2</sub> storage. In such water-wet systems, the rock surface is covered by a continuous aqueous film. The film stability is a function of the Electrical Double Layer (EDL) repulsion, formed as a consequence of surface charge rock/fluid/fluid interfaces. Other factors that control the surface chemistry are i.e. mineralogy, nature of dissolved ions and concentration, and alterations in the molecular lattice [15, 16].

Numerous studies were conducted to characterize wetting properties of the rock-CO<sub>2</sub>-brine system [17–25]. Authors proposed various methods to assess wettability of reservoir rocks, including the contact angle measurements [17, 19, 21, 22, 24, 25] and the USBM/Amott-Harvey method [20, 26–29]. Nevertheless, all of the commonly used techniques for characterization of the wettability alteration have their limitation and are not applicable in-situ [30–32]. Consequently, as a selection of the proper measurement techniques for carbonated water flooding requires obtaining information on fluid-rock interaction at in-situ conditions, the focus of this study is placed on the determination of zeta potential by Streaming Potential (SP) measurements. This technique can provide information on the effective surface charges. The streaming potential is obtained from the actual surface charges, modified by the molecules and ions that are dragged along with a fluid as it moves with the flow [33].

Over the last two decades, many studies, both theoretical and laboratory, have been conducted to improve the understanding of variations in the streaming potential in relation to the fluid composition with application to numerous rocks and minerals [32, 34–47]. However, literature data regarding the surface behavior of sedimentary reservoirs containing significant amounts of carbon dioxide as a pore fluid are limited. Few studies were conducted on pure CO<sub>2</sub> flow in sedimentary rocks [48, 49]. Moore et al. (2004) reported liquid CO<sub>2</sub> floods on water saturated samples, concluding that bound and trapped water control the electrokinetic response [48]. Vinogradov et al. (2011) investigated the multiphase streaming potential in sedimentary rocks during both drainage and imbibition. They found significant differences between these two displacement models [49]. In regard to the limited amount of information in the literature about in-situ wettability alteration due to CO<sub>2</sub>, a study on wettability alteration, as a result of CO<sub>2</sub> dissolution in water, was performed. The effect of secondary minerals on electrokinetic properties was assessed by comparison of sedimentary rock to pure silica behavior.

The objective of the study is to investigate and quantify the effect of water carbonation on reservoir wettability. The electrokinetic properties of pure silica and Bentheimer sandstone cores, exposed to the flow of aqueous solution with varying CO<sub>2</sub> concentra-

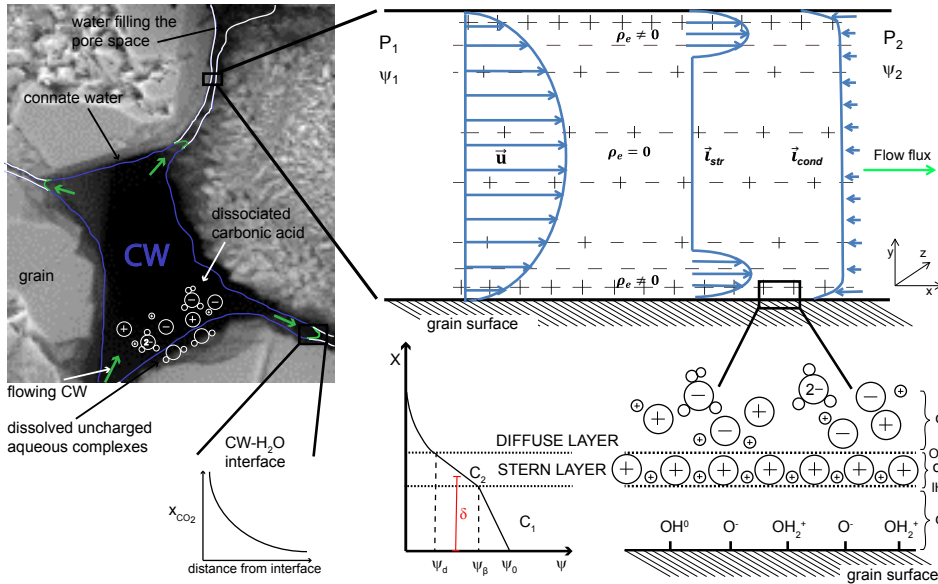


Figure 4.1: Conceptual representation of the electrokinetic effects that occur at different scales during CW flooding in Bentheimer sandstone. (top left) Pore space during the CW displacement of water, with indication of CW-H<sub>2</sub>O interface and dissolved uncharged complexes and ions created as a result of H<sub>2</sub>CO<sub>3</sub> dissociation; (top right) Development of streaming current during CW flooding through a channel of a porous medium; (bottom right) Schematic representation of the ion and potential distribution at the negatively charged grain–electrolyte interface [50].

tions, were studied experimentally. The streaming potentials and electric conductivities were measured and zeta potentials were determined. To estimate the effect of minerals other than quartz, Bentheimer Sandstone (BS) and a pure silica core were used as reservoir rocks. The tests were performed at pressures up to 18.5 bar and at temperature 308 K.

This chapter is organized as follows: Section 4.2 introduces the theoretical framework and provides the background to analyze the experiments presented in this chapter. Section 4.3 describes the experimental approach, presents materials, the setup, the method and procedures. Section 4.4 combines the results and discussion on the individual stages of the experiments, on the effect of CO<sub>2</sub> concentration and on the effect of the porous material on wetting behavior. Finally, Section 4.5 presents the conclusions.

### 4.2. ELECTROKINETIC PHENOMENA

According to the Deryaguin-Landu-Verwey-Overbeek (DLVO) theory both the electric potential,  $\psi_0$ , at mineral surfaces in contact with an electrolyte, and the potential,  $\psi$ , increases with decreasing distance from the bulk solution towards the surface. Two regions of EDL are of primary importance (Fig. 4.1): the Stern layer and a diffuse layer (outside the Stern region).

In water and carbonated water flooding, flow along charged mineral surfaces is im-

posed by the applied external force. Hence, the movement of molecules in the diffuse layer in relation to the rock surface occurs at a surface of shear. This is an imaginary surface positioned not directly at the interface, but outside the Stern layer, at a certain distance  $\delta$  away from the surface (Fig. 4.1). For practical reasons, it is chosen to coincide with the Stern surface. The potential at the Stern layer,  $\psi_\beta$ , is the actual potential influencing the transport behavior of charged species [51].

Pressure-driven transport of the mobile part (diffuse layer) of the EDL, due to water or CW injection forms an electric current along the direction of the flow of the injected fluids (Fig. 4.1), known as the streaming current ( $I_s$ ) [52, 53]. Consequently, the ions accumulate in the downstream section of the channel developing an electric field. This streaming field imposes a conduction current ( $I_c$ ) that flows in the opposite direction to the pressure-driven transport. The induced electrical field establishes the conduction currents in both the EDL and in the pore filling electrolyte. Therefore, the net ionic current ( $I_i$ ) is represented as the sum of the streaming current and the conduction current:

$$I_i = I_s + I_c. \quad (4.1)$$

The streaming current is a result of the advection of the ionic charges and can be represented as [54]

$$I_s = \frac{\epsilon_r \epsilon_0 A \Delta P}{\mu_e L} \zeta, \quad (4.2)$$

where  $\epsilon_r$  and  $\epsilon_0$  are the relative permittivity of the electrolyte and vacuum permittivity respectively,  $\mu_e$  stands for electrolyte viscosity,  $\Delta P$  represents pressure drop across the core of the length  $L$ , and of a cross-sectional area,  $A$ . The conduction current ( $I_c$ ), generated by the migration of ions due to an induced streaming potential, is given by [54]

$$I_c = \sigma_{eff} A \frac{\Delta V_s}{L_1}, \quad (4.3)$$

where  $\sigma_{eff}$  is the effective conductivity and  $\Delta V_s$  represents the response to the streaming potential between two electrodes placed a distance  $L_1$  apart from each other. Under the electrokinetic equilibrium, the total current

$$I_s + I_c = 0, \quad (4.4)$$

and the extended Helmholtz-Smoluchowski (HS) equation is obtained:

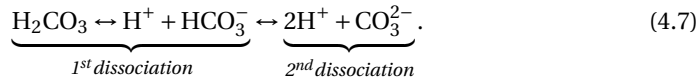
$$\frac{\Delta V_s}{\Delta P} = \frac{-\epsilon_r \epsilon_0}{\mu_e \sigma_{eff}} \zeta. \quad (4.5)$$

As no direct measurement of the zeta potential for intact porous media exists, the standard HS equation is commonly applied to rocks, even though it has never been validated [55]. The HS equation shows a lack of validity in the regions where the electromigration and the EDL polarization influence the mobility and requires careful selection of parameters [55, 56]. To accurately define the electrical conductivity of the electrolyte filling the pore space, further called effective conductivity,  $\sigma_{eff}$ , it is important to account not only for the bulk fluid that is creating the streaming potential, but to account

for the mobile parts of the diffuse layer as well [57]. Therefore, two aspects influencing the effective conductivity need to be taken into consideration: (1) the equivalent volumetric conductivity of the material,  $\sigma_s$ , representing the grains' surface coated with clay and oxides, and (2) the electrolyte conductivity  $\sigma_e$  that comprises free and bounded pore fluids [58]. In this study, the estimate of the effective conductivity is based on the characteristics of the reservoir rock showing low clay content. The model, represented by two resistors in parallel, was established by Pride (1994) and is given by [59–61]

$$\sigma_{eff} = \frac{1}{F}(\sigma_e(T, C) + (F - 1)\sigma_s) \quad (4.6)$$

where  $F = 1/\phi^m$  represents the formation factor,  $\phi$  stands for porosity and  $m$  is the cementation exponent. The electrolyte conductivity strongly depends on temperature and concentration of ions [62]. For carbonated water, dissolved  $\text{CO}_2$  at the macroscopic scale creates mainly electrically neutral aqueous complexes [15, 50, 63]. The remaining portion of the  $\text{CO}_2$  dissolved in water forms carbonic acid ( $\text{H}_2\text{CO}_3$ ), which is unstable. In an aqueous solution carbonic acid undergoes a reversible two-stages dissociation:



This clearly results in the increase of ionic strength and the decrease of the pH of the system, further altering the wetting characteristics of the rock surface. The concentration of ions depends on the  $\text{CO}_2$  partial pressure. The equivalent volumetric conductivity  $\sigma_s$  is evoked at the surface of the surface of the charged matrix, further imposing the conduction current density and consequently lowering the downstream electrical field [64–66]. Surface conductivity magnitude is related to the type of the pore filling fluid, dispersion of minerals within the reservoir, matrix geometry, and spatial fluid distribution. It can be defined by the "equivalent grain conductivity approach" [61, 67, 68] and correlated to the specific surface conductance  $\Sigma_s$  by a relation [69]

$$\sigma_s = \frac{2\Sigma_s}{\Lambda}, \quad (4.8)$$

where  $\Lambda$  is a characteristic length scale, describing the dimension of the pores, i.e. the median grain diameter [34, 55, 70]. The specific surface conductance is represented by the sum of three contributing conductions that are respectively a result of ionic conduction  $\Sigma_{DL}$  in the EDL, in the Stern layer  $\Sigma_{St}$ , and the proton transfer  $\Sigma_P$  [71]:

$$\Sigma_s = \Sigma_{DL} + \Sigma_{St} + \Sigma_P. \quad (4.9)$$

The corresponding equations for each conduction and associated parameters are not discussed in this study and can be found elsewhere [55]. However, the surface conductivity is a complex phenomenon currently being researched and models used in the literature are a theoretical construction based on estimated values.

## 4.3. EXPERIMENTAL APPROACH

### 4.3.1. MATERIALS

**Core samples and core holder.** Core displacement tests were conducted on the Bentheimer sandstone and silica cores (Table 4.1). *Bentheimer sandstone* matrix is repre-

sented by a monocrystalline detrital quartz with authigenic overgrowth (91.7 wt%) and main accessory minerals (8.3 wt%) such as feldspars, iron (hydr)oxides and clays. The grains and pores exhibit homogeneities, represented by well sorted, rounded to sub-rounded grains with a regular and narrow pore-size distribution of about 0.23 and a permeability of  $\sim 2 \cdot 10^{-12} \text{ m}^2$ . A detailed characterization of the Bentheimer sandstone can be found in Chapter 2. *Silica cores* were used as a reference material that contain 99.99%

Table 4.1: List of conducted experiments.

Material	Experiment	Back pressure $P_{bp}$ [bar]	CO <sub>2</sub> saturation pressure $P_s$ [bar]
BS	CW <sub>1a</sub>	7.0	6.5
	CW <sub>1b</sub>	12.5	6.5
	CW <sub>1c</sub>	18.5	6.5
	CW <sub>2a</sub>	12.5	12.0
	CW <sub>2b</sub>	18.5	12.0
	CW <sub>3a</sub>	18.5	18.0
SiO <sub>2</sub>	CW <sub>4a</sub>	2.5	2
	CW <sub>5a</sub>	3.5	3

SiO<sub>2</sub> with a porosity of 0.38. Core samples with a diameter of 3.8 cm and a length of 17 cm (main study) and a diameter of 3 cm and a length of 3.6 cm (pre-study) were drilled with a water-cooled diamond saw and dried in an oven at 323 K for 72 hours. Next, the core samples were surrounded by a layer of epoxy glue to avoid bypassing of fluids along the side of the core. The thickness of the epoxy layer and the penetration depth into the core sample were estimated with CT-scans, resulting in an effective core diameter further used for pore volume calculations. Dried samples were placed in the core holder. The core holder was made of PolyEther Ether Ketone (PEEK), a material of good mechanical properties that can stand high pressures and temperatures. Two electrode ports were drilled through the glue layer into the core body at a distance 8.4 cm (electrode 1) and 12.9 cm (electrode 2) from the bottom of the core.

**Fluids** In the experiments, the operational phases were water and carbonated water. *Water*: Water used in this study consisted of degassed, demineralized water. *Carbonated water*: CW solution was prepared in advance in an external isothermal system. A water-filled cylinder was introduced to pure CO<sub>2</sub> inflow. The solution was instantaneously mixed by a magnetic stirrer to establish equilibrium at experimental conditions. During the whole procedure, the system was kept in the isothermal environment at  $T = 308$  K.

#### 4.3.2. EXPERIMENTAL SETUP

The experimental setup was designed and built to conduct integrated core flow and electrical measurements. The schematic of the setup is shown in Fig. 4.2.

*Differential pressure measurements*: The core flow setup consists of a vertically-placed core holder. A radial confining pressure was applied through the core holder wall, to

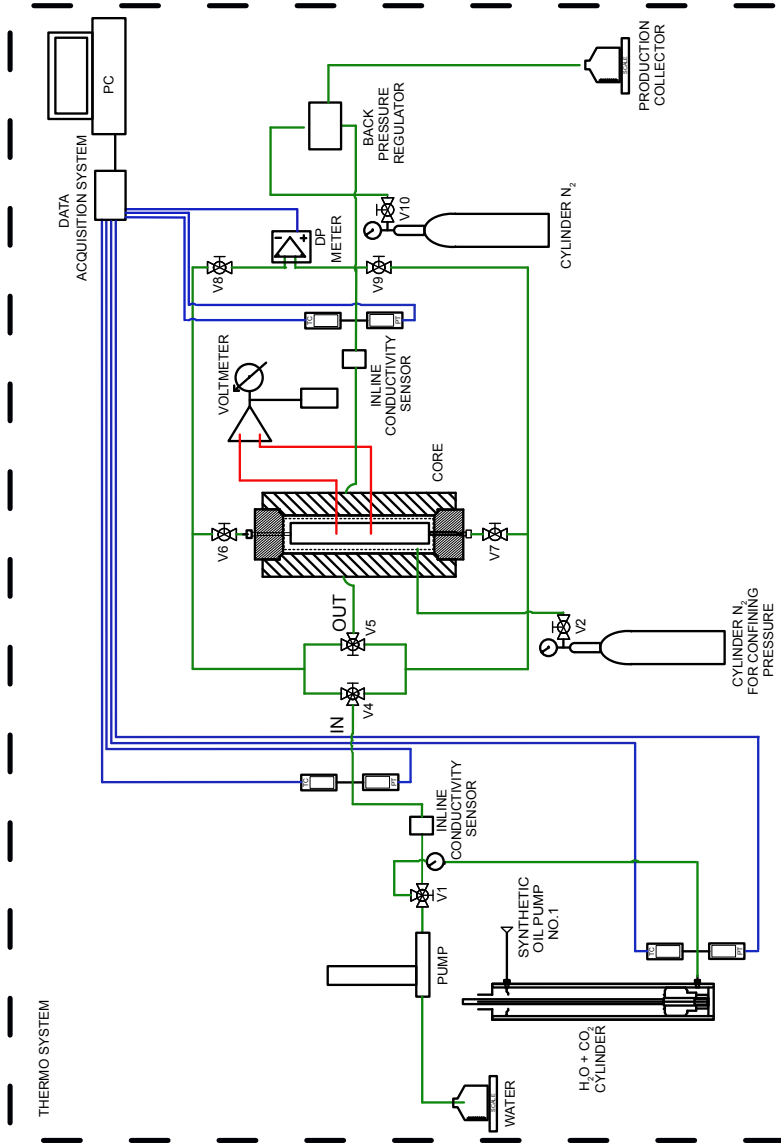


Figure 4.2: Schematic description of the experimental setup to study electrokinetic effects during water and CW floods. The dashed line represents the thermal box in which the experimental setup was built. The green lines illustrate the tubing and the various flow lines. The blue lines are data cables connecting pressure transducers and thermocouples to a computer for acquisition and controlling, the red lines represent connections to the electrodes.



compensate for the pore pressure. The core holder was in line with a high-pressure ISCO pump connected to the cross-connection, from where fluid could be injected to the top or bottom side of the core. The ISCO pump was used to inject water and to pressurize the system. CW was injected with another high-pressure ISCO pump, initially through the bottom side of the core holder. The pressure in the core was maintained by a nitrogen pressure regulator inserted in the production line of the system. The pressure,  $P$ , in the system and the pressure difference,  $\Delta P$  over the length of the sample, were measured by a system of pressure gauges before and after the core. The production line led to a glass CO<sub>2</sub>/water separator, where water was placed in a specially designed glass tube with volume scale and CO<sub>2</sub> was redirected to a wet gas meter (Schlumberger) placed at the end of the production line. The whole experimental setup was placed in a heated build chamber, isolated with Mylar films, at  $T = 308$  K. The temperature was monitored by a system of 8 thermocouples, placed both in the tubing lines of the system and in the thermal box.

*Electrical Measurements:* For streaming potential measurements, the Ag/AgCl electrodes were placed and fixed with the PEEK connectors into the electrode ports. Further electrodes were connected to a high input impedance voltmeter (accuracy 0.2%, resolution 15 nV) and an oscilloscope. The high input impedance voltmeter is necessary to measure the low conductive electrolyte solutions and to avoid loading effect on a circuit [70].

The resistance,  $R_{el}$ , of the operational fluids was measured between two spatially fixed Ag/AgCl electrodes mounted in inline conductivity cells placed in the upstream and downstream line of the core. The cell was regularly calibrated against reference solutions. In order to diminish polarization effects, an alternating current was applied for resistance measurements. Moreover, the pH of the produced electrolyte (after CO<sub>2</sub> separation) was determined by a Metrohm electrode.

### 4.3.3. EXPERIMENTAL PROCEDURE

#### CALIBRATION TESTS

The main experiments and measurements of SP during CWF are very sensitive to a number of parameters, among others mineral composition, petrophysical and petrological properties of the samples. Simplified streaming potential experiments were conducted on multiple samples in prior to main tests to investigate and quantify the variation in electrokinetic properties, such as streaming potential coupling coefficient with respect to different samples. The measurement sequence of streaming potential consisted of applying different flow rates of an aqueous solution through a sample. Simultaneously, streaming potential between the electrodes and a pressure drop along the core were continuously recorded. This procedure was repeated for various Bentheimer samples.

#### MAIN TESTS

*Core preparation and saturation with water:* The core was initially dried by flushing with CO<sub>2</sub> at atmospheric back pressure. Further, the system was vacuumed to remove excess amount of CO<sub>2</sub>. Water was injected into the core from the bottom at atmospheric pressure and at a constant flow rate of 1 ml/min. Subsequently, the system was slowly pressurized to 20 bar. 10 pore volumes (PV) of water were injected through the core

to attain dissolution and removal of remaining  $\text{CO}_2$  and at the same time a full water saturation of the core. Subsequently, the permeability of the core was determined by measuring pressure drops at different applied flow rates. Further, the system pressure was set to the pre-defined operational  $P$ - $T$  conditions, and permeability measurements were repeated.

*Coupled Streaming Potential (SP), Differential Pressure (DP) and Resistivity (R) measurements:* After the system was fully saturated with water, SP and DP were simultaneously measured. Additionally, the resistivity of electrolyte (upstream and downstream of the core) was measured, and its independence on applied pore pressure and the flow rate was verified. Further, based on the measured  $R_{el}$  values and determined cell constant, the conductivity of the operational solution,  $\sigma_{el}$ , was calculated.

The SP measurements consisted of paired Pressure Ramping Streaming Potential Measurements (PRSPM). PRSPM consisted of applying a set of 10 linearly increasing flow rates through a sample, first from the bottom and further from the top of the sample in order to decrease polarization effects of the Ag/AgCl electrodes. The elimination of the polarization effect cannot be achieved to the same negligible level, like in the case of the Paired Stabilization (PS) experiments [46]. However, the PS method is not applicable, due to the presence of dissolved  $\text{CO}_2$  in the water and the difficulty of establishing stable zero-flow voltage. Linearity is observed only in the lower range of applied flow rates, thus the maximum flow rate used for the measurements of streaming potentials was 5 ml/min.

*Carbonated water injection:* When the reference SP-DP-R measurements on the water saturated core were completed, the carbonated water was injected. The saturation process was monitored by measuring the pressure drop and the streaming potential until stable conditions were established. Subsequently, the main SP-DP-R measurements were conducted for each  $\text{CO}_2$  concentration.

*Pressure lift up:* To investigate the stability of the measurements in relation to the pressure and the compressibility of the electrolyte, the back pressure of the system was increased, first doubled, and then tripled, in respect to the initial saturation pressure of the particular test. Note, that the concentration of the  $\text{CO}_2$  solution was kept constant. At each back pressure, the coupled SP-DP-R were conducted.

*Post-water injection between experimental runs:* In order to ensure comparable conditions for all tested CW solutions with varying  $\text{CO}_2$  saturation pressures, the core was flooded with 6 PV of water in between the experimental runs. As a result of this,  $\text{CO}_2$  was removed from the sample and, when again stable conditions were established (a constant pressure drop over the core), the permeability and streaming potential were measured.

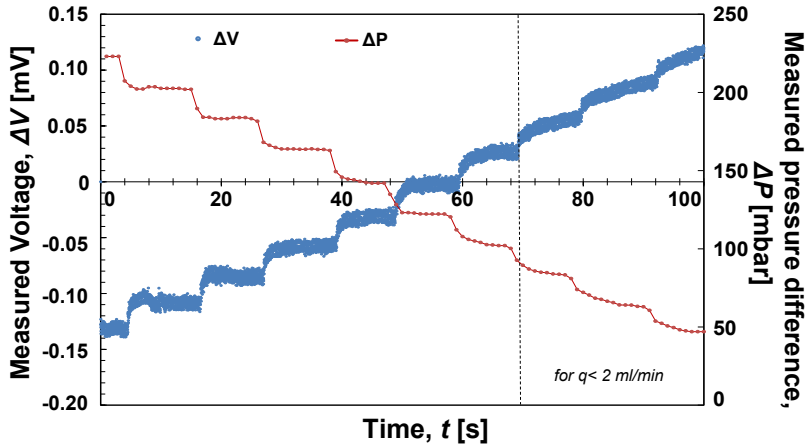
#### 4.4. RESULTS AND DISCUSSION

This section includes the results of (1) the calibration study conducted to determine the variations in the streaming potential response related to variation in BS cores composition and structure; (2) the baseline experiment conducted on BS with CW at  $\text{CO}_2$  saturation and  $P_s = 6.5$  bar, together with the determination and a discussion on saturated rock conductivity and fluid resistivity; (3) the effect of  $\text{CO}_2$  concentration on wetting behavior and  $\text{CO}_2$  storage.

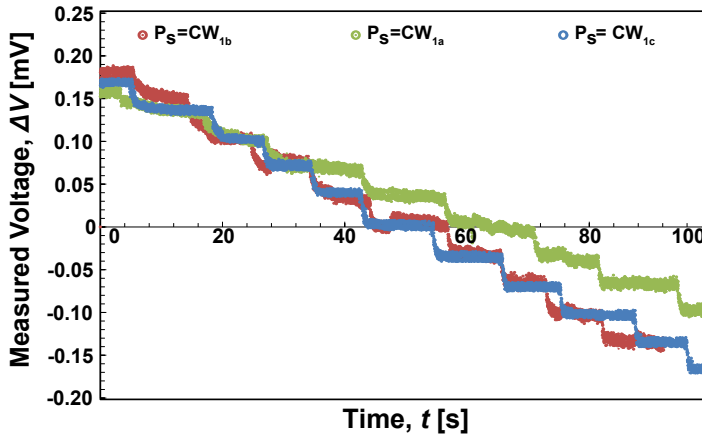
#### 4.4.1. CALIBRATION TESTS

Results obtained on multicores indicated an influence of the mineral composition and its distribution on the response of the streaming potential over investigated BS core. Using multicores could create additional variation due to heterogeneity in the structure/composition of the rock. Therefore, in order to minimize the number of parameters affecting the system behavior during CWE, the study was conducted on a single core.

#### 4.4.2. BASELINE EXPERIMENT



(a)



(b)

Figure 4.3: (a) An example of a streaming potential difference between two electrodes with the applied pressure drop across the sample represented as a function of time ( $P_s = 6.5$  bar,  $P_{bp} = 7$  bar); (b) Measured voltage difference during CW flood at  $P_s = 6.5$  bar and  $P_{bp} = 7, 12.5$  and  $18.5$  bar.

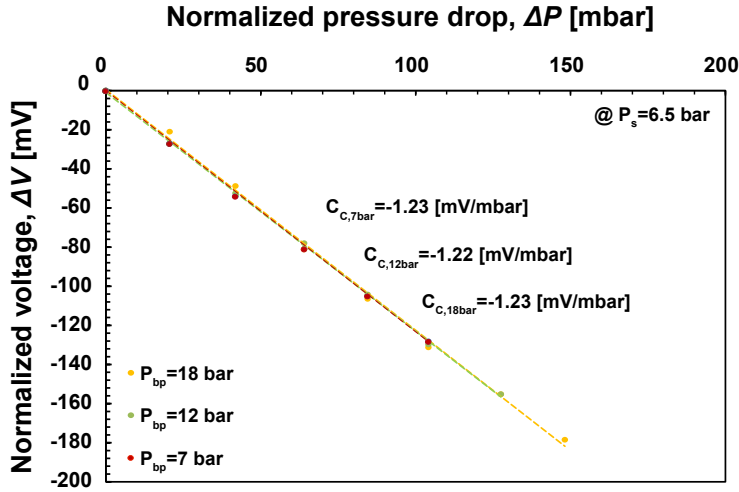


Figure 4.4: Normalized streaming potential against the corresponding pressure drop from PRSPM for the same BS sample at different back pressures and constant  $\text{CO}_2$  saturation ( $P_s = 6.5$  bar).

**Carbonated water injection and electrokinetic measurements.** Fig. 4.3a and Fig. 4.3b show examples of typical results obtained from the PRSPM. Fig. 4.3a represents a plot of measured streaming potential and pressure drop over the experimental time. Change in the applied flow rate gives a linear response in the pressure drop across the sample and a linear change in the streaming potential value. Results indicate that for larger volumes passing the sample ( $q > 1.5$  ml/min), the time of the response to both SP and pressure is shorter and the distortion of the output less pronounced. For smaller flow rates, it can be seen that balance between the streaming and conduction currents is not fully established, so the equilibrium state is not reached. Therefore, for further analysis, including zeta potential, only measurements where equilibrium was reached are used.

In order to investigate the stability of the measurements in relation to the pressure, the PRSPM were repeated at elevated back pressures (12.5 and 18.5 bar) without changing  $\text{CO}_2$  saturation ( $P_s = 6.5$  bar). As experimental conditions are maintained such that CW is below its bubble point, slight differences in flow behavior can be observed with increasing pressure (Fig. 4.3b). Measurements representing higher back pressure give a slightly better response.

The normalized streaming potential against the corresponding pressure drop for equilibrium dissolution at  $P_s = 6.5$  bar at various back pressures (7, 12.5 and 18.5 bar) is presented in Figure 4.4. A regression applied to the data confirms a linear variation of the effective streaming potential coupling coefficient. The PRSPM for the same BS sample gives a value of around -1.23 mV/mbar for the coupling coefficient for all applied back pressures. The results for the constant  $\text{CO}_2$  saturation in CW differ by less than 1%.

**Determination of saturated rock conductivity and measurements of fluid resistivity.** In order to assess the processes occurring during injection of the electrolyte into the

porous medium, it is necessary to understand and quantify the effective conductivity of the saturated rock. Following Eq. 4.6, two terms need to be determined: electrolyte conductivity and surface conductivity. The first, electrolyte conductivity, was measured experimentally against frequency and results are depicted in Fig. 4.5a.

Fig. 4.5a shows the measured electrolyte conductivity for water and CW solution at various back pressures (7, 12.5 and 18.5 bar) before and after passing the core sample. The effects of CO<sub>2</sub> dissolution, dissociation, and newly formed ions are clearly exhibited by an increase in pore fluid conductivity over one order of magnitude (water:  $\sigma_e = 10^{-6}$  S/m and CW:  $\sigma_e = 10^{-5}$  S/m for  $f = 10^5$  Hz). Moreover, a difference in response of the electrolyte before and after passing the porous sample at lower frequencies ( $f < 10^3$  Hz for water and  $f < 10^4$  Hz for CW) is observed in all experimental runs. This is in good agreement with others, who observed a similar behavior for the "low salinity regime" [72]. Moreover, the repeatability of the measurements for the solution containing the same mole fraction of CO<sub>2</sub>, but at varying back pressure, confirms that the conductivity of constant CO<sub>2</sub> concentration does not depend on the applied pressure.

The dissolution of CO<sub>2</sub> decreases the pH value and affects surface conductivity. However, as mentioned in section 4.2, the surface conductivity is a complex phenomenon and currently used models in the literature are a theoretical construction based on estimated values [71]. Therefore, despite the model based values, it is necessary to understand the influence of the surface conductance on the effective conductivity at a specified pore fluid conductivity (Fig. 4.5b).

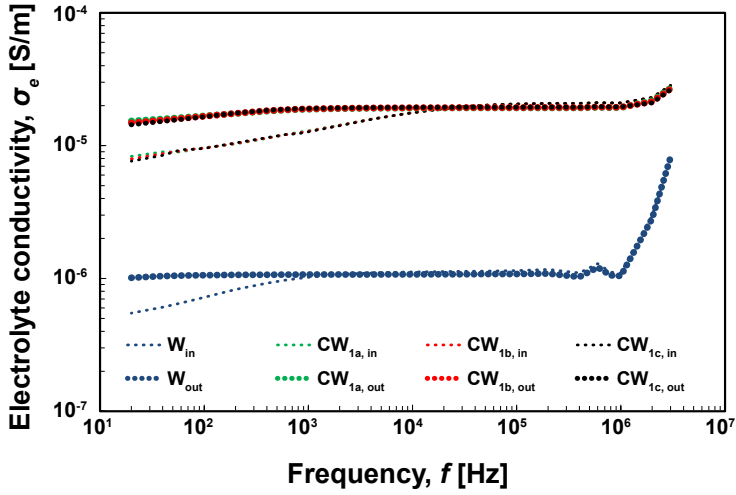
Fig. 4.5b shows that for conductivities of electrolytes used in this study ( $\sim 10^{-6} - 10^{-5}$ ) surface conductances smaller than  $10^{-12}$  have a minor effect on the effective conductivity, and thus, the associated error neglecting the surface conductance is insignificant. The increase of its value has a substantial influence on the effective conductivity and further on the decrease of the streaming potential coupling coefficient. Hence, the range of possible values were estimated based on: (1) literature correlations for both clean and clayey rocks [73, 74] and (2) on the double layer model derived by [55], which studies the influence of pH on surface conductance. The data obtained for water and CW at  $P_s = 6.5$  bar are summarized in Table 4.2.

Table 4.2: Literature data and surface conductance estimates.

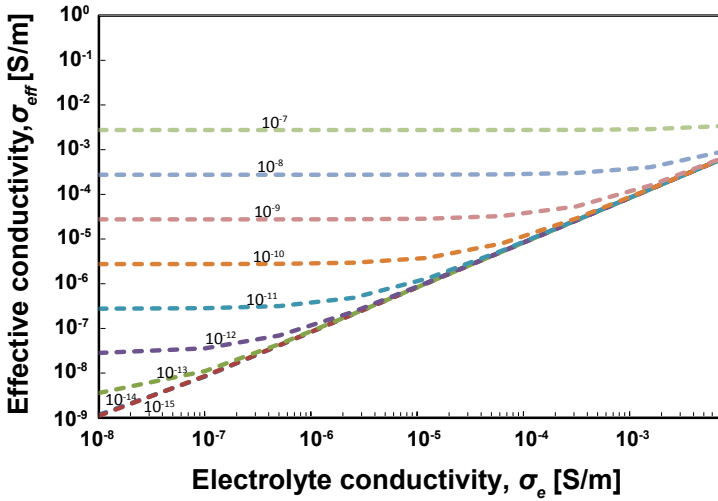
	$\Sigma_s$ [73]	$\Sigma_s$ [74]	$\Sigma_s$ [47]
Water	$10^{-9}$	$10^{-10}$	$3.48 \cdot 10^{-9}$
CW1			$2.61 \cdot 10^{-9}$

As the surface conductance was not measured experimentally, and an estimated value may hold significant uncertainty, a 'cloud' of surface conductance values will be used for further zeta potential analysis ( $15\% \pm$  the estimated values).

**Post injection between the experimental runs.** Fig. 4.6a shows the PRSPM results for water, before CW injection and water injection after CW flooding, indicating that no significant changes in permeability and in the electrical properties occurred between the



(a)



(b)

Figure 4.5: (a) Measured conductivity of the electrolyte solution over frequency range; (b) Effective electrical conductivity vs. electrolyte conductivity for different surface conductance values.

experimental runs. Therefore, comparable conditions for all tested CW solutions were maintained.

#### 4.4.3. EFFECT OF CO<sub>2</sub> CONCENTRATION ON WETTING BEHAVIOR AND CO<sub>2</sub> STORAGE

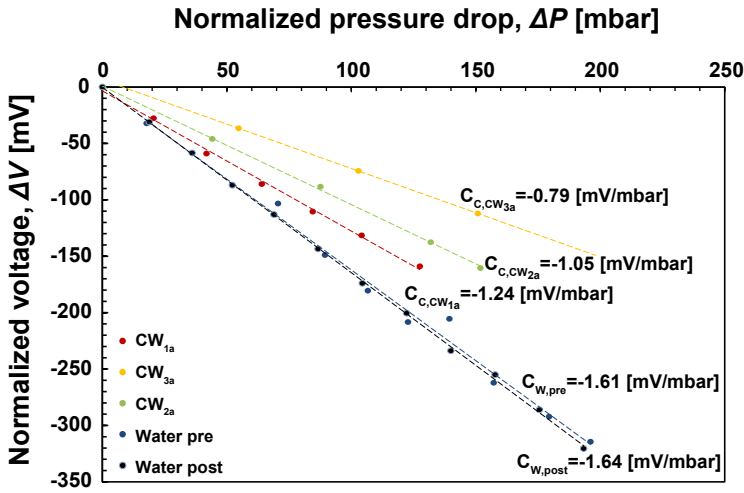
This work discusses the relative changes in the streaming potential coupling coefficient and the zeta potential with varying CO<sub>2</sub> concentrations. The relative streaming potential coupling coefficient ( $C_c$ ) was measured with respect to CO<sub>2</sub>-H<sub>2</sub>O saturation, for both Bentheimer sandstone and silica samples. In both cases (Figs. 4.6a and 4.6b) the streaming potential coupling coefficient is inversely proportional to the CO<sub>2</sub> concentration. CW injection in the porous system results in a decrease of the streaming coupling coefficient by a factor of 2 for  $P_{sat} = 18$  bar in relation to water flooding. In contrast, the non-conductive CO<sub>2</sub> floods reported by Moore et al. (2004) decreased the streaming coupling coefficient by a factor of  $\sim 10$  in relation to water flooding. The value of the streaming potential coupling coefficient declined until the entire mobile water was displaced from the rock matrix [48].

The changing pH of the reservoir fluid strongly affects the zeta potential. CO<sub>2</sub> saturation and the related formation of weak carbonic acid result in (1) a conductivity increase due to the creation of ions for electrical conduction, (2) a viscosity and permittivity change, and (3) a change of the streaming potential coupling coefficient. Subsequently, the viscosities of the solutions were calculated based on the viscosity model after Islam et al. (2012) [75] and the relationship between the effective permittivity of the electrolytes were estimated based on the mixing models of Looyenga and Bruggeman-Hanai [76, 77]. The zeta potential, for both samples and all injected fluids, was deduced from Equation 4.5 using the estimated and calculated values of fluid properties, such as viscosity, effective conductivity, and electrical permittivity (Table 4.3).

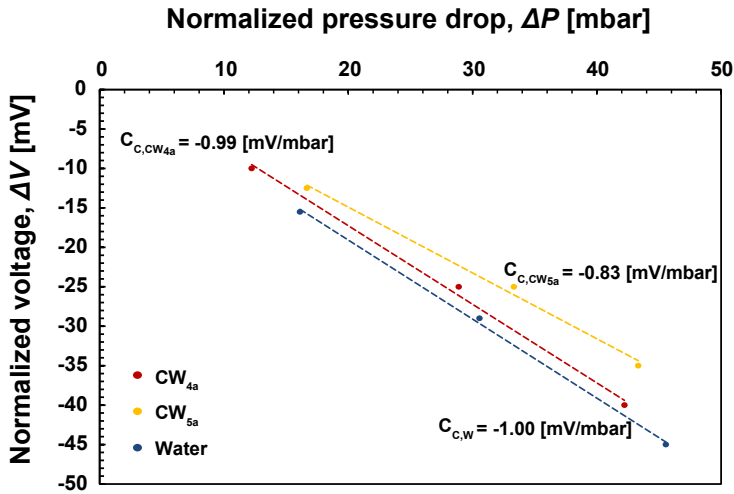
Table 4.3: Parameters used for zeta potential determination.

	Mol fraction $X_{CO_2}$	Viscosity $\eta$ [ $\mu\text{Pa}\cdot\text{s}$ ]	Effective permittivity $\epsilon_{eff}$ [ $10^{-10}$ F/m]	Surface conductance $\Sigma_s$ [ $10^{-9}$ S/m]	Electrolyte conductivity $\sigma_e$ [ $10^{-5}$ S/m]
W	0	721.30	6.9	3.48	0.20
CW1	0.050	721.31	5.3	2.60	1.23
CW2	0.090	721.32	4.4	2.42	4.51
CW3	0.014	721.42	3.5	2.40	6.61
CW4	0.002	721.30	6.8	2.45	0.82
CW5	0.001	721.30	6.7	2.50	0.93

Figure 4.7 presents the zeta potential as a function of pH of the solution. The zeta potential is in the range of the values reported for BS and quartz in the literature. The experiments are in good agreement with the experiments of Stoll (2005), who measured



(a)



(b)

Figure 4.6: (a) Normalized streaming potential against the corresponding pressure drop for Bentheimer sandstone; (b) Normalized streaming potential against the corresponding pressure drop for silica core.



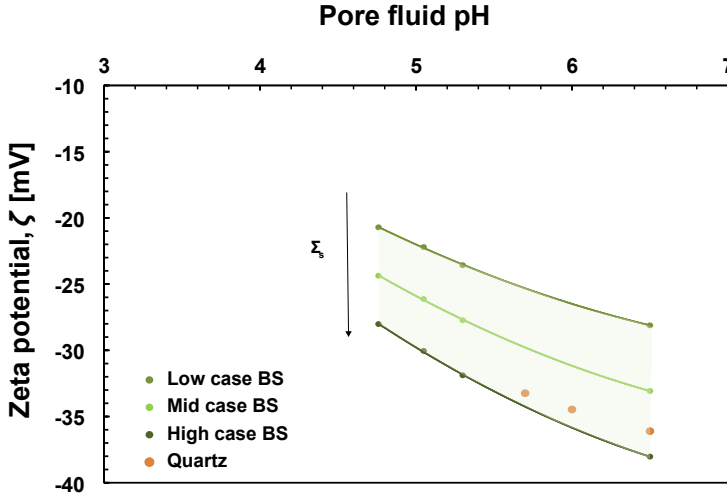
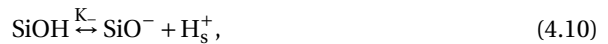


Figure 4.7: Calculated zeta potential vs. pH. For BS a cloud of surface conductivities is plotted.

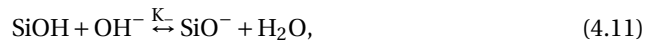
the zeta potential between 20-40 mV [78]. For BS, a cloud of results is plotted (low case to high case) showing the effect of surface conductivity on the zeta potential.

#### 4.4.4. EFFECT OF POROUS MATERIAL

The discrepancy in the obtained values between pure silica and Bentheimer sandstone lies in the mineral composition and the presence of accessory minerals within the BS matrix. Pure quartz ( $\text{SiO}_2$ ) exhibits a relatively limited capability for ion exchange. It was shown in the literature that at the surface of insoluble oxides, functional groups exist (i.e. hydroxyl groups) [79]. The main surface chemical reactions that occur are hydration and subsequent dissociations [74, 80]. Contact of silicon dioxide and water results in water dissociation on  $\text{SiO}_2$  surfaces and further silanol groups ( $\text{SiOH}$ ) formation (Figure 4.8). Due to the interaction of  $\text{H}_2\text{O}$  with reactive centers, silanol groups are created as small-membered Si-O rings that exist on the  $\text{SiO}_2$  surface [82–84]. Therefore, as a result of dissociation the surface may become negatively charged:



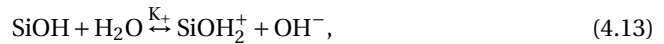
alternatively



or, under high acidic conditions ( $\text{pH} < 2-3$ ), positively charged due to the subsequent protonation of the uncharged silanol groups [85]



alternatively



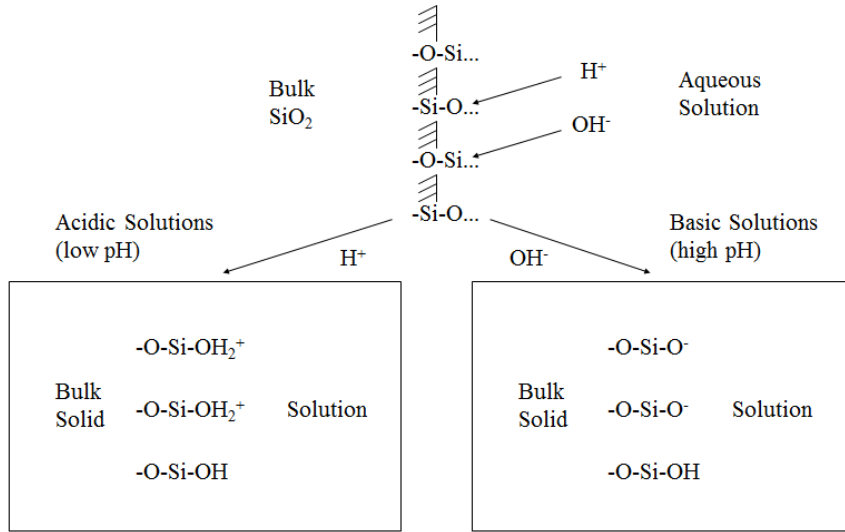


Figure 4.8: Surface charge development on SiO<sub>2</sub> immersed in aqueous solutions (from [81]).

where SiOH, SiO<sup>-</sup>, SiOH<sub>2</sub><sup>+</sup> are respectively neutral, negatively charged, and positively charged surface hydroxyl groups; H<sub>s</sub><sup>+</sup> stands for a hydronium ion near the surface; K<sub>+</sub> and K<sub>-</sub> represent mass action expressions and are the apparent constants for a distinct electrolyte.

For the CW, the pH of the pore fluid is reduced and the value of zeta potential changes to smaller negative values. This response is related to the diminishing silica surface charge, as the repulsive interactions between the interfaces decrease. Similar behavior was previously observed in contact angle wettability studies [18, 86–89] and explained as an increase in contact angle due to water film destabilization. In addition, findings of Kim et al.(2012) from a CO<sub>2</sub> storage micro model experiment indicate a significant change in wetting of the silica surface [87, 88].

Moreover, the influence of accessory minerals was discussed in Chapter 2. The presence of clays and iron oxides cause a shift of the Point of Zero Charge (PZC) from 2-3 for quartz (the main constituent of BS) to 8 for Bentheimer sandstone. However, in the analyzed results in this chapter, the influence is less distinct. The less distinct influence may be related to the difference in values of zero charge obtained by electrokinetic methods, such as streaming potential that gives an IsoElectric Point (IEP) representing the external charge of the investigated rock; not the total net surface charge. Based on this difference (PZC-IEP), the general conclusion can be drawn from the distribution of the charges in the Bentheimer sandstone. For strongly acidic and basic conditions, a homogeneous distribution of the surface charges is recognized and for low acidic and basic conditions, more external than internal negatively charged particles are present [90].

## 4.5. CONCLUSIONS

The electrokinetic properties of the Bentheimer Sandstone surface, mainly as a function of the CO<sub>2</sub> concentration in an aqueous solution, were measured in a streaming potential experiment. Obtained results were compared with the tests conducted on the silica core that was free of any accessory minerals. The main findings are as follows:

- measurements show that with increasing CO<sub>2</sub> concentration in the pore water, the silica surface charge diminishes, as the repulsive interactions between the interfaces decrease;
- the zeta potential depends on the pore fluid CO<sub>2</sub> concentration and related pH, as well as mineral composition. The results confirmed the influence of accessory minerals, a variation in their response to streaming potential, and titration experiments;
- for further studies on CWF, the measured streaming potential values can be used as a base case for the determination of surface behavior of Bentheimer sandstone when oil is present;
- the measured streaming potential of carbonated water floods was higher than of CO<sub>2</sub> floods and the suggested preliminary values may be measurable at a larger scale.

**REFERENCES**

- [1] J. R. Christensen, E. H. Stenby, and A. Skauge, *Review of WAG Field Experience*, Society of Petroleum Engineers (2001), 10.2118/71203-PA.
- [2] N. R. Morrow, *Wettability and Its Effect on Oil Recovery*, Journal of Petroleum Technology (1990), 10.2118/21621-PA.
- [3] J. Bobek, C. Mattax, and M. Denekas, *Reservoir rock wettability—its significance and evaluation*, Trans. AIME **213**, 155 (1958).
- [4] J. S. Buckley, C. Bousseau, and Y. Liu, *Wetting alteration by brine and crude oil: from contact angles to cores*, SPE Journal **1**, 341 (1996).
- [5] L. L. Schramm, A. T. Turta, and J. J. Novosad, *Microvisual and coreflood studies of foam interactions with a light crude oil*, SPE reservoir engineering **8**, 201 (1993).
- [6] D. J. Ligthelm, J. Gronsveld, J. Hofman, N. Brussee, F. Marcelis, and H. van der Linde, *Novel Waterflooding Strategy By Manipulation Of Injection Brine Composition*, in *EUROPEC/EAGE Conference and Exhibition* (Society of Petroleum Engineers, 2009).
- [7] W. Owens and D. Archer, *The effect of rock wettability on oil-water relative permeability relationships*, Journal of Petroleum Technology **23**, 873 (1971).
- [8] Y. Chang, K. Mohanty, D. Huang, and M. Honarpour, *The impact of wettability and core-scale heterogeneities on relative permeability*, Journal of Petroleum Science and Engineering **18**, 1 (1997).
- [9] M. Van Dijke and K. Sorbie, *The relation between interfacial tensions and wettability in three-phase systems: consequences for pore occupancy and relative permeability*, Journal of Petroleum Science and Engineering **33**, 39 (2002).
- [10] J. C. Melrose, *Wettability as related to capillary action in porous media*, Society of Petroleum Engineers Journal **5**, 259 (1965).
- [11] W. G. Anderson, *Wettability literature survey-part 4: Effects of wettability on capillary pressure*, Journal of Petroleum Technology **39**, 1,283 (1987).
- [12] S. A. Bradford and F. J. Leij, *Predicting Two-and Three-Fluid Capillary Pressure-Saturation Relationships of Porous Media With Fractional Wettability*, Water Resources Research **32**, 251 (1996).
- [13] S. K. Masalmeh, *The effect of wettability heterogeneity on capillary pressure and relative permeability*, Journal of Petroleum Science and Engineering **39**, 399 (2003).
- [14] G. Hirasaki, *Wettability: fundamentals and surface forces*, SPE Formation Evaluation **6**, 217 (1991).
- [15] W. Stumm, *Chemistry of the solid-water interface: processes at the mineral-water and particle-water interface in natural systems* (John Wiley & Son Inc., 1992).

- [16] M. R. Sheffer, *Forward modelling and inversion of streaming potential for the interpretation of hydraulic conditions from self-potential data*, Ph.D. thesis, University of British Columbia (2007).
- [17] Z. Zhu, M. Li, M. Lin, B. Peng, L. Sun, and L. Chen, *Investigation on Variations in Wettability of Reservoir Rock Induced by CO<sub>2</sub>-Brine-Rock Interactions*, Society of Petroleum Engineers (2011), 10.2118/142979-MS, SPE-142979-MS.
- [18] P. Chiquet, D. Broseta, and S. Thibeau, *Wettability alteration of caprock minerals by carbon dioxide*, *Geofluids* **7**, 112 (2007).
- [19] N. S. Kaveh, E. S. J. Rudolph, K.-H. A. Wolf, and S. N. Ashrafizadeh, *Wettability determination by contact angle measurements: hvBb coal-water system with injection of synthetic flue gas and CO<sub>2</sub>*, *Journal of colloid and interface science* **364**, 237 (2011).
- [20] J. Mills, M. Riazi, and M. Sohrabi, *Wettability of common rock-forming minerals in a CO<sub>2</sub>-brine system at reservoir conditions*, in *International Symposium of the Society of Core Analysts* (Society of Core Analysts Fredericton, Canada, 2011) pp. 19–21.
- [21] J.-W. Jung and J. Wan, *Supercritical CO<sub>2</sub> and ionic strength effects on wettability of silica surfaces: Equilibrium contact angle measurements*, *Energy & Fuels* **26**, 6053 (2012).
- [22] A. Al-Menhali and S. Krevor, *Pressure, temperature and ionic strength effects on the wettability of CO<sub>2</sub>-brine-sandstone system: Core-scale contact angle measurements*, in *SCA2013-003 paper presented at the 2013 Society of Core Analysts Symposium in Napa Valley, California* (2013).
- [23] R. Farokhpoor, B. J. Bjørkvik, E. Lindeberg, and O. Torsæter, *CO<sub>2</sub> Wettability Behavior During CO<sub>2</sub> Sequestration in Saline Aquifer-An Experimental Study on Minerals Representing Sandstone and Carbonate*, *Energy Procedia* **37**, 5339 (2013).
- [24] A. Al-Menhali and S. Krevor, *Effective wettability measurements of CO<sub>2</sub>-brine-sandstone system at different reservoir conditions*, *Energy Procedia* **63**, 5420 (2014).
- [25] C. Chen, J. Wan, W. Li, and Y. Song, *Water contact angles on quartz surfaces under supercritical CO<sub>2</sub> sequestration conditions: Experimental and molecular dynamics simulation studies*, *International Journal of Greenhouse Gas Control* **42**, 655 (2015).
- [26] C. Chalbaud, M. Robin, J.-M. Lombard, H. Bertin, and P. Egermann, *Brine/CO<sub>2</sub> interfacial properties and effects on CO<sub>2</sub> storage in deep saline aquifers*, *Oil & Gas Science and Technology—Revue de l’Institut Français du Pétrole* **65**, 541 (2010).
- [27] D. Yang, Y. Gu, and P. Tontiwachwuthikul, *Wettability determination of the reservoir brine- reservoir rock system with dissolution of CO<sub>2</sub> at high pressures and elevated temperatures*, *Energy & Fuels* **22**, 504 (2007).
- [28] A. Brautaset, *In situ fluid dynamics and CO<sub>2</sub> injection in porous rocks*, (2009).

- [29] I. B. Enge, *The Effect of Brine Composition and Rock Type on Oil Recovery by the Use of Combined Low-Salinity Waterflooding and Surfactant Flooding: A Literature Review and Experimental Study*, (2014).
- [30] S. Ma, X. Zhang, N. Morrow, and X. Zhou, *Characterization of wettability from spontaneous imbibition measurements*, *Journal of Canadian Petroleum Technology* **38** (1999).
- [31] S. G. Ghedan, C. H. Canbaz, D. A. Boyd, G. M. Mani, and M. K. Haggag, *Wettability profile of a thick carbonate reservoir by the new rise in core wettability characterization method*, in *Abu Dhabi International Petroleum Exhibition and Conference* (Society of Petroleum Engineers, 2010) pp. 2203–2217.
- [32] G. Bassioni and S. Taha Taqvi, *Wettability Studies Using Zeta Potential Measurements*, *Journal of Chemistry* **2015**, 6 (2015).
- [33] A. Peksa, P. Zitha, and K. Wolf, *Role of rock surface charge in the carbonated water flooding process*, in *75th EAGE Conference & Exhibition incorporating SPE EUROPEC 2013* (2013).
- [34] T. Ishido and H. Mizutani, *Experimental and theoretical basis of electrokinetic phenomena in rock-water systems and its applications to geophysics*, *Journal of Geophysical Research: Solid Earth* **86**, 1763 (1981).
- [35] L. Jouniaux and J. Pozzi, *Streaming potential and permeability of saturated sandstones under triaxial stress: Consequences for electrotelluric anomalies prior to earthquakes*, *Journal of Geophysical Research: Solid Earth* **100**, 10197 (1995).
- [36] B. Lorne, F. Perrier, and J. Avouac, *Streaming potential measurements: 1. Properties of the electrical double layer from crushed rock samples*, *Journal of Geophysical Research: Solid Earth* **104**, 17857 (1999).
- [37] B. Lorne, F. Perrier, and J. Avouac, *Streaming potential measurements: 2. Relationship between electrical and hydraulic flow patterns from rock samples during deformation*, *Journal of Geophysical Research: Solid Earth* **104**, 17879 (1999).
- [38] D. B. Pengra, S. Xi Li, and P. Wong, *Determination of rock properties by low-frequency AC electrokinetics*, *Journal of Geophysical Research: Solid Earth* **104**, 29485 (1999).
- [39] A. Revil, P. Pezard, and P. Glover, *Streaming potential in porous media, 1. Theory of the zeta potential*, *Journal of Geophysical Research: Solid Earth* **104**, 20,021 (1999).
- [40] A. Revil, H. Schwaeger, L. Cathles, and P. Manhardt, *Streaming potential in porous media: 2. Theory and application to geothermal systems*, *Journal of Geophysical Research: Solid Earth* **104**, 20033 (1999).
- [41] L. Jouniaux and J. P. Pozzi, *Streaming potential in volcanic rocks from Mount*, *Journal of Geophysical Research* **105**, 8391 (2000).

- [42] X. Guichet, L. Jouniaux, and J.-P. Pozzi, *Streaming potential of a sand column in partial saturation conditions*, Journal of Geophysical Research: Solid Earth **108** (2003).
- [43] X. Guichet and P. Zuddas, *Effect of secondary minerals on electrokinetic phenomena during water-rock interaction*, Geophysical Research Letters **30** (2003).
- [44] A. Maineult, Y. Bernabé, and P. Ackerer, *Detection of advected concentration and pH fronts from self-potential measurements*, Journal of Geophysical Research: Solid Earth **110** (2005).
- [45] M. Jaafar, J. Vinogradov, and M. Jackson, *Measurement of streaming potential coupling coefficient in sandstones saturated with high salinity NaCl brine*, Geophysical Research Letters **36** (2009).
- [46] J. Vinogradov, M. Jaafar, and M. Jackson, *Measurement of streaming potential coupling coefficient in sandstones saturated with natural and artificial brines at high salinity*, Journal of Geophysical Research: Solid Earth **115** (2010).
- [47] Z. Zhu and M. Nafi Toksöz, *Experimental measurements of the streaming potential and seismoelectric conversion in Berea sandstone*, Geophysical Prospecting **61**, 688 (2013).
- [48] J. R. Moore, S. D. Glaser, H. F. Morrison, and G. M. Hoversten, *The streaming potential of liquid carbon dioxide in Berea sandstone*, Geophysical Research Letters **31** (2004), 10.1029/2004GL020774, 117610.
- [49] J. Vinogradov and M. Jackson, *Multiphase streaming potential in sandstones saturated with gas/brine and oil/brine during drainage and imbibition*, Geophysical Research Letters **38** (2011).
- [50] J. H. Börner, *Electrical phenomena during CO<sub>2</sub>-rock interaction under reservoir conditions: experimental investigations and their implications for electromagnetic monitoring applications*, Journal article, TU Bergakademie Freiberg, Freiberg, Germany (2016).
- [51] J. Peeters, M. Mulder, and H. Strathmann, *Streaming potential measurements as a characterization method for nanofiltration membranes*, Colloids and Surfaces A: Physicochemical and Engineering Aspects **150**, 247 (1999).
- [52] S. Mondal and S. De, *Mass transfer of a neutral solute in porous microchannel under streaming potential*, Electrophoresis **35**, 681 (2014).
- [53] J. Lyklema, *Fundamentals of interface and colloid science: Solid-liquid interfaces* (Academic Press, 2001).
- [54] A. V. Delgado, *Interfacial electrokinetics and electrophoresis*, Vol. 106 (CRC Press, 2001).
- [55] P. W. J. Glover and N. Déry, *Streaming potential coupling coefficient of quartz glass bead packs: Dependence on grain diameter, pore size, and pore throat radius*, Geophysics **75**, F225 (2010).

- [56] E. M. Egorova, *The validity of the Smoluchowski equation in electrophoretic studies of lipid membranes*, *Electrophoresis* **15**, 1125 (1994).
- [57] S. R. Pride and F. Morgan, *Electrokinetic dissipation induced by seismic waves*, *Geophysics* **56**, 914 (1991).
- [58] M. Waxman and L. Smits, *Electrical conductivities in oil-bearing shaly sands*, *Society of Petroleum Engineers Journal* **8**, 107 (1968).
- [59] S. Pride, *Governing equations for the coupled electromagnetics and acoustics of porous media*, *Physical Review B* **50**, 15678 (1994).
- [60] A. Brovelli, G. Cassiani, E. Dalla, F. Bergamini, D. Pitea, and A. M. Binley, *Electrical properties of partially saturated sandstones: Novel computational approach with hydrogeophysical applications*, *Water Resources Research* **41**, n/a (2005).
- [61] A. Brovelli and G. Cassiani, *Combined estimation of effective electrical conductivity and permittivity for soil monitoring*, *Water Resources Research* **47** (2011).
- [62] A. Revil, L. Cathles, S. Losh, and J. Nunn, *Electrical conductivity in shaly sands with geophysical applications*, *Journal of Geophysical research* **103**, 925 (1998).
- [63] M. Alizadeh Nomeli, *Geochemical reaction modeling of carbon dioxide*, *Journal article*, University of Maryland, College Park, US (2014).
- [64] M. Rink and J. Schopper, *Interface conductivity and its implications to electric logging*, in *SPWLA 15th Annual Logging Symposium* (Society of Petrophysicists and Well-Log Analysts, 1974).
- [65] M. Sharma, L. Jang, and T. Yen, *Transient interfacial tension behavior of crude-oil/caustic interfaces*, *SPE Reservoir Engineering* **4**, 228 (1989).
- [66] A. Revil and P. Glover, *Theory of ionic-surface electrical conduction in porous media*, *Physical Review B* **55**, 1757 (1997).
- [67] A. Bussian, *Electrical conductance in a porous medium*, *Geophysics* **48**, 1258 (1983).
- [68] O. A. de Lima, M. B. Clennell, G. G. Nery, and S. Niwas, *A volumetric approach for the resistivity response of freshwater shaly sandstones*, *Geophysics* **70**, F1 (2005).
- [69] C. T. O’Konski, *Electric properties of macromolecules. V. Theory of ionic polarization in polyelectrolytes*, *The Journal of Physical Chemistry* **64**, 605 (1960).
- [70] F. Morgan, E. Williams, and T. Madden, *Streaming potential properties of westerly granite with applications*, *Journal of Geophysical Research: Solid Earth* **94**, 12449 (1989).
- [71] D. Luong and R. Sprik, *Examination of a theoretical model of streaming potential coupling coefficient*, *International Journal of Geophysics* **2014** (2014).



- [72] J. H. Börner, V. Herdegen, J.-U. Repke, and K. Spitzer, *The electrical conductivity of CO<sub>2</sub>-bearing pore waters at elevated pressure and temperature: a laboratory study and its implications in CO<sub>2</sub> storage monitoring and leakage detection*, *Geophysical Journal International* **203**, 1072 (2015).
- [73] P. Leroy and A. Revil, *A triple-layer model of the surface electrochemical properties of clay minerals*, *Journal of Colloid and Interface Science* **270**, 371 (2004).
- [74] A. Revil and P. Glover, *Nature of surface electrical conductivity in natural sands, sandstones, and clays*, *Geophysical Research Letters* **25**, 691 (1998).
- [75] A. W. Islam and E. S. Carlson, *Viscosity models and effects of dissolved CO<sub>2</sub>*, *Energy & Fuels* **26**, 5330 (2012).
- [76] T. Hanai, *Dielectric theory on the interfacial polarization for two-phase mixtures*, (1962).
- [77] H. Looyenga, *Dielectric constants of heterogeneous mixtures*, *Physica* **31**, 401 (1965).
- [78] J. Stoll, *Stoneley wave induced electrokinetic potentials in large sandstone blocks*, in *21st Kolloquium Elektromagnetische Tiefenforschung* (2005).
- [79] R. M. Cornell and U. Schwertmann, *The iron oxides: structure, properties, reactions, occurrences and uses* (John Wiley & Sons, 2003).
- [80] G. A. Parks, *The isoelectric points of solid oxides, solid hydroxides, and aqueous hydroxo complex systems*, *Chemical Reviews* **65**, 177 (1965).
- [81] S. Raghavan, *Wet Etching and Cleaning: Surface Considerations - plastics and polymers*. (1999), retrieved December 05, 2016, from <http://megaslides.com/doc/911094/wet-etching-and-cleaning-surface-considerations>.
- [82] B. Bunker, *Molecular mechanisms for corrosion of silica and silicate glasses*, *Journal of Non-Crystalline Solids* **179**, 300 (1994).
- [83] A. Grabbe, T. Michalske, and W. Smith, *Strained siloxane rings on the surface on silica: their reaction with organosiloxanes, organosilanes, and water*, *The Journal of Physical Chemistry* **99**, 4648 (1995).
- [84] B. Morrow and I. Cody, *Infrared studies of reactions on oxide surfaces. 5. Lewis acid sites on dehydroxylated silica*, *The Journal of Physical Chemistry* **80**, 1995 (1976).
- [85] T. Hiemstra, W. Van Riemsdijk, and G. Bolt, *Multisite proton adsorption modeling at the solid/solution interface of (hydr) oxides: A new approach: I. Model description and evaluation of intrinsic reaction constants*, *Journal of colloid and interface science* **133**, 91 (1989).
- [86] D. Broseta, N. Tonnet, and V. Shah, *Are rocks still water-wet in the presence of dense CO<sub>2</sub> or H<sub>2</sub>S?* *Geofluids* **12**, 280 (2012).

- [87] T. W. Kim, T. K. Tokunaga, D. B. Shuman, S. R. Sutton, M. Newville, and A. Lanzirotti, *Thickness measurements of nanoscale brine films on silica surfaces under geologic CO<sub>2</sub> sequestration conditions using synchrotron X-ray fluorescence*, *Water Resources Research* **48** (2012).
- [88] Y. Kim, J. Wan, T. J. Kneafsey, and T. K. Tokunaga, *Dewetting of silica surfaces upon reactions with supercritical CO<sub>2</sub> and brine: pore-scale studies in micromodels*, *Environmental science & technology* **46**, 4228 (2012).
- [89] M. Sarmadivaleh, A. Z. Al-Yaseri, and S. Iglauer, *Influence of temperature and pressure on quartz–water–CO<sub>2</sub> contact angle and CO<sub>2</sub>–water interfacial tension*, *Journal of colloid and interface science* **441**, 59 (2015).
- [90] J. Menendez, M. Illán-Gómez, C. L. y Leon, and L. Radovic, *On the difference between the isoelectric point and the point of zero charge of carbons*, *Carbon* **33**, 1655 (1995).



# 5

## FLUID–FLUID INTERACTIONS IN STAGNANT PORE GEOMETRIES

### CO<sub>2</sub> FLOODING IN REGIONS OF RELATIVELY STAGNANT FLOW

CO<sub>2</sub> flooding is one of the most widely used enhanced oil recovery (EOR) process in combination with geological CO<sub>2</sub> storage. Many laboratory and theoretical, as well as field studies, demonstrated that the process has a potential of incremental oil recovery and a safe, long-term CO<sub>2</sub> storage. However, its efficiency in the regions of low and stagnant flow is still underrepresented in the literature.

*In this study, three different CO<sub>2</sub> injection scenarios used after water flooding are evaluated and compared: (1) Scenario A - displacement with favorable density difference and unfavorable viscosity ratio; (2) Scenario B - displacement with unfavorable density difference and viscosity ratio; (3) Scenario C - displacement with favorable density difference and unfavorable viscosity ratio. To mimic the stagnant zone, a glass micromodel with a single dead-end pore placed vertically down was designed. With this geometry, the efficiency of the processes in relation to oil recovery and CO<sub>2</sub> storage for all three applied scenarios is studied. Additionally, the influence of the nature of the flow and the oil volume in the system geometry is investigated.*

*For the studied geometry, liquid injection is the most efficient due to a favorable density difference. The importance of flow rate, viscosity ratio and starting volume of the oil ganglia entrapped in the dead-end pores and water barriers, is evident in all scenarios. The applied flow rate determines if the flow regime is gravity or capillary dominated. The water layer, created after passing the CO<sub>2</sub> front, delays the mass transfer of CO<sub>2</sub> into oil. At pore scale, the water barrier is a limiting factor. At the field scale, ample time to rupture the barrier exists, such that the recovery time in the range of hours may not have a large impact on the overall recovery, but might be of importance in the near-well bore area.*

## NOMENCLATURE AND SUBSCRIPTS

$P$	Pressure, bar
$\mu_{CO_2}$	Viscosity of carbon dioxide, cP
$\mu_{decane}$	Viscosity of decane, cP
$\rho_{CO_2}$	Mass density of carbon dioxide, kg/m <sup>3</sup>
$\rho_{decane}$	Mass density of decane, kg/m <sup>3</sup>
$T$	Temperature, K
$t_0$	Time of water flooding switch to CO <sub>2</sub> flooding, s
$t_m$	Time of oil migration from the dead-end pore, s, min, h (indicated in the text)
$t_r$	Time of the full recovery, s, min, h (indicated in the text)
$t_{tz,1}$	Initial time of transition zone, s
$t_{tz,2}$	End time of transition zone, s
$t_v$	Time of maximum oil volume observed in the dead-end pore, s
$V_t$	Volume of the experimental tube, mm <sup>3</sup>

## ABBREVIATIONS

DCO	Molecular diffusion of CO <sub>2</sub> into oil
DEP	Dead-end pore
FPS	Frame per second
TZ	Transition zone

## 5.1. INTRODUCTION

Tertiary CO<sub>2</sub> injection is a technique within the oil industry, not only for increasing oil recovery, but also to facilitate CO<sub>2</sub> storage in oil reservoirs [1–6]. Oil displacement and CO<sub>2</sub> storage rely on the phase behavior of the pure components (the injected gas and hydrocarbons in place) and mixtures of both, and strongly depend on reservoir temperature, pressure, and hydrocarbon composition. The hydrocarbon accumulations are usually found at such depths, that pressure and temperature conditions establish the supercritical behavior of CO<sub>2</sub> (>7.4 MPa and 304 K) [7]. However, shallow reservoirs are also candidates for CO<sub>2</sub> injections, for example, when exceptionally low reservoir temperatures, e.g. permafrost, are present [8]. In these cases, temperatures are below the critical CO<sub>2</sub> temperature and, thus, provide an opportunity for liquid CO<sub>2</sub> injection and storage.

The displacement and storage processes are controlled by a complex matrix structure of the rock, including pore size and pore geometry [9]. Often, porous media contain low permeability zones, or even stagnant regions, with respect to a hydraulic flow that may alter transient fluid flow or diffusion behavior. In most cases, a conventional pressure-driven flow is not possible to attain. The stagnant regions usually are located in dead-end pores (defined as volume through which there is no flux during steady-state fluid flow or diffusion), and regions of closed streamlines [10–14]. As the oil displacement and CO<sub>2</sub> storage may be clearly influenced by stagnant regions, a detailed process evaluation is needed to improve our understanding.

The role of the stagnant zones during CO<sub>2</sub> injection was investigated by several researchers [15–19], showing the importance of molecular diffusion of CO<sub>2</sub> into oil and the role of the water barrier. Campbell et al. (1985) [15] demonstrated in their experiments, that CO<sub>2</sub> can reach trapped oil that is blocked in dead-end pores by water and that the phase behavior of CO<sub>2</sub>-crude oil mixtures gave rise to capillary forces that acted to remove oil from dead-end pores bounded by capillary grooves. Grogan and Pinczewski (1987) [16] first quantified the effect of molecular diffusion on tertiary CO<sub>2</sub> flooding and showed that the molecular diffusion of CO<sub>2</sub> through the water barrier is the main mechanism for establishing miscibility conditions between oil and gas at micro or pore scale. Bijeljic et al. (2002) [17] investigated the tertiary miscible gas displacement and modeled the behavior of multicomponent mass transfer through a water barrier. Sohrabi et al. (2007) [18] stated, that in a homogeneous porous medium bypassing of the oil occurs at pore level due to the presence of dead-end pores. In 2011, Kazemzadeh et al. [20] modeled the role of molecular diffusion in a mobilization of water flooded residual oil. The diffusion process through the separating water layer and its behavior were discussed elsewhere [16, 21–31].

Despite numerous theoretical, experimental and numerical studies on the CO<sub>2</sub> flood in the stagnant zones [15–20], a comparison of the efficiency of different injection strategies was not conducted and the interactions of CO<sub>2</sub>-water-oil in the stagnant zones in porous media is not completely understood. In particular, the influence of an applied flow rate and initial volumes of oil ganglia entrapped in the Dead-End Pore (DEP), combined with a pre-defined injection scheme, did not get much attention in theory and experiments.

A number of experiments were performed as tertiary injection methods to evaluate

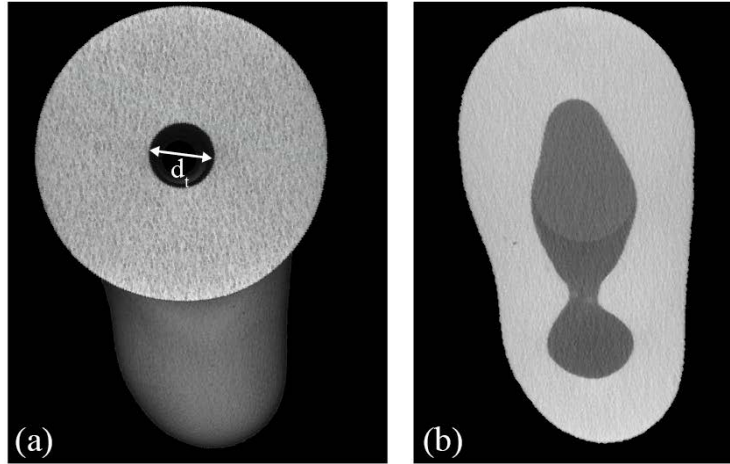


Figure 5.1: CT reconstruction (a) 3D view of the glass model; Tube volume,  $V_T=26.5 \text{ mm}^3$  (b) cross section through the middle of the glass model (voxel size:  $0.015 \times 0.015 \times 0.015 \text{ mm}$ ).

5

the effects on the mechanisms occurring in the stagnant zones. These methods involve liquid, near supercritical and supercritical  $\text{CO}_2$  injection for recovery of hydrocarbon that is entrapped in a microscopic heterogeneous dead-end pore volume. Tests were conducted in a single glass DEP. Injection methods were studied for both the varying flow rates and the starting volumes of oil ganglia entrapped in the DEP, to observe the impact of the viscosity ratio on the operational fluids, the density difference between fluids and the time of the flood on mechanisms occurring in the stagnant zones.

In essence, the main objective of this study is to investigate the viscosity and density differences during  $\text{CO}_2$  floods and their relations in the scope of the efficiency of  $\text{CO}_2$  flooding processes in the regions of the stagnant flow. Moreover, attention is directed toward two additional parameters: (1) the applied flow rates and, (2) initial volumes of oil ganglia entrapped in the dead-end pores after water flooding.

## 5.2. EXPERIMENTAL APPROACH

### 5.2.1. MATERIALS

Flooding experiments were done in a transparent glass model representing a single pore connected to a flow channel. The glass model was placed in the horizontal direction with the opening towards the monopore at the bottom (Figures 5.1 and 5.2). The glass model consists of pure silicon dioxide ( $\text{SiO}_2$ ), which can hold 150 bar gas pressure. During the experiments, the wettability of the glass wall against the other phases may change. This, however, is of no concern for this chapter. In the experiments, the operational wetting phase was water, the intermediate wetting phase was oil and the non-wetting phase was  $\text{CO}_2$ . *Water*: Water used in this study consists of degassed, demineralized water. *Oil*: As an oleic phase, decane doped with a solvent red dye was used. *Carbon dioxide*:  $\text{CO}_2$  of 99.95% purity (Linde Gas Benelux<sup>TM</sup>) was used in the tests as provided, without further

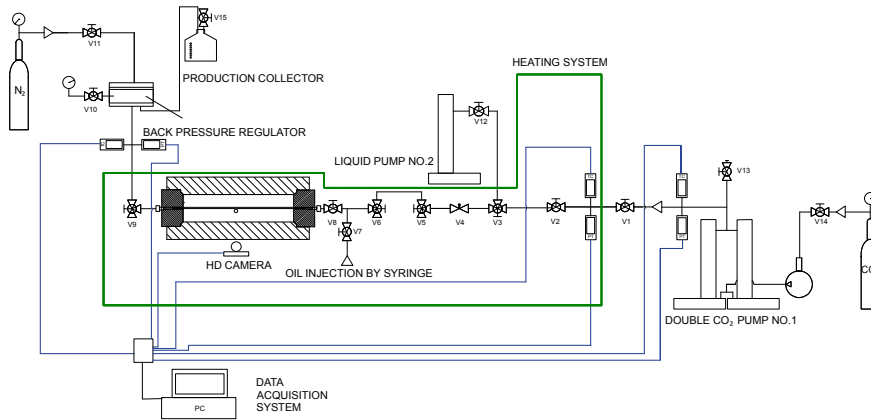


Figure 5.2: Schematic of the high-pressure experimental setup to study oil displacement by CO<sub>2</sub> flooding in the DEPs. The green line represents the oven in which the experimental setup was built. The black lines illustrate the tubing and the various flow lines. The blue lines are data cables connecting pressure transducers and thermocouples to a computer for acquisition and controlling.

treatment.

### 5.2.2. EXPERIMENTAL SETUP

To visualize the oil displacement in the DEP, an experimental setup was designed and built (Fig. 5.2). The setup is described in detail in [32]. The most important part of the setup is a glass tube with a DEP placed in a PEEK core holder. The tube withstands pressures up to 150 bar. To avoid corrosion, all other parts were made of stainless steel. The inlet of the glass tube was connected to a double cylinder ISCO pump, which is the source of the CO<sub>2</sub>. The CO<sub>2</sub> in the pump was preheated to the experimental conditions and the connection to the system was isolated in order to avoid changes of the phases. On one side, the cylinder was connected to the system, on the other side to the pump. The required temperatures of  $295\text{ K} \pm 0.1\text{ K}$  and  $309\text{ K} \pm 0.1\text{ K}$  were achieved by using an oven in which the cell was placed. A low flow back-pressure regulator maintained the pressure in the system. To control and monitor the pressure, two pressure transducers were placed in the upstream and one in the downstream of the flow. To control the temperature, a system of inline thermocouples was used. The CO<sub>2</sub> flooding process was monitored and recorded by an HD camera at 1 FPS. The measurements were repeated for each experimental volume to ensure satisfactory repeatability at each specified pressure, temperature, and flow rate.

### 5.2.3. EXPERIMENTAL PROCEDURE

*Preparations of the transparent glass model:* The system was thoroughly cleaned (i.e. de-greased and micro-sized dust). Thereafter the system was vacuumed. *Primary drainage:*



During primary drainage, the degassed intermediate wetting phase was injected from valve 7 with a flow rate of 0.25 ml/min, in order to fill the entire system with oil. At the same time, no air was allowed to enter the monopore. *Imbibition:* The system was water flooded till residual oil saturation was reached. For each experiment, the irreducible oil saturation varied. In each experiment, flooding was started with a flow rate of 0.5 ml/min, which gradually increased to rates up to 10 ml/min, combined with a variation of pressures. The resulting two phase system was pressurized to operational conditions. *CO<sub>2</sub> injection:* After imbibition flooding was switched to CO<sub>2</sub> with a flow rate depending on the experiment (0.1 -1 ml/min), using a double cylinder ISCO pump for fluid injection. The outlet was connected to the production collector. *Data and image acquisition:* Temperature, pressure and injection/production rates were acquired starting from the primary drainage phase. Image acquisition was also completed over the entire experimental time until the final result stopped to change visually.

#### 5.2.4. PHYSICAL AND CHEMICAL PROPERTIES

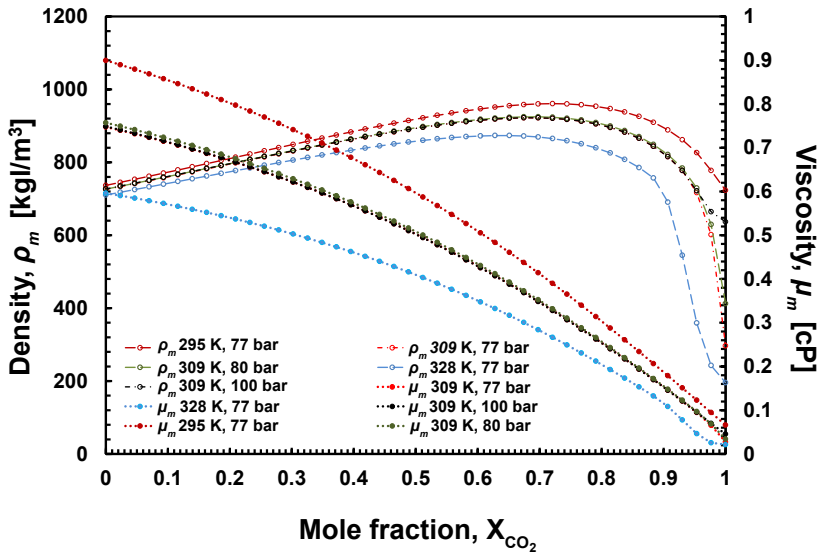
Three components are present in the system during the displacement test: oil, water, and CO<sub>2</sub>. During CO<sub>2</sub> flooding, CO<sub>2</sub> is transferred into the oil phase and, in particular cases, into the water phase that separates oil and CO<sub>2</sub>. The time scale of the mass transfer is directly related to the contact area between two phases: the larger the contact area, the faster mass can be transferred across the interface [33, 34]. As a result of the CO<sub>2</sub> transfer in the system, the density and viscosity of oil and water are altered, as presented in detail below.

The phase behavior of the CO<sub>2</sub>-decane system was investigated experimentally and theoretically in the literature [35–40]. However, not all of the temperature and pressure conditions that are used in this study are reported. The phase behavior of the CO<sub>2</sub>-decane system at the experimental temperatures was determined using the HYSR EOS. To obtain "solubility" factors, the HYSR EOS was tuned against the experimental data obtained by Reamer et al., 1963 [35]. The calculated liquid saturated properties (i.e. density and viscosity behavior patterns) of oil under the presence of CO<sub>2</sub> are modeled in Figure 5.3a. The figure shows that at CO<sub>2</sub> concentrations up to 0.8, the density rises, reaching a peak where the mixture starts to behave like pure CO<sub>2</sub>. In the concentration range >0.8, the density decreases with increasing CO<sub>2</sub> content. It is a consequence of the lower molecular weight of CO<sub>2</sub> compared to the molecular weight of decane. The densities of binary CO<sub>2</sub>-decane mixtures decrease with increasing temperature. A boundary is observed due to the different slopes depending on the CO<sub>2</sub> mole fractions.

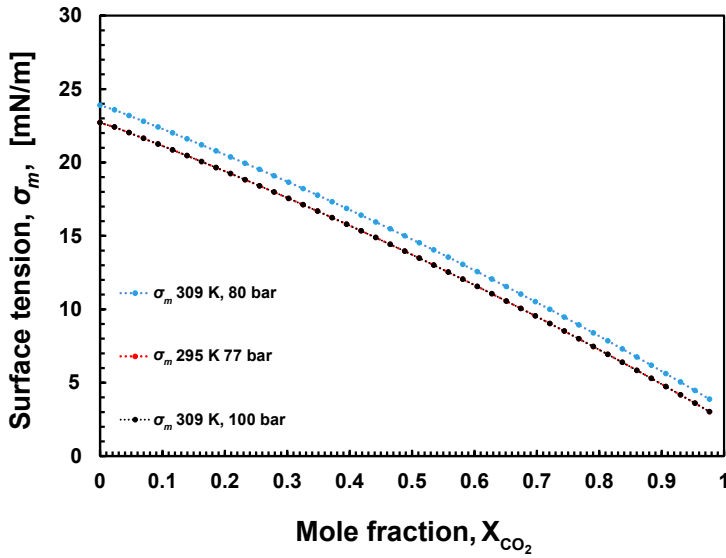
As presented in Fig. 5.3a, the saturated liquid viscosity diminishes as CO<sub>2</sub> concentration increases. The viscosities of binary CO<sub>2</sub>-decane mixtures decrease, as in the case of density, with increasing temperature. Fig. 5.3b shows the CO<sub>2</sub>-decane surface tension modeled at experimental conditions. Surface tension decreases with increasing CO<sub>2</sub> concentration.

### 5.3. RESULTS AND DISCUSSION

In this study, experiments were conducted to investigate the mechanisms that occur at the regions near the DEP and in the DEP volume, during different CO<sub>2</sub> injection sce-



(a)



(b)

Figure 5.3: (a) Density and viscosity of CO<sub>2</sub>-decane mixtures versus mole fraction of CO<sub>2</sub> at experimental pressures and temperatures; (b) Surface tension of CO<sub>2</sub>-decane mixtures versus mole fraction of CO<sub>2</sub> at experimental pressures and temperatures.

narios. Initially, oil was entrapped in the DEP, where, due to viscous and gravity forces, surface tension, and pressure conditions, the fluid flow is very low or/and almost non-existing. The influence of particular forces and the role of the applied volumetric flow rate was investigated. Note, that the discussed images represent a visual illustration of the physical mechanisms occurring in the DEP, rather than a quantitative determination of the improved oil recovery.

### 5.3.1. MECHANISMS IN THE STAGNANT ZONE DURING DIFFERENT CO<sub>2</sub> INJECTION SCHEMES

CO<sub>2</sub> was injected into the water flooded system to examine the mechanisms controlling oil recovery in the regions of the relatively stagnant zones for different CO<sub>2</sub> injection scenarios. The flow rate was kept constant over the investigated scenarios (1 ml/min). The characteristics of the three types of injection experiments and visual representations of the displacement process are shown in Figures 5.4- 5.6, as sequences of time-lapse photos consisting of six sequential stages occurring in a DEP. In this study, the volumetric flow rate and the oil volume were maintained constant. The experiments showed that in each scenario different mechanisms can be recognized. These mechanisms are directly related to the fluid viscosities and density ratios, and to the flooding period. In all cases, the viscosity ratio is greater than unity (the displacing phase is the less viscous material). Each scenario is evaluated in accordance with six of the following stages: water flooding (oil trapped in the DEP after water flooding), the transition zone (period of time when the concentration of the displacing fluid at the DEP increases from 0 to 100 percent), water blocking (the mass transfer across a water barrier by molecular diffusion, resulting in a volume increase and a reduction in the dynamic interfacial tension), rupture of water barrier (CO<sub>2</sub> diffuses into the oil leading to a swelling of the trapped oil droplets and an ultimate rupture of the water barrier), oil migration (oil is swept away from DEP by the gas), and full recovery.

#### SCENARIO A - DISPLACEMENT WITH FAVORABLE DENSITY DIFFERENCE AND UNFAVORABLE VISCOSITY RATIO (FIG. 5.4)

CO<sub>2</sub> was injected at the pressure below minimum miscibility pressure, thus, immiscible displacement occurs. The gravity forces dominate the flow in the transition zone displacing most of the oil ganglia from the DEP within 5 seconds. Despite the gravity as a major driving mechanism, the remaining oil is swept away due to a reduction in interfacial tension and viscosity, and volume expansion.

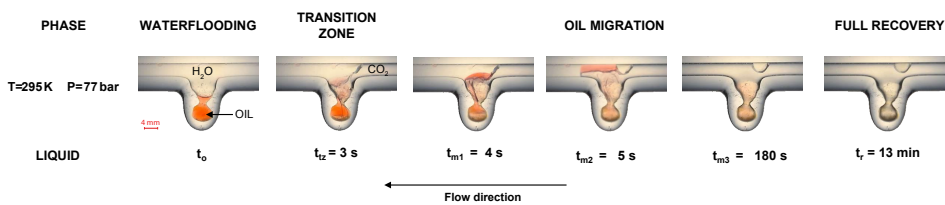


Figure 5.4: CO<sub>2</sub> displacement at liquid conditions at the DEP.

### SCENARIO B - DISPLACEMENT WITH UNFAVORABLE DENSITY DIFFERENCE AND VISCOSITY RATIO (FIG. 5.5)

Injection of near supercritical CO<sub>2</sub> results in gravity segregation between water and CO<sub>2</sub> in the transition zone. As the density difference between the two fluids is large, the effect of gravity becomes important [41, 42]. A water barrier is developed that separates the volumes of oil trapped within DEP from the stream of CO<sub>2</sub>. The injected CO<sub>2</sub> is not in direct contact with the oil and, therefore, recovery is delayed. During water blocking, the mass transfer of CO<sub>2</sub> into oil through water occurs, resulting in the swelling of both phases, water and oil. The observed mechanisms are supported by results reported in the literature [15–17] and are quantified by numerous researchers [16, 26, 28, 43]. As oil volume increases, the interface between oil and water moves up vertically. At the same time water is moved out of the stagnant zone into the flow channel, where it is gradually displaced by the CO<sub>2</sub> stream. After ~21 hours the water barrier is removed and direct contact between oil and the CO<sub>2</sub> stream is established. Due to mass transfer of CO<sub>2</sub> into oil, the density of oil-CO<sub>2</sub> increases, the viscosity of the mixture decreases significantly (Fig. 5.3a) and oil becomes mobile (Fig. 5.5). The process of oil recovery from the DEP after the rupture of the water barrier is rapid, efficient and takes place within 27 hours.

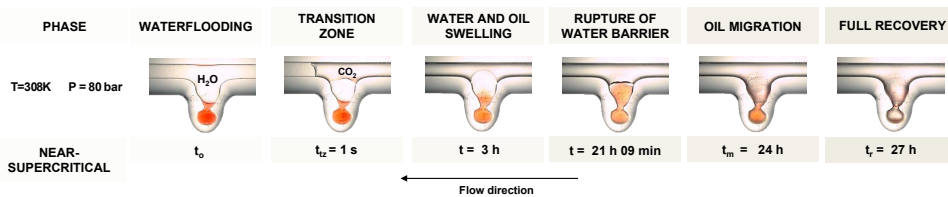


Figure 5.5: CO<sub>2</sub> displacement at near-supercritical conditions.

### SCENARIO C - DISPLACEMENT WITH FAVORABLE DENSITY DIFFERENCE AND UNFAVORABLE VISCOSITY RATIO (FIG. 5.6)

The injected CO<sub>2</sub> moves toward the CO<sub>2</sub>-oil interface, then in the transition zone penetrates the interface and diffuses into the oil. No water barrier is created due to the small density contrast. Molecular diffusion at the interface between two miscible fluids results in the change of oil and gas interfacial properties; the CO<sub>2</sub> concentration gradient near the interface decreases, reducing the interfacial tension between oil and CO<sub>2</sub> (Fig. 5.3b). The CO<sub>2</sub> mass transfer into the oil continues until the oil drop is completely saturated with CO<sub>2</sub> and the phases are miscible ( $t_n = 57 \text{ s}$ ). Subsequently, the volume of the CO<sub>2</sub>-oil mixture in the DEP is reduced by a migration out of the pore along the pore wall into the flow channel.

#### 5.3.2. FLOW RATE - FACTOR INFLUENCING MOLECULAR DIFFUSION IN DEP

To investigate the effect of the CO<sub>2</sub> flow rate on oil mobilization from the stagnant zone, a set of experiments was conducted at constant pressure, temperature and entrapped volume of the oil such that only flow rate could cause any changes in each of the scenarios.

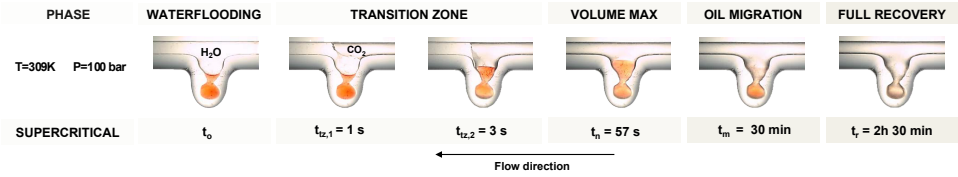


Figure 5.6: CO<sub>2</sub> displacement at supercritical conditions.

### SCENARIO A

The results shown in Figure 5.7 confirm that the process of CO<sub>2</sub> injection is dominated by strong gravitational forces for tested flow rates. At the flow rate of 0.1 ml/min (Scenario A2), the length of the mixing zone is larger than in Scenario A1 and the time is long enough for the gravity forces to cause fluid movement. In addition, due to the mentioned reasons, a slight oil volume increase is observed. At the higher flow rate (Scenario A1) the observed process is more dynamic, and the interface between the phases is unstable. In both scenarios, the recovery is very rapid and takes less than an hour.

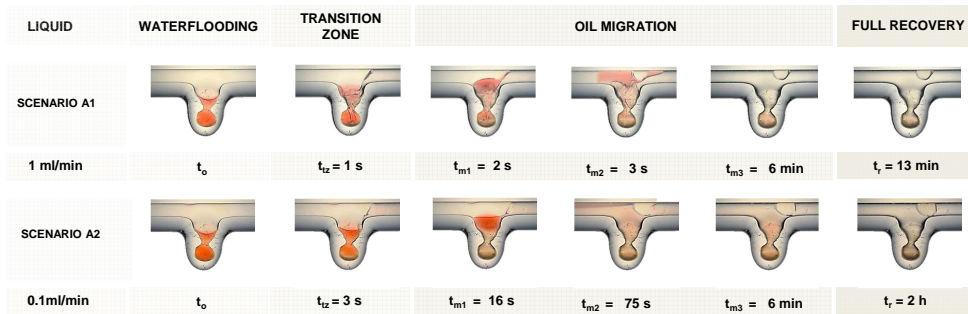


Figure 5.7: Flow rate magnitude influence on the injection process for Scenario A ( $T = 295 \text{ K}$ ,  $P = 77 \text{ bar}$ ). Scenario A1 represents injection of CO<sub>2</sub> with flow rate 1 ml/min, and Scenario A2 represents injection of CO<sub>2</sub> with flow rate 0.25 ml/min.

### SCENARIO B

The visualization presented in Figure 5.8 clearly shows the importance of the applied flow rate on the nature of the flow. The significant difference in the behavior can be seen between Scenario B1 and B2. Based on the literature [44–46] and on the observations, the injection Scenario B1 can be classified as flow occurring in the gravity dominated regime, and Scenario B2 as flow in the capillarity dominated regime. In Scenario B1 the high flow rate and the pronounced density difference in the order of 300 kg/m<sup>3</sup>, cause the gravity segregation effect between water and CO<sub>2</sub> in the stagnant zone. The entrapped oil in the pore is in contact with CO<sub>2</sub> via a water layer. The time required to remove the water barrier was almost 15 h. During this time, the CO<sub>2</sub> was not in direct contact with the oil, but the oil was subjected to the CO<sub>2</sub> mass transfer through the water barrier. This is supported by the fact that a volume increase of oil during the time interval between the

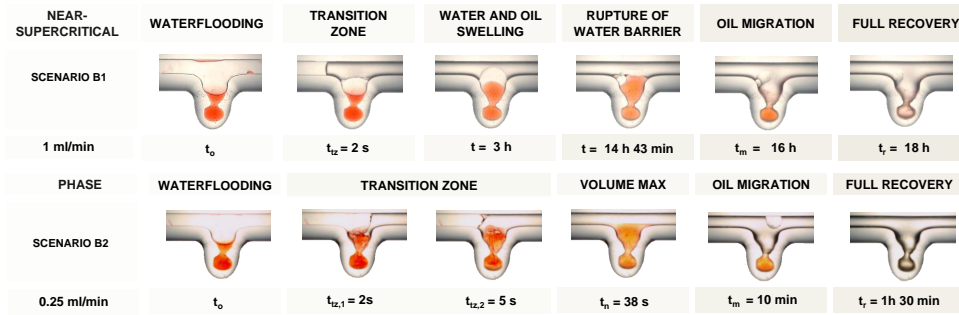


Figure 5.8: Flow rate magnitude influence on the injection process for Scenario B ( $T = 309 \text{ K}$ ,  $P = 80 \text{ bar}$ ). Scenario B1 represents injection of  $\text{CO}_2$  in the gravity dominated regime with flow rate 1 ml/min, and Scenario B2 represents injection of  $\text{CO}_2$  in the capillarity dominated regime with flow rate 0.25 ml/min.

transition zone and the rupture of water barrier was observed. In Scenario B2, where the applied flow rate is very low and where the area of the dead-end pore is near to stagnant, capillary forces are more dominant over gravity forces. In relation to that, direct contact between  $\text{CO}_2$  and oil is established as soon as the non-wetting phase reaches the DEP. This results in a very fast mass transfer of  $\text{CO}_2$  and rapid oil recovery (1.5 h). The images shown in Figure 5.8 indicate that the applied flow regime can strongly influence oil recovery. In the discussed cases, the time to recover oil in the gravity-dominated flow regime was 12 times longer than in the capillary dominated regime.

### SCENARIO C

In this scenario, supercritical  $\text{CO}_2$  injection for both applied flow rates (Scenario C1: 0.25 ml/min and Scenario C2: 1 ml/min) required the same time ( $\sim 150 \text{ min}$ ) to reach the final recovery. The effect of the injection rate was most pronounced in the transition zone and in the following stage, where oil swelled until its maximum observable volume. In order to compare scenarios with different injection rates the volumetric coefficient of the oil- $\text{CO}_2$  system was measured (Fig. 5.9). For that reason, the digital image of the particular scenario at  $t_0$  was used to define the physical domain  $V_o$  for the volumetric coefficient determination. The results exhibit a proportional relation between the length of the transition zone and the applied flow rate. At a flow rate of 0.25 ml/min, the transition zone interval is four times longer compared to the flow rate of 1 ml/min. It allows sufficient time for  $\text{CO}_2$  to gradually dissolve into the oil (9 s), leading to a larger swelling coefficient (1.47) at the last stage of the transition zone ( $t_{tz,2}$ ) when compared to 1 ml/min (1.30). In both scenarios, the mass transfer process continues after  $t_{tz,2}$  scenarios until the maximum swelling coefficient is reached ( $t_v = 37 \text{ s}$  for 0.25 ml/min and  $t_v = 57 \text{ s}$  for 1 ml/min) and oil is completely saturated with  $\text{CO}_2$ . After  $t_v$ , the oil is gradually removed from the DEP.

In order to evaluate the reason behind the much lower volume swelling coefficient at flow rate 1 ml/min, it is essential to identify the conditions that determine the flow in the high-pressure cell. For that reason, a simple laminar flow model was used and velocity profiles with respect to the applied flow rates were obtained. The modeled streamlines were overlaid on the experimental visualizations of the oil trapped in the DEP at the end

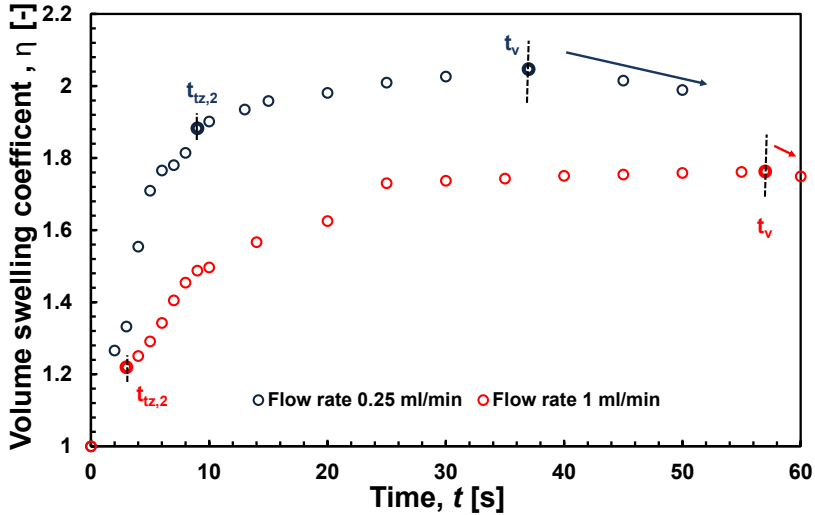


Figure 5.9: The measured volumetric coefficient of the oil-CO<sub>2</sub> system at two different flow rates at a pressure of 100 bar and temperature 308 K (0.25 ml/min for scenario C1 and 1 ml/min for scenario C2). The figure represents the behavior of the oil trapped in the DEP in the transition zone ( $t_{tz,1} - t_{tz,2}$ ), then a subsequent volume change until achieving maximum observed volume ( $t_{tz,2} - t_v$ ) and further the oil removal from the DEP ( $> t_v$ ).

of the transition zone (Fig. 5.10). Results indicate an influence of the flow rate magnitude on the displaced volumes. The difference in the CO<sub>2</sub> streamline positions for 0.25 and 1 ml/min is in line with the  $\sim 1.5$  times larger volume swelling coefficient observed at the end of the transition (Fig. 5.9).

### 5.3.3. EFFECT OF WATER BARRIER AND OIL VOLUME ENTRAPPED IN DEP

The amount of oil that was left in place after water flooding was chosen to differ significantly in order to study its influence on the recovery process. The pressure and temperature were kept constant. The operating flow rate is 1 ml/min in all tests. Moreover, to continue the previous study [32], a flow rate of 0.1 ml/min was tested.

#### SCENARIO A

In the previous study, the different oil volumes were evaluated at a single flow rate of 0.5 ml/min and at the same operational conditions as presented in the current study (77 bar and 295 K) [32]. The findings from the study were as follows: (1) the water barrier is created only when oil occupies less volume than the pore body and the narrow end of the pore throat; above this level, when oil occupies pore body and throat, no water barrier is created within the limit of the investigated flow rate of 0.5 ml/min; (2) comparing the time of the water rupture between the evaluated cases, where water initially occupies the pore throat and the case where water occupies the area just above the pore throat, gives a 2.6 times larger result for the first case. Figure 5.11 shows two different oil droplets geometries obtained after secondary recovery. In relation to the oil volume, a change

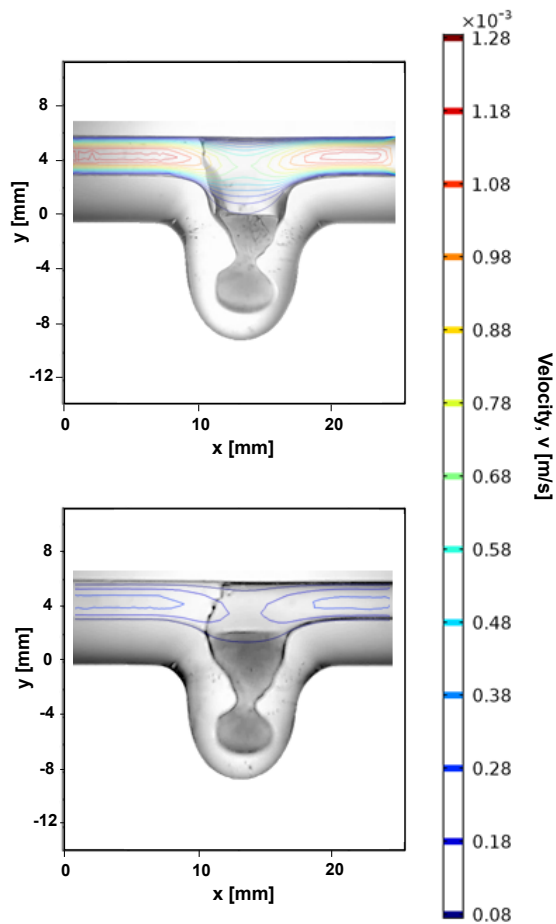


Figure 5.10: Representation of different behaviors of oil ganglia at various flow rates (top 1 ml/min, bottom 0.25 ml/min) at 100 bar and 308 K. The color bar represents the velocity in m/s and the  $x, y$  coordinates stand for the position of the glass tube in mm.




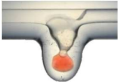





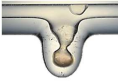
LIQUID	WATERFLOODING	TRANSITION ZONE	OIL MIGRATION	FULL RECOVERY
SCENARIO A3				
1 ml/min	$t_o$	$t_{tz} = 3 \text{ s}$	$t_{m1} = 50 \text{ min}$	$t_r = 1 \text{ h } 2 \text{ min}$
SCENARIO A1				
1 ml/min	$t_o$	$t_{tz} = 3 \text{ s}$	$t_{m1} = 13 \text{ s}$	$t_r = 1 \text{ h}$

Figure 5.11: Influence of the volume of oil entrapped in the DEP on the injection process in the Scenario A ( $T = 295 \text{ K}$ ,  $P = 77 \text{ bar}$ ) for the flow of 1 ml/min. Scenario A1 represents injection of  $\text{CO}_2$  in the system where oil droplet occupies the pore body and the pore throat, and Scenario A3 represents the system where oil droplet occupies only the pore body.

5



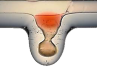

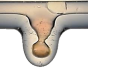







LIQUID	WATERFLOODING	TRANSITION ZONE	OIL MIGRATION			FULL RECOVERY
SCENARIO A2						
0.1 ml/min	$t_o$	$t_{tz} = 3 \text{ s}$	$t_{m1} = 16 \text{ s}$	$t_{m2} = 75 \text{ s}$	$t_{m3} = 6 \text{ min}$	$t_r = 2 \text{ h}$
SCENARIO A4						
0.1 ml/min	$t_o$	$t_{tz} = 3 \text{ s}$	$t_{m1} = 11 \text{ s}$	$t_{m2} = 13 \text{ s}$	$t_{m3} = 6 \text{ min}$	$t_r = 1 \text{ h}$

Figure 5.12: Influence of the volume of oil entrapped in the DEP on the injection process in the Scenario A ( $T = 295 \text{ K}$ ,  $P = 77 \text{ bar}$ ) for the flow of 0.1 ml/min. Scenario A2 represents injection of  $\text{CO}_2$  in the system where oil droplet occupies the pore body and the pore throat, and Scenario A4 represents the system where oil droplet occupies only the pore body.

in the phase behavior was observed. In Scenario A3, after passing the  $\text{CO}_2$  front, the oil droplet remains isolated from the flow channel by a water barrier. After the water barrier is removed, the gravity comes into play and immediately recovers oil from the pore.

Fig. 5.11 indicates the existence of a flow regime for a given geometry, where the gravity was not a main recovery factor. In order to determine if the volume of initially trapped oil in the DEP is the only factor determining the water barrier creation, an additional test at a flow rate of 0.1 ml/min was conducted. Data provided in Fig. 5.12 show that for low flow regimes, no water barrier is created and the gravity is the main oil recovery mechanism.

### SCENARIO B

Figure 5.13 shows two scenarios, B1 and B3, with different initial volumes of oil. In Scenario B1, oil occupies the entire pore body and larger volume of the pore throat than in Scenario B3. In both cases, the water was displaced by  $\text{CO}_2$  in the transition zone leaving behind a layer of water that separates oil from the  $\text{CO}_2$  source. The mass transfer

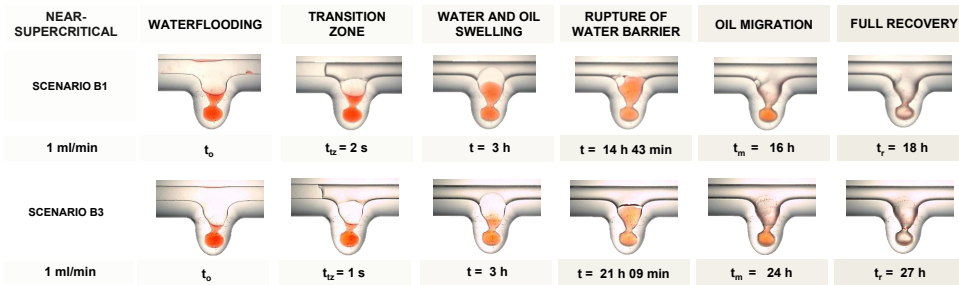


Figure 5.13: Representation of different behaviors of various volumes of oil ganglia and water barriers (80 bar, 309 K, 1 ml/min).

of  $\text{CO}_2$  into water and, subsequently, into oil resulted in a significant increase of the oil volume and, to a smaller extent, of the water volume. When the oil volume increased, a corresponding movement of the water in the direction of the flow channel was observed. The resulting water rupture was much faster in the Scenario B1 (6 h 26 min earlier than in Scenario B3). This can be explained by the larger initial volume of oil entrapped after water flooding in Scenario B1. As the entire pore body and throat was filled with the decane- $\text{CO}_2$  mixture, the transfer of the water barrier into the flow channel took less time. The observed water barrier removal by the expansion of oil due to diffusion of  $\text{CO}_2$  corresponds to the findings of the theoretical study of Zhang et.al on the role of the water barrier [31]. After the water barrier was removed, production of decane continued due to pure  $\text{CO}_2$  injection. As the water barrier was thinner in Scenario B1 and the interface between water and oil larger (allocated higher in the pore throat), more  $\text{CO}_2$  was transferred into the oil phase resulting in a larger decrease in viscosity and a faster recovery after the rupture of the water barrier (Scenario B1: 3 h 17 min, Scenario B3: ~6 h). The starting oil volume influences the efficiency of the process. Not only the existence of a water barrier is important, but, as visualized, specifically the position of the water barrier in the DEP is of importance.

### SCENARIO C

Figure 5.14 represents the injection of supercritical  $\text{CO}_2$  into the system where different oil volumes are left behind after water flooding. In the Scenario C3, where oil was placed only in the pore body, water occupied the remaining pore body and the narrowest volume of the pore throat after passing the transition zone. The volume of water, partly trapped in the body of the DEP, resulted in a long time period to achieve the direct contact of the source  $\text{CO}_2$  and oil (20 h 30 min from the start of the injection to the water rupture). The minimized interfacial area leads to a reduction in mass transfer and to an increase in surface tension and, consequently, to a delayed recovery. As mentioned by Aguilera et al. (2002), changes in the surface area can lead to a quantitative alteration of the mass transfer [47]. Moreover, as long as oil is disconnected from the direct source of  $\text{CO}_2$ , even if  $\text{CO}_2$  can diffuse easily through the water barrier, the miscibility would never be achieved [23].

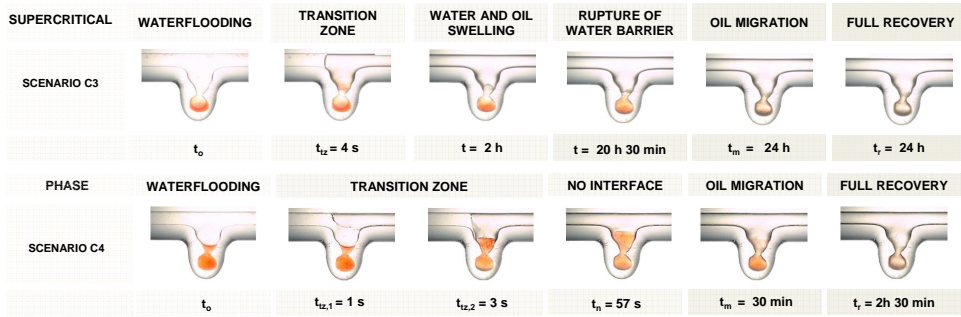


Figure 5.14: Influence of the volume of oil entrapped in the DEP on the injection process in Scenario A ( $T = 309 \text{ K}$ ,  $P = 100 \text{ bar}$ ) for the flow of  $1 \text{ ml/min}$ . Scenario C4 represents injection of  $\text{CO}_2$  in the system where the oil droplet occupies the pore body and the pore throat, and Scenario C3 represents the system where the oil droplet occupies only the pore body.

## 5

### 5.3.4. DISCUSSION ON EFFICIENCY OF DIFFERENT SCENARIOS USED FOR EOR

Three different injection scenarios using  $\text{CO}_2$  after water flooding were investigated: (1) Scenario A - displacement with favorable density difference and unfavorable viscosity ratio; (2) Scenario B - displacement with unfavorable density difference and viscosity ratio; (3) Scenario C - displacement with favorable density difference and unfavorable viscosity ratio. For the reservoir pressure and temperature ( $P$ - $T$ ) conditions use of Scenario C for oil recovery and geological storage, where  $\text{CO}_2$  behaves as a supercritical fluid, is the most common. As seen in Scenario C, the density difference is relatively low, and the viscosity exhibits a gas behavior. With the lack of the water barrier, the recovery from a stagnant zone occurs within 2-3 hours.

The second most occurring conditions are represented by Scenario B. The complete miscibility may not be achieved when the pressure is too low in the reservoir, however as visible in the conducted test,  $\text{CO}_2$  is transferred into oil resulting in a volume increase, a change in the surface tension and a decrease in the viscosity. The main difference with Scenario C is the unfavorable density contrast, resulting in the creation of the water barrier in most of the scenarios (despite the very low flow rates when the gravity dominated flow is overtaken by the capillarity dominated flow), slowing down the  $\text{CO}_2$  mass transfer into oil. It suggests as well, that the injected fluid may bypass more dense reservoir fluids due to low density and viscosity and may not be stored in the dissolved form [48].

The most efficient in relation to the majority of the investigated parameters was liquid  $\text{CO}_2$  injection. As a result of the immiscible displacement with favorable density difference ( $\text{CO}_2$  heavier than oil in the transition zone), the recovery was very rapid (within minutes). It can be concluded that due to density, the volume of stored  $\text{CO}_2$  would be larger than in the case of Scenarios B and C. However, liquid  $\text{CO}_2$  injection is not very common as reservoirs are mainly above the critical  $\text{CO}_2$  temperature and pressure, and thus this injection scheme represents unfavorable economics [49].

## 5.4. CONCLUSIONS

In this work, different CO<sub>2</sub> injection scenarios taking place in the stagnant zone were presented. The obtained results show the importance of the flow rate, the viscosity ratio, water barriers and the starting volume of oil ganglia entrapped in the dead-end pore. On the basis of the experimental observation the following conclusions are drawn:

- The efficiency of the oil recovery from the stagnant zones strongly depends on the applied injection scenario. Liquid CO<sub>2</sub> injection might benefit from favorable density ratio compared to supercritical and near-supercritical CO<sub>2</sub> injection. Moreover, higher density of CO<sub>2</sub> helps to minimize the risk of leakage;
- In the displacement experiments oil recovery was achieved due to gravity forces (liquid CO<sub>2</sub> injection), and due to CO<sub>2</sub> diffusion from an injected CO<sub>2</sub> stream into oil (supercritical and near-supercritical CO<sub>2</sub> injection);
- The results developed over the range of flow rates clearly showed the importance of gravity in the DEP systems when the density difference is in the order of 300 kg/m<sup>3</sup>;
- The effect of CO<sub>2</sub> diffusion into oil was observed in all experiments. The diffusion rate of CO<sub>2</sub> into oil and the subsequent oil swelling change with the phase of the injected CO<sub>2</sub> (from small to large extent: Scenario A to Scenario B/C);
- The main factors controlling the transition zone and the time of oil recovery are the viscosity and density differences in between the fluids;
- The removal of oil from the dead-end pore and the time required are strongly affected by the position, volume and geometry of the water barrier located above the oil;
- The time to recover oil at pore scale in the presence of a water barrier takes about 9-10 (Scenario C) and up to 18 (Scenario B) times longer when compared to a direct contact of oil with the CO<sub>2</sub> stream. However, at the field scale, this might not be a limiting factor. Taking into account migration time of operational fluids from the injector to the producer, the transport speed is within orders of magnitudes and the effect of the type of CO<sub>2</sub> source probably does play a lesser role. Although, the role of the water barrier might be of importance for the near well injection area.

## REFERENCES

- [1] Q. M. Malik and M. Islam, *CO<sub>2</sub> Injection in the Weyburn field of Canada: optimization of enhanced oil recovery and greenhouse gas storage with horizontal wells*, in *SPE/DOE improved oil recovery symposium* (Society of Petroleum Engineers, 2000).
- [2] E. Tüzünoğlu and S. Bağcı, *Scaled 3-D model studies of immiscible CO<sub>2</sub> flooding using horizontal wells*, *Journal of Petroleum Science and Engineering* **26**, 67 (2000).
- [3] A. R. Kovscek, *Screening criteria for CO<sub>2</sub> storage in oil reservoirs*, *Petroleum Science and Technology* **20**, 841 (2002).
- [4] F. Gozalpour, S. Ren, and B. Tohidi, *CO<sub>2</sub> EOR and storage in oil reservoir*, *Oil & gas science and technology* **60**, 537 (2005).
- [5] K. Jessen, A. R. Kovscek, and F. M. Orr, *Increasing CO<sub>2</sub> storage in oil recovery*, *Energy Conversion and Management* **46**, 293 (2005).
- [6] M. L. Godec, V. A. Kuuskraa, and P. Dipietro, *Opportunities for using anthropogenic CO<sub>2</sub> for enhanced oil recovery and CO<sub>2</sub> storage*, *Energy & Fuels* **27**, 4183 (2013).
- [7] P. M. Jarrell, *Practical aspects of CO<sub>2</sub> flooding* (Richardson, Tex.: Henry L. Doherty Memorial Fund of AIME, Society of Petroleum Engineers, 2002).
- [8] A. Y. Dandekar, *Petroleum reservoir rock and fluid properties* (CRC press, 2013).
- [9] F. Dullien and H. Brenner, *Porous Media: Fluid Transport and Pore Structure* (Elsevier Science, 2012).
- [10] R. C. Goodknight, W. A. Klikoff, and I. Fatt, *Non-steady-state fluid flow and diffusion in porous media containing dead-end pore. Volume 1*, *The Journal of Physical Chemistry* **64**, 1162 (1960).
- [11] K. H. Coats and B. D. Smith, *Dead-end pore volume and dispersion in porous media*, (1964), 10.2118/647-pa.
- [12] D. L. Koch and J. F. Brady, *Nonlocal dispersion in porous media: Nonmechanical effects*, *Chemical Engineering Science* **42**, 1377 (1987).
- [13] J. S. Andrade, M. P. Almeida, J. Mendes Filho, S. Havlin, B. Suki, and H. E. Stanley, *Fluid Flow through Porous Media: The Role of Stagnant Zones*, *Physical review letters* **79**, 3901 (1997).
- [14] D. Kandhai, D. Hlushkou, A. G. Hoekstra, P. M. Slood, H. Van As, and U. Tallarek, *Influence of stagnant zones on transient and asymptotic dispersion in macroscopically homogeneous porous media*, *Physical review letters* **88**, 234501 (2002).
- [15] B. T. Campbell and F. M. Orr Jr, *Flow visualization for CO<sub>2</sub>/crude-oil displacements*, *Society of Petroleum Engineers Journal* **25**, 665 (1985).
- [16] A. T. Grogan and W. V. Pinczewski, *The role of molecular diffusion processes in tertiary CO<sub>2</sub> flooding*, (1987), 10.2118/12706-pa.

- [17] B. R. Bijeljic, A. Muggeridge, and M. J. Blunt, *Effect of composition on waterblocking for multicomponent gasfloods*, in *SPE Annual Technical Conference and Exhibition* (Society of Petroleum Engineers, 2002).
- [18] M. Sohrabi, A. Danesh, D. H. Tehrani, and M. Jamiolahmady, *Microscopic mechanisms of oil recovery by near-miscible gas injection*, *Transport in Porous Media* **72**, 351 (2007).
- [19] M. Sohrabi, M. Riazi, M. Jamiolahmady, S. Ireland, and C. Brown, *Mechanisms of oil recovery by carbonated water injection*, in *SCA annual meeting* (2009).
- [20] E. Kazemzadeh, H. Alok Bakhtiari, M. Khodabakhshi, and M. R. Esfahani, *A fast and simple method for modeling of oil swelling in CO<sub>2</sub> injection*, *Geopersia* **1**, 39 (2011).
- [21] G. H. Thomas, G. R. Countryman, and I. Fatt, *Miscible displacement in a multiphase system*, *Society of Petroleum Engineers Journal* **3**, 189 (1963).
- [22] F. I. Stalkup, *Miscible displacement*, (1983).
- [23] J. W. Gardner and J. G. J. Ypma, *An Investigation of Phase Behavior-Macroscopic Bypassing Interaction in CO<sub>2</sub> Flooding*, *Society of Petroleum Engineers Journal* (1984), 10.2118/10686-PA.
- [24] L. Holm, *Mobilization of waterflood residual oil by miscible fluids*, *SPE Reservoir Engineering* **1**, 354 (1986).
- [25] E. C. Lin and E. T. Huang, *The effect of rock wettability on water blocking during miscible displacement*, *SPE Reservoir Engineering* **5**, 205 (1990).
- [26] T. Muller and L. W. Lake, *Theoretical study of water blocking in miscible flooding*, *SPE Reservoir Engineering* **6**, 445 (1991).
- [27] D. Tiffin, H. Sebastian, and D. Bergman, *Displacement mechanism and water shielding phenomena for a rich-gas/crude-oil system*, *SPE Reservoir Engineering* **6**, 193 (1991).
- [28] H. D. Do and W. V. Pinczewski, *Diffusion-controlled swelling of reservoir oil by indirect contact with injection gas*, *Chemical Engineering Science* **48**, 3243 (1993).
- [29] P. Wylie and K. K. Mohanty, *Effect of water saturation on oil recovery by near-miscible gas injection*, *SPE Reservoir Engineering* **12**, 264 (1997).
- [30] M. Sohrabi, M. Riazi, M. Jamiolahmady, S. Ireland, and C. Brown, *Carbonated water injection for oil recovery and CO<sub>2</sub> storage*, in *Sustainable energy UK conference: meeting the science and engineering challenge*, Oxford, UK (2008).
- [31] Y. Zhang, H. K. Sarma, et al., *Modelling of Possible Impact of Reservoir Brine Salinity During CO Injection*, in *SPE Enhanced Oil Recovery Conference* (Society of Petroleum Engineers, 2013).

- [32] A. E. Peksa, P. L. J. Zitha, and K.-H. A. A. Wolf, *Molecular Diffusion of CO<sub>2</sub> From Carbonated Water (CW) Into the Oil - Experimental Observations*, Report (2013).
- [33] J. Wesselingh and R. Krishna, *Mass transfer* (Ellis Horwood Chichester, 1990).
- [34] J. O. Helland and S. M. Skjaeveland, *Physically based capillary pressure correlation for mixed-wet reservoirs from a bundle-of-tubes model*, SPE Journal **11**, 171 (2006).
- [35] H. Reamer and B. Sage, *Phase Equilibria in Hydrocarbon Systems. Volumetric and Phase Behavior of the n-Decane-CO<sub>2</sub> System*, Journal of Chemical and Engineering Data **8**, 508 (1963).
- [36] F. M. Orr Jr and M. K. Silva, *Equilibrium Phase Compositions of CO<sub>2</sub>/Hydrocarbon Mixtures Part 1: Measurement by a Continuous Multiple-Contact Experiment*, Society of Petroleum Engineers Journal **23**, 272 (1983).
- [37] M. N. Okafor, *Phase equilibria from PVT measurements for carbon dioxide, water, and n-decane*, Report (Missouri Univ., Rolla (USA), 1987).
- [38] G. F. Chou, R. R. Forbert, and J. M. Prausnitz, *High-pressure vapor-liquid equilibria for carbon dioxide/n-decane, carbon dioxide/tetralin, and carbon dioxide/n-decane/tetralin at 71.1 and 104.4 °C*, Journal of Chemical and Engineering Data **35**, 26 (1990).
- [39] R. Shaver, R. Robinson, and K. Gasem, *An automated apparatus for equilibrium phase compositions, densities, and interfacial tensions: data for carbon dioxide + decane*, Fluid Phase Equilibria **179**, 43 (2001).
- [40] E. Forte, *Measurement and prediction of the phase behaviour of carbon dioxide, alkane and water mixtures at reservoir conditions* (Imperial College London, 2011).
- [41] W. Rossen and C. Van Duijn, *Gravity segregation in steady-state horizontal flow in homogeneous reservoirs*, Journal of Petroleum Science and Engineering **43**, 99 (2004).
- [42] A. Kopp, H. Class, and R. Helmig, *Investigations on CO<sub>2</sub> storage capacity in saline aquifers—Part 2: Estimation of storage capacity coefficients*, International Journal of Greenhouse Gas Control **3**, 277 (2009).
- [43] R. Shearn and R. Wakeman, *Theoretical mass transfer models for assessing tertiary recovery by miscible fluid displacement*, in *Proc., European Symposium on Enhanced Oil Recovery, Edinburgh* (1978) pp. 253–69.
- [44] D. Zhou, F. Fayers, and F. Orr Jr, *Scaling of multiphase flow in simple heterogeneous porous media*, SPE Reservoir Engineering **12**, 173 (1997).
- [45] S. Jonoud and M. D. Jackson, *New criteria for the validity of steady-state upscaling*, Transport in Porous Media **71**, 53 (2008).

- [46] C.-W. Kuo and S. M. Benson, *Analytical study of effects of flow rate, capillarity, and gravity on CO<sub>2</sub>/brine multiphase-flow system in horizontal corefloods*, SPE Journal **18**, 708 (2013).
- [47] R. Aguilera, *Incorporating capillary pressure, pore throat aperture radii, height above free-water table, and Winland r<sub>35</sub> values on Pickett plots*, AAPG bulletin **86**, 605 (2002).
- [48] C. M. Oldenburg, *Migration mechanisms and potential impacts of CO<sub>2</sub> leakage and seepage*, Carbon Capture and Sequestration Integrating Technology, Monitoring, and Regulation , 127 (2007).
- [49] M. Sohrabi, M. Jamiolahmady, A. Al Quraini, *et al.*, *Heavy Oil Recovery by Liquid CO<sub>2</sub>/Water Injection*, in *EUROPEC/EAGE Conference and Exhibition* (Society of Petroleum Engineers, 2007).



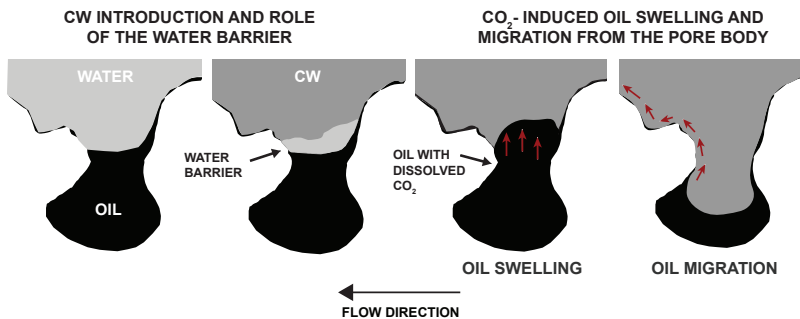


# 6

## INFLUENCE OF FLUID–FLUID INTERACTIONS ON DIFFUSION

### CWF IN THE REGIONS OF DEAD-END PORE VOLUME

Carbonated Water Flooding (CWF), an enhanced oil recovery method in which an oil reservoir is flooded with  $\text{CO}_2$ -enriched water, is a promising method for recovering residual oil and for limiting  $\text{CO}_2$  concentration in the atmosphere. One of the important aspects of the CWF process is molecular Diffusion of  $\text{CO}_2$  from Carbonated Water into Oil (DCWO). The process benefits from oil viscosity reduction, an increase in oil relative permeability and, as a result, enhancement of oil mobility. In contrast to many previous studies on the diffusion of carbon dioxide directly into oil by  $\text{CO}_2$  flooding, DCWO was a subject to much less modeling and experimental studies. To investigate the phase behavior of the system, indirect pore-scale diffusion experiments were conducted. Oil was initially placed in a dead-end pore and covered with water presumed to be from the first secondary recovery phase. Swelling of oil due to  $\text{CO}_2$  diffusion under  $P$ - $T$  conditions was visualized and recorded over time. A model was developed using Comsol Multiphysics<sup>TM</sup> software for the processes observed in the experiments. Model predictions were matched to the experiment to determine the diffusion coefficient. Pore geometry appears to be a limiting factor.



## NOMENCLATURE AND SUBSCRIPTS

$C_{ph}$	Molar concentration of CO <sub>2</sub> in one of the phases, mol/(kg·m <sup>3</sup> )
$C_{ph,eq}$	Molar concentration of CO <sub>2</sub> in one of the phases, mol/(kg·m <sup>3</sup> )
$D_{ph}$	Molecular diffusion coefficient of CO <sub>2</sub> in one of the phases, m <sup>2</sup> /s
$d_t$	Tube diameter, mm
$M_{CO_2}$	Molar mass of CO <sub>2</sub> , kg/mol
$P$	Pressure, bar
$Kp_{w/o}$	Distribution coefficient, [-]
$\rho_m$	Mass density, kg/m <sup>3</sup>
$R$	Gas constant, J/(K·mol)
$T$	Temperature, K
$t$	Time, h
$t_{MV}$	Time when the maximum volume change was achieved, s
$\mu_m$	Viscosity of the CO <sub>2</sub> -decane mixture, cP
$\mu_{ph}^0$	Standard chemical potential, G
$w_{ph}$	Mass fraction of CO <sub>2</sub> in the phase, [-]
$v_{ph}$	Partial specific volume of the phase, m <sup>3</sup> /kg
$V_{do}$	Voltage, V
$V_t$	Tube volume, mm <sup>3</sup>
$x_{CO_2}$	Mole fraction CO <sub>2</sub> , [-]
$y_{H_2O}$	Mole fraction H <sub>2</sub> O, [-]

## ABBREVIATIONS

ave	Average
CW	Carbonated water
CWF	Carbonated water flooding
DCWO	Molecular diffusion of CO <sub>2</sub> from carbonated water into oil
DEP	dead-end pore
EOR	Enhanced oil recovery
H	Hydrate
IFT	Interfacial tension
$L_{aq}$	CO <sub>2</sub> bearing water-rich liquid phase
$l_b$	Imaginary pore bottom line
$L_{CO_2}$	CO <sub>2</sub> -rich liquid phase
$l_t$	Imaginary pore top line
LCEP	Lower critical end point
MMP	Minimum miscibility pressure
o	Oil phase
PH	Phase
PV	Pore volume
V	CO <sub>2</sub> rich vapor phase
w	Water phase

## 6.1. INTRODUCTION

Carbonated Water Flooding (CWF) is a tertiary oil recovery technique combined with CO<sub>2</sub> utilization by CO<sub>2</sub>-rich water injection. CWF demonstrates satisfactory sweep efficiencies due to the comparable viscosities of Carbonated Water (CW) and oil. These similar viscosities together with a gradual breakthrough of CO<sub>2</sub> reduce the problem of high viscosity contrasts between CO<sub>2</sub> and residual oil [1–5]. Moreover, it minimizes the negative effect of water-shielded oil and high water saturation through a direct mixing with the residual water [6].

CWF comprises similar physical phenomena as the conventional CO<sub>2</sub> injection but requires less CO<sub>2</sub>. For CO<sub>2</sub> flooding at pore level, especially in nanochannels and Dead-End Pores (DEP), fluid flow is very low or non-existing. DEPs commonly found in geological systems in nature, create a trap for residual oil. As presented in Chapter 5, achieving fluid flow with CO<sub>2</sub> in the DEPs, through only conventional pressure-driven mechanisms, is not always possible. Thus, the Diffusion of CO<sub>2</sub> into the Oil (DCO) is the main mixing and rate controlling mechanism of oil recovery. Many studies on the diffusion of carbon dioxide during CO<sub>2</sub> flooding in DEP volumes were conducted by [7–11]. DCO occurs due to a much higher solubility of carbon dioxide in oil than in water [12]. Consequently, due to CO<sub>2</sub> solubility, a reduction in the interfacial tension and viscosity and a further increase in oil mobility is expected. The DCO process is time and phase composition dependent [9]. At specific reservoir *P-T* conditions, CO<sub>2</sub> primarily dissolves in water and is directly transferred to the oil, without creating a separate gas phase. It was proven that CO<sub>2</sub> easily dissolves in oil through molecular diffusion; however, when water is shielding the oil in the pore, the latter acts as a buffer and reduces the rate of diffusion [10, 13–15]. The existence of a water barrier and the time required for its removal (rupture time) was investigated in Chapter 5 and defined as the limiting factor for recovery of hydrocarbons.

Investigation of carbonate water injection in water wet reservoirs has been a research subject since the 1940s. Over the years, numerous theoretical studies [2, 5, 16–20] with scaled laboratory experiments [5, 20–26] and field trials [1, 27–31], showed the significant prospect of CWF to increase oil recovery. Despite the vast amount of literature about CWF, there is still a need to understand the processes occurring in the relatively stagnant zones. Pore-scale studies on micro-mechanisms of the CWF process were performed by a limited amount of research groups. Several studies were conducted using a high-pressure visualization setup. They reported similar findings as in the case of CO<sub>2</sub> flooding. Due to them, the primary CWF mechanism of oil recovery is the oil volume increase as a result of Diffusion of CO<sub>2</sub> from CW to Oil (DCWO), followed by a mobilization of isolated oil ganglia [6, 20, 25, 26]. Sohrabi et al. experimentally confirmed incremental oil recovery by applying CWF as a secondary and tertiary method. Moreover, the authors highlighted the importance of improved sweep efficiency, oil volume increase, and further agglomeration of remobilized oil droplets. They have reported a 23% volume increase of decane at experimental conditions of 138 bar and 311 K. Additionally, Riazi et al. (2011) [25] developed a theoretical approach for pore scale analysis of oil entrapped in a DEP and exposed to direct contact with carbonated water and/or indirect contact (through a water film) to CO<sub>2</sub>.

Despite a large number of studies devoted to CO<sub>2</sub> and CW flooding, the pore scale

mechanisms for CWF in the dead-end zones remain unclear. DCWO in series of systematic experiments were examined in order to (1) understand the interaction occurring between oil entrapped in DEPs and injected CW, (2) investigate the differences in interactions to injection of CO<sub>2</sub> and (3) establish the CO<sub>2</sub> diffusion coefficient. A water flooded system containing an oil-filled monopore is exposed to CW injection to visualize the physics of oil in contact with CW ( $P \in 77, 100$  bar,  $T \in 309, 328$  K). In order to study the governing mechanisms of the oil swelling, based on mass balance and volume measurements, a two-dimensional model in an open system was developed. The numerical model was solved using a commercial finite element package (Comsol Multiphysics<sup>TM</sup>).

This study is an extension of the work of Peksa et al. (2013) [32] on the role of molecular diffusion in tertiary recovery of hydrocarbons. It contributes to a better understanding of processes such as molecular diffusion in stagnant areas of flow in CWF by using visualizations, experimental and simulation results of new experiments. The effect of a first and second CW contact with oil, swelling of oil by dissolved CO<sub>2</sub> and recovery are analyzed. Further, the influence of temperature and pressure is investigated and the obtained results are compared to the pure CO<sub>2</sub> injection conducted at the same experimental conditions. In addition, DCWO results are analyzed for process improvements and with an option for CO<sub>2</sub> sequestration, with the aim to achieve recovery in both laboratory core floods and in the field.

## 6

The chapter is organized as follows. In the next section, the theory regarding the co-existence of two binary systems is presented, followed by a theoretical characterization of the compositional changes arising from Fickian diffusion and convective transport processes. Subsequently, the experimental approach together with a setup and the procedure are shown. In the result section, the focus lies on describing the base case for both simulation and experiments. In the last section, the work is concluded by comparing the conducted simulation and experiments on the CW injection to a CO<sub>2</sub> injection test.

## 6.2. OIL RECOVERY BY CWF

In this study, the injection of carbonated water in a water-flooded oil system is investigated. As we are interested in the bulk behavior of the present phases, we assume, for the further analysis of the process, that reservoir rocks are inert (here a glass model). The thermodynamics and properties of a CO<sub>2</sub>-water-hydrocarbon (>C<sub>6</sub>) system were extensively studied in the literature [33–37]. This case will be treated as proposed by Vetter et al. 1987 [36]. Water and oil do not behave as isolated, independent phases in the system since gas is mutually soluble in both liquids. Dissolved CO<sub>2</sub> alters the chemo-physical properties of water (i.e. pH, density) and the physical properties of the oil (viscosity, density, swelling, interfacial tension with water, etc.) [38–42]. To analyze the problem of molecular diffusion in the carbonated water flooding process, we first evaluate the  $P$ - $T$  conditions under which the process occurs, followed by a study of the swelling behavior of oil.

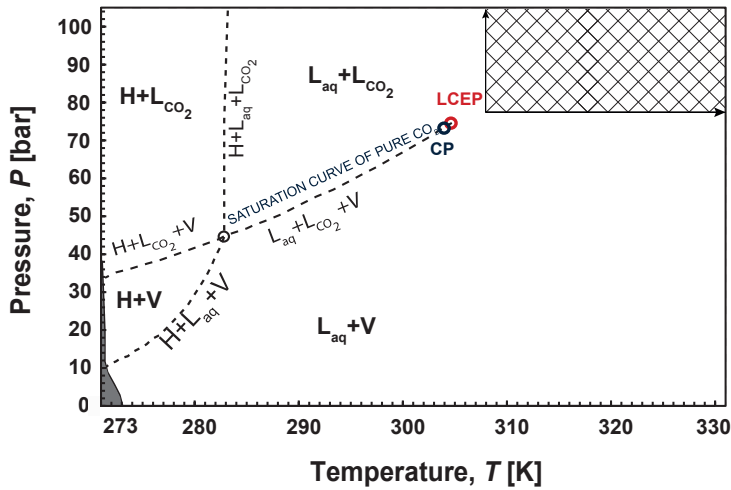


Figure 6.1:  $P$ - $T$  projection of the phase diagram of the binary  $\text{CO}_2$ - $\text{H}_2\text{O}$  system (after Spycher, 2003 [45]). Figure abbreviations: **H** -  $\text{CO}_2$ -clathrate-hydrate; **L<sub>aq</sub>** -  $\text{CO}_2$  bearing water-rich liquid phase; **L<sub>CO<sub>2</sub></sub>** -  $\text{CO}_2$ -rich liquid phase; **V** -  $\text{CO}_2$  rich vapor phase.

### 6.2.1. BINARY SYSTEM $\text{CO}_2$ - $\text{H}_2\text{O}$

For the CW process, the thermodynamic properties of the main working fluid  $\text{CO}_2$ - $\text{H}_2\text{O}$  were defined. CW was investigated by several authors at various pressures and temperatures [43–47]. Fig. 6.1 shows the  $P$ - $T$  projection of the  $\text{CO}_2$ - $\text{H}_2\text{O}$  according to literature. The ranges of pressure and temperature, as adequate for this study, are indicated by the diagonal crossing rectangular pattern.

Fig. 6.1 shows that, at the  $P$ - $T$  conditions for this study, the differences between vapor and liquid  $\text{CO}_2$  disappears and is replaced by an  $\text{H}_2\text{O}$ -rich liquid phase in coexistence with a  $\text{CO}_2$ -gas-rich phase. The Lower Critical End Point (LCEP) is located at 304.63 K and 74.11 bar, almost coinciding with the critical point of pure  $\text{CO}_2$ . The three-phase equilibrium curve  $\text{L}_{\text{aq}}\text{-L}_{\text{CO}_2}\text{-V}$  almost coincides with the pure  $\text{CO}_2$  saturation curve.

Data from the literature for temperatures 308 and 332 K (Fig. 6.2) show that  $\text{CO}_2$  solubility in water first increases abruptly with pressure up to the three-phase pressure interval, then bends, followed by a subsequent gradual increase away from this point. As the presented data lie above the critical temperature, the  $\text{CO}_2$  solubility over pressure follows the solubility curve for gaseous  $\text{CO}_2$ . The  $\text{H}_2\text{O}$  solubility in the  $\text{CO}_2$ -rich phase decreases with declining pressure. The difference from the ideal behavior of the  $\text{H}_2\text{O}$  solubility for  $\text{CO}_2$  is a result of the presence of a large amount of  $\text{CO}_2$  molecules around  $\text{H}_2\text{O}$  molecules [54]. For both temperatures, above the three phase pressure interval, an increment of the  $\text{H}_2\text{O}$  solubility in the  $\text{CO}_2$ -rich phase is observed with raising pressure.

### 6.2.2. BINARY SYSTEM $\text{CO}_2$ - OIL

The efficiency of oil displacement by CW depends on, among others, the generated phase behavior of  $\text{CO}_2$ -hydrocarbon mixtures, and the resulting densities and viscosi-

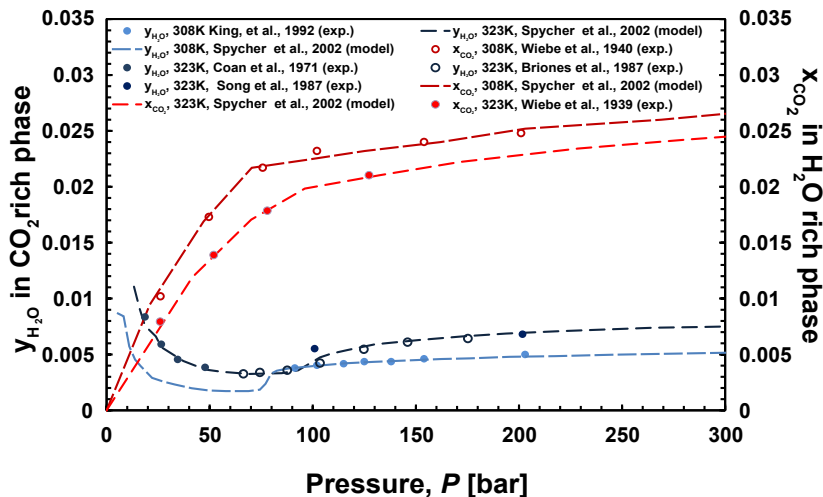


Figure 6.2: Mutual solubilities of H<sub>2</sub>O and CO<sub>2</sub> at 308 and 323 K and pressures up to 300 bar [45, 48–53]. The diagonal crossing pattern range represents the experimental condition of this study.

## 6

ties of the phases present. Fig. 6.4 shows the binary phase composition data for mixtures of CO<sub>2</sub> and decane at 309 and 328 K. A detailed description of the parameters can be found in Chapter 5.

### 6.2.3. THREE COMPONENT SYSTEM

As mentioned above, the independent oil and water phases do not act as isolated phases within the system, as CO<sub>2</sub> is mutually soluble in both liquid phases. Vetter et al. (1987) showed that the three-phase bubble point pressure depends on the varying amounts of the two coexisting liquid phases [36]. By that, the three-phase bubble point pressure in the decane/water/CO<sub>2</sub> system depends on the ratio of the two liquid phases (water and decane) and the distribution of CO<sub>2</sub>-concentration in both liquids.

### 6.2.4. MODEL OF THE SINGLE DEAD-END PORE

#### PHYSICAL MODEL

A 2-D model for molecular diffusion of CO<sub>2</sub> from the aqueous phase into oil was developed. The model attempts to implicate the experiments on the CO<sub>2</sub> induced oil volume increase in a DEP. Modeling was performed for the main experiment at 77 bar and 328 K. A schematic diagram of an isolated oil droplet in a DEP system is shown in Fig. 6.4. For further analysis, both numerical and experimental, four regions in the  $xy$ -plane of the monopore were defined: (1) the tube, (2) the pore neck, (3) the pore throat and (4) the pore body (Fig. 6.4a).

When CW is injected into a glass cell containing n-decane, direct contact between the injected fluid and oil takes place at their interface, and CO<sub>2</sub> gradually dissolves into the oil. The interface between the media (red dashed line in Fig. 6.4b) may shift within

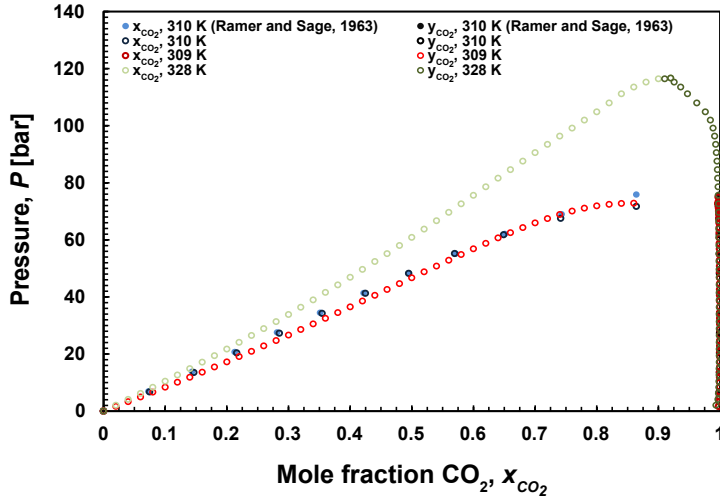


Figure 6.3: Isothermal pressure-composition ( $P, x_{CO_2}$ ) phase diagram for the data for the  $CO_2$ -decane system at experimental pressures and temperatures.

the monopore from its initial position down to the imaginary pore bottom line ( $l_b$ ) and up to the imaginary pore top line ( $l_t$ ).

6

### GOVERNING EQUATIONS

Here, the situation with the conventional continuity equation and 2<sup>nd</sup> Fick's law is described. Similar approaches were used previously in the literature [9, 20]. Diffusional processes cause transport of  $CO_2$  and its transfer from one medium to the other. Following a component concentration gradation, diffusion between CW and the oil phase occurs, the density and viscosity of oil phase changes and the volume of  $CO_2$ -decane mixture increases.

Two liquid phases, consisting of three components (decane, water and  $CO_2$ ) are present in the system. The reservoir temperature is assumed to remain constant and the horizontal and vertical diffusivities are assumed to be equal (isotropic media). Chemical reactions between CW, n-decane and glass are disregarded. There is no dissolution of oil in water and, respectively, of water in oil. Gravity effects are ignored in this study.

The molecular diffusion process with the hypothesis of incompressibility can be expressed by an unsteady state condition ( $ph \in (o,w)$ ), as follows:

$$\frac{\partial C_{ph}}{\partial t} + (\vec{u} \cdot \nabla C_{ph}) = D_{ph} \nabla^2 C_{ph} \quad (6.1)$$

In the context of a time-dependent process, Eq. 6.1 permits the following interpretation:  $C_{ph}$  is the molar concentration distribution of  $CO_2$  in one of the phases at time  $t$ ,  $\vec{u}$  is a velocity vector of moving  $CO_2$  and  $D_{ph}$  is the molecular diffusion coefficient of  $CO_2$  in one of the phases.



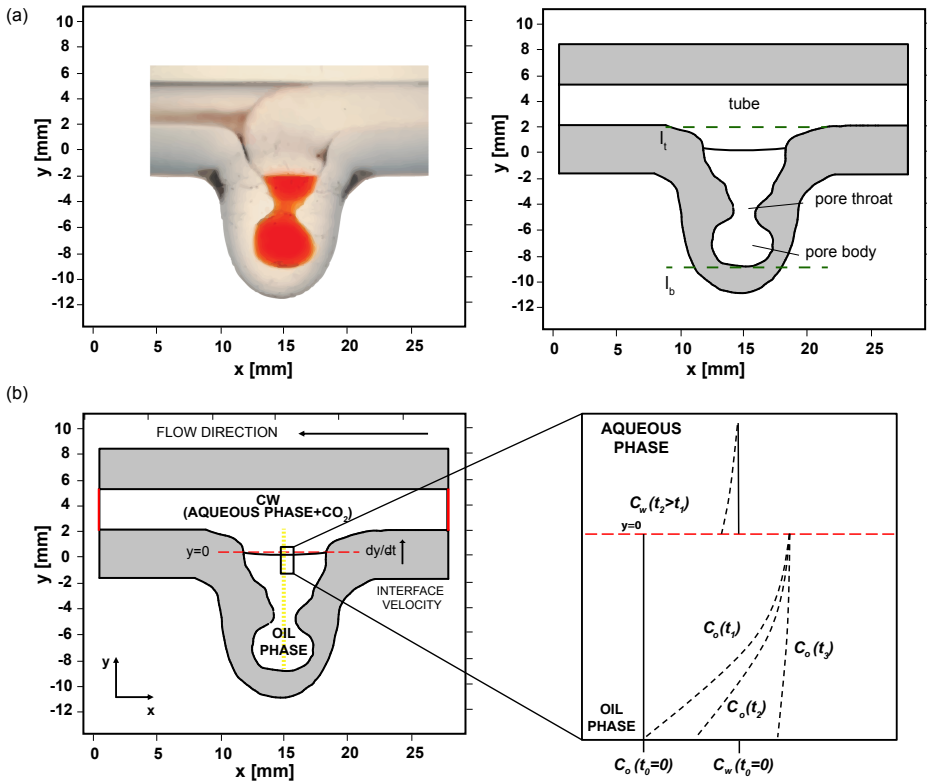


Figure 6.4: (a) An image and a schematic drawing of the isolated oil droplet in a DEP system with defined regions; (b) Schematic drawing of physical model with CO<sub>2</sub> concentration profiles. The red dashed line indicates initial position of the interface; the yellow line indicates the position for which the results will be provided in the next sections.

In this study, the diffusion coefficient was used as a fitting parameter. Based on the experimental results, a diffusion coefficient of CO<sub>2</sub> was obtained by matching the experimental volume change:  $D_{o,2} = -1.92 \times 10^{-9} + 1.35 \times 10^{-13} \times C_{ave,o} + 1.40 \times 10^{-24} \times (C_{ave,o})^4 - 2.38 \times 10^{-33} \times (C_{ave,o})^6 - 1.46 \times 10^{-20} \times (C_{ave,o})^3$ . The fitted coefficient was tested against varying diffusion coefficients of CO<sub>2</sub> in decane obtained from the literature: (1) a constant diffusion coefficient  $D_{o,1} = 3.5 \times 10^{-9} \text{ m}^2/\text{s}$ ; and (2) a diffusion coefficient that inversely changes with CO<sub>2</sub> concentration  $D_{o,3} = -7.86 \times 10^{-10} \mu_m^{-0.1667}$  [55].

#### INTERFACE, INITIAL AND BOUNDARY CONDITIONS

The interface between the immiscible phases is assumed to be represented by an infinitesimally small film. At both sides of the oil/aqueous phase boundary, the chemical potentials of the diffusing CO<sub>2</sub> are equal. However, at  $t = 0$ , the concentration profile of CO<sub>2</sub> over the coexisting phases exhibits a substantial variation at the boundary. Such a behavior is associated with the CO<sub>2</sub> distribution coefficient  $Kp_{w/o}$  between the immiscible phases. By writing the equilibrium conditions for these systems, Equation 6.2 can

be derived in terms of thermodynamic parameters. Under the assumption of ideal, diluted solutions, the equality of the chemical potentials in the two phases gives the ratio between the equilibrium concentrations  $C_o$  and  $C_w$

$$K p_{w/o} = \frac{\nu_o}{\nu_w} \exp\left(-\frac{\mu_o^0 - \mu_w^0}{RT}\right) = \frac{C_{o,eq}}{C_{w,eq}} \quad (6.2)$$

where  $C_{o,eq}$  is the molar concentration of  $\text{CO}_2$  in the oil phase and  $C_{w,eq}$  is the molar concentration of  $\text{CO}_2$  in the water phase,  $\nu_o$  and  $\nu_w$  are the molar volumes,  $\mu_o^0$  and  $\mu_w^0$  are the standard chemical potentials, and  $R$  and  $T$  are the gas constant and the absolute temperature.

The initial condition of the  $\text{CO}_2$  concentration at  $t = 0$  for the concentration profile are (Fig. 6.4b)

$$\begin{cases} C_o = 0 & \text{for } -11 < y < 0 \quad t = 0 \\ C_w = C_{w,eq}(P, T) & \text{for } 0 < y < 4 \quad t = 0 \end{cases} \quad (6.3)$$

In this model, the movement of the interface in the  $y$  direction is taken into account as a result of oil volume increase due to  $\text{CO}_2$  mass transfer between water and oil phases. At any time, the equality of the mass flux of  $\text{CO}_2$  leaving the water phase and entering the oil phase can be represented by a general Danckwerts (1950) relation, where the concentrations at both sides on the interface are related by an equilibrium expression ( $C_w(y_o) = QC_o(y_w) + R$ ), where  $Q$  and  $R$  are physical constants [56].

In the system, the  $\text{CO}_2$  is conserved at the interface:

$$\frac{\partial}{\partial y} D_o \left( \frac{\partial C_o}{\partial y} \right) + C_o \frac{\partial y_{m,o}}{\partial t} = \frac{\partial}{\partial y} D_w \left( \frac{\partial C_w}{\partial y} \right) + C_w \frac{\partial y_{m,w}}{\partial t} \quad (6.4)$$

However, following [10] the velocity of each point of the interface should be represented by the rate of the transport of volume per unit area  $\frac{dy_{v,o}}{dt}$  with implementation of the partial specific volumes

$$\frac{dy_{v,o}}{dt} = \left( \frac{\partial}{\partial y} D_{ph} \left( \frac{\partial C_o}{\partial y} \right) + C_o \frac{\partial y_{m,o}}{\partial t} \right) \nu_o \quad (6.5)$$

$$\frac{dy_{v,o}}{dt} = \frac{M_{\text{CO}_2} D_{ph} \left( \frac{\partial C_o}{\partial y} \right) \nu_o}{1 - C_o M_{\text{CO}_2} \nu_o} [1 + C_o M_{\text{CO}_2} (\nu_o^o - \nu_o)] \quad (6.6)$$

where  $M_{\text{CO}_2}$  is the molar mass of  $\text{CO}_2$ ;  $C_o$  is the volumetric molar concentration of  $\text{CO}_2$  in oil and  $\frac{\partial C_o}{\partial y}$  represents the spatial gradient of the  $\text{CO}_2$  molar concentration in oil with respect to time;  $\nu_o^o$  and  $\nu_o$  are partial specific volumes of the oil component in the oil phase and  $\text{CO}_2$  in the oil phase.

The initial conditions of the interface movement hold the relationship:

$$\frac{dy_{v,o}}{dt} = 0, \quad t = 0. \quad (6.7)$$

Moreover, there are three types of boundaries in the model domain: the boundary representing the inlet, the boundary representing the outlet and boundaries modeled with

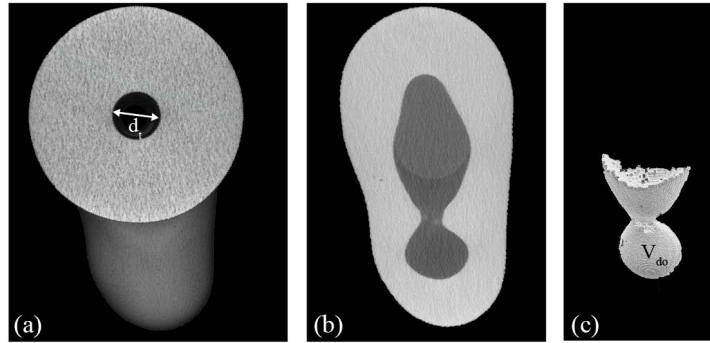


Figure 6.5: Example of the CT reconstruction (a) 3D view of the glass model; Tube volume,  $V_t=26.5 \text{ mm}^3$  (b) cross-section through the middle of the glass model (c) CT-image of the starting volume of oil after standard water flooding subtracted from the image by removing the glass phase and water phase  $V_{do}=20.55 \text{ mm}^3$ ; voxel size:  $0.015 \times 0.015 \times 0.015 \text{ mm}$ .

zero-flow conditions. At distance zero from the imaginary bottom line and at the walls of the pore body and throat, the  $\text{CO}_2$  concentration profile at the boundary of the oil phase fulfills the zero-flux condition.

With specific initial and boundary conditions, the above partial differential equations for molecular diffusion in two phases in a three component system are solved with the finite element analysis in COMSOL<sup>TM</sup> Multiphysics 5.1, to provide the concentration as a function of spatial position and time.

## 6.3. EXPERIMENTAL APPROACH

### 6.3.1. MATERIALS

Flooding experiments were conducted in a transparent glass model representing a single pore connected to a flow channel. The glass model was placed in the horizontal direction with the opening to the monopore at the bottom (Figure 6.5). The glass model consists of pure silicon dioxide ( $\text{SiO}_2$ ), which can hold 150 bar gas pressure. In the experiments, the operational fluids consist of water phase, oil phase and carbonated water.

The *water* used in this study consists of degassed, demineralized water and for the *oil phase* decane doped with solvent red dye was used. *Carbonated Water (CW)* solution was prepared by filling a cylinder with 80 vol.% of water and, then, introducing pure  $\text{CO}_2$  into the pressurized system. The experimental conditions presented in this study cover temperatures 309 and 328 K, and pressures 77 and 100 bar.

### 6.3.2. EXPERIMENTAL SETUP

The experimental setup used in this study to conduct volume increase measurements and to visually observe the diffusion of  $\text{CO}_2$  from carbonated water into oil (Fig. 6.6) is similar to the setup presented in Chapter 5. The setup was described in detail in Peksa et al., 2013 [32]. The most important part of the setup is a glass tube with a dead-end pore placed in a PEEK core holder. To avoid corrosion and to withstand high pressures,

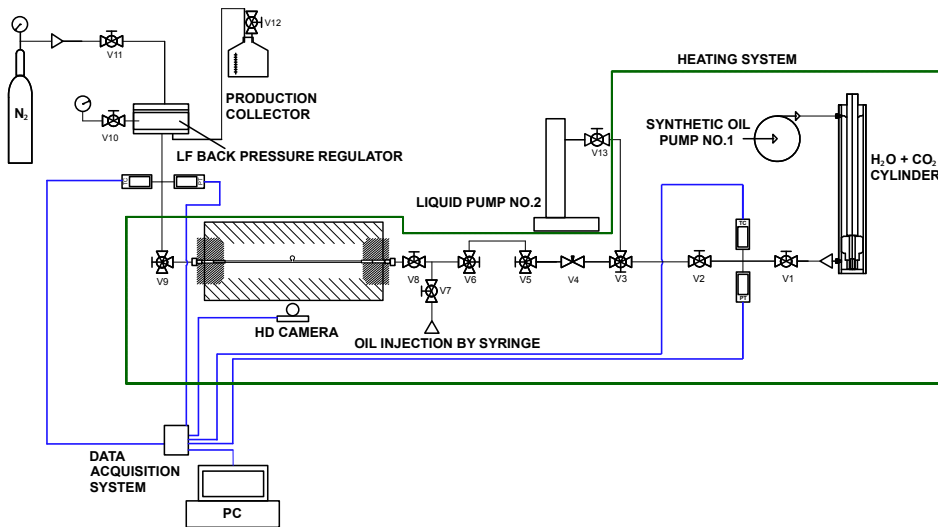


Figure 6.6: Schematic description of the high-pressure experimental setup for a study on molecular diffusion of  $\text{CO}_2$  from CW into oil. The green line represents the oven in which the experimental setup was built. The black lines illustrate the tubing and the various flow lines. The blue lines are data cables connecting pressure transducers and thermocouples to a computer for acquisition and controlling.

all other parts were made of stainless steel. The inlet of the glass tube was connected to a double acting cylinder accumulator, which is the source of the CW. At one side the cylinder was connected to the system, and at the other side to a silicon oil controlled pump. The required temperatures of  $309 \text{ K} \pm 0.1 \text{ K}$  and  $328 \text{ K} \pm 0.1 \text{ K}$  were achieved by using an oven in which the cell and cylinder were placed. A back-pressure regulator maintained the pressure in the system. The pressure and temperature are monitored by a system of pressure transducers and thermocouples. The CWF process was constantly monitored and recorded by an HD megapixel full-color camera at 1 FPS.

### 6.3.3. EXPERIMENTAL PROCEDURE

*Preparations of the transparent glass model:* The system was thoroughly cleaned (i.e. degreased and micro-sized dust removed). Thereafter the system was placed under vacuum. *Primary drainage:* During primary drainage, the degassed oil was injected from valve 7 with a flow rate of  $0.25 \text{ ml/min}$ , in order to fill the entire system with oil. At the same time, no air was allowed to enter the monopore. *Imbibition:* The system was water flooded till residual oil saturation was reached. For each experiment, the irreducible oil saturation varied. In each experiment, flooding was started with a flow rate of  $0.5 \text{ ml/min}$ , which gradually increased to rates up to  $10 \text{ ml/min}$ , combined with a variation of pressures. The resulting two phase system was pressurized to operational conditions. *Carbonated water injection:* After imbibition, the injection was switched to CW with a

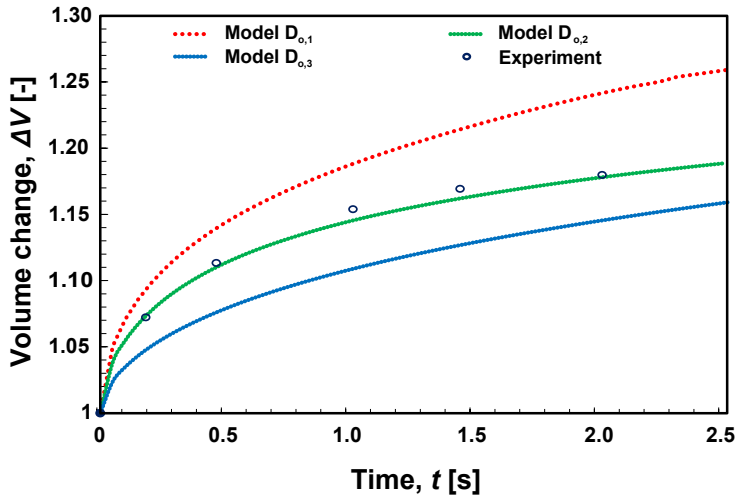


Figure 6.7: Comparison of decane volume change variation in the DEP for different diffusion coefficients.

flow rate of 0.1 ml/min. The outlet was connected to the production collector. *Data and image acquisition:* Temperature, pressure and injection/production rates were acquired starting from the primary drainage phase. Image acquisition was executed over the entire experimental time until the final result stopped to change visually.

## 6.4. RESULTS AND DISCUSSIONS

### 6.4.1. SIMULATIONS

The oil volume entrapped in the DEP is not displaced directly, but it is initially bypassed by CW. Displacement of oil occurs slowly as a result of a mass transfer between the main flow channel and the stagnant zone. Due to the finite-rate mass transfer between the flowing and stagnant fractions, the length of the mixing zone increases. Below we discuss the influence of the diffusion coefficient as an input parameter on the mass transfer process, the variation in the concentration profiles over time (first 3 h), the average  $\text{CO}_2$  concentrations in relation to the average diffusive and convective  $\text{CO}_2$  fluxes in the oil phase and the two-dimensional profiles of the diffusive fluxes magnitudes and concentrations at the early stage of the mass transfer. Figure 6.7 shows the evolution of the volume change as a function of the diffusion coefficient.

One can see that with varying diffusion tests, different volume change rates were obtained. It should be noted that the diffusion coefficients obtained from the literature were established based on pressure decay data in a closed system. In contrast, in this study, the system is open to inflow and outflow. Moreover, according to Aguilera et al. (2002), the value of the diffusion coefficient is related to the system geometry [57]. They reported two different diffusion coefficients for a  $\text{CO}_2$ -decane system in square ( $12 \times 10^{-8}$ ) and cylindrical ( $12 \times 10^{-10}$ ) capillary tubes. The calculated value  $D_{o,2}$  shows that the established model and testing method are both reasonable. For further analysis, the

fitted diffusion coefficient is used.

CO<sub>2</sub> concentration profiles in the oil phase as a function of time along the middle of the DEP (yellow cut line indicated in Figure 6.5) are shown in Figure 6.8a. Figure 6.8a indicates that high concentration gradients exist along the diffusion direction and with longer mass transfer time the internal concentration gradient was gradually reduced. At the initial stage ( $t < 0.3$  h), the CO<sub>2</sub> concentration gradient in the oil phase is large, and its concentration at the bottom of the DEP remains zero. The concentration gradient in the water phase above the moving interface is negligible in the model.

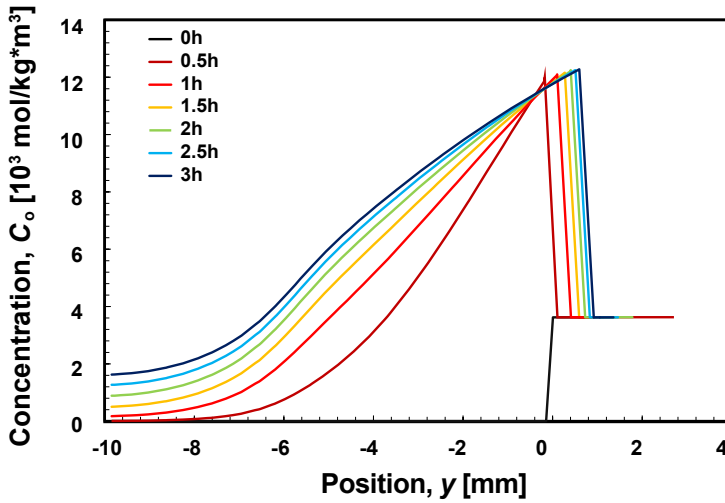
Since the diffusion and convective fluxes play a role in the mixing in the oil phase, we analyze the diffusive mass flux and the convective mass flux to determine the transport processes controlling the mixing. The average changes in CO<sub>2</sub> diffusive and convective fluxes magnitudes over time and change in the average concentration are presented in Fig. 6.8b. At the beginning of the CO<sub>2</sub> mass transfer from the CW, the large concentration gradient leads to rapid diffusion. Initially, the diffusive flux is an order of magnitude higher than the convective flux. With continuous diffusion and convection, the CO<sub>2</sub> concentration gradient decreases. The diffusion process decelerates along the diffusion direction. This indicates that diffusion dominates the mass transfer at the early stages. At the later stage, after the characteristic time for the oil phase (2.5 h), the role of convection increases. For a detailed characterization of the diffusion process in the oil phase at the early stages of the injections, when diffusion dominates the CO<sub>2</sub> mass transfer, snapshots of the diffusion flux profiles at various times are plotted in Figs. 6.9a-d. Figures 6.9e-h show the corresponding concentration profiles in the DEP geometry. The CO<sub>2</sub> fluxes progress in the direction of a lower concentration in the oil. It results in the change in the concentration profile and volume of the oil phase (see Figs. 6.8 and 6.9). It can be pointed out that the diffusion fluxes are a function of both time and distance from the interface. The diffusion fluxes decrease with distance and time, until reaching an equilibrium state.

#### 6.4.2. EXPERIMENT: BASE CASE

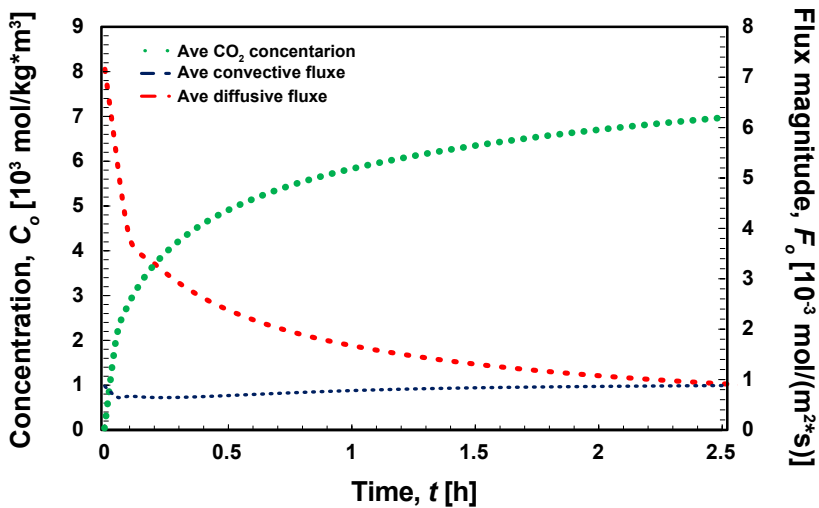
The results that are presented in the example below cover the visual observations of the process when the most significant DCWO phenomena occurred. The effect of factors, such as first and second CW contact with oil, swelling of oil by dissolved CO<sub>2</sub> and recovery, is observed, recorded and further analyzed by image analysis techniques.

##### CW INTRODUCTION

At early times of CW-injection, the injected fluids are not in a thermodynamic equilibrium with the in-situ fluids, which consist of trapped oil in the DEP and water (Fig. 6.10a). First, the DEP is reached by a small volume of the initial CW ( $CW_{int}$ ) (Fig. 6.10b), which is created at the interface of CW and pure water. It is the result of CO<sub>2</sub> diffusion. While flowing, the  $CW_{int}$  bridges across the pore body and snaps off due to pore-scale capillary instability. The displacement process of the  $CW_{int}$  is very rapid (a few seconds) as the volumes passing DEP are relatively small (~5 ml). Subsequently, the operational CW is reaching the DEP (Fig. 6.10c).



(a)



(b)

Figure 6.8: (a) Evolution of CO<sub>2</sub> composition profile inside the oil phase as a function of time, based on the constant CO<sub>2</sub> diffusivity for the CO<sub>2</sub> concentration profiles of one realization for 77 bar, 328 K as a function of time and distance, respectively at  $t_0 = 0$  h,  $t_1 = 0.5$  h,  $t_2 = 1$  h,  $t_3 = 1.5$  h,  $t_4 = 2$  h,  $t_5 = 2.5$  h,  $t_6 = 3$  h; (b) Average CO<sub>2</sub> concentration profiles over experimental time for 77 bar, 328 K and an average CO<sub>2</sub> diffusive and convective flux magnitude in the oil phase over time.

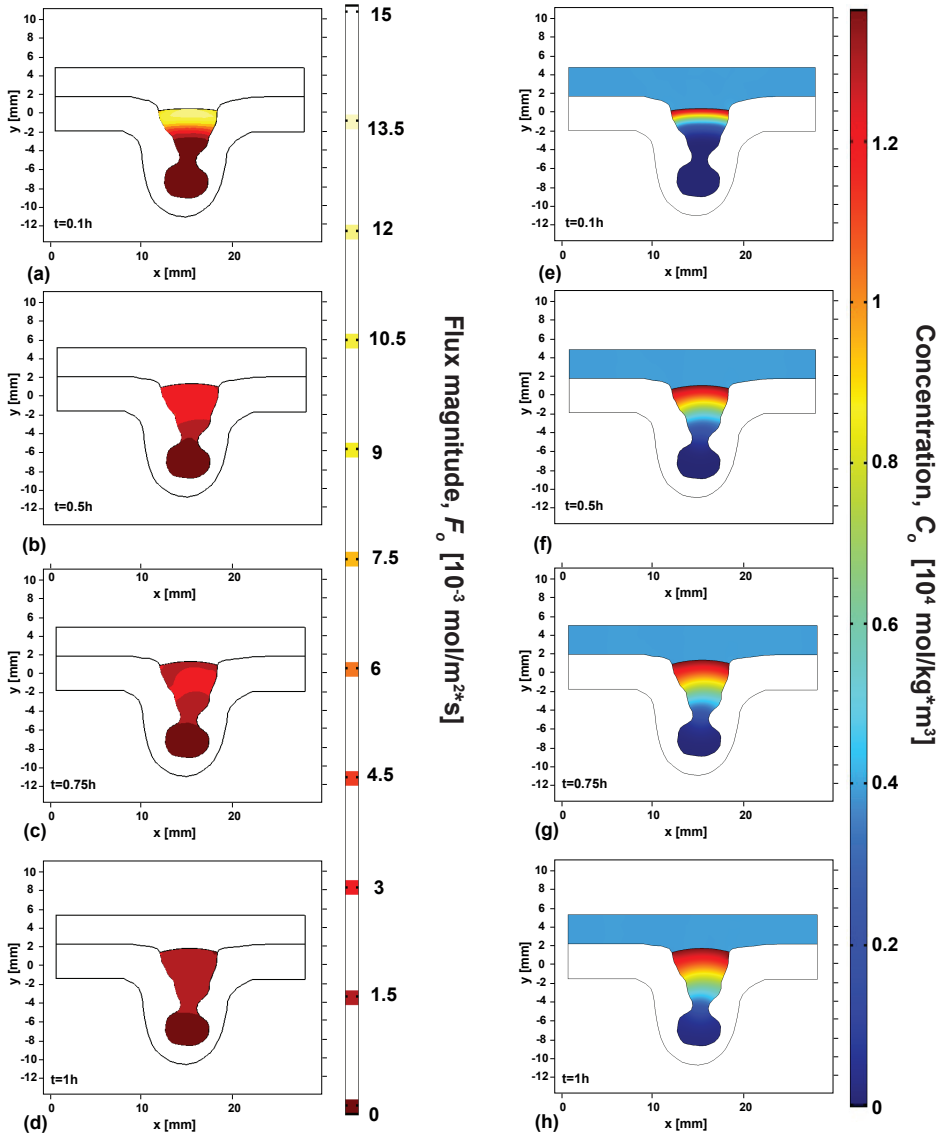


Figure 6.9: Diffusive flux magnitude (a-d) and concentration profiles (e-h) at times of one realization ( $P = 77$  bar,  $T = 328$  K) at  $t = 0.1$  h,  $t = 0.5$  h,  $t = 0.75$  h and  $t = 1$  h.



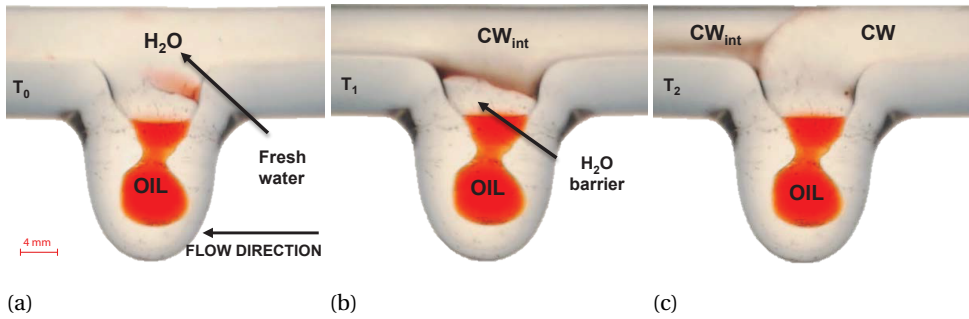


Figure 6.10: CW introduction and role of the water barrier.

### CW-OIL CONTACT AND CO<sub>2</sub> INDUCED OIL VOLUME INCREASE

In the CW flooding, the flow in the DEP geometries is related to the presence of the CO<sub>2</sub> gradients. The physical system CW-oil attains to establish the equilibrium. The gradients are time dependent and initiate from both diffusion and convection forces. As a result, shortly after the DEP is reached by CW, the oil volume increases over time maintaining the sharp interface that separates water and oil phases (Fig. 6.11a). The interfacial area changes over time. Moreover, the literature measurements show that the dynamic interfacial tension (IFT) decreases linearly between oil and water with rising CO<sub>2</sub> mole fraction [34]. Forte (2011) showed that if the water-CO<sub>2</sub> and oil-CO<sub>2</sub> interactions are sufficiently strong, and the difference between the two interactions is sufficiently small, the CO<sub>2</sub> is favorable to decrease the IFT of water-oil.

We calculate the volume increase coefficient for different time steps to quantify the volume change ( $\eta$ ) of the CO<sub>2</sub> dissolution in decane by:

$$\eta = \frac{V}{V_o} \quad (6.8)$$

where  $V$  is the volume of the CO<sub>2</sub> saturated decane at  $P$ - $T$  conditions,  $V_o$  is the volume of pure decane at the same temperature and at atmospheric pressure. The uncertainties related to the volume change coefficient are related to the uncertainty in the images obtained.

Carbonic acid, H<sub>2</sub>CO<sub>3</sub>(aq) may have a minor effect on the mass transfer. It is a product of a reaction of aqueous carbon dioxide, CO<sub>2</sub>(aq) with water. Carbonic acid may lose protons to form bicarbonates, HCO<sub>3</sub><sup>-</sup>, and carbonates, CO<sub>3</sub><sup>2-</sup>. In this case, the proton is liberated to the water. The produced carbonate ions are of different size and diffuse at different rates creating an equivalent electric field. This effect may contribute to the displacement of the CO<sub>2</sub>-saturated oil towards the outlet [58].

### OIL MIGRATION FROM THE PORE BODY

The addition of CO<sub>2</sub> to decane leads to the disconnection and the stretch of decane molecules, inducing reduction of the viscosity, improvement of the oil-water mobility ratio and, thereby, enhancement in sweep efficiency of water. Moreover, at increased CO<sub>2</sub> saturations, the inflow of CO<sub>2</sub> to a dead-end pore leaves fluid flow with no exit way.

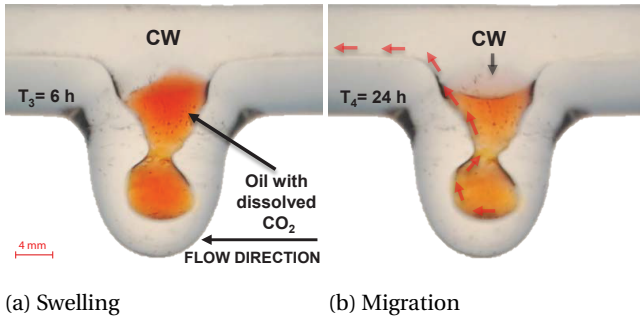


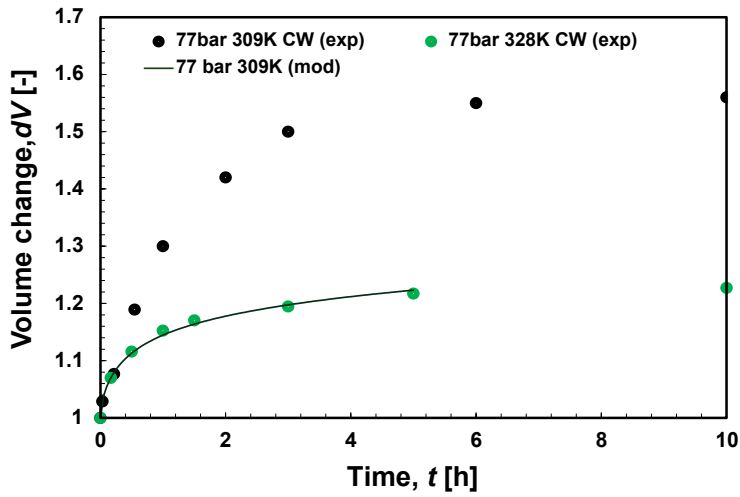
Figure 6.11: CO<sub>2</sub>-induced oil swelling and migration from the pore body.

Then, conservation of mass requires an equal and opposite fluid flux towards the tube. The interface of the liquid phases moves towards the bottom of the DEP and oil starts to migrate along the wall out of the dead-end pore (Fig. 6.11b).

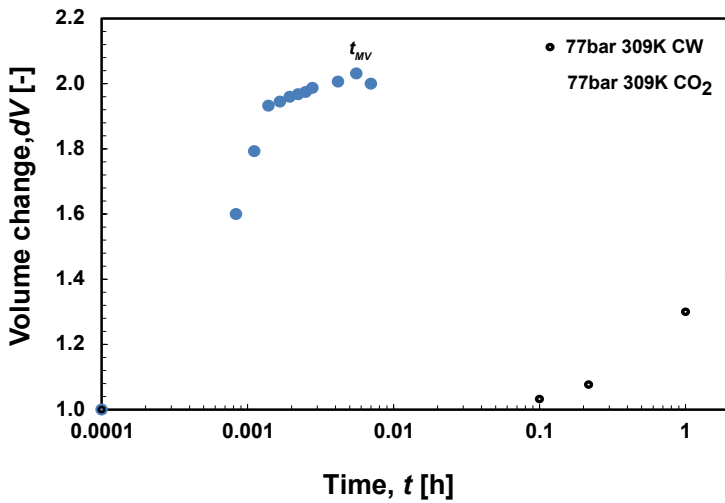
## 6.5. OVERALL RESULTS AND DISCUSSION

Experimental volume change coefficients for the CW-oil and CO<sub>2</sub>-oil injection schemes are depicted in Figs. 6.12 and 6.13. Figure 6.12a shows measured and calculated volume change coefficients as a function of mass transfer time. The tests were conducted at  $P$ - $T$  conditions below Minimum Miscibility Pressure (MMP) for a pure CO<sub>2</sub> stream-oil system, where an unfavorable density difference and viscosity ratio occurs. It is observed that the increase in operational temperature leads to a decrease in the solubility of CO<sub>2</sub> in decane and at the same time to a thermal expansion of decane. The effect of solubility of CO<sub>2</sub> on the swelling of decane is more pronounced than the thermal expansion of decane. Figs. 6.12 and 6.13 show that the volume change coefficient has the same expansion development at various temperatures. The calculated volume change coefficients are generally in good agreement with the experimental results. Moreover, the results are in accordance with the range of the literature results, though it has to be noted that condition and geometry differ [20, 59]. Figure 6.12b shows a comparison of CW flooding to pure CO<sub>2</sub> injection at the same  $P$ - $T$  conditions, and in the same geometry. The results are presented for the time interval related to pure CO<sub>2</sub> injection during which the maximum volume change was achieved ( $t_{MV}$ ). Figure 6.12b demonstrates that larger concentrations of CO<sub>2</sub> at the interface between two fluids (for pure CO<sub>2</sub> injection) result in a higher volume change in the short time (maximum volume change equal to 2.03 was achieved in  $t_{MV} = 20$  s).

Regardless of time and position, the CW injection results showed that the volume change coefficient increased with operating pressure (Figs. 6.12a and 6.13). This is mainly attributed to the proportional relation between the CO<sub>2</sub> concentration and the CO<sub>2</sub> pressure. Under the same temperature conditions, the CO<sub>2</sub> concentration gradient and the free energy of the CO<sub>2</sub> molecular increased with raising pressure. Due to the same reason, the volume change coefficient decreases with increasing temperature. Figure 6.13 shows the same trend as the results provided for the conditions below MMP (for the pure



(a)



(b)

Figure 6.12: (a) The measured volumetric coefficient of the oil-CO<sub>2</sub> system during CW together with the simulation results of paragraph 6.4.1, following identical *PVT*-conditions; (b) Comparison of the volume change coefficient of CW and CO<sub>2</sub> injections. Experiments are conducted at a pressure of 77 bar and temperature 309 K and 328 K, resulting in pure CO<sub>2</sub>-decane unfavorable density difference and viscosity ratio, and below MMP.

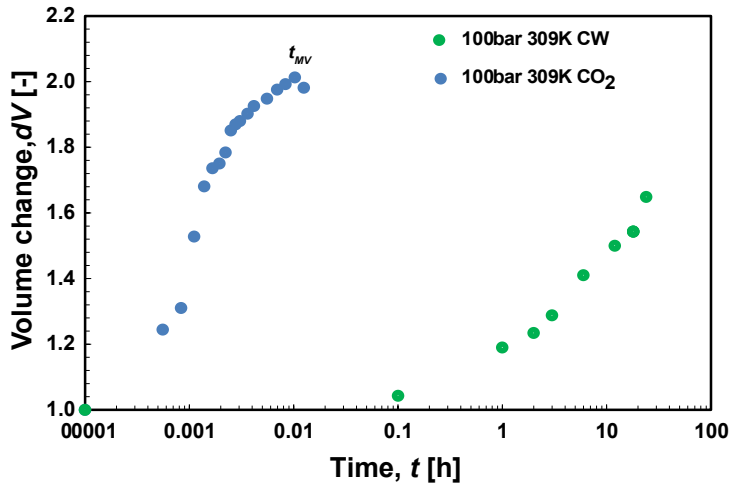


Figure 6.13: Oil displacement with CW and  $\text{CO}_2$ , at pure  $\text{CO}_2$ -decane with favorable density difference and unfavorable viscosity ratio, and above MMP. Experiments are conducted at pressure of 100 bar and temperature 309 K.

$\text{CO}_2$ -decane system).

## 6.6. CONCLUSIONS

In this study, an experimental and a theoretical methodology was established to analyze the  $\text{CO}_2$  mass transfer and its effects during the injection of the carbonated water into the system where oil was entrapped after water flooding in the dead-end pore. Moreover, in the last section of the chapter, the CW tests were compared to the  $\text{CO}_2$  flooding process conducted at the same operational conditions. In all experiments, the oil volume change coefficient, due to  $\text{CO}_2$  diffusion, was determined visually and quantitatively with images. Thereafter, the concentration profiles at different locations and time, and convective and diffusive fluxes under experimental pressure, were calculated with a numerical model.

Conducted experiments showed, that the swelling of oil which is controlled by molecular diffusion is the mechanism that occurs during the CW injection. Thus, the mobility of oil entrapped in the stagnant zones can be improved. The volume change coefficient of oil, due to  $\text{CO}_2$  dissolution, was determined based on the information obtained from the acquired images.

Although the initial CW bridges the pore body and snaps off due to pore-scale capillary instability, the process is very rapid at the start of the CW-decane interaction and is not affecting the final recovery. The CW-decane contact establishes time-dependent gradients and a progressive oil volume increase. As a result, a visible interface between oil and CW, with a decreasing IFT due to  $\text{CO}_2$  solubility, is maintained during the entire process.  $\text{CO}_2$  solubility in decane induces reduction of the viscosity, improvement of the

oil–water mobility ratio and thereby enhancement in sweep efficiency of water with oil.

All CW flooding experiments show similar CO<sub>2</sub>–decane dissolution trends. Consequently, the volume change coefficient follows the same expansion development at various temperatures and pressures with no significant discrepancy in shape. Its magnitude in volume change, however, varies in accordance to the (*P*-*T*) dependence of CO<sub>2</sub> solubility in decane.

For pure CO<sub>2</sub>, the volume change coefficient in the CW flooding experiments below and above MMP was compared. All graphs show similarity in behavior of the volume changing profile. The volume change coefficient in the case of the pure CO<sub>2</sub>–oil contact is much higher than for the CW in all the experiments. The time to recover oil at pore scale with water barrier takes about  $1.5 \times 10^3$  times more time when compared to the direct contact of a CO<sub>2</sub> stream. However, at the field scale, this might not be a limiting factor. Taking into account migration time of operational fluids from the injector to the producer at the field scale, the transport speed is within order of magnitude and the effect of the type of CO<sub>2</sub> source probably does play a lesser role. However, as mentioned in Chapter 5, it can have an influence in the near wellbore area. More injection tests should be conducted.

In this work, a numerical model was established for the evaluation of CO<sub>2</sub> mass transfer rates induced by diffusion and convection between operational fluids in a dead-end pore at isothermal conditions. Numerical simulations were performed with the Comsol Multiphysics<sup>TM</sup> simulator and matched with the CW visualization experiment with oil recovery through diffusion.

The model confirms that molecular diffusion from the CW to the oil is the dominating recovery mechanism at the primary phase of the mass transfer. The diffusion coefficient for the specific geometry and *P*-*T* conditions was determined. The geometry was found as a strong limiting factor. The decreasing influence of the diffusion and increasing convection role on the concentration gradient over time was observed.

This research is the base for further studies involving extensive temperature and pressure ranges. The experiments have an investigating role regarding the MMP pressure in the binary system CW-CO<sub>2</sub>/oil.

**REFERENCES**

- [1] R. Christensen, *Carbonated Waterflood Results—Texas And Oklahoma*, in *Annual Meeting of Rocky Mountain Petroleum Engineers of AIME* (Society of Petroleum Engineers, 1961).
- [2] N. De Nevers, *A calculation method for carbonated water flooding*, *Society of Petroleum Engineers Journal* **4**, 9 (1964).
- [3] Y. Dong, B. Dindoruk, C. Ishizawa, and E. J. Lewis, *An experimental investigation of carbonated water flooding*, in *SPE Annual Technical Conference and Exhibition* (Society of Petroleum Engineers, 2011).
- [4] L. Holm, *A comparison of propane and carbon dioxide solvent flooding processes*, *AIChE Journal* **7**, 179 (1961).
- [5] N. I. Kechut, M. Sohrabi, and M. Jamiolahmady, *Experimental and Numerical Evaluation of Carbonated Water Injection (CWI) for Improved Oil Recovery and CO<sub>2</sub> Storage*, in *SPE EUROPEC/EAGE Annual Conference and Exhibition* (Society of Petroleum Engineers, 2011).
- [6] M. Riazi, *Pore scale mechanisms of carbonated water injection in oil reservoirs*, Thesis (2011).
- [7] B. R. Bijeljic, A. Muggeridge, and M. J. Blunt, *Effect of composition on waterblocking for multicomponent gasfloods*, in *SPE Annual Technical Conference and Exhibition* (Society of Petroleum Engineers, 2002).
- [8] B. T. Campbell and F. M. Orr Jr, *Flow visualization for CO<sub>2</sub>/crude-oil displacements*, *Society of Petroleum Engineers Journal* **25**, 665 (1985).
- [9] A. Grogan, V. Pinczewski, G. J. Ruskauff, and F. Orr Jr, *Diffusion of CO<sub>2</sub> at reservoir conditions: models and measurements*, *SPE Reservoir Engineering* **3**, 93 (1988).
- [10] A. T. Grogan and W. V. Pinczewski, *The role of molecular diffusion processes in tertiary CO<sub>2</sub> flooding*, (1987), 10.2118/12706-pa.
- [11] P. McGuire and F. Stalkup, *Performance analysis and optimization of the Prudhoe Bay miscible gas project*, *SPE Reservoir Engineering* **10**, 88 (1995).
- [12] L. W. Holm, *Carbon dioxide solvent flooding for increased oil recovery*, (1959).
- [13] H. D. Do and W. V. Pinczewski, *Diffusion-controlled swelling of reservoir oil by indirect contact with injection gas*, *Chemical Engineering Science* **48**, 3243 (1993).
- [14] T. Muller and L. W. Lake, *Theoretical study of water blocking in miscible flooding*, *SPE Reservoir Engineering* **6**, 445 (1991).
- [15] D. Tiffin and W. Yellig, *Effects of mobile water on multiple-contact miscible gas displacements*, *Society of Petroleum Engineers Journal* **23**, 447 (1983).

- [16] E. L. Claridge and P. L. Bondor, *A Graphical Method for Calculating Linear Displacement With Mass Transfer and Continuously Changing Mobilities*, (1974), 10.2118/4673-pa.
- [17] J. Foroozesh, M. Jamiolahmady, and M. Sohrabi, *Mathematical modeling of carbonated water injection for EOR and CO<sub>2</sub> storage with a focus on mass transfer kinetics*, *Fuel* **174**, 325 (2016).
- [18] A. B. Ramesh and T. N. Dixon, *Numerical Simulation of Carbonated Waterflooding In A Heterogeneous Reservoir*, (Society of Petroleum Engineers, 1973).
- [19] S. Shenawi, C. Wu, C. Jiang, Z. Luan, *et al.*, *A New Iterative Mathematical Model for the Analysis of Imbibition Carbonated Waterflood in Naturally Fractured Reservoirs*, in *Permian Basin Oil and Gas Recovery Conference* (Society of Petroleum Engineers, 1994).
- [20] M. Sohrabi, M. Riazi, M. Jamiolahmady, S. Ireland, and C. Brown, *Carbonated water injection for oil recovery and CO<sub>2</sub> storage*, in *Sustainable energy UK conference: meeting the science and engineering challenge*, Oxford, UK (2008).
- [21] M. A. Ahmadi, M. zeinali Hasanvand, S. S. Behbahani, A. Nourmohammad, A. Vahidi, M. Amiri, and G. Ahmadi, *Effect of operational parameters on the performance of carbonated water injection: Experimental and numerical modeling study*, *The Journal of Supercritical Fluids* **107**, 542 (2016).
- [22] J. W. Martin, *Additional oil production through flooding with carbonated water*, *Producers Monthly* **15**, 18 (1951).
- [23] N. Mosavat and F. Torabi, *Performance of Secondary Carbonated Water Injection in Light Oil Systems*, *Industrial & Engineering Chemistry Research* **53**, 1262 (2014).
- [24] N. Mosavat and F. Torabi, *Micro-optical analysis of carbonated water injection in irregular and heterogeneous pore geometry*, *Fuel* **175**, 191 (2016).
- [25] M. Riazi, M. Sohrabi, and M. Jamiolahmady, *Experimental Study of Pore-Scale Mechanisms of Carbonated Water Injection*, *Transport in porous media* **86**, 73 (2011).
- [26] M. Sohrabi, M. Riazi, M. Jamiolahmady, S. Ireland, and C. Brown, *Enhanced Oil Recovery and CO<sub>2</sub> Storage by Carbonated Water Injection*, in *International Petroleum Technology Conference* (International Petroleum Technology Conference, 2009).
- [27] C. Hickok, R. Christensen, and H. Ramsay Jr, *Progress review of the K&S carbonated waterflood project*, *Journal of Petroleum Technology* **12**, 20 (1960).
- [28] J. Martin and N. Tuckahoe, *Process of recovering oil from oil fields involving the use of critically carbonated water*, (1959).
- [29] H. Ramsay Jr, *Case histories of carbonated waterfloods in Dewey-Bartlesville field*, (1962).

- [30] H. Ramsay Jr and F. Small, *Use of carbon dioxide for water injectivity improvement*, Journal of Petroleum Technology **16**, 25 (1964).
- [31] J. Scott and C. Forrester, *Performance of domes unit carbonated waterflood-first stage*, Journal of Petroleum Technology **17**, 1,379 (1965).
- [32] A. E. Peksa, P. L. J. Zitha, and K.-H. A. A. Wolf, *Molecular Diffusion of CO<sub>2</sub> From Carbonated Water (CW) Into the Oil - Experimental Observations*, Report (2013).
- [33] G. Brunner, J. Teich, and R. Dohrn, *Phase equilibria in systems containing hydrogen, carbon dioxide, water and hydrocarbons*, Fluid Phase Equilibria **100**, 253 (1994).
- [34] E. Forte, *Measurement and prediction of the phase behaviour of carbon dioxide, alkane and water mixtures at reservoir conditions* (Imperial College London, 2011).
- [35] M. N. Okafor, *Phase equilibria from PVT measurements for carbon dioxide, water, and n-decane*, Report (Missouri Univ., Rolla (USA), 1987).
- [36] O. Vetter, M. Bent, V. Kandarpa, D. Salzman, and R. Williams, *Three-Phase PVT and CO<sub>2</sub> Partitioning*, in *SPE California Regional Meeting* (Society of Petroleum Engineers, 1987).
- [37] L. Zhao, L. Tao, and S. Lin, *Molecular Dynamics Characterizations of the Supercritical CO<sub>2</sub>-Mediated Hexane-Brine Interface*, Industrial & Engineering Chemistry Research **54**, 2489 (2015).
- [38] F. T. Chung, R. A. Jones, and H. T. Nguyen, *Measurements and correlations of the physical properties of CO<sub>2</sub>-heavy crude oil mixtures*, SPE Reservoir Engineering **3**, 822 (1988).
- [39] M. Emera and H. Sarma, *Prediction of CO<sub>2</sub> solubility in oil and the effects on the oil physical properties*, Energy Sources, Part A **29**, 1233 (2007).
- [40] C. A. Mulliken and S. I. Sandler, *The prediction of CO<sub>2</sub> solubility and swelling factors for enhanced oil recovery*, Industrial & Engineering Chemistry Process Design and Development **19**, 709 (1980).
- [41] R. Simon and D. Graue, *Generalized correlations for predicting solubility, swelling and viscosity behavior of CO<sub>2</sub>-crude oil systems*, Journal of Petroleum Technology **17**, 102 (1965).
- [42] J. Zhang, Z. Pan, K. Liu, and N. Burke, *Molecular Simulation of CO<sub>2</sub> Solubility and Its Effect on Octane Swelling*, Energy & Fuels **27**, 2741 (2013).
- [43] Z. Duan and R. Sun, *An improved model calculating CO<sub>2</sub> solubility in pure water and aqueous NaCl solutions from 273 to 533 K and from 0 to 2000 bar*, Chemical geology **193**, 257 (2003).
- [44] K. A. Evelein, R. G. Moore, and R. A. Heidemann, *Correlation of the Phase Behavior in the Systems Hydrogen Sulfide-Water and Carbon Dioxide-Water*, Industrial & Engineering Chemistry Process Design and Development **15**, 423 (1976).



- [45] N. Spycher, K. Pruess, and J. Ennis-King, *CO<sub>2</sub>-H<sub>2</sub>O mixtures in the geological sequestration of CO<sub>2</sub>. I. Assessment and calculation of mutual solubilities from 12 to 100°C and up to 600 bar*, *Geochimica et Cosmochimica Acta* **67**, 3015 (2003).
- [46] S. Takenouchi and G. C. Kennedy, *The binary system H<sub>2</sub>O-CO<sub>2</sub> at high temperatures and pressures*, *American Journal of Science* **262**, 1055 (1964).
- [47] K. Tödheide and E. Franck, *Das Zweiphasengebiet und die kritische Kurve im System Kohlendioxid-Wasser bis zu Drucken von 3500 bar*, *Zeitschrift für Physikalische Chemie* **37**, 387 (1963).
- [48] J. Briones, J. Mullins, M. Thies, and B.-U. Kim, *Ternary phase equilibria for acetic acid-water mixtures with supercritical carbon dioxide*, *Fluid Phase Equilibria* **36**, 235 (1987).
- [49] A. D. King Jr and C. Coan, *Solubility of water in compressed carbon dioxide, nitrous oxide, and ethane. Evidence for hydration of carbon dioxide and nitrous oxide in the gas phase*, *Journal of the American Chemical Society* **93**, 1857 (1971).
- [50] M. King, A. Mubarak, J. Kim, and T. Bott, *The mutual solubilities of water with supercritical and liquid carbon dioxides*, *The Journal of Supercritical Fluids* **5**, 296 (1992).
- [51] K. Song and R. Kobayashi, *Water content of CO<sub>2</sub> in equilibrium with liquid water and/or hydrates*, *SPE Formation Evaluation* **2**, 500 (1987).
- [52] R. Wiebe and V. Gaddy, *The solubility in water of carbon dioxide at 50, 75 and 100, at pressures to 700 atmospheres*, *Journal of the American Chemical Society* **61**, 315 (1939).
- [53] R. Wiebe and V. Gaddy, *The solubility of carbon dioxide in water at various temperatures from 12 to 40 and at pressures to 500 atmospheres. critical phenomena*, *Journal of the American Chemical Society* **62**, 815 (1940).
- [54] J. M. Prausnitz, R. N. Lichtenthaler, and E. G. de Azevedo, *Molecular thermodynamics of fluid-phase equilibria* (Pearson Education, 1998).
- [55] S. Zheng, H. A. Li, H. Sun, and D. Yang, *Determination of Diffusion Coefficient for Alkane Solvent-CO<sub>2</sub> Mixtures in Heavy Oil with Consideration of Swelling Effect*, *Industrial & Engineering Chemistry Research* **55**, 1533 (2016).
- [56] P. Danckwerts, *Unsteady-state diffusion or heat-conduction with moving boundary*, *Transactions of the Faraday Society* **46**, 701 (1950).
- [57] M. E. Aguilera, R. L. Cerro, and A. L. López de Ramos, *Enhanced CO<sub>2</sub> diffusion in wedges*, *Chemical Engineering Journal* **87**, 31 (2002).
- [58] A. Kar, *Auto-electrokinetic flows in dead-end pores from mixed ion systems*, Thesis (2013).
- [59] B. Liu, J. Shi, B. Sun, Y. Shen, J. Zhang, X. Chen, and M. Wang, *Molecular dynamics simulation on volume swelling of CO<sub>2</sub>-alkane system*, *Fuel* **143**, 194 (2015).

# 7

## COMBINED EOR AND CO<sub>2</sub> STORAGE

*The most prospective subsurface areas that have the characteristics to assure the trapping of CO<sub>2</sub> are geological deposits of hydrocarbons and gases. The CO<sub>2</sub> Enhanced Oil Recovery (CO<sub>2</sub>-EOR and CW-EOR) techniques are accepted as a mitigation prospect for CO<sub>2</sub> reduction and recovery of oil left behind in water-wet rock after water flooding. CO<sub>2</sub>-EOR and CW-EOR also show a potential for safe storage after the production stage.*

*Numerous theoretical works on CO<sub>2</sub>-EOR coupled with storage in depleted oil fields can be found in the literature. However, experimental works are still rather limited. To investigate the oil displacement and CO<sub>2</sub> sequestration a series of CO<sub>2</sub> and CW flooding experiments were conducted. Incremental oil recovery and storage of CO<sub>2</sub> were determined by mass balance and were visualized by a CT-scanner. Four different CO<sub>2</sub> stream injection scenarios were implemented as a 2<sup>nd</sup> stage EOR after water flooding: gas CO<sub>2</sub>, liquid CO<sub>2</sub>, supercritical CO<sub>2</sub> and carbonated water.*

*This chapter shows prospective recoveries and demonstrates storage efficiency. Incremental recoveries in the range 11-23% OOIP were obtained proving the CO<sub>2</sub> injection to be an effective EOR technique. Recovery was mainly achieved by oil swelling and reduction in oil viscosity due to CO<sub>2</sub> dissolution. The highest amount of CO<sub>2</sub> was stored at liquid conditions and by CW flooding. The efficiency of liquid CO<sub>2</sub> floods is a consequence of the high density of CO<sub>2</sub>. The process of CO<sub>2</sub> storage in CWF is strongly related to the maximum amount of CO<sub>2</sub> that can be dissolved in water and/or oil at specific pressure and temperature conditions.*

---

Parts of this chapter have been published as: Peksa, A. E., Wolf, K.-H. A. A., Daskaroli, M., & Zitha, P. L. J. (2015, June 1). The Effect of CO<sub>2</sub> Gas Flooding on Three Phase Trapping Mechanisms for Enhanced Oil Recovery and CO<sub>2</sub> Storage. Society of Petroleum Engineers. doi:10.2118/174283-MS

## NOMENCLATURE

<i>A</i>	Reservoir area, m <sup>2</sup>
<i>BS</i>	Bentheimer Sandstone
<i>h</i>	Reservoir thickness, m
<i>HU<sub>1</sub></i>	Scan of fully water saturated core at 140 keV, HU
<i>HU<sub>2</sub></i>	Scan of fully water saturated core at 120 keV, HU
<i>HU<sub>gs</sub></i>	gas CT number, HU
<i>HU<sub>g1</sub></i>	Scan of gas saturated core at 140 keV, HU
<i>HU<sub>g2</sub></i>	Scan of gas saturated core at 120 keV, HU
<i>HU<sub>o1</sub></i>	Scan of fully oil saturated core at 140 keV, HU
<i>HU<sub>o2</sub></i>	Scan of fully oil saturated core at 120 keV, HU
<i>HU<sub>wog1</sub></i>	Scan of fluid saturated core at 140 keV, HU
<i>HU<sub>wog2</sub></i>	Scan of fluid saturated core at 120 keV, HU
<i>HU<sub>ws</sub></i>	water CT number, HU
<i>HU<sub>w</sub></i>	Scan of fully water saturated core, HU
<i>D</i>	Diameter, cm
keV	kilo-electron volt, J
<i>L</i>	Length, cm
<i>MW</i>	Molecular weight, g/mol
<i>M<sub>CO<sub>2</sub>t</sub></i>	CO <sub>2</sub> mass storage capacity
$\varphi$	Porosity, [-]
$\rho_{CO_2r}$	Density of CO <sub>2</sub> at reservoir conditions, kg/m <sup>3</sup>
<i>P</i>	Pressure, bar
<i>PV</i>	Pore volume, ml
<i>R<sub>f</sub></i>	Recovery factor
<i>S<sub>iir</sub></i>	Irreducible water saturation, [-]
<i>S<sub>g</sub></i>	Gas saturation, [-]
<i>S<sub>o</sub></i>	Oil saturation, [-]
<i>S<sub>oi</sub></i>	Initial oil saturation, [-]
<i>S<sub>w</sub></i>	Water saturation
<i>T</i>	Temperature, K
<i>V<sub>iw</sub></i>	Volumes of injected water, ml
<i>V<sub>pw</sub></i>	Volumes of produced water, ml

## 7.1. INTRODUCTION

The most prospective subsurface areas that have the characteristics to assure the trapping of CO<sub>2</sub> are geological deposits of hydrocarbons and gases. CO<sub>2</sub> storage in hydrocarbon reservoirs is relatively straightforward compared to other geological formations, since the reservoirs are already characterized as a result of oil exploration and production [1]. Thus, first, they are exploited with a developed infrastructure, thereafter, they are charged with CO<sub>2</sub>, using the same transport infrastructure. Besides geological storage, CO<sub>2</sub> injection into depleted oil reservoirs also helps to mobilize hydrocarbons. One of the main advantages of CO<sub>2</sub> compared to other types of gases used for EOR, like methane or nitrogen, is the considerably lower Minimum Miscibility Pressure (MMP). As a consequence, CO<sub>2</sub> is a candidate for EOR and CO<sub>2</sub> storage in a wide range of oil reservoirs [2].

Oil displacement and CO<sub>2</sub> storage rely on the phase behavior of the pure components (the injected gas and hydrocarbons in place) and mixtures of both, and strongly depend on reservoir temperature, pressure, and hydrocarbon composition. The hydrocarbon accumulations are usually found at such depths that, due to pressure and temperature conditions of the reservoirs, the supercritical CO<sub>2</sub> is used. At pressure conditions higher than MMP, CO<sub>2</sub> can achieve miscible conditions with the crude oil, and satisfactory solubility in the formation water [3]. However, shallow reservoirs as well are candidates for CO<sub>2</sub> injections, for example, when exceptionally low reservoir temperatures, e.g. permafrost, are present [4]. In these cases, temperatures are below the critical CO<sub>2</sub> temperature and, thus, provide an opportunity for liquid CO<sub>2</sub> injection and storage. Even if, due to reservoir characteristics, CO<sub>2</sub> does not achieve full miscibility with oil, it partially dissolves in oil, leading to swelling and viscosity reduction. In the immiscible displacement process, larger volumes of stored CO<sub>2</sub> than in the miscible displacement process can be expected [5]. Another effective injection strategy for oil recovery and CO<sub>2</sub> storage could be CO<sub>2</sub>-enriched water. The carbonated water is considered to sweep oil more efficiently than a CO<sub>2</sub> flooding, because of the lower mobility and density contrasts.

Experimental and theoretical studies on CO<sub>2</sub>-EOR coupled with storage in depleted oil fields are rather limited. Existing studies usually show a theoretical approach without verification by experimental work [3, 6–8], or are dedicated to reservoir simulation [9–14]. Xiao et al (2011) [15] conducted a theoretical study of coupled CO<sub>2</sub>-EOR in the SACROC unit in the Permian Basin. They conclude that CO<sub>2</sub> sequestration could be increased by decreasing the mobility of CO<sub>2</sub>. Ghomian (2008) [9] reported that, the effects of the produced gas/oil ratio constraint, production and the injection well types and injection scheme are the most sensitive parameters for maximizing both profit and amount of stored CO<sub>2</sub>. Bachu et al. (2003) [7] reported an influence of the strength of an underlying aquifer on oil recovery and CO<sub>2</sub> storage capacity and found a reduction of the CO<sub>2</sub> storage capacity by 3% for a weak aquifer and by 50% for a strong aquifer. Experimental and theoretical work on CW-EOR coupled with storage were discussed in Chapter 1.

In this study, laboratory core-flooding experiments were conducted to investigate the potential for both enhanced oil recovery and storage of CO<sub>2</sub> at different flooding scenarios. The described experiments comprise CO<sub>2</sub> injection into vertical cylindrical Ben-

theimer cores at a constant flow rate, after conducting water flooding to mimic depleted oil reservoirs. Computed Tomography scanning was used to visualize the distribution of different phases through time and to determine saturation profiles.

The objective of this study was twofold: (1) to investigate the variation in injection scenarios on tertiary oil recovery, and (2) to quantify the CO<sub>2</sub> trapping, as a preliminary study for designing optimal conditions for CO<sub>2</sub> core floods in sandstone type reservoirs. In this chapter, first, the methods and results at 50 bar back pressure are described, followed by comprehensive tables with results at other pore pressures.

## 7.2. THEORETICAL CO<sub>2</sub> STORAGE CAPACITY

The CO<sub>2</sub> storage capacity of a reservoir includes the CO<sub>2</sub> that remains in the reservoir after completion of an EOR operation and any additional volume of CO<sub>2</sub> that can be injected after the EOR phase. According to the CO<sub>2</sub> mass storage capacity ( $M_{CO_2t}$ ) model [1], the theoretical storage capacity with experimental results were compared. The calculations of  $M_{CO_2t}$  are based on the primary reservoir properties such as oil in place, recovery factor, temperature, pressure, rock characteristics and CO<sub>2</sub> phase behavior:

$$M_{CO_2t} = \rho_{CO_2r} [R_f A h \phi (1 - S_w) - V_{iw} + V_{pw}], \quad (7.1)$$

where  $\rho_{CO_2r}$  is density of CO<sub>2</sub> at reservoir conditions;  $R_f$  is a recovery factor,  $A$ ,  $h$ ,  $\phi$ ,  $S_w$  stands for area, thickness and porosity of the reservoir and water saturation, respectively, and  $V_{iw}$  and  $V_{pw}$  are injected and produced volumes of water. In addition, the mass balance of injected gas is taken into account for CO<sub>2</sub> storage estimation. In the calculations of CO<sub>2</sub> storage, the CO<sub>2</sub> storage efficiency can be defined as the mass of stored CO<sub>2</sub> divided by the mass of CO<sub>2</sub> injected, with the assumption that the entire pore space is filled [16].

## 7.3. EXPERIMENTAL APPROACH

### 7.3.1. MATERIALS

**Core samples and core holder.** Core displacement tests were carried out on the Ben-theimer Sandstone (BS) cores. BS matrix is represented by a monocrystalline detrital quartz with authigenic overgrowth (91.7 wt%) and by main accessory minerals (8.3 wt%), such as feldspars, iron (hydr)oxides and clays. Grains and pores exhibit homogeneities represented by well sorted, rounded to sub-rounded grains with a regular and narrow pore-size distribution. Porosity and permeability were measured during the flow experiments and calculated from CT-scans (Table 7.1). The detailed characteristics of the rock can be found in Chapter 2.

Core samples with a diameter of 3.8 cm and a length of 17 cm were drilled with a water-cooled diamond saw and dried in an oven at 323 K for 72 hours. Next, the core samples were surrounded by a layer of epoxy glue to avoid bypassing of fluids along the side of the core. The thickness of the epoxy layer and the penetration depth into the core sample were estimated with CT-scans resulting in an effective core diameter further used for pore volume calculations. Dried samples were placed in the core holder. The core holder was made of PolyEther Ether Ketone (PEEK), a material of good mechanical properties able to stand high pressures and temperatures.

Table 7.1: Properties of Bentheimer sandstone cores used in the experiments.

Material	Dimensions [cm]		Mineralogy [wt%]		Porosity [%]	Brine permeability [D]
Core I <sub>a</sub>					23	2.6±0.1
Core I <sub>b</sub>					24	3.2±0.1
Core I <sub>c</sub>	Diameter	3.8±0.1	Quartz	91.70	25	2.9±0.1
Core II	Length	17.0±0.1	Feldspars	4.86	23	2.5±0.1
Core III			Clay minerals	2.68	24	2.5±0.1
Core IV			Trace	0.76	25	2.9±0.1

**Fluids.** In the experiments, the operational wetting phase was water, the intermediate wetting phase was oil and the non-wetting phase was carbon dioxide. *Water:* Synthetic brine, used in this study, consists of degassed, demineralized water with 0.1 M sodium chloride (NaCl). *Oil:* N-Hexadecane doped with 10 vol% 1-Iodo-hexadecane was used as the oleic phase. *Carbon dioxide:* CO<sub>2</sub> with a purity of 99.95% (Linde Gas Benelux<sup>TM</sup>) was used as provided for core saturation and oil displacement experiments, without further treatment. The physical properties of the operational fluids and gases at the experimental conditions are presented in Table 7.2. *Carbonated Water:* CW solution was prepared by filling a cylinder with 80 vol.% of water and then introducing pure CO<sub>2</sub> into the pressurized system. The solution was mixed by a magnetic stirrer until reaching equilibrium at the specified operational conditions.

Table 7.2: Properties of operational fluids and gases at experimental condition.

Fluid property	Experiment	Brine	CO <sub>2</sub>
	I <sub>a</sub>	1002.7	52.9
	I <sub>b</sub>	1002.9	80.9
Density (kg/m <sup>3</sup> )	I <sub>c</sub>	1003.3	140.9
	II	1003.5	800.4
	III	1000.1	436.2
	IV	1000.1	1020.1
	I <sub>a</sub>	1.004	0.0151
	I <sub>b</sub>	1.004	0.0155
Viscosity (mPa·s)	I <sub>c</sub>	1.003	0.0167
	II	0.938	0.0707
	III	0.726	0.0310
	IV	0.726	0.728 (CW)

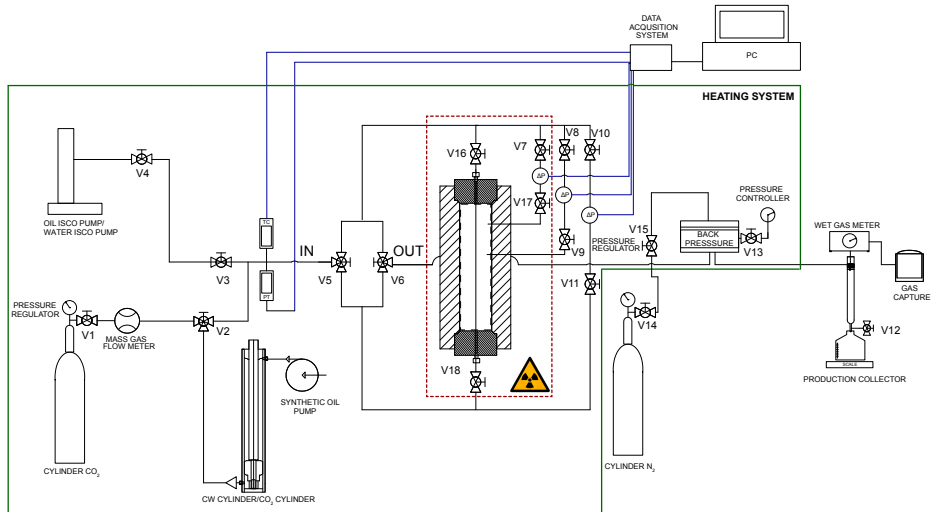


Figure 7.1: Experimental setup for the study on combined EOR and CO<sub>2</sub> storage.

### 7.3.2. EXPERIMENTAL SETUP

Figure 7.1 shows schematically the setup used to conduct core flood experiments. The core flow setup consists of a vertically-placed core holder. A radial confining pressure was applied through the core holder wall to compensate for the pore pressure. On the upstream side, the core holder was connected to the different injection systems, depending on the injected fluid. A high-pressure Quizix<sup>TM</sup> QX pump was used to inject water, to pressurize the system and, subsequently, to inject carbon dioxide into the system. The Quizix<sup>TM</sup> QX pump was further connected in series to the water or CO<sub>2</sub> vessels, respectively. To inject CW, the inlet was connected to a double acting cylinder accumulator, connected to the pump injecting silicon oil. To inject oil, the core holder was connected to the high-pressure ISCO pump. On the downstream side of the core holder, the production line led to a back-pressure regulator and, depending on the injection fluids, to a fraction collector or to a glass CO<sub>2</sub>/oil/water separator. Produced CO<sub>2</sub> was redirected to a wet gas meter (Schlumberger). The pressure,  $P$ , in the system and pressure difference,  $\Delta P$ , over the length of the sample, were measured by a system of pressure gauges before and after the core. The whole experimental setup was placed in a heated build chamber, isolated with Mylar films located on the table of a third generation SAMATOM Volume Zoom Quad slice scanner. The temperature was monitored by a system of 10 thermocouples, placed both in the tubing lines of the system and in the thermal box.

### 7.3.3. EXPERIMENTAL PROCEDURE

*Initial core saturation:* The core was initially dried by CO<sub>2</sub> flushing at atmospheric back pressure. Next, the system was vacuumed. First, the water was from the bottom injected into the core at ambient conditions and at 1 ml/min. Subsequently, the system was slowly pressurized to 25 bar. 10 Pore Volumes (PV) of water were injected to achieve

complete dissolution and removal of remaining CO<sub>2</sub>, and a full water saturation of the core. The water production line was connected to the production container and the effluent was monitored. Permeability was determined by measuring pressure drops at different flow rates. Then, the system pressure was increased to the pre-defined operational pressure and temperature conditions (Table 7.3) and permeability measurements were repeated. *Primary drainage*: Oil was injected from the top of the core at 2.5 ml/min, in order to meet the requested injection capacity. *Imbibition*: The core was water flooded to a residual oil saturation with water at 1 ml/min (Table 7.3). *CO<sub>2</sub> stream injection*: After imbibition, flooding was switched to CO<sub>2</sub> or CW, depending on the injection scenario. The outlet was connected to the production collector (water and oil) and the "wet gas" meter. Subsequently, the amount of CO<sub>2</sub> trapped in the core was calculated.

#### 7.3.4. CT SCANNING

The imaging settings used in the experiments are shown in Table 7.3. A series of 8 slices per scan were recorded where the thickness between CT slices was set to 1 mm. To obtain

Table 7.3: Overview of conducted experiments.

	I <sub>a</sub>	I <sub>b</sub>	I <sub>c</sub>	II	III	IV
Fluid		Gas		Liquid	Super-critical	CW
Back Pressure (bar)	25	35	50	80	80	80
Temperature (K)	293	293	293	296	308	308
Pore Volume (ml)	41.8	44.5	42.6	41.8	44.1	45.7
Initial oil saturation ( <i>S<sub>oi</sub></i> )	0.77	0.74	0.82	0.82	0.8	0.81
Irreducible water saturation ( <i>S<sub>iir</sub></i> )	0.23	0.26	0.19	0.18	0.2	0.19

the porosity,  $\varphi$ , of the dry cores from the measured coefficients in Hounsfield units (HU), the following equation was used [17]

$$\varphi = \frac{HU_w - HU_g}{HU_{ws} - HU_{gs}}. \quad (7.2)$$

The subscripts ws and gs refer to water and gas HU numbers, whereas w and g represent water- and gas-saturated core, respectively.

At each stage of the experiment, the distribution of fluid saturation and position of the front were determined with CT-scans by eliminating the rock contribution. The oil saturation,  $S_o$ , during drainage and imbibition was calculated according to [17, 18]

$$S_o = \frac{HU_{wo} - HU_w}{HU_o - HU_w}. \quad (7.3)$$

Oil,  $S_o$ , water,  $S_w$ , and CO<sub>2</sub> saturation,  $S_g$ , in the core during the CO<sub>2</sub> stream injection



were obtained by [17]:

$$S_o = \frac{[(HU_{wog})_1 - (HU_w)_1][(HU_g)_2 - (HU_w)_2] - [(HU_{wog})_2 - (HU_w)_2][(HU_g)_1 - (HU_w)_1]}{[(HU_o)_1 - (HU_w)_1][(HU_g)_2 - (HU_w)_2] - [(HU_o)_2 - (HU_w)_2][(HU_g)_1 - (HU_w)_1]} \quad (7.4)$$

$$S_g = \frac{[(HU_{wog})_1 - (HU_w)_1][(HU_o)_2 - (HU_w)_2] - [(HU_{wog})_2 - (HU_w)_2][(HU_o)_1 - (HU_w)_1]}{[(HU_o)_2 - (HU_w)_2][(HU_g)_1 - (HU_w)_1] - [(HU_o)_1 - (HU_w)_1][(HU_g)_2 - (HU_w)_2]} \quad (7.5)$$

$$S_w = 1 - S_o - S_g. \quad (7.6)$$

where the subscripts 1 and 2 correspond to different energy levels of 120 and 140 keV, respectively.

## 7.4. RESULTS AND DISCUSSION

In the following section, the core floods at 50 bar and 295 K are discussed in detail. The results of all conducted experiments are presented in tables for the purpose of comparison.

### 7.4.1. BASELINE EXPERIMENT

**Initial core saturation.** The series of CT images recorded at different injected PVs are presented in Figure 7.2. The most left image in the dashed box represents a dry core and the most right image (28 water PV injected) represents a core fully saturated with water. A change in the color of the images from blue to yellow depicts the frontal displacement of gas by water. Water breakthrough occurs at about 0.8 PV. The color change to orange at the final stage of the process results from dissolution and removal of CO<sub>2</sub> from the core and from fully saturated pore space with water ( $S_w = 1$  at 28 PV);

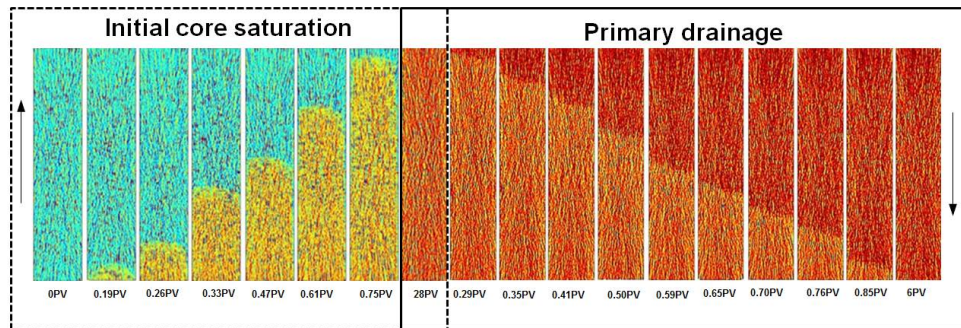


Figure 7.2: CT images of the progressing core saturation during initial core saturation (dashed box) and primary drainage (solid box). CT scan at 28 PV corresponds to  $S_w = 1$ .

**Drainage and imbibition.** The saturation maps of Bentheimer sandstone during drainage are presented in Figure 7.2 in the solid box. The color change from orange

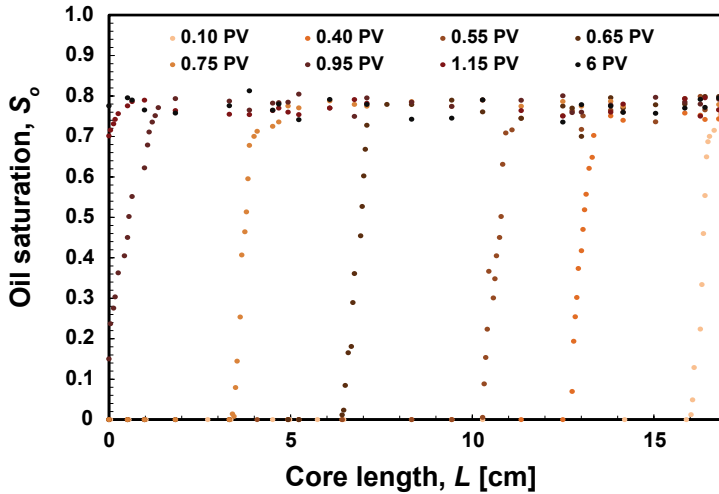


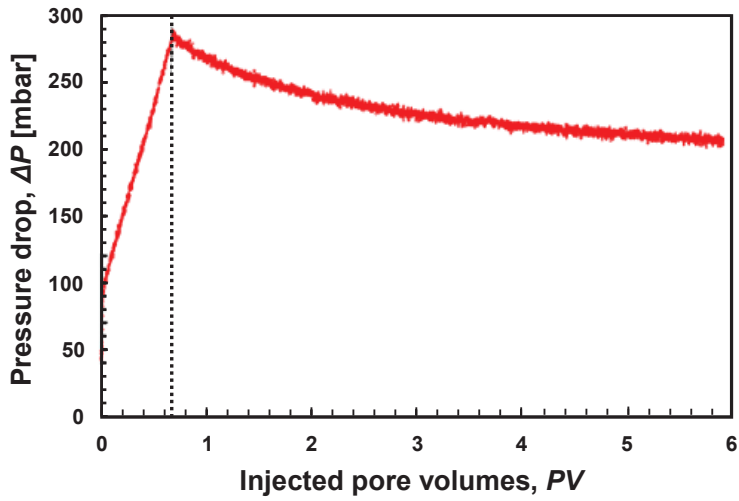
Figure 7.3: Oil saturation profiles for drainage.

to red indicates the displacement of water by oil. In addition, the oil saturation profile for 6 PV of oil injection is shown in Figure 7.3. Figures 7.2 and 7.3 indicate a Buckley-Leverett displacement. The saturation changes in the core show a piston-like profile, the front advancing with the change from high  $S_w$  to high  $S_o$  until breakthrough. Oil breakthrough occurred at  $\sim 0.9$  PV. The oil saturation at the breakthrough time at the end of the core was low due to a capillary end effect, however, it increased with a further injection of oil. At the end of primary drainage  $S_{irr} = 0.19$ . The obtained value is consistent with the previously measured data for Bentheimer sandstone [19].

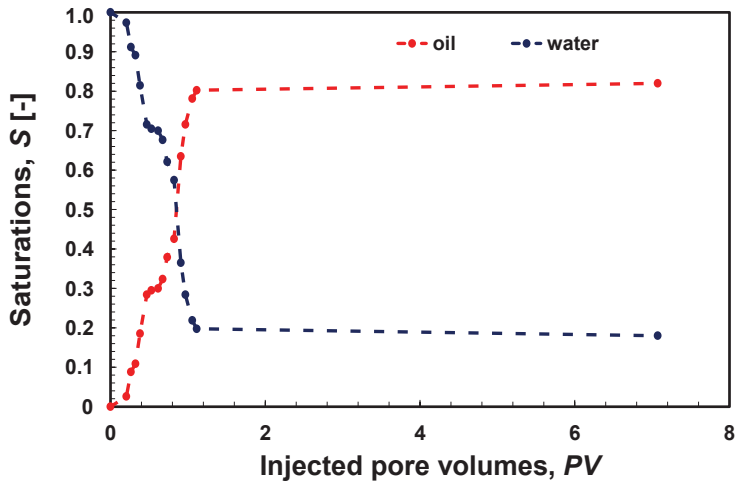
Figure 7.4a shows the differential pressure over PV of injected oil, representing the typical characteristics of a drainage process with an early oil breakthrough accompanied by a long tail of oil production that gradually reaches a plateau. At decreasing water saturation, the capillary pressure rises, causing an increasing injection pressure when oil is injected into the system. Each new pressure level means that another pore-size class would be required to force water out. Figure 7.4b presents the changes of average oil/water saturation in the core.

The kinetics of oil displacement are presented against pressure, water cut and saturation data (respectively Figures 7.5a and 7.5b). Figure 7.5a shows that after the breakthrough and fast initial oil production, the oil production was reduced to almost zero (at breakthrough 93.3% of the totally produced oil was recovered). Hence, it instantly reached the plateau after breakthrough and the pressure difference response shows a long tail of water production. It confirms the water-wet properties of Bentheimer Sandstone [20].

Figure 7.6 shows the oil saturation profile during imbibition. The behavior of the sharp shock region, followed by a refraction wave, is similar to the behavior observed during primary drainage. However, the influence of capillary pressure on the moving

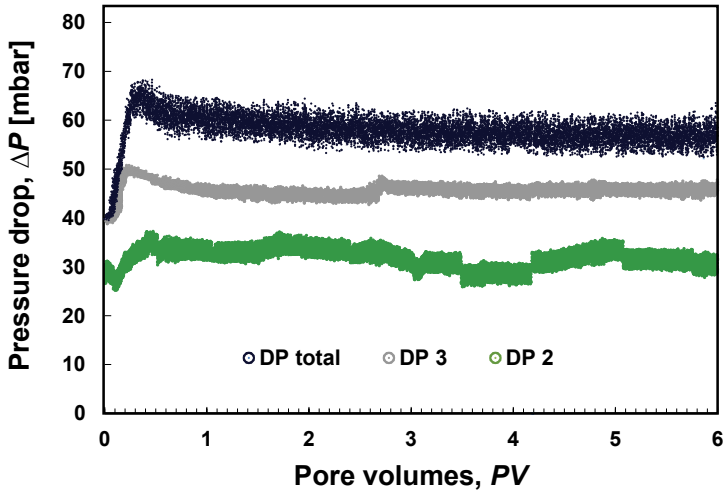


(a)

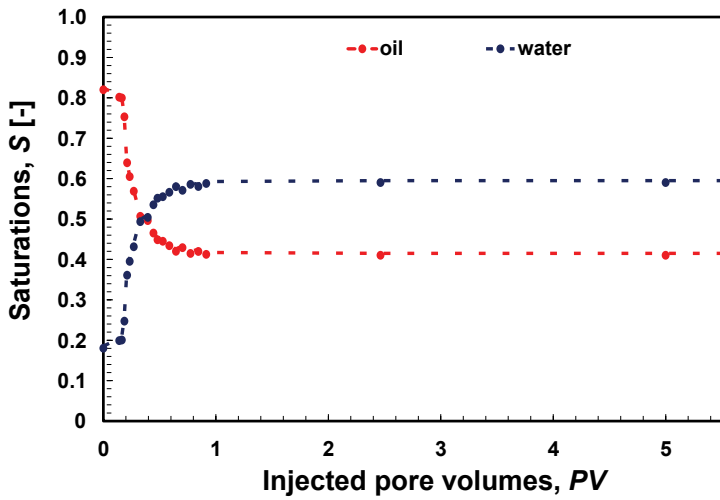


(b)

Figure 7.4: (a) Pressure drop across the core during primary drainage; (b) Average oil and water saturation during primary drainage.



(a)



(b)

Figure 7.5: (a) Pressure drop across the core and water cut during water flooding; (b) Average oil and water saturation during waterflooding.

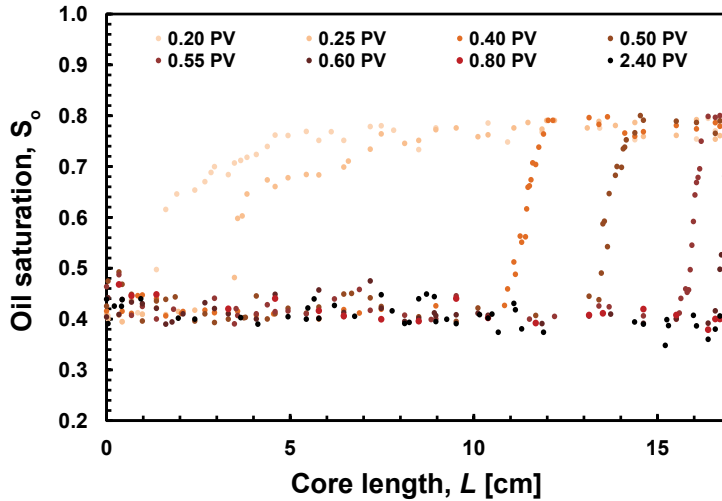


Figure 7.6: Oil saturation profiles for imbibition.

front is more visible. Ahead of the front, water saturation is irreducible and behind the front, water saturation is increased. The saturation profiles (Figure 7.5b) indicate the residual oil saturation at  $0.41 \pm 0.02$ . The remaining oil was uniformly distributed over the core.

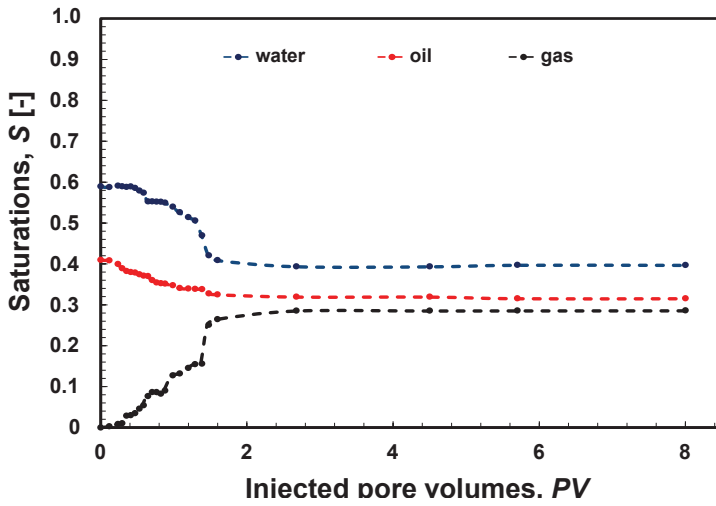
**CO<sub>2</sub> injection.** Directly after imbibition, at gravity stable conditions, a carbon dioxide stream was injected to mobilize and recover the remaining oil. 100 PV of CO<sub>2</sub> were injected at 1 ml/min. In this paragraph, the first 8 PV are discussed, as further injection did not show significant changes.

Figure 7.7a shows averaged saturation profiles during CO<sub>2</sub> injection. The initial saturation corresponds to the end of the water injection. The oil saturation decrease from  $0.41 \pm 0.02$  to  $0.31 \pm 0.02$ , corresponding to 10% of initial oil in place. The increase in the oil recovery as a result of CO<sub>2</sub> injection is related to the relative permeability effects.

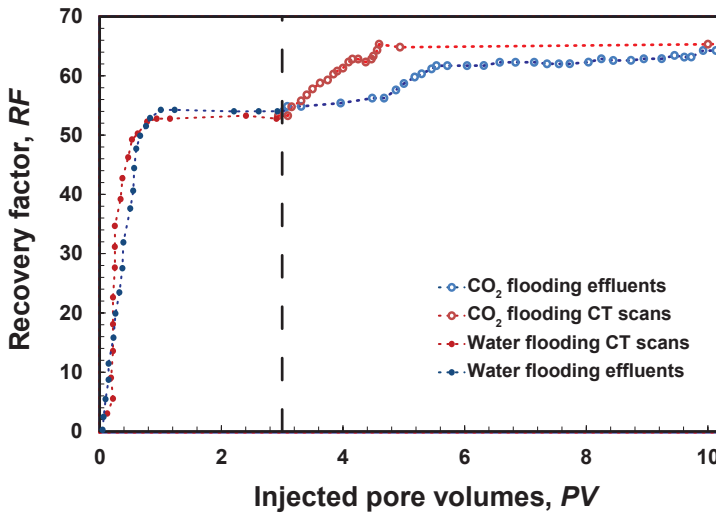
During the experiment, significant fluctuations in the pressure drop were observed indicating the presence of three phases in the core due to dissolution processes. Figure 7.7b shows the recovery factor obtained during water flooding followed by CO<sub>2</sub> injection. The recovery factor obtained through CT scans and effluent measurements are in line. Residual oil saturation of ~47% was obtained by water flooding and an additional 18% by CO<sub>2</sub> injection. The highest recovery of oil was observed until 4.0 PV of CO<sub>2</sub> were injected.

### CO<sub>2</sub> STORAGE

Figure 7.8 presents the ratio of injected/produced mass of CO<sub>2</sub> versus injected pore volumes of CO<sub>2</sub>. After  $\sim 30.0 \pm 5.0$  injected PV the ratio of injected/produced mass reaches 1. It shows that despite additional injection, no more CO<sub>2</sub> is being stored in the core. For other comparison studies, the CO<sub>2</sub> stored in the system is compared to the estimates of CO<sub>2</sub> stored.



(a)



(b)

Figure 7.7: (a) Oil, water and gas saturation during CO<sub>2</sub> flooding. (b) Recovery factor based on effluents and CT scans.

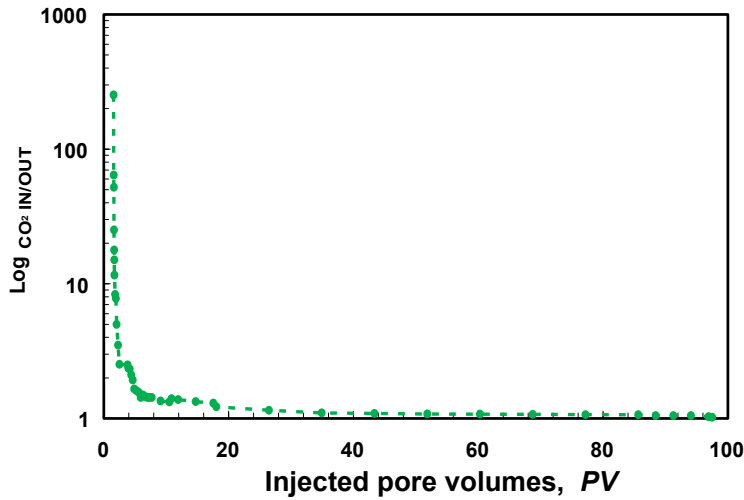


Figure 7.8: The ratio of injected/produced CO<sub>2</sub> versus injected PV.

#### 7.4.2. EFFECT OF INJECTION SCENARIOS ON OIL RECOVERY

Table 7.4 presents the results for water flooding followed by different injection scenarios: gas CO<sub>2</sub>, liquid CO<sub>2</sub>, supercritical CO<sub>2</sub>, and CW flooding. During water flooding, recovery factors in the range between 49-54% were obtained. The oil left behind after water floods was trapped by capillary forces and rock-fluid interactions [21]. The Recovery Factors (RF)s are slightly higher than the results obtained by Simjoo 2012 (46% [19]) and similar to the results of Andrianov et al. (49-56% [22]). The results show that in all CO<sub>2</sub> injection scenarios, the injection of CO<sub>2</sub> displaces the water and leads to incremental oil recovery. The largest RFs were obtained for liquid CO<sub>2</sub> injection ( $RF = 23\%$ ) and the smallest for gas CO<sub>2</sub> ( $RF = 5 - 11\%$ ). There is a direct relation between the amount of dissolved CO<sub>2</sub> in oil and the obtained ultimate recovery. The oil recovery is a result of the mass transfer of CO<sub>2</sub> from the water into the oil phase. The main effect that controls CO<sub>2</sub> transfer into oil for both pure CO<sub>2</sub> and CW injections is preferential CO<sub>2</sub> solubility in oil above the solubility of CO<sub>2</sub> in water. Dissolved CO<sub>2</sub> reduces the oil viscosity, causes the oil swelling and, as a result, increases the oil mobility, the oil relative permeability and enhances oil recovery [23]. In the cases where lower density CO<sub>2</sub> was injected, the effect of the density difference between CO<sub>2</sub> and both oil and water led to gravity override. A significant role of buoyancy in relatively homogeneous, highly permeable reservoirs, was previously reported [24, 25].

Direct comparison of the data, obtained in this study and with data from the literature, is challenging as little previous experimental data could be found for the  $P$ - $T$  conditions and the salinity used. The literature RFs are in a range between 10-30% [22]. In this work, the obtained RF for CWF was 15%. Incremental oil recovery in the CWF process is related to CO<sub>2</sub> transfer from injected water into oil. It results in a volume increase of oil and viscosity reduction and a further mobility increase. Therefore, the efficiency of the CWF is limited by the chemistry of the water and the amount of dissolved CO<sub>2</sub>. The

limit is driven mainly by pressure, temperature and salinity of the injection water. The RF for CWF is consistent with the value obtained by Asghari [26] and is lower than the measured SCAL data for the sand pack [27].

In addition, the pressure effect in the gas CO<sub>2</sub> injection was studied. The highest oil recovery was achieved at the highest applied pressure (50 bar). Results are as well correlated to CO<sub>2</sub>-oil phase behavior.

Table 7.4: Oil recovery factor obtained during water floods and CO<sub>2</sub> stream floods.

	I <sub>a</sub>	I <sub>b</sub>	I <sub>c</sub>	II	III	IV
Recovery Factor by water (% of OIIP)	49	53	52	50	53	54
Recovery Factor by CO <sub>2</sub> (% of OIIP)	5	6	11	23	20	15

### 7.4.3. EFFECT OF EXPERIMENTAL CONDITIONS ON CO<sub>2</sub> STORAGE

The amount of CO<sub>2</sub> stored in the porous media is presented in Table 7.5. Based on the experimental results, the maximum storage efficiency for different pressures in the gas phase was achieved at 50 bar. At 50 bar, CO<sub>2</sub> has the highest density and achieves larger solubility in both oil and water.

Overall, the highest storage was achieved by liquid CO<sub>2</sub> injection for both CO<sub>2</sub> and CW injection. The CO<sub>2</sub> storage capacity is reduced in all scenarios by the presence of water introduced during water flooding and by irreducible water remaining in the system as a result of capillary forces. It is concluded by the mass balance that, at the end of an experiment, the major part of the porosity was filled with free CO<sub>2</sub> for CO<sub>2</sub> floods and with CW for CW floods. Remaining stored CO<sub>2</sub> is dissolved in oil and water. Based on the above results, the following trapping mechanisms contributing to the total storage efficiency can be distinguished: the mobile CO<sub>2</sub> and the solubility trapping. The efficiency of CW lies in the primary dissolution of CO<sub>2</sub> in the aqueous phase eliminating the free CO<sub>2</sub> phase. The efficiency is similar to the value obtained by Hasanvand et al. (2013) [28].

Table 7.5: Mass balance for CO<sub>2</sub> storage for the three experiments.

Experiment	Total CO <sub>2</sub> storage efficiency (%)	Theoretical total CO <sub>2</sub> storage efficiency (%)
I <sub>a</sub>	16.9±0.1	19.2
I <sub>b</sub>	19.1±0.1	22.3
I <sub>c</sub>	23.7±0.1	25.1
II	39.9±0.1	41.4
III	36.7±0.1	38.0
IV	41.3±0.1	43.0

The theoretical values included in Table 7.5 show that the theoretical value of stored CO<sub>2</sub> overestimates the storage capacity of ~15%. The differences with the experimental



results are a consequence of model simplifications. However, the theoretical CO<sub>2</sub> storage capacity model will be useful in the general planning of the CO<sub>2</sub> deposition.

## 7.5. CONCLUSIONS

An experimental study on combined EOR and CO<sub>2</sub> storage was conducted to evaluate the efficiency of the process and to quantify the effect of different injected phases of CO<sub>2</sub>. Based on the experimental results, the following conclusions can be drawn:

- In this laboratory scale study, continuous CO<sub>2</sub> stream injection was proven to be an efficient technique for coupled CO<sub>2</sub> sequestration and EOR;
- In all conducted experiments, CO<sub>2</sub> was sequestered, while at the same time oil was recovered. Incremental recoveries in the range of 11-23% OOIP indicated that the use of CO<sub>2</sub> is an effective EOR technique. Recovery was achieved by oil swelling and reduction in oil viscosity due to CO<sub>2</sub> dissolution; the highest amount of CO<sub>2</sub> stored and oil recovered was at liquid conditions and by CW flooding;
- The buoyancy between the CO<sub>2</sub>, oil and water negatively affects the CO<sub>2</sub> storage and the oil recovery in the case of EOR;
- The process of oil recovery and CO<sub>2</sub> storage is strongly related to the maximum amount of CO<sub>2</sub> that can be dissolved in water and/or oil at specific pressure and temperature conditions;
- The following trapping mechanisms contributing to the total storage efficiency can be distinguished: preferential solubility trapping next to mobile CO<sub>2</sub>.

**REFERENCES**

- [1] S. Bachu, D. Bonijoly, J. Bradshaw, R. Burruss, S. Holloway, N. P. Christensen, and O. M. Mathiassen, *CO<sub>2</sub> storage capacity estimation: Methodology and gaps*, International Journal of Greenhouse Gas Control **1**, 430 (2007).
- [2] S. F. Ali and S. Thomas, *A Realistic Look at Enhanced Oil Recovery*, Scientia Iranica **1** (1994).
- [3] J. Shaw and S. Bachu, *Screening, evaluation, and ranking of oil reservoirs suitable for CO<sub>2</sub> flood EOR and carbon dioxide sequestration*, Journal of Canadian Petroleum Technology **41**, 51 (2002).
- [4] A. Y. Dandekar, *Petroleum reservoir rock and fluid properties* (CRC press, 2013).
- [5] G. Rojas and S. Ali, *Dynamics of subcritical CO<sub>2</sub>/brine floods for heavy-oil recovery*, SPE Reservoir Engineering **3**, 35 (1988).
- [6] B. Hill, S. Hovorka, and S. Melzer, *Geologic Carbon Storage Through Enhanced Oil Recovery*, Energy Procedia **37**, 6808 (2013).
- [7] S. Bachu and J. Shaw, *Evaluation of the CO<sub>2</sub> sequestration capacity in Alberta's oil and gas reservoirs at depletion and the effect of underlying aquifers*, Journal of Canadian Petroleum Technology **42**, 51 (2003).
- [8] A. R. Kovscek, *Screening criteria for CO<sub>2</sub> storage in oil reservoirs*, Petroleum Science and Technology **20**, 841 (2002).
- [9] Y. Ghomian, *Reservoir simulation studies for coupled carbon dioxide sequestration and enhanced oil recovery*, Dissertaion (2008).
- [10] T. Holt, J.-I. Jensen, and E. Lindeberg, *Underground storage of CO<sub>2</sub> in aquifers and oil reservoirs*, Energy Conversion and Management **36**, 535 (1995).
- [11] H. R. Jahangiri and D. Zhang, *Optimization of the net present value of carbon dioxide sequestration and enhanced oil recovery*, in *Offshore Technology Conference* (Society of Petroleum Engineers., 2011).
- [12] A. Kovscek and M. Cakici, *Geologic storage of carbon dioxide and enhanced oil recovery. II. Cooptimization of storage and recovery*, Energy Conversion and Management **46**, 1941 (2005).
- [13] S. Poordad and M. Jamialahmadi, *A Review of Early Opportunity-Analysis on CO<sub>2</sub> Sequestration and Enhanced Oil Recovery for Iran*, Advances in Petroleum Exploration and Development **7**, 13 (2014).
- [14] Y. Xiao, T. Xu, and K. Pruess, *The effects of gas-fluid-rock interactions on CO<sub>2</sub> injection and storage: Insights from reactive transport modeling*, Energy Procedia **1**, 1783 (2009).

- [15] C. Xiao, M. L. Harris, F. P. Wang, R. B. Grigg, *et al.*, *Field Testing and Numerical Simulation of Combined CO<sub>2</sub> Enhanced Oil Recovery and Storage in the SACROC Field*, in *Canadian Unconventional Resources Conference* (Society of Petroleum Engineers, 2011).
- [16] E. O. I. Obi and M. J. Blunt, *Streamline based simulation of carbon dioxide storage in a north sea aquifer*, *Water Resources Research* **42** (2006).
- [17] S. Akin and A. Kovscek, *Computed tomography in petroleum engineering research*, Geological Society, London, Special Publications **215**, 23 (2003).
- [18] B. Niu, W. Yan, A. A. Shapiro, and E. H. Stenby, *Phase identification and saturation determination in carbon dioxide flooding of water flooded chalk using X-Ray computed tomography*, in *Paper SCA2009-19 presented at the International Symposium of the Society of Core Analysts held in Noordwijk, The Netherlands* (2009) pp. 27–30.
- [19] M. Simjoo, *Immiscible foam for enhancing oil recovery*, Ph.D. thesis, TU Delft, Delft University of Technology (2012).
- [20] M. Feali, W. Pinczewski, Y. Cinar, C. H. Arns, J.-Y. Arns, N. Francois, M. L. Turner, T. Senden, M. A. Knackstedt, *et al.*, *Qualitative and quantitative analyses of the three-phase distribution of oil, water, and gas in bentheimer sandstone by use of micro-CT imaging*, *SPE Reservoir Evaluation & Engineering* **15**, 706 (2012).
- [21] D. Green and G. Willhite, *Enhanced Oil Recovery; SPE Textbook Series, Vol. 6; Society of Petroleum Engineers (SPE)*, There is no corresponding record for this reference (1998).
- [22] A. Andrianov, R. Farajzadeh, M. Mahmoodi Nick, M. Talanana, and P. L. Zitha, *Immiscible foam for enhancing oil recovery: bulk and porous media experiments*, *Industrial & Engineering Chemistry Research* **51**, 2214 (2012).
- [23] M. Emera and H. Sarma, *A genetic algorithm-based model to predict CO<sub>2</sub>-oil physical properties for dead and live oil*, *Journal of Canadian Petroleum Technology* **47**, 52 (2008).
- [24] P. Bondor, *Applications of carbon dioxide in enhanced oil recovery*, *Energy Conversion and Management* **33**, 579 (1992).
- [25] D. J. Stephenson, A. G. Graham, R. W. Luhning, *et al.*, *Mobility control experience in the Joffre Viking miscible CO<sub>2</sub> flood*, *SPE Reservoir Engineering* **8**, 183 (1993).
- [26] K. Asghari, M. M. Araghi, F. Ahmadloo, P. Nakutnyy, *et al.*, *Utilization of CO for Improving the Performance of Waterflooding in Heavy Oil Recovery*, in *Canadian International Petroleum Conference* (Petroleum Society of Canada, 2009).
- [27] Y. Dong, C. Ishizawa, E. Lewis, and B. Dindoruk, *Carbonated water flood: what we observed in sand pack experiments*, in *International Symposium of the Society of Core Analysts, Austin, Texas, USA* (2011).

- [28] M. zeinali Hasanvand, M. A. Ahmadi, S. R. Shadizadeh, R. Behbahani, and F. Feyzi, *Geological storage of carbon dioxide by injection of carbonated water in an Iranian oil reservoir: a case study*, Journal of Petroleum Science and Engineering **111**, 170 (2013).



# 8

## CONCLUSION

In this chapter, I summarize the conclusions reached as a result of the research. The main microscopic and macroscopic parameters that control the multiphase displacement and storage processes are the matrix structure, the mineralogical composition and the occurrence of accessory minerals, pore fluids and the interaction between previous. Consequently, the efficiency of CO<sub>2</sub> and CW EOR, combined with CCS, is controlled by wettability. Injected fluids establish a low pH in the system; thus, the surface of the rock and electrokinetic properties of the matrix are influenced, affecting static wettability and wetting kinetics. This effect has an impact on oil recovery and CO<sub>2</sub> storage.

To recognize the previously named interactions, I performed my studies at one type of homogeneous rock, i.e. Bentheimer sandstone, that exhibits minor anisotropy in mineral composition and a narrow band in grain size distribution at block scale (m<sup>3</sup>). At reservoir scale, rocks show heterogeneities where accessory minerals can have a more distinct effect on the flow behavior. A detailed literature review was completed on Bentheimer petrophysics, petrographics and a laboratory characterisation of the grain and pore matrix with its physical properties was conducted (Chapter 2). This base study is the reference for all flow experiments named hereafter. The shallow marine and beach type depositional environment of Bentheimer sandstone gives it a homogeneous, almost isotropic and narrow distribution of pore sizes (10-50 μm diameter of pore throats), resulting in a high permeability ( $k = 1.35 - 3.09$  D) and porosity ( $\phi = 0.23-0.27$ ). It predominantly consists of well-sorted, mostly rounded, monocrystalline detrital quartz with authigenic quartz overgrowth. The uniaxial compressive test proved that the high quartz content results in a uniform mechanical stability (~15 GPa).

The variety of accessory minerals recognized in the Bentheimer sandstone (feldspars, clays and oxides) may lower its chemical and mechanical stability. As a result of the interaction of the sandstone with electrolytes, random dissolution of heterogeneous K-feldspars and precipitation of clays occurred and still occurs (the softening coefficient of Bentheimer is 87.3%). However, apart from an incidental migration of clays that created a clogging zone, no significant effect of the bulk reservoir porosity and permeability was observed. The local accessory minerals concentrations, differences in the crystal

structure and the interaction of the various constituents were validated by surface charge measurements and dispersion in the dielectric permittivity over a range of frequencies (Chapter 3). Accessory amounts of iron oxides were found not to alter the relative electrical permittivity of the solid phase directly. Based on the determined depositional environment and the presented rock characteristics, a general understanding regarding the formation at reservoir scale was developed. However, an exact parameter distribution is still unknown and may only be predicted by a mathematical approach.

Subsequently, I have applied the acquired knowledge of rock composition and grain geometry to study the sensitivity of the reservoir minerals on varying CO<sub>2</sub> concentration in carbonated water flooding (Chapter 4). Since the standard methods to measure wettability, such as the Amott-Harvey tests and the Pendant Drop Cell, meet a number of limitations in estimating the overall wetting state of the rock, I measured it in-situ, during core floods. Via changes in streaming potential, due to different pore pressure drops and changing bulk conductivity values, it is shown that, with rising CO<sub>2</sub> concentration, the stability of the aqueous film at the pore wall decreases. Nevertheless, for the CO<sub>2</sub> saturations investigated in this study, CO<sub>2</sub> storage strength and capacity is maintained.

Experimental results of the Bentheimer sandstone's porous matrix structure, together with results of the flow studies on heterogeneous rock matrices and data available from the literature, show limitations in oil recovery from areas of relatively low flow. For this reason, the subsequent study focused on understanding the mechanisms taking place in minimum flow or "stagnant" zones of a reservoir (Chapter 5 and 6). To mimic the stagnant zones, a monopore glass model was constructed. The monopore study showed that the efficiency of the oil recovery strongly depends on the applied injection scenario, the geometry of the matrix and on residual oil saturation. The overall nature of the flow is determined by the physical properties of CO<sub>2</sub>-rich type fluids and their interactions. It was shown that oil recovery occurs due to gravity forces (liquid CO<sub>2</sub> injection) or to CO<sub>2</sub> diffusion from an injected CO<sub>2</sub> stream into oil (CW, supercritical and near-supercritical CO<sub>2</sub> injection).

## 8

In all experiments, CO<sub>2</sub> diffused into oil resulting in volume expansion, an induced reduction of the viscosity, an improvement of the oil-water mobility ratio and thereby enhanced sweep efficiency of carbonated water flood. Depending on the injection scenario, the scale and the speed of CO<sub>2</sub> diffusion into oil, subsequent oil swelling changes with the phase of the injected CO<sub>2</sub>. The contact between CO<sub>2</sub>-source and oil establishes time-dependent gradients of CO<sub>2</sub> saturation in oil and a progressive oil volume increase. A decreasing effect of diffusion and an increasing role of convection were recognized on the concentration gradient over time. The volume change coefficient in the case of a pure CO<sub>2</sub>-oil contact is much higher than for the CW in all the experiments (~1.5 times larger). At pore scale, I observed the bridging effect of water. The created water barrier snaps off the pore body due to pore-scale capillary instability; it has a limiting effect on oil migration. This phenomenon also occurs in CW; however, it is not limiting the final recovery. The time to recover oil at pore scale, with indirect CO<sub>2</sub> contact through existing water barrier, takes about 25 times more time when compared to direct contact of a CO<sub>2</sub> stream; when compared to CW flooding, it takes 600 times more time.

As a result of Chapter 5 and 6, thinking in field terms, the following mechanisms can be expected. Liquid CO<sub>2</sub> injection may benefit from a favorable density ratio when

compared to supercritical and near-supercritical CO<sub>2</sub> injection and CW flooding. The results developed over the range of flow rates clearly showed the importance of gravity in the DEP systems, when the density difference is in the order of 300 kg/m<sup>3</sup>. The higher density of CO<sub>2</sub> achieved in the liquid injections helps to minimize the risk of leakage. The same accounts for the CW flooding where CO<sub>2</sub> is dissolved in the aqueous phase. When taking into account transport time of operational fluids from the injector to the producer, the limiting concerns recognized at pore scale might not have a significant impact at the field scale. Yet, it could be of importance for the near well bore injection areas.

The general conclusion of my thesis is, that carbonated water injection has a potential of combining oil recovery and, finally, CO<sub>2</sub> storage. It gives an incremental recovery over secondary water flooding and satisfactory storage, that can be explained by a viscosity decrease (Chapter 7). The uniform distribution of CO<sub>2</sub> and the stability of the CW film proven in the laboratory, indicate safe storage at field conditions. However, in comparison to CO<sub>2</sub> flooding investigated in the laboratory, it gives a lower recovery at the same operational conditions. This is a result of CO<sub>2</sub>-favorable miscibility achieved in the pure CO<sub>2</sub> injection. Hence, in favor of the CW process, injectivity improvement is observed, followed by the ability of a simple separation at the production well and a smaller amount of CO<sub>2</sub> required for handling at the injection and production site. The economical attractiveness of carbonated water flooding is twofold: (1) benefits, due to a physical and financial combination of high injectivity and maximum storage capacity, as well as tax credits from CO<sub>2</sub> storage together with EOR; (2) the amount of incremental oil might be profitable in a plausible economic condition. To conclude, the EOR projects with CO<sub>2</sub> storage are challenging due to the involvement of multiple stakeholders, risks in all stages of the investment and the need for monitoring.





# SUMMARY

With increasing emissions of anthropogenic CO<sub>2</sub> and the rising need for defining suitable techniques to recover oil that is left behind after primary and secondary recovery, combining Carbon Capture and Storage (CCS) with Enhanced Oil Recovery (EOR) is gaining importance. Conventional CO<sub>2</sub> flooding is one of such techniques, where, by transferring CO<sub>2</sub> into the oil phase to induce swelling, viscosity and interfacial tension reduction, hydrocarbons are mobilized. CO<sub>2</sub> flooding offers the advantage of high miscibility with oil at relatively low minimum miscibility pressures. However, the main disadvantage is that the buoyancy of CO<sub>2</sub> imposes gravity separation and, in the worst case, leakage from the storage reservoir upwards into the groundwater and, finally, to the surface. Therefore, dissolving CO<sub>2</sub> in water and creating sparkling water (Carbonated Water) as an enhancing agent, has the potential to minimize issues arising during CO<sub>2</sub> flooding. The main objective of this thesis is to examine and define the physical and dynamical processes and the associated phenomena that occur during injection of Carbonated Water (CW) into porous systems containing brine and oil. The second objective is to conduct Carbonated Water Flooding (CWF) studies, within the scope of CO<sub>2</sub> injection, in order to determine similarities, differences and related advantages and disadvantages between the two processes. The thesis consists of four separate studies that cover detailed research on (1) the fluid–rock interactions, i.e. electrokinetic phenomenon, which were investigated via zeta potential and potentiometric titration measurements; (2) fluid–fluid interactions or fundamental mechanisms, that control mobilization and recovery of residual oil, e.g. molecular diffusion of CO<sub>2</sub> from a CO<sub>2</sub>-rich source (carbonated water/CO<sub>2</sub>) into oil; (3) fluid–fluid–rock interactions, i.e. thermodynamics, multiphase flow and mass transfer via core flooding experiments, and; (4) a detailed study on Bentheimer sandstone as the reference reservoir rock. Rock characterization was conducted by qualitative and quantitative laboratory and theoretical analysis. To define the previously listed interactions, the thesis starts with evaluating Bentheimer sandstone properties and their characteristics to advance the understanding on the mineral accessory, the grain surface physical and the electrical transport properties. A detailed literature review was done on Bentheimer petrophysics, the petrographics, and a laboratory characterization of the grain and pore matrix with its physical properties was conducted. Bentheimer sandstone predominantly consists of well-sorted, mostly rounded, monocrystalline detrital quartz with authigenic quartz overgrowth. Bentheimer sandstone shows a homogeneous, almost isotropic, and narrow distribution of pore sizes (10-50 μm diameter of pore throats), resulting in a high permeability ( $k = 1.35\text{--}3.09$  D) and porosity ( $\phi = 0.23 - 0.27$ ). A uniaxial compressive test proved that the high quartz content results in a uniform mechanical stability (~15 GPa). At the reservoir scale, the investigated rock shows heterogeneities, where accessory minerals can have a more distinct effect on the flow behavior. Furthermore, the effect of the accessory constituents, besides quartz (clays, feldspars, and oxides), on the physical and

electrical transport properties was investigated. Fluids, especially formation water, CW, and CO<sub>2</sub>, may cause fluid-rock interaction and result in geochemical reactions, such as dissolution and recrystallization, that lead to changes in mineralogy and rock structure. Moreover, the fluid flow path characteristics and the electrical response can be modified. The local accessory mineral concentrations, differences in the crystal structure and the interaction of the various constituents were validated by surface charge measurements and dispersion in the dielectric permittivity over a range of frequencies. Based on the determined depositional environment and the presented rock characteristics, a general understanding regarding the formation at reservoir scale was developed. Subsequently, the acquired information of rock composition and grain geometry was implemented to study the sensitivity of the reservoir minerals on the interaction between rock and fluids, through experimental work and theory. The sensitivity depends on the rock surface charge variations and wettability and leads to adsorption or/and chemical mobilization. Therefore, the in-situ Bentheimer sandstone surface behavior in an aqueous solution (water and brine) was investigated, with and without dissolved CO<sub>2</sub>. Streaming potential experiments show that, with a rising CO<sub>2</sub> concentration, the stability of the aqueous film at the pore wall decreases. Nevertheless, for the CO<sub>2</sub> saturation investigated in this study, CO<sub>2</sub> storage strength and capacity was maintained. Experimental results of the Bentheimer sandstone's porous matrix structure, together with experimental results of the flow studies on heterogeneous rock matrices and data available from the literature, show limitations in oil recovery from areas of relatively low flow. For that reason, the succeeding study was focused on understanding the mechanisms taking place in minimum flow or "stagnant" zones of a reservoir. To mimic the stagnant zone, a glass micromodel with a single dead-end pore was designed. The study showed that the efficiency of the oil recovery strongly depends on the applied CO<sub>2</sub> injection scenario, the geometry of the matrix, and on the residual oil saturation. The overall nature of the flow was determined by the physical properties of CO<sub>2</sub>-rich type fluids and their interactions. Having the knowledge of fluid-fluid behavior at different density ratios and at various flow rates, the phase behavior of the CW-oil system was investigated in indirect pore-scale diffusion experiments. In essence, swelling of oil due to CO<sub>2</sub> diffusion under *P-T* conditions was recorded and visualized over time. Pressure and oil composition dependent recovery of oil occur and a dominant role for diffusion in the CW recovery process was determined. In addition, a mathematical model was developed with Comsol Multiphysics™ that explains the processes observed in the experiments. The results predicted by the model were linked to the results obtained during the experiments and the diffusion coefficient was determined. In all experiments, CO<sub>2</sub> diffused into oil resulting in a volume expansion, an induced reduction of the viscosity, an improvement of the oil-water mobility ratio and, thereby, enhanced sweep efficiency of carbonated water flood. In the last part, the thesis focuses on the overall mechanisms controlling oil displacement and CO<sub>2</sub> sequestration, the interactions between pore and the matrix system, and between the flow and phase equilibrium. Carbonated water injection has a potential of combining oil recovery with CO<sub>2</sub> storage. It gives an incremental recovery over secondary water flooding and satisfactory storage that can be explained by viscosity decrease. The laboratory results can be used as input parameters for upgrading and building a model for three-phase flow in clastic rocks.

# SAMENVATTING

Met stijgende emissies van antropogene CO<sub>2</sub> en de toenemende behoefte aan een definitie om toepasselijke technieken te formuleren om de achtergebleven olie na primaire en secundaire winning te herwinnen neemt het combineren van 'Carbon Capture & Storage' (CCS) met 'Enhanced Oil Recovery' (EOR) toe aan belang. Conventionele CO<sub>2</sub> overstroming is een van dergelijke technieken, waar, door de overdracht van CO<sub>2</sub> in de olie fase om zwellen, viscositeit en drukvermindering van de interface te weeg te brengen, koolwaterstoffen worden gemobiliseerd. CO<sub>2</sub> overstroming biedt het voordeel van een hoge mengbaarheid met olie bij een relatief lage minimale mengbaarheidsdruk. Echter, het grootste nadeel is dat het drijfvermogen van CO<sub>2</sub> scheiding van de zwaartekracht en, in het ergste geval, lekkage uit het opslagreservoir in het grondwater en ten slotte naar het oppervlak veroorzaakt. Daarom, heeft ontbinding van CO<sub>2</sub> in water en het creëren van bruiswater (koolstofhoudend water) als een verbeteringsagent, het potentieel om problemen tijdens CO<sub>2</sub> overstromingen te minimaliseren.

Het hoofddoel van deze thesis is om de fysieke en dynamische processen en de bijbehorende fenomenen die zich tijdens de injectie van koolzuurhoudend water (CW) in poreuze systemen met pek en olie voordoen, te onderzoeken en te definiëren. Het tweede doel is om koolzuurhoudende wateroverstromingen (CWF) studies binnen het kader van CO<sub>2</sub> injectie uit te voeren, teneinde de overeenkomsten, de verschillen en de betreffende voor- en nadelen tussen de twee processen te bepalen. De thesis bestaat uit vier afzonderlijke studies die betrekking hebben op het onderzoek naar (1) vloeistof-gesteente interacties, d.w.z. het elektrokinetische fenomeen werd onderzocht via zeta potentiële en potentiometrische titratie metingen; (2) vloeistof-vloeistof interacties of fundamentele mechanismen, waarmee mobilisatie en terugwinning van residuele olie, bijvoorbeeld een moleculair verspreiding van CO<sub>2</sub> vanuit een CO<sub>2</sub> rijke bron (koolzuurhoudend water/CO<sub>2</sub>) in olie; (3) vloeistof-vloeistof-gesteente interacties, d.w.z. thermodynamiek, multi fase stroming en massaoverdracht via kern overstromingsexperimenten; en, (4) een gedetailleerde studie over Bentheimer zandsteen als het referentie reservoir gesteente. Een karakterisering van het gesteente werd uitgevoerd door kwalitatieve en kwantitatieve laboratorium- en theoretische analyses.

Voor het definiëren van de eerder genoemde interacties, begint de thesis met de evaluatie van de eigenschappen en bijbehorende kenmerken van Bentheimer zandsteen om de minerale accessorische eigenschappen, de fysieke oppervlakte van de korrel en de elektrisch vervoerseigenschappen te begrijpen. Een uitgebreide literatuurstudie werd gedaan op petro-fysica en petro-graphica van Bentheimer, en een laboratorium karakterisering van de korrel en porie matrix met haar fysieke eigenschappen werd uitgevoerd. Bentheimer zandsteen bestaat voornamelijk uit goed gesorteerde, meestal ronde, mono-kristallijn geërodeerde kwarts met authigenische kwarts begroeiing. Het toont een homogene, bijna isotrope, en kleine distributie van porie-grootte (10-50 μm diameter van porie keel), resulterend in een hoge permeabiliteit ( $k = 1.35-3.09$  D) en porositeit

( $\phi = 0.23 - 0.27$ ). Uit een uni axiale drukkrachttest bleek dat het hoge kwarts gehalte resulteert in een uniforme mechanische stabiliteit ( $\sim 15$  GPa). Op de schaal van het reservoir, toont het onderzochte gesteente heterogeniteiten, waar secundaire mineralen een duidelijker effect kunnen hebben op de gedraging van de stroming.

Bovendien werd het effect van de secundaire bestanddelen, naast kwarts (klei, feldspars en stikstofoxiden), op het transport van fysieke en elektrische eigenschappen onderzocht. Vloeistof, vooral formatie water CW en CO<sub>2</sub>, kan tot vocht-gesteente interactie leiden en resulteren in geo-chemische reacties, zoals ontbinding en her-kristallisatie, vervolgens resulteren in een gewijzigde mineralogie en structuur van het gesteente. Verder, is het mogelijk dat de kenmerken van de stroming en de elektrische respons wijzigen. De lokale, secundaire mineraal concentraties, de verschillen in kristalstructuur en de interactie van de verschillende bestanddelen werden gevalideerd door oppervlakte ladingsmetingen en de dispersie in de diëlektrische permittiviteit over een aantal frequenties. Op basis van het vastgestelde sedimentaire milieu en de aanwezige kenmerken van het gesteente, werd, ten aanzien van de formatie op reservoir schaal, een algemeen begrip ontwikkeld.

De verworven informatie over de samenstelling van gesteente en korrel geometrie werd vervolgens zowel experimenteel en theoretisch bestudeerd op de gevoeligheid van mineralen in interactie tussen gesteente en vloeistof. De gevoeligheid hangt af van de variaties van de oppervlakte lading en bevochtigbaarheid van het gesteente, hetgeen kan resulteren leidt tot adsorptie en/of chemische mobilisatie. Het in-situ Bentheimer zandsteen oppervlakte gedrag in een wateroplossing (van water en pek) werd daarom onderzocht, met en zonder opgeloste CO<sub>2</sub>. De potentiële stromingsexperimenten tonen aan dat, met een stijgende CO<sub>2</sub> concentratie, de stabiliteit van de wateroppervlak afneemt aan de buitenkant van de porie. Niettemin, voor de CO<sub>2</sub> verzadiging onderzocht in deze studie, CO<sub>2</sub> opslagsterkte en capaciteit is gehandhaafd.

Experimentele resultaten van de poreuze matrix structuur van Bentheimer zandsteen, samen met experimentele resultaten van de stroomstudies in heterogene gesteente matrices en uit de literatuur, tonen aan dat oliewinning uit gebied met relatieve lage stroming beperkt is. Om deze reden concentreerde de volgende studie zich op het begrijpen van de mechanismes die plaats vinden in zones van een reservoir met minimale of "stilstaande" zones. Een glazen micromodel met een enkele doodlopende porie werd ontworpen om de stagnerende zone na te bootsen. Uit de studie bleek dat de efficiëntie van de oliewinning sterk afhankelijk is van het toegepaste CO<sub>2</sub> injectie scenario, van de geometrie van de matrix en van de residuele olieverzadiging. De algemene aard van de stroom werd bepaald door de fysieke eigenschappen van CO<sub>2</sub>-rijke vloeistoffen en hun interacties. Met de kennis hebben van het vloeistof-vloeistof gedrag op verschillende dichtheidsratio's en bij verschillende stroming, werd het fase-gedrag van het CW-olie systeem onderzocht in indirecte porie-schaal diffusie experimenten. Kortom, zwelling van olie als gevolg van CO<sub>2</sub> verspreiding onder  $P$ - $T$  voorwaarden werd na verloop van tijd geregistreerd en gevisualiseerd. Druk en terugwinning van olie treedt op afhankelijk van de samenstelling van de olie en een dominante rol voor verspreiding in de CW proces werd vastgesteld. Daarnaast werd een wiskundig model ontwikkeld met Comsol Multiphysics TM, dat de processen, waargenomen in de experimenten, verklaart. De door het model voorspelde resultaten werden gekoppeld aan de resultaten van de experimenten

en de diffusie-coëfficiënt werd bepaald. In alle experimenten verspreidde CO<sub>2</sub> in olie, resulterend in volume-expansie, geïnduceerde verlaging van de viscositeit, verbetering van de olie-water-verhouding voor mobiliteit, en, daardoor nam ook strijk efficiëntie toe van koolzuurhoudend water innundatie.

Het laatste deel van het proefschrift is gericht op het totaal van mechanismes met betrekking tot de controle van olie verplaatsing en CO<sub>2</sub> isolatie, de interacties tussen porie en matrix-systeem en tussen stroming en fase evenwicht. Koolzuurhoudende waterinjectie heeft de potentie van het combineren van oliewinning met CO<sub>2</sub>-opslag. Het geeft een stapsgewijze herwinning over secundaire overstroming en een effectieve wateropslag ten gevolge van afname van viscositeit. De laboratoriumresultaten kunnen worden gebruikt en ingevoerd als parameters voor upgrading en bouwen van een model voor drie-fase stroom in klastisch gesteente.



# ACKNOWLEDGEMENTS

At the end of this thesis, I would like to express my gratitude to people and institutions that have largely contributed to my project with their help, support, and guidance.

First of all, I would like to thank my promotor Prof. Pacelli Zitha who provided me with the opportunity to do Ph.D. research and offered me a large degree of freedom in organizing it, making it a truly rewarding experience. Dr. Karl-Heinz Wolf for taking the role of my daily supervisor. Thank you for supporting my ideas, for our discussions, for your patience reading my documents, especially when I was delivering them just before submission deadlines. This project would not be possible without financial support of CATO-2 that formulated and focused the research on the pathways to implementation of CCS. Many thanks to the CATO-2 “team” for all the efforts and commitments that made this program unique.

It has been a pleasure to conduct my research at the Laboratory of Geoscience and Engineering. Without the excellent support of all the technical staff, the experimental work performed during this project would not have been done. Especially, I would like to thank Marc Friebel for his continuous support, his “yes” to all my new ideas, his unbreakable commitment to deliver high-quality results and his enthusiasm in the lab. Marc, it was a great time to work with you. Karel Heller for his efforts, knowledge and extensive support in getting the experiments running. Michiel Slob, Henk van Asten and Jan Etienne for always helping me out when equipment was short or not working properly. I am also very grateful to Jolanda van Haagen-Donker for her patience in dealing with all my orders from all parts of the world. Ellen Meijvogel-de Koning, Wim Verwaal and Joost van Meel for their constant help with CT scanning. Dirk Delforterie and Jens van den Berg for their precious contributions with everything about rocks and samples. Apart from that, I would like to thank the High Voltage Laboratory, for the possibility of running my tests in their laboratory, which resulted in a fruitful collaboration between their and our department. It was a great pleasure to work and collaborate with all of you.

In addition, I would like to thank Prof. Evert Slob. Next to his valuable scientific contributions, his personal support was of great importance to me. His positive attitude and empathy made my life much easier. I am truly grateful to Koonraad Elewaut for his time and efforts to revise my papers right down to the last detail. His comments and suggestions have significantly improved its quality and resulted in a painless revision process. Further, I would like to thank the supporting staff of the Geoscience and Engineering Department. A special thanks to Hannie Zwieters for her constant contributions.

Even with all these names of people, the list of people to be acknowledged is not yet complete. Also, my great thanks to my colleagues at the Department that were accompanying me during the “long and rocky” way of my Ph.D. Special thanks to your positive nature, friendship, support, and interest.

Last but not least, thanks to all those close to my heart, family and friends, without whose love, patience, understanding and support, this project would not have started,



would not have progressed and, most certainly, would not have been finished.

I am extremely grateful to have had the chance to get to know all of you and work together with you. Thank you very much for unforgettable 6 (uff) years!

## ABOUT THE AUTHOR

Anna Peksa was born on 4 September 1986 in Zakopane in Poland. In 2009, she obtained an M.Sc. degree in the field of Environmental Engineering Mechanical Engineering from the University of Science and Technology Cracow and a second M.Sc. degree in Applied Earth Sciences at the Delft University of Technology. In 2011, she started a PhD project at Delft University of Technology under the supervision of Prof. dr. Pacelli Zitha and dr. Karl-Heinz Wolf. In September 2015, she joined a one year research project in geothermal engineering. Since September 2016, she works as a reservoir engineer for Royal Dutch Shell.



# LIST OF PUBLICATIONS

## *Peer-reviewed journal papers*

1. **Peksa, A. E.**, Wolf, K. H. A., Slob, E. C., Chmura, L., & Zitha, P. L. (2017). *Original and pyrometamorphical altered Bentheimer sandstone; petrophysical properties, surface and dielectric behavior*. Journal of Petroleum Science and Engineering, **149**, 270-280.
2. **Peksa, A. E.**, Wolf, K. H. A., & Zitha, P. L. (2015). *Bentheimer sandstone revisited for experimental purposes*. Marine and Petroleum Geology, **67**, 701-719.

## *Conference proceedings*

1. Ameri, A., Nick, H. M., Ilangovan, N., & **Peksa, A. E.** (2016, November 7). *A Comparative Study on the Performance of Acid Systems for High Temperature Matrix Stimulation*. Society of Petroleum Engineers. doi:10.2118/183399-MS.
2. **Peksa, A. E.**, Wolf, K.-H. A. A., Daskaroli, M., & Zitha, P. L. J. (2015, June 1). *The Effect of CO<sub>2</sub> Gas Flooding on Three Phase Trapping Mechanisms for Enhanced Oil Recovery and CO<sub>2</sub> Storage*. Society of Petroleum Engineers. doi:10.2118/174283-MS.
3. **Peksa, A. E.**, & Wolf, K. H. A. A. (2014, June). *Experimental Work on the Molecular Diffusion in the Carbonated Water (CW) Flooding Process at Reservoir Conditions*. In 76th EAGE Conference and Exhibition 2014.
4. Chmura, L., Kanaas, B., **Peksa, A. E.**, Morshuis, P. H. F., Smit, J. J. (2014). *Effect of water on the service ability of oil-filled 10 kV switch-gear*. International Conference on Condition Monitoring and Diagnosis 2014.
5. **Peksa, A. E.**, Wolf, K. H. A., & Zitha, P. L. (2013, October). *Molecular Diffusion of CO<sub>2</sub> From Carbonated Water (CW) Into the Oil-Experimental Observations*. In SPE Asia Pacific Oil and Gas Conference and Exhibition. Society of Petroleum Engineers.
6. **Peksa, A. E.**, Zitha, P. L. J., & Wolf, K. H. A. A. (2013, June). *Role of rock surface charge in the carbonated water flooding process*. In 75th EAGE Conference & Exhibition incorporating SPE EUROPEC 2013.
7. **Peksa, A. E.**, Wszolek, G. (2008). *Mechanical vibration caused by drilling machines during engineering works as a factor detrimental to human health and environment*. Materials for the 15th Conference of Acoustic and Biomedical Engineering.

## *Other*

1. **Peksa, A. E.**, Friebel, M. & Tang, T. (2015, June). *Equilibrar. Equilibrar Plays Key Role in Research of Enhanced Oil Recovery Using Carbonated Water Flooding*. Fletcher, North Carolina.